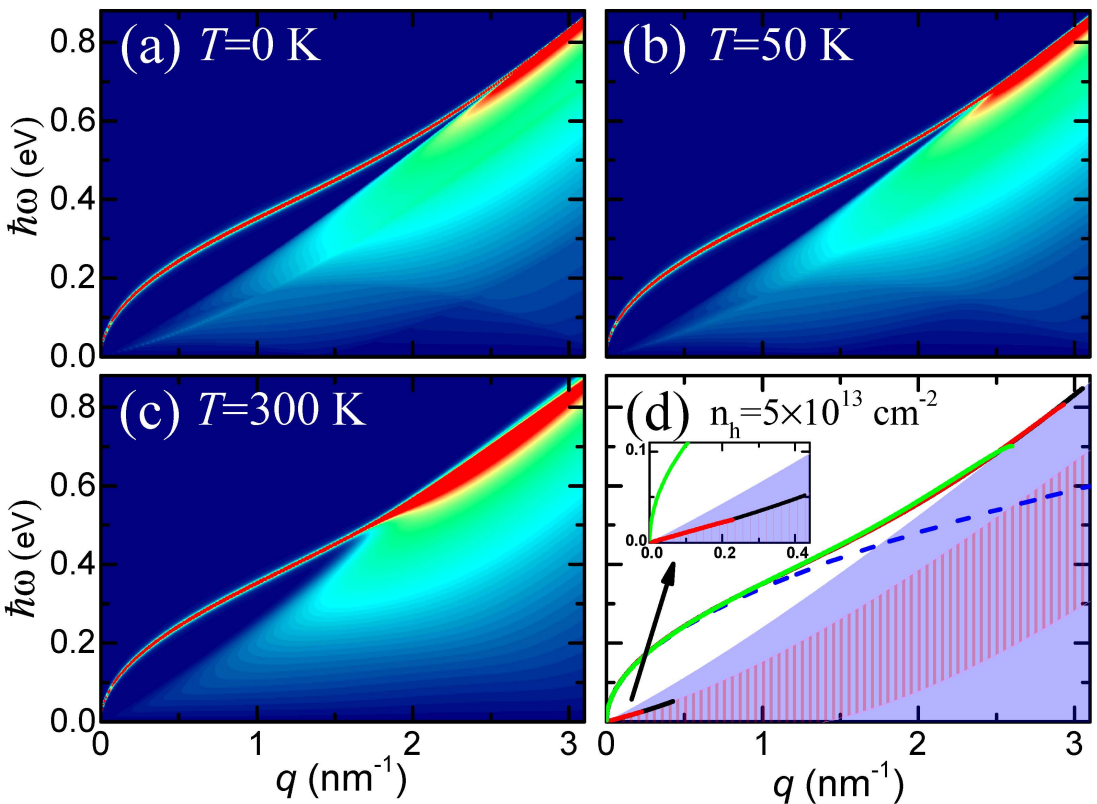


# Theoretical study of the optoelectronic properties of new type 2DEG materials: multilayer graphene and monolayer MoS<sub>2</sub>

Proefschrift voorgelegd tot het behalen van de graad van doctor in de wetenschappen aan de Universiteit Antwerpen te verdedigen door

Yiming Xiao



Theoretical study of the optoelectronic properties of new type 2DEG materials: multilayer graphene and monolayer MoS<sub>2</sub>

Yiming Xiao

Promotores  
Prof. Dr. Wen Xu  
Prof. Dr. François Peeters  
Dr. Ben Van Duppen

Faculteit Wetenschappen  
Departement Fysica  
Antwerpen 2017



云南大学  
Yunnan University

Universiteit  
Antwerpen

分类号 0469 密级 公开  
UDC \_\_\_\_\_ 编号 \_\_\_\_\_

# 雲南大學

## 博士研究生学位论文

题 目 新型二维电子气材料多层石墨烯和  
单层二硫化钼光电特性的理论研究

Title Theoretical study of the optoelectronic properties of new type  
2DEG materials: multilayer graphene and monolayer MoS<sub>2</sub>

学院（所、中心） 物理与天文学院

专业名称 凝聚态物理

研究方向 半导体材料光电特性

研究生姓名 肖宜明 学号 22013000192

导师姓名 徐文 职称 教授

导师姓名 Francois Peeters 职称 教授

导师姓名 Ben Van Duppen 职称 博士

2017 年 6 月



Faculteit Wetenschappen  
Departement Fysica

School of Physics  
and Astronomy

## Theoretical study of the optoelectronic properties of new type 2DEG materials: multilayer graphene and monolayer MoS<sub>2</sub>

Theoretische studie van de opto-elektronische  
eigenschappen van de nieuwe types  
tweedimensionaal elektronen gasses: multilaag  
grafeen en MoS<sub>2</sub>

Proefschrift voorgelegd tot het behalen  
van de graad van doctor in de wetenschappen  
aan de Universiteit Antwerpen te verdedigen door

**Yiming Xiao**

### Promotors

Prof. Dr. Wen Xu

Prof. Dr. François Peeters

Dr. Ben Van Duppen

Kunming June 2017

## **Members of the Jury:**

### **Chairman**

Prof. Dr. Jinming Cai, Kunming University of Science and Technology, China

### **Supervisors**

Prof. Dr. Wen Xu, Yunnan University, China

Prof. Dr. François Peeters, Universiteit Antwerpen, Belgium

### **Members**

Prof. Dr. Yingkai Liu, Yunnan Normal University, China

Prof. Dr. Yanfei Lv, Yunnan University, China

Prof. Dr. Zhu Liu, Yunnan University, China

Prof. Dr. Yao He, Yunnan University, China

扉页：

## 论文独创性声明及使用授权

本论文是作者在导师指导下取得的研究成果。除了文中特别加以标注和致谢的地方外，论文中不包含其他人已经发表或撰写过的研究成果，不存在剽窃或抄袭行为。与作者一同工作的同志对本研究所做的任何贡献均已在论文中作了明确的说明并表示了谢意。

现就论文的使用对云南大学授权如下：学校有权保留本论文（含电子版），也可以采用影印、缩印或其他复制手段保存论文；学校有权公布论文的全部或部分内容，可以将论文用于查阅或借阅服务；学校有权向有关机构送交学位论文用于学术规范审查、社会监督或评奖；学校有权将学位论文的全部或部分内容录入有关数据库用于检索服务。

（内部或保密的论文在解密后应遵循此规定）

研究生签名：\_\_\_\_\_ 导师签名：\_\_\_\_\_ 日 期：\_\_\_\_\_



## 摘要

传统二维电子气材料在过去的几十年里对科技的进步起到了极大的推动作用。石墨烯的发现开启了研究新型原子层厚度级二维电子气材料的热潮。对这类新型二维电子气材料光电性质的研究能够加深对材料的理解并能探索其潜在的应用价值。在本学位论文中，我们对多层石墨烯和单层二硫化钼系统的光电特性进行了理论研究。石墨烯的层数和堆垛次序会影响石墨烯系统的电子结构以及光学性质。单层二硫化钼在几年前被成功的制备出来，其中较强的内秉自旋-轨道耦合和奇异的谷选择性吸收定则使得单层二硫化钼成为研究谷电子学和自旋电子学的绝佳材料。单层二硫化钼中对自旋-轨道耦合的人工调控可以通过 Rashba 效应来实现，并且单层二硫化钼的光学性质同样会受到影响。等离激元光子学是当前极具前景的科学领域之一。在本学位论文中，我们使用平衡方程法和 Kubo-Greenwood 公式来计算材料的光电导。在无规则相近似 (RPA) 下计算了动态介电函数和等离激元特性。本学位论文主要的研究内容和结果如下：

(1) 研究和比较了单层和多层石墨烯系统的光电导和光透射系数。证实了  $N$  层石墨烯系统在可见光区域的普适光电导为  $\sigma_0^N = N\pi e^2/(2h)$ 。对于层数大于三的奇数层 AB-堆垛多层石墨烯系统，可以看到由迷你带隙引起的吸收边并且吸收边的数量和位置由多层石墨烯的层数决定。同时，可以看到这些石墨烯系统中有一个从红外到太赫兹频段 (0.2 – 150 THz) 的光吸收窗口。这个光学吸收窗口的深度和宽度不仅受到温度和电子浓度的调节，同样可以被石墨烯的层数和堆垛次序来调节。此项研究为不同层数和堆垛次序多层石墨烯在红外和太赫兹频段的光学和光电子器件上的应用打下了理论基础。

(2) 研究了 Rashba 效应对  $n$ -型和  $p$ -型掺杂单层二硫化钼光电特性的影响。单层二硫化钼系统的光电导由 Kubo-Greenwood 公式计算得到。我们可以看到 Rashba 效应所引起的自旋-翻转跃迁能够导致低能量频段吸收谱中的宽吸收峰或光吸收窗口。吸收峰或吸收窗口的位置、宽度、以及形状可以被温度、载流子浓度和 Rashba 自旋-轨道耦合强度所调节。这项研究为单层二硫化钼在红外和太赫兹频段的频率可调器件应用提供了理论依据。

(3) 在有 Rashba 效应和没有 Rashba 效应的情况下分别使用四带哈密顿量模型和二带哈密顿量模型计算了单层二硫化钼的带间跃迁光电导。在 Rashba 自旋-轨道耦合参数趋于零时，四带模型与二带模型的结果是相同的。Rashba 效应会增加带间跃迁光吸收通道的数量并对带隙附近的光电导曲线/光吸收产生影响，表明可以利用 Rashba 效应来调节带隙附近的光吸收。

(4) 在无规则相近似下，研究了在有圆偏振光场泵浦激发和无光场激发下单层二

硫化钼多组份系统的动态介电函数和等离激元特性。单层二硫化钼多组份系统的等离激元特性分别使用有质量狄拉克-费米子 (MDF) 模型和二维抛物带 (2DPB) 模型进行了计算。单层二硫化钼的电荷等离激元模式与二维电子气中的等离激元模式类似。更有趣的是，在多组份系统的单层二硫化钼系统中存在新奇的弱阻尼线性声学等离激元模式。这项研究进一步阐明了单层二硫化钼系统中存在的不同等离激元模式的物理机制。

(5) 考虑放置在二氧化硅薄片上的单层二硫化钼系统，计算了单层二硫化钼中等离激元与内秉光学声子和衬底中表面光学声子耦合下耦合的等离激元-声子模式。耦合的等离激元-声子模式的色散关系能够被载流子浓度进行有效的调节。突出了衬底中的表面光学声子会对单层二硫化钼系统等离激元特性产生影响的特点。

本学位论文中的研究表明多层石墨烯和单层二硫化钼系统具有优异的光电特性并可以应用于工作在红外和太赫兹频段范围内频率可调的光学和光电子学器件。

**关键词：** 多层石墨烯；单层二硫化钼；Rashba 自旋-轨道耦合；光电导；等离激元

## Abstract

Traditional two dimensional electron gas materials have played a significant role in promoting the development of science and technology over the past few decades. Since the discovery of graphene, the researches of new type of atomic thin two dimensional materials have received a great attention. The investigation of new type of two dimensional electron gas material's optical property can enrich the understanding of it and explore the potential applications. In this thesis, we conduct a theoretical study on the optoelectronic of multilayer graphene and monolayer MoS<sub>2</sub> (ML-MoS<sub>2</sub>) systems. The layers number and stacking order can affect the electronic structure and optical property of graphene system. ML-MoS<sub>2</sub> was successful fabricated in a few years ago. The presence of a strong intrinsic spin-orbit coupling (SOC) and the curious valley contrasting selective rules have led to the proposal that ML-MoS<sub>2</sub> can be an interesting material for valleytronics and spintronics. The artificial manipulation of SOC in ML-MoS<sub>2</sub> can be realized through the Rashba effect and the optical property is also affected. At present, plasmonics is one of the most promising areas of scientific research. In this thesis, we use the balance equation approach and Kubo-Greenwood formula to calculate the optical conductivity. The dynamical dielectric function and plasmon property are calculated under Random Phase Approximation (RPA). The main contents and results of this thesis are as follows.

(1) The optical conductivity and transmission coefficient of monolayer and multilayer graphene systems are examined and compared. The universal optical conductivity  $\sigma_0^N = N\pi e^2/(2h)$  for  $N$  layer graphene systems in the visible region are verified. For  $N \geq 3$  layer graphene, the mini-gap induced absorption edges can be observed in odd layers AB-stacked multilayer graphene, where the number and position of the absorption edges are decided by the layers number. Meanwhile, we can observe optical absorption windows for those graphene systems in the infrared to terahertz (THz) bandwidth (0.2 – 150 THz). The depth and width of the absorption window can be tuned not only via varying temperature and electron density but also by changing the number of graphene layers and the stacking order. This study has laid a theoretical foundation for the application of multilayer graphene with different layers and stacking orders in optical and optoelectronic devices working in infrared and THz bandwidths.

(2) We investigate the effect of Rashba SOC on the optoelectronic property of *n*- and *p*-type ML-MoS<sub>2</sub>. The optical conductivity is calculated within the Kubo-Greenwood formalism. We find that the spin-flip transitions enabled by the Rashba effect result in a wide absorption window in low frequency optical spectrum. We find that the position,

width, and shape of the absorption peak or absorption window can be tuned by varying temperature, carrier density and the strength of Rashba SOC parameter. This study provides a theoretical basis for the application of ML-MoS<sub>2</sub> in frequency tunable devices working in infrared and THz range.

(3) The interband optical conductivity of ML-MoS<sub>2</sub> with and without Rashba effect are calculated with the four band and two band hamiltonian modes, respectively. When the Rashba parameter approaches to zero, the results of four band model are identical to the two band model. The Rashba effect will increase the number of optical absorption channels and affects the optical conductivity curve near the band gap, which indicates that Rashba effect can be used to adjust the light absorption near the band gap spectrum range.

(4) We investigate the dynamical dielectric function and plasmons of ML-MoS<sub>2</sub> under RPA with and without the circularly polarized optical pumping. The plasmons of the multi-component ML-MoS<sub>2</sub> system has been calculated with the massive Dirac fermion (MDF) and two dimensional parabolic band (2DPB) models. The charge plasmon mode in ML-MoS<sub>2</sub> is similar to a traditional 2D electron gas. More interesting, novel weakly damped linear acoustic plasmons could be observed in a multi-component ML-MoS<sub>2</sub> system. This study further elucidates the physical mechanism of different plasmon modes in ML-MoS<sub>2</sub> system.

(5) Considering a ML-MoS<sub>2</sub> layer placed on a SiO<sub>2</sub> wafer, we calculate the intrinsic optical phonon and substrate surface optical phonon coupled plasmon-phonon modes in ML-MoS<sub>2</sub>. The dispersion relation of the coupled plasmon-phonon modes can be effectively tuned by carrier density. This study shows that surface optical phonon in the substrate would have an impact on plasmon property of ML-MoS<sub>2</sub>.

The study in this thesis shows that multilayer graphene and ML-MoS<sub>2</sub> systems have excellent optoelectronic properties and can be applied as frequency tunable optical and optoelectronic devices working in infrared to terahertz bandwidth.

**Keywords:** Multilayer graphene; Monolayer MoS<sub>2</sub>; Rashba spin-orbit coupling; Optical conductivity; Plasmon

## Abstract

Materialen met een traditioneel tweedimensionaal elektronengas hebben een belangrijke rol gespeeld in de ontwikkeling van wetenschap en technologie in de laatste decennia. Sinds de ontdekking van grafeen is het onderzoek naar nieuwe types atomair dunne tweedimensionale materialen ook enorm toegenomen. Deze nieuwe tweedimensionale materialen onderzoeken op hun optische eigenschappen kan het begrip ervan vergroten en kan nieuwe potentiële toepassingen voortbrengen. In deze thesis voeren we een studie uit naar de opto-elektronische eigenschappen van grafeen multilagen en monolaag MoS<sub>2</sub> (ML-MoS<sub>2</sub>). Het aantal lagen en de wijze van stapeling kan de elektronische en optische eigenschappen van grafeen beïnvloeden. ML-MoS<sub>2</sub> is enkele jaren geleden voor de eerste keer gefabriceerd. Zijn sterke spin-baan koppeling (SBK) en de speciale vallei afhankelijke selectiecriteria hebben ertoe geleid dat ML-MoS<sub>2</sub> meer en meer beschouwd wordt als mogelijke kandidaat voor valleitronica en spintronica. SBK in ML-MoS<sub>2</sub> kan door middel van Rashba SBK artificieel worden aangepast en zo de optische eigenschappen van het materiaal aanpassen. Vandaag de dag is plasmonica één van de meest belovende wetenschapsvelden. In deze thesis maken we gebruik van de evenwichtsvergelijking en de Kubo-Greenwood formule om de optische conductiviteit te berekenen. De dynamische dielektrische functie en plasmon eigenschappen zijn binnen de willekeurige fase benadering (WFB) berekend. We kunnen de belangrijkste punten in deze thesis als volgt samenvatten:

- (1) De optische conductiviteit en transmissie coëfficiënt van monolaag en multilaag grafeen zijn berekend en met elkaar vergeleken. De universele conductiviteit  $\sigma_0^N = N\pi e^2/(2h)$  voor een  $N$ -laag grafeen systeem in het visuele deel van het spectrum is geverifieerd. Voor  $N \geq 3$  wordt een mini bandkloof geïnduceerd wat leidt tot absorptie randen die geobserveerd kunnen worden in AB gestapeld multilaag grafeen met een oneven aantal lagen. De positie van de randen wordt bepaald door het aantal lagen. Tegelijk zien we ook dat er absorptie vensters zijn voor deze systemen in het IR tot het THz regime (0.2 – 150 THz). De diepte en breedte van deze vensters kan worden aangepast, niet enkel via het variëren van de temperatuur en elektronen dichtheid, maar ook door het aantal grafeen lagen en diens stapel orde te wijzigen. Deze studie heeft een theoretisch fundament gelegd voor de toepassing van grafeen multilagen met verschillende lagen en stapel orde in optische en opto-elektronische toepassingen die werken in het IR en THz gebied.
- (2) We onderzoeken het effect van Rashba SBK op de opto-elektronische eigenschap-

pen van *n*- en *p*-type ML-MoS<sub>2</sub>. De optische conductiviteit is berekend binnen het Kubo-Greenwood formalisme. We vinden dat de spin-flip transities die mogelijk gemaakt worden door het Rashba effect resulteren in een breed absorptie venster bij lange golflengten. We vinden dat de positie, de breedte en de vorm van dit venster kan worden aangepast door de temperatuur, landingsdragerdichtheid en sterkte van de Rashba SBK parameter te variëren. Deze studie zorgt voor een theoretische basis voor de toepassing van ML-MoS<sub>2</sub> in toepassingen waarbij de frequentie gevarieerd moet kunnen worden en die actief zijn in het IR tot THz gebied.

(3) De interband optische conductiviteit van ML-MoS<sub>2</sub> is berekend binnen een vier-en twee-band Hamiltoniaan met en zonder Rashba effect. Wanneer de Rashba parameter nul nadert zijn de resultaten van een vierbandsmodel benaderend gelijk aan die van het tweebandsmodel. Het Rashba effect zal het aantal absorptiekanalen doen stijgen en heeft een invloed op de kromming van de optische conductiviteit in de buurt van de bandkloof. Dit wijst erop dat het Rashba effect gebruikt kan worden om absorptie van licht met fotonenergie in de buurt van de grootte van de bandkloof kan beïnvloeden.

(4) We onderzoeken de dynamische dielektrische functie en plasmonen in ML-MoS<sub>2</sub> binnen de WFB met en zonder circulair gepolariseerd licht. De plasmonen van het multi-component ML-MoS<sub>2</sub> systeem zijn berekend met een model van massieve Dirac Fermionen en een twee-dimensionaal parabolisch band model. De geladen plasmon tak in ML-MoS<sub>2</sub> is gelijkaardig aan die van een traditioneel 2D elektronen gas. Meer interessant is echter nieuwe licht gedempte akoestische modi die ook geobserveerd kunnen worden in multicomponent ML-MoS<sub>2</sub> systemen. Deze studie legt verder ook het fysische karakter bloot van verschillende plasmon modi in ML-MoS<sub>2</sub> systemen.

(5) We beschouwen een ML-MoS<sub>2</sub> laag geplaatst op een SiO<sub>2</sub> wafer. We berekenen de intrinsieke optische fononen en de substraatafhankelijke oppervlakte optische fonen die gekoppeld zijn aan plasmon-fonon modi in ML-MoS<sub>2</sub>. De dispesierelatie van gekoppelde plasmon-fonon modi kan effectief aangepast worden door de ladingsdichtheid. Deze studie toont aan dat oppervlakte optische fononen in het substraat een grote invloed kunnen hebben op de plasmon eigenschappen van ML-MoS<sub>2</sub>.

Het onderzoek in deze thesis toont aan dat grafeen multilagen en ML-MoS<sub>2</sub> systemen uitzonderlijke opto-elektronische eigenschappen hebben en toegepast kunnen worden in frequentie aanpasbare optische en opto-elektronische toepassingen die werken in het infrarood tot terahertz gebied van het elektromagnetische spectrum.

**Trefwoorden:** multilaag grafeen; monolaag MoS<sub>2</sub>; Rashba Spin-lane coupling; optische conductiviteit; plasmonen

# 目 录

<b>摘要</b>	<b>I</b>
<b>目录</b>	<b>VII</b>
<b>第一章 引言</b>	<b>1</b>
1.1 传统二维电子气 . . . . .	3
1.2 新型二维电子气材料 . . . . .	4
1.2.1 石墨烯的发现及其重要性质 . . . . .	5
1.2.2 单层过渡金属硫化物 . . . . .	10
1.3 太赫兹光谱学 . . . . .	12
1.4 自旋-轨道耦合相互作用 . . . . .	14
1.4.1 Rashba 自旋-轨道耦合 . . . . .	14
1.4.2 Dressalhaus 自旋-轨道耦合 . . . . .	15
1.5 等离激元光子学 . . . . .	16
1.6 本论文的创新性、研究意义和研究内容 . . . . .	17
<b>第二章 研究方法和基本理论</b>	<b>21</b>
2.1 半经典玻尔兹曼方程及平衡方程法 . . . . .	21
2.1.1 玻尔兹曼方程 . . . . .	21
2.1.2 费米黄金定律 . . . . .	22
2.1.3 光电导的能量平衡方程 . . . . .	23
2.2 线性响应理论 . . . . .	25
2.3 电导的 Kubo 公式 . . . . .	26
2.4 无规则相近似 (RPA) . . . . .	28
2.5 RPA 介电函数 . . . . .	29
<b>第三章 单层和多层石墨烯系统的红外到太赫兹光吸收窗口</b>	<b>31</b>
3.1 单层和多层石墨烯系统的光电导 . . . . .	32
3.1.1 单层石墨烯 . . . . .	32
3.1.2 AB-堆垛双层石墨烯 . . . . .	33

3.1.3 ABC-堆垛三层石墨烯	34
3.1.4 AB-堆垛多层石墨烯	35
3.1.5 ABC-堆垛多层石墨烯	36
3.2 结果和讨论	37
3.3 本章小结	42
<b>第四章 Rashba 自旋-轨道耦合下单层二硫化钼红外到太赫兹波段的光电导</b>	<b>45</b>
4.1 单层二硫化钼在 Rashba 自旋-轨道耦合下的电子结构	46
4.2 单层二硫化钼在 Rashba 效应下的光电导	48
4.3 结果与讨论	50
4.4 本章小结	59
<b>第五章 Rashba 自旋-轨道耦合下单层二硫化钼在可见光波段范围的光吸收</b>	<b>61</b>
5.1 单层二硫化钼在零 Rashba 自旋-轨道耦合下的电子结构	61
5.2 单层二硫化钼在无 Rashba 自旋-轨道耦合下的光电导	62
5.3 结果与讨论	63
5.4 本章小结	65
<b>第六章 圆偏振光场泵浦下单层二硫化钼中的多组份等离激元</b>	<b>67</b>
6.1 理论方法	68
6.1.1 电子能带结构和载流子浓度	68
6.1.2 光泵浦下准平衡系统	72
6.1.3 无规则相近似 (RPA) 下的极化函数和等离激元	73
6.2 结果与讨论	76
6.2.1 圆偏振光下的光吸收	76
6.2.2 有效质量模型和双曲线模型的比较	78
6.2.3 有限温度下的自旋极化二组份系统	81
6.2.4 自旋极化的三组份系统	82
6.2.5 四组份系统	87
6.3 本章小结	88
<b>第七章 单层二硫化钼在二氧化硅衬底上耦合的等离激元-声子模式</b>	<b>91</b>
7.1 LO 声子和 SO 声子参与下耦合的等离激元-声子模式	91
7.2 结果与讨论	93
7.3 本章小结	96

## 目 录

---

<b>第八章 论文总结与展望</b>	<b>97</b>
8.1 论文总结 . . . . .	97
8.2 下一步研究计划和展望 . . . . .	98
<b>附录 A 单层二硫化钼极化函数的解析解表达式</b>	<b>101</b>
A.1 RPA 介电函数和自由极化函数 . . . . .	101
A.2 极化函数的相关解析表达式 . . . . .	102
<b>附录 B 单层二硫化钼中电子-电子相互作用的形状因子</b>	<b>107</b>
B.1 电子-电子相互作用的形状因子 . . . . .	107
B.2 长波极限下电子-电子相互作用形状因子 . . . . .	107
<b>附录 C 计算中用到的重要公式</b>	<b>109</b>
C.1 直积 . . . . .	109
C.2 泡利矩阵 . . . . .	109
C.3 Kramers-Kronig (K-K) 关系 . . . . .	109
C.4 极化函数计算中用到的积分公式 . . . . .	110
<b>附录 D The published papers and preprint related to the thesis</b>	<b>111</b>
<b>参考文献</b>	<b>i</b>
<b>攻读博士期间发表论文、获得奖励与科研项目参与情况</b>	<b>xvii</b>
<b>致谢</b>	<b>xix</b>



# 第一章 引言

材料是人类进行生产活动和生活的基础，材料学的发展对人类生产力的提高和社会的发展起到了无与伦比的推动作用。往往新技术是在基于新材料发现的前提下诞生的。新材料和新器件结构研究的不断进步和发展是推动整个人类社会不断进步的源动力。而凝聚态物理学的研究则是推动整个材料领域不断发展进步并探究其物理机制及内涵的基础。

凝聚态物理学是目前物理学发展最大的学科分支之一<sup>[1]</sup>，是基于固体物理学<sup>[2]</sup> 和半导体物理学等学科发展起来并与其它学科如化学、材料学、纳米科学技术等学科领域发生交叉的描述原子和分子尺度材料电子能带结构及各种物理性质的重要学科。在过去的几十年里，凝聚态物理学的发展所带来的成果促进了社会的变革并使人类的生活方式发生了翻天复地的变化。在如今日常用到的各种高科技电子产品如计算机、手机和电池等都离不开凝聚态领域不断的创新和突破。不论是在当今还是未来，凝聚态物理学都是最富有挑战性和最具有社会生产推动力的领域。而且在国家战略上，加大对这个领域的投入和加强这个学科的发展能极大的促进我国在高科技和工程技术方面的发展，并且能在将来的国际竞争中占领领先地位。

在 20 世纪中叶，半导体科学的研究方兴未艾，其中最重要的便是 p-n 结和晶体管的发明。基于 p-n 结的电子元件如今出现在人们日常生活中的方方面面。而在 1947 年美国物理学家巴丁、肖克莱和布拉顿发明的晶体管（见图 1.1），并于 1956 年获得诺贝尔物理学奖，则是 20 世纪最重要的科技成就之一。众所周知，现代科技改变人们生



图 1.1：巴丁与肖克莱、布拉顿发明的首个晶体管的复制品

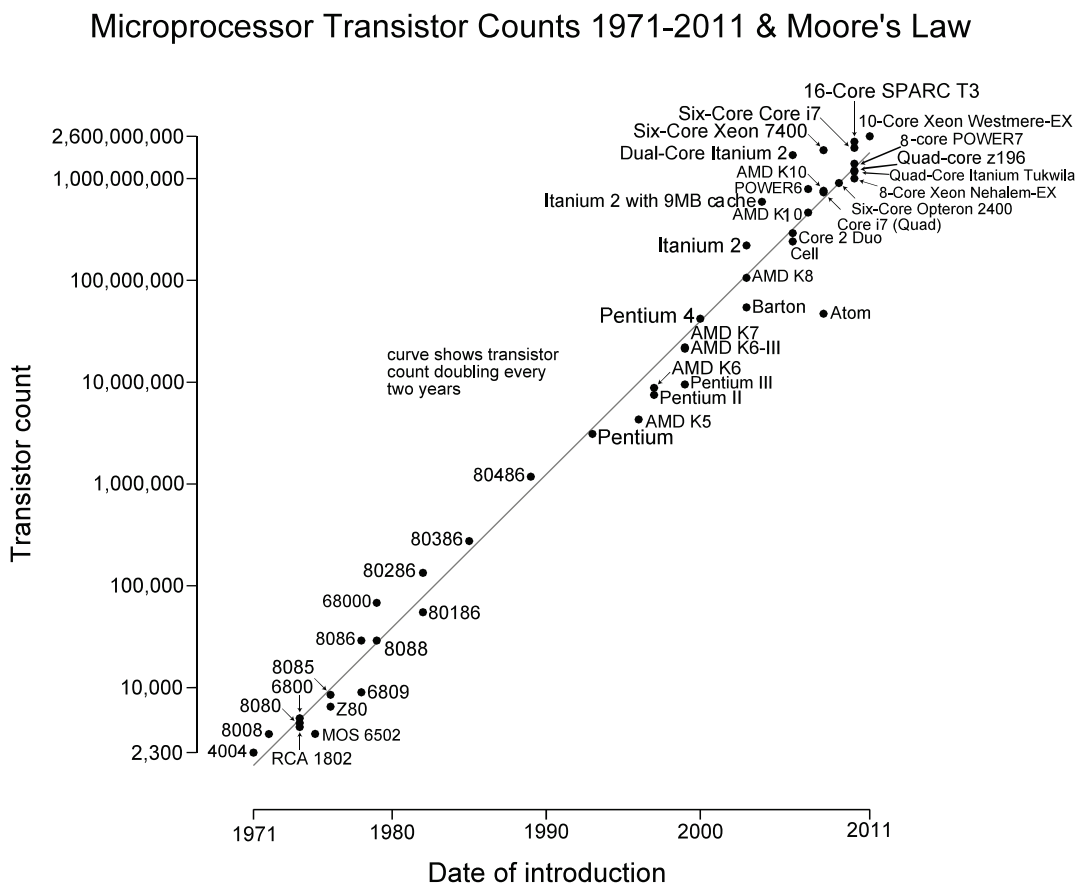


图 1.2: CPU 中晶体管数量随时间的变化关系以及摩尔定理的拟合

活方式最重要的成就就是基于晶体管集成化芯片的诞生。在近 40 年里，计算机从神秘的巨型机器变成如今人们日常生活中必不可少的工具，同时信息通过互联网得到迅速的传播。与此同时，软件技术和多媒体技术的不断发展也丰富着每个人的日常生活。在这几十年的发展当中，摩尔定理一直适用于计算机中央处理器 (Central Processing Unit; CPU) 的发展规律。50 年前，英特尔公司 (Intel Corp.) 的创始人之一戈登·摩尔 (Gordon Moore) 对计算机芯片的发展提出预言：在单位价格不变的时候，硅芯片的计算处理性能将每隔 18–24 月时便会翻一翻<sup>[3]</sup>。图 1.2 给出了近 40 年的时间里计算机中央处理器中晶体管数量随时间的变化关系和摩尔定理的曲线拟合。摩尔定理深刻的揭示了半导体信息科技产业迅猛发展的规律。

然而随着时间的推移，人们发现摩尔定理并不能无限期的应用于目前基于硅材料的半导体芯片制造。因为受物理规律的限制，当晶体管的尺寸做到足够小的时候，控制电流的晶体管门电极 (transistor gate) 以及晶体管的氧化栅极 (gate oxide) 之间的距离将会非常接近。因此，晶体管中将发生电子漂移现象 (electrons drift)。如果产生了这种情况，晶体管在工作过程中将会失去可靠性。研究表明，传统的硅基晶体管的尺寸无法小于 5 纳米。而目前市面上高端芯片中晶体管的工艺已经达到了 14 纳米。因

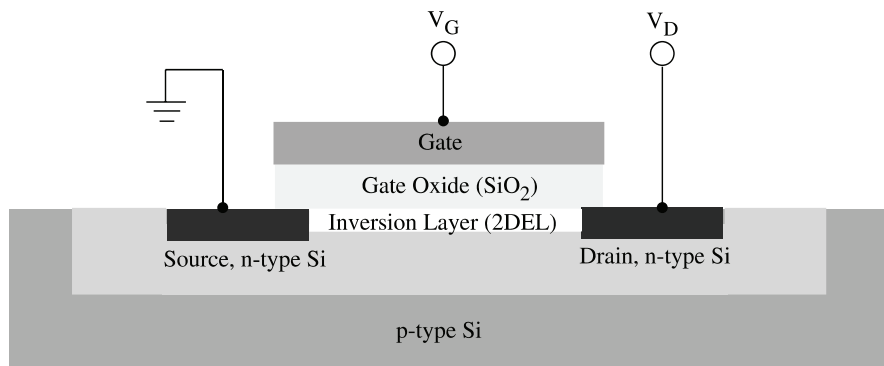


图 1.3: 金属氧化物半导体场效应晶体管 (MOSFETs) 的器件结构示意图<sup>[6]</sup>。门电压所产生的电势改变了反型层中的载流子浓度因此能够控制源极和漏极之间的电流

而，摩尔定理所预示的增长在未来的十几年之后将达到瓶颈。为了推动电子信息领域的不断进步与创新，人们将几十年后延续摩尔定律的期望寄托在基于新材料的先进晶体管器件上。

## 1.1 传统二维电子气

二维电子气 (two dimensional electron gas; 2DEG) 的这一概念是由 Fowler, Fang, Howard 和 Stiles 在 1966 年首次提出的<sup>[4]</sup>。一般是指材料中电子能在 x-y 平面上进行运动而在 z 方向上受到较大势场的限制情况下电子特殊行为的物理模型上的定义。同时，对于 p-型掺杂材料中具有类似行为的空穴则被称作二维空穴气体 (two dimensional hole gas; 2DHG)。通常来说，在半导体异质节、半导体超晶格中和液氦表面的电子可以表现出准二维电子气的行为<sup>[5]</sup>。

最常见的二维电子气是金属氧化物半导体场效应晶体管 (metal oxide semiconductor filed effect transistor; MOSFETs) 中的电子层。图 1.3 给出了 MOSFETs 器件的结构示意图<sup>[6]</sup>。从图 1.3 中可以看到，当晶体管工作在反型模式时，氧化电极层下面的电子被限制在半导体-氧化物的界面反型层，因而能非常好的占据在限定的能级上。近似的来看，只有最低的能级被电子占据，因而电子在垂直方向上的运动可以被忽略。与此同时，电子能够在平行界面内自由运动，因此是准二维的系统。

其它实现二维电子气的方法如高电子迁移率晶体管 (high electron mobility transistors; HEMTs) 和矩形量子阱。HEMTs 是利用两种半导体材料的异质结来将电子限定在三角型量子阱中。HEMTs 中被局域的电子能表现出比 MOSFETs 更高的迁移率。由两种不同禁带宽度材料组成的邻近空间结构的异质结界面能够将电子限定在矩形的量子阱中。选择不同的材料和合金的成分可以自由控制二维电子气中的载流子浓度。二十世纪下半叶里半导体物理学的蓬勃发展对我们探索和研究低维电子气系统的能力与手段有着巨大的影响。

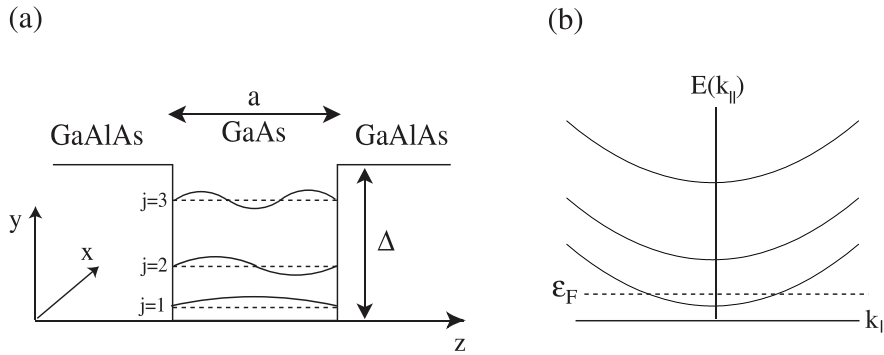


图 1.4: GaAs-GaAlAs 量子阱的结构示意图<sup>[6]</sup>。(a) 垂直于平面  $z$  方向的量子化能级和波函数。  
(b) 电子能级的能量随平面波矢的变化关系。在示例中仅有最低的子带被电子占据

目前已经能够成功制备基于 Si 和 GaAs 的高质量量子阱，其中载流子在一个空间方向的运动是量子化的。图 1.4 给出了量子阱的结构示意图。在最简单的情况下，由于只考虑其中的电子或空穴在量子阱 ( $x-y$ ) 平面上的运动，因而表现出自由量子粒子的特性。因而，系统中的能级由 ( $x-y$ ) 平面上的波矢  $k_{\parallel}$  表示，同时  $z$  方向上由离散指数  $j = 1, 2 \dots$  表示。如图 1.4 所示，量子阱中的整个能级谱由一系列有着不同  $j$  指数的二维子能带组成。根据基本的量子力学原理，子带能级的底端有着能量关系  $E_j = \hbar^2 j^2 / (2ma^2)$  其中  $a$  是量子阱的宽度。当  $a$  足够小的时候，可以使得两个最低子能带之间的能量间距比平面内运动的动能大得多。在这种情况下，只有最低的子带被电子占据并且它们的电子能量只取决于二维波矢  $k_{\parallel}$ 。由于系统中的电子没有足够的能量激发到更高的子带上，因而通过量子阱可以有效的实现二维电子气。

二维电子气同样可以在液氦的表面得到。电子可以在液氦的表面自由移动，同时有一个大约为 1 eV 的势垒阻止电子向液氦内部扩散。在这种情况下，可以得到区域电荷密度在  $10^9 \text{ cm}^{-2}$  量级的二维电子气系统<sup>[6]</sup>。

1982 年，日本物理学家 T. Ando 对传统二维电子气的研究现状及其电子性质做了系统性的总结<sup>[5]</sup>。

## 1.2 新型二维电子气材料

随着 2004 年石墨烯革命性的发现<sup>[7]</sup>，单原子层二维材料所具备的独特物理性质激起了人们对新型二维单原子层材料探索的无尽热潮。与传统二维电子气材料需要特殊的方法和材料结构使得在  $z$  方向产生一个较大的限制势来迫使载流子在二维平面内运动不同，新型二维电子气材料通常是由单原子层或者少数原子数层沿着平面展开的二维材料。由于平面膜状材料天然的结构，其在平面外与空气或其它绝缘体材料的接触使得材料本身具有二维电子气材料的物理特性并且其能带结构等物理特性受到材料组成元素、原子排列结构的影响非常大，使得这类材料具有广阔的发展空间。

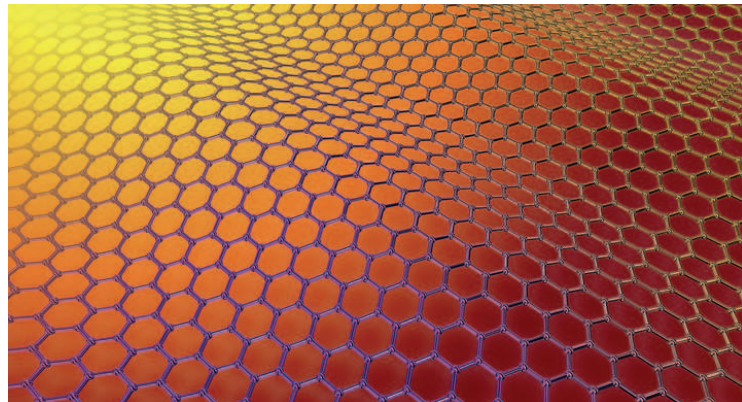


图 1.5: 石墨烯晶体的原子结构示意图

自石墨烯的发现之后，其它新型的单原子层二维电子气材料如硅烯 (silicene)<sup>[8]</sup>，锗烯 (germanene)<sup>[9]</sup>，锡烯 (stanene)<sup>[10]</sup>，过渡金属硫化物 (transitional metal dichalcogenides; TMDCs)<sup>[11]</sup>，和石墨烯-过渡金属硫化物复合结构<sup>[12]</sup> 等材料的相继发现更为新型二维电子气材料这一家族增添了更多新的成员，并鼓舞着人们在新材料的平台上对下一代高性能电子器件、光学器件和光电子器件进行研究。

### 1.2.1 石墨烯的发现及其重要性质

石墨烯是由碳原子紧密的排列在二维六角蜂巢晶格中的单层碳原子层 (如图 1.5 所示)。石墨烯是构建其它维度碳材料如零维的富勒烯、一维碳纳米管以及三维石墨的基础结构。理论上对石墨烯的研究已经进行了约 70 年<sup>[13-15]</sup>。早在 80 多年前，Landau 和 Peierls 认为严格的二维晶体材料由于热力学的不稳定性因而是不存在的<sup>[16, 17]</sup>。这个观点后来又被 Mermin 所拓展<sup>[18]</sup>，并被大量实验发现所支持。在相当长的一段时间内，单原子层的二维材料被认为是不存在的。直到 2004 年 K. S. Novoselov 和 A. K. Geim 成功的制备出单层石墨烯<sup>[7]</sup>，并因此项杰出的贡献而获得 2010 年的诺贝尔物理学奖。

#### 1.2.1.1 紧束缚法下石墨烯的电子结构

如图 1.6 所示，石墨烯中的碳原子排列在六方晶系结构上。这种结构可以看作每个元胞有着两个碳原子的三角形晶格，其晶格矢量可以写成

$$\mathbf{a}_1 = \left( \frac{3a}{2}, \frac{\sqrt{3}a}{2} \right), \mathbf{a}_2 = \left( \frac{3a}{2}, -\frac{\sqrt{3}a}{2} \right), \quad (1.1)$$

其中碳-碳原子之间的间距为  $a \approx 1.42 \text{ \AA}$ 。晶格的倒格矢为

$$\mathbf{b}_1 = \left( \frac{2\pi}{3a}, \frac{2\sqrt{3}\pi}{3a} \right), \mathbf{b}_2 = \left( \frac{2\pi}{3a}, -\frac{2\sqrt{3}\pi}{3a} \right). \quad (1.2)$$

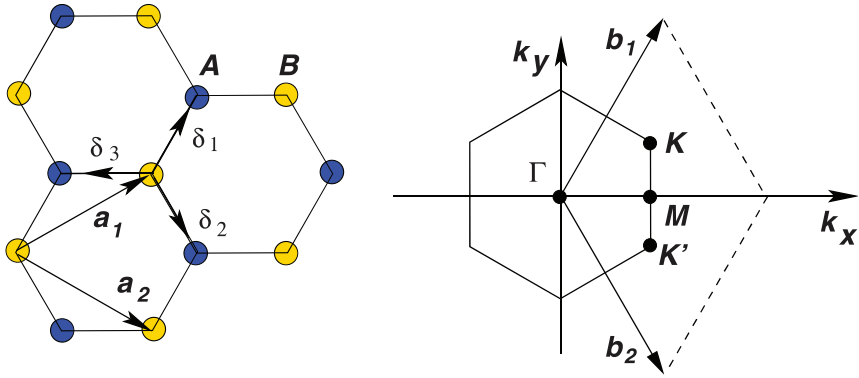


图 1.6: 石墨烯的蜂巢结构晶格以及布里渊区<sup>[19]</sup>。左图: 石墨烯的晶格结构, 其中  $a_1$  和  $a_2$  是晶格基矢, 同时  $\delta_i$  ( $i=1,2,3$ ) 是最近邻矢量。右图: 与晶格结构相对应的布里渊区, 其中  $K$  和  $K'$  点为狄拉克锥所在的位置

石墨烯物理中最重要的是两个在布里渊区中的  $K$  点和  $K'$  点。它们在动量空间中的位置分别是

$$\mathbf{K} = \left( \frac{2\pi}{3a}, \frac{2\pi}{3\sqrt{3}a} \right), \mathbf{K}' = \left( \frac{2\pi}{3a}, -\frac{2\pi}{3\sqrt{3}a} \right). \quad (1.3)$$

在实空间中三个最近邻碳原子的波矢分别为

$$\delta_1 = \left( \frac{a}{2}, \frac{\sqrt{3}a}{2} \right), \delta_2 = \left( \frac{a}{2}, -\frac{\sqrt{3}a}{2} \right), \delta_3 = (-a, 0). \quad (1.4)$$

如果只考虑石墨烯中的电子能向最近邻的原子跳跃, 此时的紧束缚哈密顿量写为

$$H = -t \sum_{i,j,s} (a_{i,s}^\dagger b_{j,s} + b_{j,s}^\dagger a_{i,s}), \quad (1.5)$$

其中  $a_{i,s}(a_{i,s}^\dagger)$  表示在子晶格 A 的  $\mathbf{r}_i$  处湮灭(产生)一个自旋为  $s$  的电子,  $b_{j,s}^\dagger(b_{j,s})$  表示在子晶格 B 的  $\mathbf{r}_j$  处产生(湮灭)一个自旋为  $s$  的电子,  $t = 3.16$  eV 是最近邻的跳跃能量。由上式中哈密顿量推导出的能量色散关系为<sup>[13]</sup>

$$E_\pm(\mathbf{k}) = \pm t \sqrt{1 + 4 \cos^2 \left( \frac{\sqrt{3}a}{2} k_y \right) + 4 \cos \left( \frac{3a}{2} k_x \right) \cos \left( \frac{\sqrt{3}a}{2} k_y \right)}, \quad (1.6)$$

其中的正负号分别代表费米能级附近的导带和价带。

在图 1.7(a) 中, 给出了公式 (1.6) 中所给出的石墨烯能带色散关系图。石墨烯在低能量处的色散关系可以通过对公式 (1.6) 中的能带结构在  $K$  或  $K'$  点处进行展开得到。当波矢从  $K$  或  $K'$  点开始测量时, 可以得到石墨烯的低能量能谱为<sup>[13]</sup>

$$E_\pm(\mathbf{k}) = \pm \hbar v_F |\mathbf{k}|, \quad (1.7)$$

其中费米速度  $v_F = 3at/2 \simeq 1 \times 10^6$  m/s, 是光速的  $1/300$ 。图 1.7(b) 中的狄拉克锥即是公式 (1.7) 所给出的费米能级附近的低能量能谱。

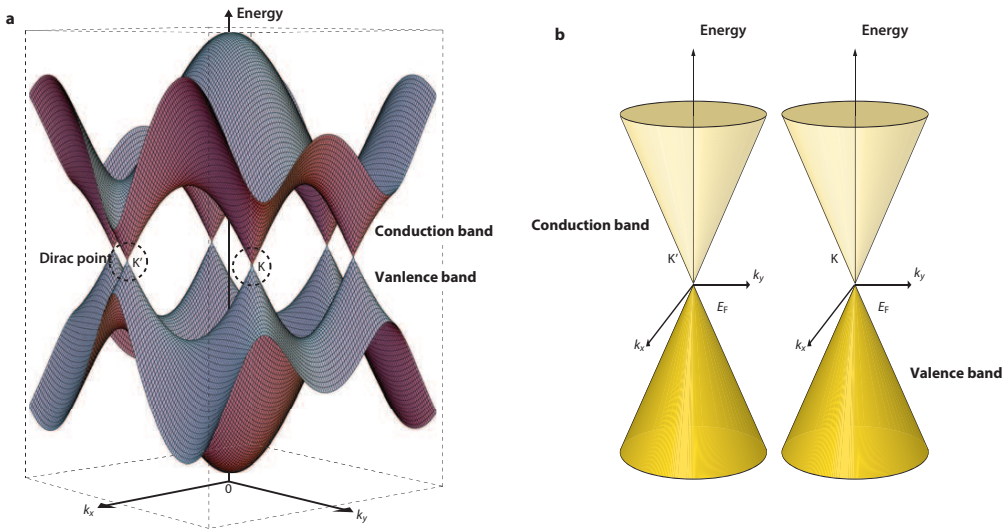


图 1.7: (a) 石墨烯中费米能级附近的能带结构和 (b) 在  $K$  点和  $K'$  点交叉的导带和价带的线性狄拉克锥色散关系<sup>[20]</sup>

单层石墨烯的研究如火如荼，多层石墨烯的研究也同样备受关注。多层石墨烯与单层石墨烯最显著的特点是在光吸收上。在白光范围内，多层石墨烯中每增加一层的石墨烯层，光吸收便会增加 2.3% (如图 1.8 所示)。随着技术的发展，实验上制备高质量、大面积的多层石墨烯已经成为可能。在多层石墨烯中，最常见的堆垛次序为 ABC 和 AB 堆垛。堆垛次序会极大的影响石墨烯的电子结构特性<sup>[22]</sup>，同时也随之影响多层石墨烯的其它物理性质。多层石墨烯的研究将会进一步促进石墨烯领域的研究并利用

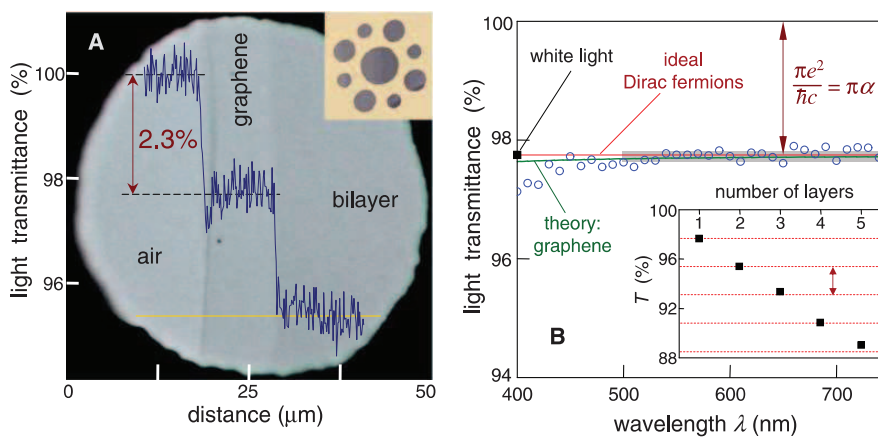


图 1.8: 原子层石墨烯晶体的光学表征图<sup>[21]</sup>。(A) 单层石墨烯和双层石墨烯的光学表征照片。(B) 实验测量单层石墨烯的透射谱系数 (空心圈)，理想二维狄拉克-费米子的透射率 (红色曲线)  $T = (1 + 0.5\pi\alpha)^{-2}$  ( $\alpha = e^2/\hbar c \approx 1/137$ ) 和理论计算石墨烯的透射率 (红色曲线)。内插图给出了多层石墨烯透射系数随着石墨烯层数的变化，每层石墨烯吸收大约 2.3% 的光

其层数可调的特性来适应于各种应用领域。

### 1.2.1.2 石墨烯的发展现状和应用前景

石墨烯从 2004 年正式面世到现在不过才 13 年时间，在此期间，石墨烯的研究获得了飞速发展。石墨烯的研究已经从最基础的物理特性研究拓展到新材料、新技术等实际应用领域中的方方面面。在近些年来的科研热点中，石墨烯一直占据着最核心的位置之一。在近些年，中国、美国、欧洲、日本、韩国等众多国家和地区都对石墨烯的研究投入了大量的资金支持，出台了多项支持政策和研究扶持计划。在八年前，世界上仅有在美国的几家小型公司（如 Angstrom Materials, Vorbeck Materials 和 XG Sciences 等）能够生产大量的小面积石墨烯层。从那以后，几十家石墨烯制造企业在世界范围内诞生，不仅能生产小面积的石墨烯层而且能制造出工业级的大面积、高质量石墨烯薄膜。我国的石墨烯研究虽然起步比较晚，但发展速度极快，有着十分巨大的潜力优势。值得一提的是，中国石墨烯工业生产能力的发展方兴未艾。早在 2014 年的时候，石墨烯层和石墨烯薄膜的年产量就分别达到了 400 吨和  $110,000 \text{ m}^2$ <sup>[23]</sup>。

在当前，基于石墨烯以及石墨烯纳米结构的应用前景主要集中在以下几个方面。

(1) 石墨烯光电子学领域：基于石墨烯的透明和柔性导电薄膜，高频率晶体管等。转印法和溶液法的发展使得将石墨烯应用于大面积电子器件成为可能。Chhowalla 等人<sup>[24]</sup> 提出了一种有效的方法，确保均匀且可控地沉积，通过还原氧化石墨烯得到的石墨烯薄膜，其厚度范围可以从单层到大面积的多层。因而其光电性质可以在几个数量级的范围内进行调节，使得石墨烯能极具潜力的应用在柔性和透明的半导体或半金属上。自从 2007 年开始，石墨烯晶体管得到的巨大发展<sup>[25]</sup>。最令人印象深刻的是证实了石墨烯 MOSFETs 具有 100 GHz 的截止频率，石墨烯纳米带 MOSFETs 具有优异的开关性能，以及在顶部门电压下石墨烯 MOSFETs 中高达  $20,000 \text{ cm}^2 \text{ V}^{-1}\text{s}^{-1}$  的通道迁移率。尽管目前将石墨烯实际应用在逻辑门晶体管存在一些困难，这一领域的蓬勃发展仍鼓舞着人们不断的进行探索和创新。

(2) 石墨烯光子学：光探测器、光调制器和太赫兹发生器等。石墨烯在可见光的范围只吸收约 2.3% 的光。由于泡利阻塞效应，石墨烯的带间跃迁光吸收能受到费米能级的有效调节。而石墨烯的零带隙特征使得其能吸收很宽频率范围内的光子，如从紫外光到太赫兹波。这些特性使得石墨烯光探测器有着很宽的光响应区域。石墨烯中的高载流子迁移率可以实现光生载流子信号的快速提取，可以允许在极高的带宽范围内进行操作。当前，石墨烯光探测器利用金属-石墨烯界面的局域势的变化来追踪光生载流子<sup>[26]</sup>。光调制器也称电光调制器，它是长距离和高速光通信元件的一个关键部分。光调制器的优异性能可以通过利用石墨烯能够在超宽频段范围内吸收少量的入射光并且有着超快的响应时间来达到。为了实现这个目的，可以通过一个驱动电压来调制石墨烯中带间跃迁的光生载流子。可以实现在近红外范围内有着超过 1 GHz 的运行速度带宽<sup>[27]</sup>。太赫兹技术的蓬勃发展使得太赫兹源也成为一大研究热点。研究表明单层

或多层石墨烯薄膜在飞秒激光的照射下，其中的光生载流子能够被加速并产生太赫兹波<sup>[28]</sup>。

(3) 电子印刷用导电油墨：在过去的十几年间打印电子学通过制造高性价比的电子电路和传感器为电子工业的革命性发展创造了机遇。英国曼彻斯特大学的研究人员在最近的一项研究工作中报道了将高电导性、高度柔性、轻质量和廉价的石墨烯油墨打印应用在可穿戴的无线通讯设备上<sup>[29]</sup>。

(4) 基于石墨烯的分离薄膜：通过带有纳米孔的石墨烯层来作为分离膜的提议早已在人们长时间的理论模拟计算中给出。Král 等<sup>[30]</sup> 通过分子动力学模拟发现含有纳米孔的石墨烯有着对水合离子高度的选择性通过率。Jiang 等<sup>[31]</sup> 通过分子动力学也证实有着给定孔洞大小的多孔石墨烯能有效的将 CO<sub>2</sub> 从 N<sub>2</sub> 中分离出来，并与最近的实验发现相符<sup>[32]</sup>。

(5) 石墨烯在生物医药上的应用：石墨烯所具备的一系列特性使其在生物应用上极具潜力。石墨烯具有较大的比表面积、化学级的纯度和易于功能化的可能使得其可以有机会应用于药物递送。其独特的力学性质可以应用于组织工程和再生医学。石墨烯超薄的厚度、导电的特性和所具备的强度的结合使其成为生物分子在透射电镜成像中的理想支持基底<sup>[33]</sup>。同时化学功能化石墨烯可能应用于快速的和超灵敏度的测量器件，并能够探测一系列的生物分子如葡萄糖、胆固醇、血红蛋白和 NDA<sup>[34]</sup>。

(6) 石墨烯储能器件：石墨烯锂离子电池和石墨烯超级电容器。如何将石墨烯应用于锂离子电池被广泛的进行了研究。对于传统的商业化锂离子电池，其阴极通常受着较弱导电性的困扰。而在电极的配方中加入石墨和碳黑之后能够克服这一问题。具有片状形态的石墨烯不仅可以作为先进的导电填料而且能用作于新型核-壳结构或者夹层型的纳米复合材料结构<sup>[35]</sup>。这些新形态将导致电导率的增加，并能够帮助克服锂离子电池低功率密度比的限制。超级电容器是基于储存能量的电化学双层电容。这种先进器件（与锂离子电池相比）所具备的优异速率性能主要是基于静电储存电能，并且由活性炭材料的高比表面积与电极-电解液界面的纳米电荷分离所决定。石墨烯是这种应用的最佳选择，它有着较高的内禀电导、可实现的自定义结构、良好的耐氧化性和高温稳定性。当前基于石墨烯的电化学双层电容器原型<sup>[36]</sup> 引领着电容器中电容量以及能量和功率密度方面的研究。

(7) 传感器领域：石墨烯材料由于具有较高的比表面积和独特的电子特性，如高迁移率和低电子噪声，因而能用作传感材料。使用基于石墨烯的传感器能够探测大量范围的化学物、生物分子和气体或蒸汽<sup>[37]</sup>。石墨烯传感器的最大优势是它们多样的功能化特性。单个器件可以被用作多维度的探测（例如，应力、气体环境、压力和磁场）。从这个角度上来说，石墨烯给多功能传感器领域提供了独特机会。随着不断增长的交互式消费级电子器件的发展，这样的传感器必将找到适合的方式应用在许多产品之中。

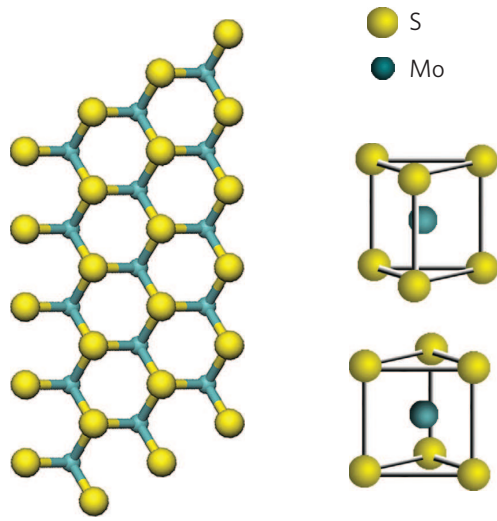


图 1.9: 单层二硫化钼的原子结构示意图<sup>[38]</sup>。(左图) 顶部视角和(右图) 元胞侧面视角

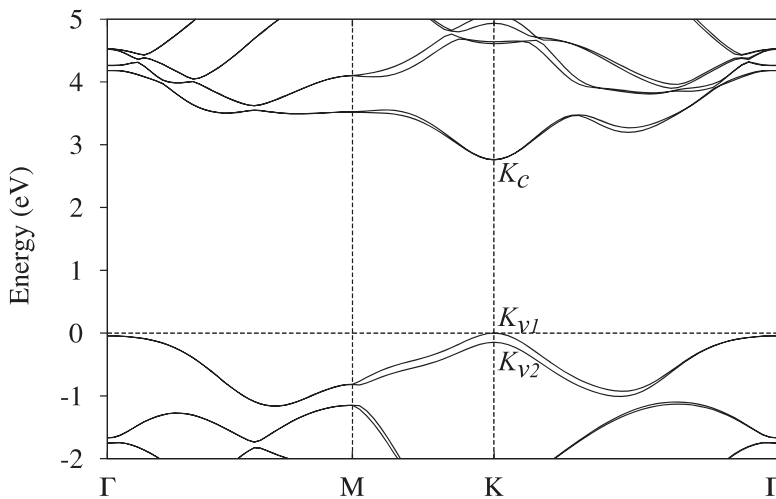
### 1.2.2 单层过渡金属硫化物

在本学位论文的研究中，主要对单层过渡金属硫化物之一的单层二硫化钼的光电性质进行了理论上的研究。二硫化钼 ( $\text{MoS}_2$ ) 在层内通过很强的共价键结合，而其在层与层之间是通过弱的范德瓦耳斯力相结合的。由于这样的层状结构特点，二硫化钼通常被广泛的应用于固体润滑剂、石油加氢脱硫催化剂、储氢材料和非水锂电池等领域。而单层过渡金属硫化物有着在六方晶系中由过渡金属原子层夹在两个硫族原子层中间的结构<sup>[38]</sup> (如图 1.9 所示)。

#### 1.2.2.1 单层过渡金属硫化物的电子结构

众所周知，由于纯的石墨烯没有带隙，因此用石墨烯制造的场效应晶体管不能有效的进行开关调节并有着很低的开关比。虽然在石墨烯中可以通过利用纳米结构、化学功能化和给双层石墨烯加一个强电场来实现带隙。但是这些方法将加大系统的复杂性和降低载流子迁移率。而单层二硫化钼等单层过渡金属硫化物系列的材料有着较大的直接带隙 (如图 1.10 所示)，可以成为十分有前途的晶体管和光电器件材料。同时单层二硫化钼也有着发射荧光的能力和对圆偏振光的谷选择性吸收特性<sup>[38, 39]</sup>。

许多过渡金属硫化物的能带结构有着相似的特性，这既可以通过第一性原理和紧束缚近似得到也可以通过不同的光谱分析工具得到。通常来说， $\text{MoX}_2$  和  $\text{WX}_2$  化合物是半导体，而  $\text{NbX}_2$  和  $\text{TaX}_2$  化合物则是金属<sup>[11]</sup>。在  $\Gamma$ -点，本征材料有着间接带隙。在单层的时候带隙则会移动到  $\mathbf{K}$  点同时表现出直接带隙。二硫化钼中的能带结构因层数而变化是因为量子限制效应和硫原子的  $p_z$  轨道与钼原子的  $d$  轨道之间杂化的改变。对于二硫化钼，密度泛函理论 (DFT) 计算表明在  $\mathbf{K}$  点导带的电子态主要是由钼原子

图 1.10：单层二硫化钼的能带结构<sup>[40]</sup>

上局域的  $d$  轨道所贡献。由于钼原子的位置在 S-Mo-S 三明治层结构的中间，因而导带电子态相对较小的受层间耦合的影响。但是，在  $\Gamma$ -点附近的电子态是由硫原子上的反键  $p_z$  轨道和钼原子上  $d$  轨道的组合而贡献。因此，当二硫化钼的层数发生改变的时候，在  $K$  点附近的直接激子态几乎是不变的而带隙则由  $\Gamma$ -点处的间接带隙变成更大的直接带隙。随着层数的减小，所有的  $\text{MoX}_2$  和  $\text{WX}_2$  化合物被认为有着相似的由间接带隙到更大直接带隙的转变，同时带隙的能量范围在 1.1-1.9 eV 的范围内。从图 1.10 中也可以看到，单层二硫化钼在价带中有着较大的自旋-轨道耦合作用，使之在价带中产生了较大的自旋-轨道劈裂。

### 1.2.2.2 单层过渡金属硫化物的应用前景

单层二硫化钼因其独特的微观结构和理、化性质从而在众多领域拥有广阔的应用前景。就在最近，科学家研究出了基于单层二硫化钼的 1 nm 场效应晶体管<sup>[41]</sup>。这进一步鼓舞着人们对高性能场效应晶体管的研究并为摩尔定理的延续提供了坚实的科学基础。由于目前基于硅半导体微纳电子器件的制造已接近理论极限，而单层二硫化钼由于所具备的独特优势使其极有期望取代硅而成为未来的决定性半导体材料。

单层二硫化钼作为新发现的又一种二维材料吸引着无数人对其进行研究和创新。当前，过渡金属硫化物的应用前景主要集中在以下几个方面。

(1) 过渡金属硫化物电子学：Kis 和合作者报道了首个基于单层二硫化钼的顶部栅极晶体管并表现出极佳的电流开关比 ( $\sim 10^8$ ) 和室温下高于  $200 \text{ cm}^2 \text{ V}^{-1}\text{s}^{-1}$  的迁移率<sup>[42]</sup>。有着高介电常数顶部栅极和单层 WSe<sub>2</sub> 活性通道的  $p$ -型场效应晶体管有着  $10^6$  的开关比和大约  $250 \text{ cm}^2 \text{ V}^{-1}\text{s}^{-1}$  的空穴迁移率<sup>[43]</sup>。二维过渡金属硫化物在近期能实现的一种应用方向是高性能柔性电子学。单层二硫化钼的力学测试表明它有着 30 倍于钢

的强度同时在碎裂前能够承受 11% 的变形。这种独特的性能使得二硫化钼成为有着最高强度的半导体材料之一并能成为十分有利的柔性衬底。

(2) 光电子学：就在光电子器件方面的应用来看，单层二硫化钼不仅可应用于柔性材料、透明电极、光探测器、发光二极管、二次电池、场效应晶体管、传感器等领域，而且在有机发光二极管、电存储等领域前景光明<sup>[44]</sup>。光电子学器件是能产生、探测、与光互相影响或控制光的电子器件。柔性的和透明的光电子器件在太阳能电池、可穿戴电子设备和透明显示器上变得越来越重要。半导体的电子能带结构会直接影响它们吸收和发射光子的能力。对于像单层过渡金属硫化物这类的直接带隙半导体，当光子的能量高于带隙时，光子能十分便捷的被吸收或者发射。由于单层过渡金属硫化物是直接带隙半导体同时有着原子层级的厚度，因而在柔性和透明光电子学上有着极具潜力的应用价值。过渡金属硫化物在地球上有着丰富的储量。同时其在可见光范围内的直接带隙使他们成为薄膜太阳能电池中极佳的光吸收材料。因而过渡金属硫化物在光伏电子学和光探测器中可以得到许多的应用。电致发光和光荧光是发光电子学应用中的两种重要机制。单层过渡金属硫化物由于具有直接带隙因而可以作为发光层应用于发光器件中。

(3) 比较重要的是，单层过渡硫化物材料由于其独特的自旋和谷特性，使其成为能应用于自旋电子学和谷电子学的理想材料<sup>[38, 39]</sup>。

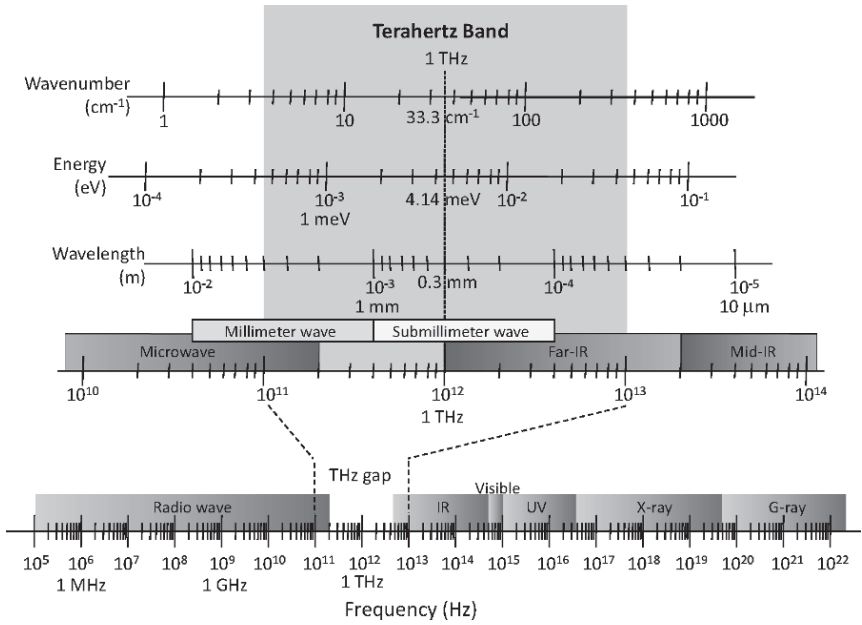
在未来几年中，单层二硫化钼的研究的推进需要进一步提高生长大规模和可控的高质量样品的工艺。随着样品生长技术的不断提高，越来越多的人将进入这一令人兴奋的研究领域。

### 1.3 太赫兹光谱学

太赫兹辐射 (Terahertz, THz,  $1 \text{ THz} = 10^{12} \text{ Hz} \sim 1 \text{ ps} \sim 300 \mu\text{m} \sim 4.1 \text{ meV}$ ) 是频率范围在微波和红外之间从 0.1 THz 到 10 THz 区域的电磁辐射波。电磁波中频率、波长和能量之间的换算关系为

$$\nu = \frac{\omega}{2\pi} = \frac{c}{\lambda}, \lambda = \frac{2\pi\hbar c}{E}.$$

太赫兹波也被称为 T 射线，在电磁波谱中有着十分重要的地位。太赫兹频段光能够穿透纸张、木材及其他固态物体等，因此非常适用于安全检测方面的应用。太赫兹波处于电子学和光子学研究的过渡区域。我们虽然看不见太赫兹波，但是我们可以感受其传递的热量因为它和远红外辐射处在相近邻的光谱区域。自然产生的太赫兹辐射充满我们日常生活的方方面面。但是，在太赫兹波段这个领域仍是我们最少了解的电磁波谱。这是因为目前在有效的和便捷的太赫兹辐射源和探测器上仍然存在技术难题。这一领域的技术难题导致了所称作的“太赫兹空隙”（如图 1.11 中的电磁波谱所示）。目前，太赫兹技术正处于飞速发展的时期<sup>[45]</sup>。2004 年美国 Technology Review 杂志将太赫兹技术列为改变未来世界的十大技术之一。日本于 2005 年将太赫兹列为“国家支柱十大重点战略目标”首位。


 图 1.11: 电磁波谱和太赫兹空隙<sup>[46]</sup>

太赫兹技术的发展主要集中在太赫兹辐射源以及太赫兹探测器<sup>[47]</sup>。太赫兹辐射源主要包括以下几种。(1) 自由电子激光器 (free-electron lasers; FELs)，FELs 通过加速电子来实现太赫兹激光辐射。加速电子在磁场下做周期性的运动，当电子的速度接近光速时，电子在洛伦兹力的作用下通过自发辐射产生太赫兹辐射。(2) 气体激光器，气体激光器的原理为通过二氧化碳激光器进行光泵浦并在分子振动或转动能级之间形成粒子数翻转因而产生受激辐射太赫兹光。(3) 真空电子学太赫兹源，回旋管是基于电子在磁场中回旋谐振受激辐射的原理工作在毫米及太赫兹波段的典型真空电子学器件。(4) 太赫兹半导体量子级联激光器 (quantum cascade laser; QCL)，QCL 是只有电子参与的单极型激光器，其中电子从高能量态跃迁到低能级态并伴随着发射太赫兹光子。(5) 光电导太赫兹源，当飞秒激光照射在电极之间的光电导材料时，光生载流子在电场的驱动下被加速同时产生太赫兹脉冲。(6) 反相波振荡器 (backward wave oscillator; BWO)，也称返波管，由电子枪发射的电子束在磁场约束下通过金属光栅慢波结构时，电子被减速并产生太赫兹辐射。由于电子运动方向和产生的太赫兹辐射相反，因此被称为返波管。(7) 耿氏振荡器，利用负微分电阻效应 (negative differential resistance; NDR) 来产生太赫兹波。

太赫兹波的探测方法主要包括如下几种。(1) 傅里叶变换光谱仪，其原理是基于迈克尔逊干涉仪，可以测量红外到太赫兹范围很宽的频谱范围。(2) 太赫兹时域光谱，是一种有效的太赫兹探测方法。在太赫兹辐射探测中，将飞秒激光分成两束，一束作为太赫兹辐射源，另外一束作为参照。当太赫兹波照射在样品上时，材料内迅速产生电子-空穴对并形成正比于太赫兹脉冲电场的光电流。通过改变探测光束的时间延迟便可

以得到太赫兹辐射电场随时间的变化。(3) 外差式探测法, 外差式探测法可以探测电场的振幅、相位和频率等信号, 具有选拨性好、鉴别能力良、信噪比小和内部噪声低的特点。典型的外差式探测器有超导太赫兹探测器和热电子辐射器。(4) 太赫兹半导体量子阱探测器 (quantum-well photodetector, QWP), 利用 GaAs/AlGaAs 量子点和金属单电子晶体管相耦合使得吸收一个光子会有大量的电子通过量子点, 因而大大的增加了探测灵敏度。随着材料生长技术和器件工艺的提高太赫兹 QWP 器件的发展将进一步得到推动。

目前太赫兹的研究不仅仅集中在太赫兹源和探测技术, 同时人们已经将太赫兹技术的研究集中在高速通信、光子光谱学、太赫兹成像、太赫兹安检和医学诊断等领域里。太赫兹研究的兴起将不断加强人们对太赫兹领域的认知并进一步强化对太赫兹波的利用。

## 1.4 自旋-轨道耦合相互作用

自旋电子学是研究如何操控和利用器件中电子的自旋自由度。它的发展起始于 1988 年 Fert 和 Gruenberg 各自分别发现的巨磁阻效应 (giant magneto-resistive, GMR)<sup>[48, 49]</sup>。近些年来自旋电子学的飞速发展, 使得自旋-轨道耦合效应越来越受到人们的关注。自旋-轨道耦合提供了一种新的控制电子自旋自由度的方法, 引起了各种新奇的相关物理现象, 如自旋霍尔效应、自旋场效应晶体管等。Datta 和 Das 在 20 世纪末提出的基于电场调控自旋-轨道耦合的自旋场效应晶体管<sup>[50]</sup>使得 Rashba 自旋-轨道耦合效应在电场调控自旋量子器件中占有十分重要的地位。

自旋-轨道劈裂是指材料体系中哈密顿量中出现的线性项, 通常由破坏结构反演对称 (structure inversion asymmetry, SIA) 的 Rashba 效应和破坏晶体反演对称 (bulk inversion asymmetry, BIA) 的 Dresselhaus 效应所导致<sup>[51]</sup>。

自旋-轨道耦合是一种相对论效应, 根据相对论原理, 在材料中电子的能量会因为自旋-轨道耦合的作用而产生修正。电子在运动过程中, 其自旋会感受到运动电场所产生的感应磁场, 因而会产生一项额外自旋-轨道作用哈密顿量项。通过 Dirac 方程可以得到<sup>[52]</sup>

$$H_{SO} = -\frac{\hbar}{4m^2c^2} [\nabla V(\mathbf{r}) \times \mathbf{p}] \cdot \hat{\sigma}, \quad (1.8)$$

其中  $m$  是电子有效质量,  $\mathbf{p} = -i\hbar\nabla$  是动量算符,  $\hat{\sigma} = (\hat{\sigma}_x, \hat{\sigma}_y, \hat{\sigma}_z)$  是泡利自旋矩阵。

### 1.4.1 Rashba 自旋-轨道耦合

E. I. Rashba 首先引入了 Rashba 自旋-轨道耦合相互作用机制<sup>[53]</sup>。在自旋场效应晶体管中, 中间层可以看作是二维电子气。在该系统中的 Rashba 自旋-轨道耦合哈密顿量可以写作

$$H_R(\mathbf{k}) = \alpha_R (\hat{\sigma}_x k_y - \hat{\sigma}_y k_x), \quad (1.9)$$

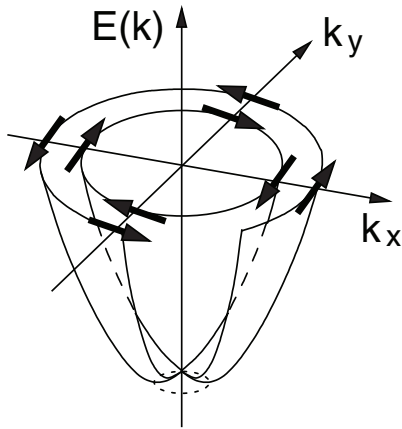


图 1.12: Rashba 自旋-轨道耦合下的自旋劈裂能带结构示意图<sup>[52]</sup>。其中箭头表示不同自旋态的自旋取向

其中  $\alpha_R$  是 Rashba 自旋-轨道耦合参数，且与电场有关因而能通过一个垂直于二维平面的门电压来进行调控。在自由二维电子气中，额外加上 Rashba 自旋-轨道耦合作用后，可以得到能量本征值

$$E_s(\mathbf{k}) = \frac{\hbar^2 \mathbf{k}^2}{2m} + s\alpha_R k, \quad (1.10)$$

以及对应的本征波函数

$$\psi_s(\mathbf{k}) = \frac{1}{\sqrt{2}} \begin{pmatrix} 1 \\ -ise^{i\theta} \end{pmatrix} e^{i\mathbf{k}\cdot\mathbf{r}}, \quad (1.11)$$

其中  $\theta$  是  $\mathbf{k}$  和  $x$  轴之间的夹角，同时系统的自旋取向为

$$\langle \hat{\sigma} \rangle_{\mathbf{k}} = \langle \psi_s(\mathbf{k}) | \hat{\sigma} | \psi_s(\mathbf{k}) \rangle = (-s \sin \theta, s \cos \theta, 0). \quad (1.12)$$

如图 1.12 所示，在 Rashba 效应下电子的自旋简并被打开。根据自旋指数  $s$  可以定义自旋向上和向下的两支能量分裂子带。根据公式 (1.12) 可以看到在 Rashba 自旋-轨道耦合下自旋分裂能带的自旋取向是在二维平面内的并且垂直于波矢的方向，且不同自旋劈裂子带有着相反的自旋取向。

### 1.4.2 Dresselhaus 自旋-轨道耦合

G. Dresselhaus 系统的研究了 Dresselhaus 自旋-轨道耦合机制<sup>[54]</sup>。大部分半导体都具有不具备体反演对称的闪锌矿晶格结构或者铅锌矿晶格结构。这种体反演不对称性会导致导带中发生自旋劈裂。在这种情况下，总的哈密顿量中会出现一项额外的 Dresselhaus 自旋-轨道耦合项。在二维体系中，Dresselhaus 自旋-轨道耦合哈密顿量通常写为

$$H_D(\mathbf{k}) = \alpha_D (\hat{\sigma}_y k_y - \hat{\sigma}_x k_x), \quad (1.13)$$

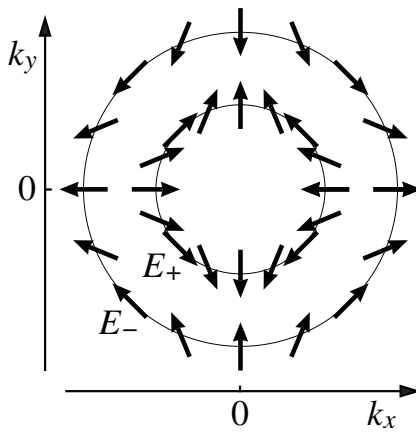


图 1.13: 在只有 Dresselhaus 自旋-轨道耦合作用下二维电子气在给定能量等值面上不同自旋态上的自旋取向<sup>[52]</sup>

在自由二维电子气中，额外加上 Dresselhaus 自旋-轨道耦合作用后，可以得到能量本征值

$$E_s(\mathbf{k}) = \frac{\hbar^2 \mathbf{k}^2}{2m} + s\alpha_D k, \quad (1.14)$$

以及对应的本征波函数

$$\psi_s(\mathbf{k}) = \frac{1}{\sqrt{2}} \begin{pmatrix} 1 \\ -se^{-i\theta} \end{pmatrix} e^{i\mathbf{k}\cdot\mathbf{r}}. \quad (1.15)$$

同时系统的自旋取向为

$$\langle \hat{\sigma} \rangle_{\mathbf{k}} = \langle \psi_s(\mathbf{k}) | \hat{\sigma} | \psi_s(\mathbf{k}) \rangle = (-s \cos \theta, s \sin \theta, 0). \quad (1.16)$$

通过公式 (1.14) 可以发现，在只有 Dresselhaus 自旋-轨道耦合作用下的自由二维电子气有着与只有 Rashba 自旋-轨道耦合作用下相同的能量色散关系。但是通过公式 (1.16) 可以看到，两个系统中的自旋态的自旋取向有着很大的不同（如图 1.13 所示）。

## 1.5 等离激元光子学

等离激元 (plasmon) 是等离子振荡的量子。就像声子是晶格力学振动的量子化产物，等离激元可以被看作是等离子振荡的准粒子。等离激元是自由电子气的集体密度振荡。在光频区域，等离激元可以和光子发生耦合从而产生另一种准粒子：等离极化激元 (plasmon polariton)。表面等离激元 (surface plasmon; SP) 则是被局域在材料表面振荡的等离激元，它与光发生耦合之后会产生表面等离极化激元 (surface plasmon polariton; SPP)。

与等离激元相关的现象最开始由 Wood 在 1902 年报道<sup>[55]</sup>，他发现衍射光栅光谱中的光存在不均匀的分布，但是没有对这个 Wood 异常现象给出合理的解释。在大约 40

年之后，Fano<sup>[56]</sup> 在 1941 年理论上揭示了 Wood 异常是由在金属型表面不间断的激发具有较大切向动量的 Sommerfeld 型的电磁波所导致的，而这是不能被 Rayleigh 近似理论所描述的。Ritchie<sup>[57]</sup> 在 1957 实验上观测到高能电子穿过金属薄片时产生了能量共振吸收并提出了金属内部电子密度纵向波动的金属等离子体概念，并迅速被 Powell 和 Swan 在实验上所证实<sup>[58]</sup>。在 1960 年，Stern 和 Farrell 对实现金属表面电磁波模式的共振条件进行了研究并提出表面等离激元共振的概念<sup>[59]</sup>。Otto<sup>[60]</sup> 和 Kretschmann<sup>[61]</sup> 采用衰减全反射的方法各自实现了在可见光区域的表面等离激元的激发。从而一个较为完整的关于等离激元现象的理论就建立起来了。随着近年来材料学和器件结构工艺的不断发展，越来越多的和等离激元相关的奇异实验现象的产生促进了一个新的领域的发展，这便是等离激元光子学 (plasmonics)。

等离激元光子学作为微纳光子学中的重要一环，是目前蓬勃发展且极具前景的研究领域之一<sup>[62]</sup>。等离激元光子学主要是研究光波长量级的电磁场以及金属界面或微纳金属结构中电磁波和自由电子的相互作用产生的奇异光学特性，这种独特的相互作用将导致亚波长尺寸的光学近场增强效应，包括光的异常透射、增强吸收等。等离激元光子学在高密度数据存储、超分辨成像、超分辨率纳米光刻、光准直、太阳能电池、生物传感器以及负折射材料等方面有着重要的应用前景<sup>[63]</sup>。目前基于石墨烯的等离激元光子学取得了长足的发展<sup>[64, 65]</sup>，而与之相关的新型二维电子气材料等离激元特性也值得我们进一步去研究。

## 1.6 本论文的创新性、研究意义和研究内容

本学位论文中的研究主要立足于近年来新兴发展起来的新型二维电子气材料石墨烯和单层二硫化钼。自 2004 年石墨烯的发现以来，探索原子层级的二维材料成为目前材料领域研究中一个十分重要的研究方向。单层过渡金属硫化物是一类非常典型的直接带隙半导体材料。对这两种材料的研究实现了从无质量狄拉克-费米子到有质量狄拉克-费米子研究的覆盖。对材料光电特性的理论研究能探究和预测材料在光学、光电子学器件上的应用前景。石墨烯材料由于具有无带隙或较小的带隙结构使得其在低频率区域有着十分特殊的光响应特性。而单层二硫化钼由于自旋-轨道耦合的作用使得其在低频率范围内也有着可观的光吸收响应。二维电子气材料有着声学的等离激元模式因而其等离激元振荡频率可以在较宽的频谱范围内受到载流子浓度的调控。研究石墨烯材料和单层过渡金属硫化物的光吸收特性以及等离激元特性能为这两种材料在光学和光电子学上的应用打下理论基础。

目前，对多层石墨烯系统光电性质的研究已经比较完备，尤其体现在对光电导的计算上。在很多工作中，多层石墨烯的电子结构和光电特性已被人们所研究。但是目前还没有对多层石墨烯系统在可见光和太赫兹频段的光电性质进行一个较为系统的对比研究。对于单层二硫化钼的光学性质如光吸收和光荧光，目前已经有了较为完善的研究，但是还没有人利用通过改变自旋-轨道耦合的方式来研究 Rashba 效应对单层二

硫化钼光电性质的影响。对于单层二硫化钼的等离激元模式特性，目前的研究都集中在通过不同掺杂浓度来研究电荷等离激元。据我们所知，还没有人通过光泵浦手段改变单层二硫化钼系统中不同组份数量的方式来研究单层二硫化钼系统中的多组份等离激元模式。同样，对单层二硫化钼中等离激元和纵向光学声子耦合的研究也较少。因而，在本论文中主要在这些新的领域对两种典型的新型二维电子气材料的光电特性开展了理论研究。

实验上在单层石墨烯中可以观看到在红外和太赫兹范围内有一个光学吸收窗口。而多层石墨烯由于具有可调控的层数和不同的堆垛方式，因而这些条件的改变对在红外至太赫兹频段的光吸收也有着重要的影响。虽然理论上对石墨烯材料的光吸收特性已经有了众多的研究，但是对多层石墨烯系统在低频段的光吸收窗口做一个系统的研究和比较对更好的利用多层石墨烯仍具有一定的现实意义。

单层过渡金属硫化物由于其独特的自旋-轨道耦合劈裂使得其在低能量区域有着奇异的光学特性，在一个外加垂直偏压的调节下，Rashba 效应能够改变自旋-轨道耦合劈裂，因而对其低频段的光吸收特性有着显著的影响。目前对于单层二硫化钼光电特性的研究主要集中在没有 Rashba 效应的情况下。我们通过考虑 Rashba 效应对单层二硫化钼能带结构的影响可以观看到由 Rashba 效应所导致的奇特光吸收响应特性。

等离激元光子学作为利用材料物理特性的一种新方法，探索和研究等离激元色散关系如何受电子结构以及载流子浓度的影响具有十分重要的意义。理论上对等离激元模式的研究能进一步加深对材料光学特性的了解并能为其实际应用打下理论基础。当前已经有对单层二硫化钼等离激元特性的研究，但是主要都是研究其二维电子气特性的电荷等离激元模式。在本学位论文中的研究中，我们考虑在一个圆偏振光泵浦激发下的多组份电子气系统，能够得到除了传统二维电子气电荷等离激元模式之外的线性声学等离激元模式。

实验和理论上已经发现单层石墨烯中的电子和衬底中的表面光学声子有着强烈的耦合作用。在具体的单层二硫化钼器件结构中，材料中的等离激元与内禀光学声子和衬底中表面光学声子的耦合作用同样十分重要。通过对耦合的等离激元-声子模式的研究能进一步丰富和了解材料的等离激元特性及应用价值。

本学位论文主要是通过理论计算对多层石墨烯和单层二硫化钼两种新型二维电子气材料的相关光电特性进行了研究。在具体的计算中采取通过对比单变量变化的手段来实现探究不同环境和物理条件对材料光电特性的影响。在实际的样品中，不同的物理变量参数之间会发生相互影响作用。例如，样品中的载流子浓度会受到温度的影响。在具体的实际样品中，载流子浓度可以通过一个门电压进行调节。所以，即使温度对材料中的载流子浓度有着影响，在实验中也可以通过门电压的调节使温度变化的时候保持样品的载流子浓度。所以在论文接下来的计算中，我们采用对比单变量的方法进行计算和讨论，特别是将温度和载流子浓度分开讨论是较为合理的。

本学位论文接下来部分的主要内容如下：

第二章中，系统的介绍了本学位论文理论研究中所用到的理论背景和理论方法。系统的回顾了平衡方程法计算光电导，基于线性响应理论光电导的 Kubo 公式和 Kubo-Greenwood 公式，以及在无规则相近似 (RPA) 下的动态介电函数。

第三章中，利用通过半经典玻尔兹曼方程得到的能量平衡方程法理论上计算了 AB-堆垛和 ABC-堆垛结构的单层和多层石墨烯系统的光电导和光透射系数。研究了石墨烯层数、堆垛方式、温度和载流子浓度对多层石墨烯系统中光吸收的影响。本章的研究工作发表在期刊 Optics Communications 上。

第四章中，使用 Kubo-Greenwood 公式计算了  $n$ -型和  $p$ -型单层二硫化钼在 Rashba 自旋-轨道耦合效应下红外到太赫兹范围内的光电导。讨论了温度、光的偏振方向、载流子浓度和 Rashba 系数的强度对光电导的影响。本章的研究工作发表在期刊 Physical Review B 上。

第五章中，使用 Kubo-Greenwood 公式在不同的哈密顿量模型下分别计算了在无 Rashba 效应下和有 Rashba 效应下可见光范围内带间跃迁贡献的光电导以及 Rashba 效应对带间跃迁光吸收通道的影响。

第六章中，在无规则相近似 (RPA) 下，计算了单层二硫化钼在无外加光场和圆偏振光泵浦激发下多组份系统单层二硫化钼的动态介电函数和等离激元特性。讨论了掺杂类型、载流子浓度和组份系统数量对单层二硫化钼等离激元特性的影响。

第七章中，通过考虑放置在二氧化硅衬底上的单层二硫化钼，计算了单层二硫化钼中电子和层内内禀光学声子和二氧化硅衬底中的表面光学声子耦合产生的耦合的等离激元-声子模式。

第八章中，对本学位论文的研究工作做了总结，并展望了下一步的研究计划以及研究方向。



## 第二章 研究方法和基本理论

在计算材料系统的光电导时，一般主要有两种方法。一种是利用费米黄金定理和半经典玻尔兹曼方程所导出的平衡方程法，另一种是通过线性响应理论得到的久保公式 (Kubo formula)。通常来说这两种方法所得到的结果是一致的。在理论研究系统的集体激发响应时，通常采用线性响应理论框架下无规则相近似 (random phase approximation; RPA) 下的介电函数来计算等离激元、以及系统对能量的吸收等。另外也可以通过求解麦克斯韦方程组<sup>[62]</sup> 的方法来计算系统的等离激元色散关系。这种方法通常用于计算具有复杂结构的材料系统。而在计算本征系统的等离激元特性时，通常我们采用求解 RPA 介电函数的方法。在这一章中，主要介绍了本论文中所采用的计算光电导和等离激元模式的理论基础。

### 2.1 半经典玻尔兹曼方程及平衡方程法

#### 2.1.1 玻尔兹曼方程

玻尔兹曼方程 (Boltzmann transport equation) 是由路德维希·玻尔兹曼于 1872 年提出的一个描述非热力学平衡状态的热力学系统统计行为的偏微分方程。

在热力学平衡下，电子占据能级  $E(\mathbf{k})$  的概率由费米-狄拉克分布函数给出<sup>[66]</sup>

$$f(\mathbf{k}) = \frac{1}{e^{(E(\mathbf{k})-\mu)/k_B T} + 1}, \quad (2.1)$$

其中  $T$  是系统的温度、 $\mu$  是系统中电子的化学势、 $k_B$  是玻尔兹曼常数。费米-狄拉克分布函数也可以写成能量分布的形式  $f(E(\mathbf{k}))$ 。

当外场微扰作用在样品上的时候 (电场，磁场，或者温度场)，电子的分布从其平衡状态下的费米-狄拉克函数分布状态上被扰动。通常上定义扰动后的分布函数为  $f(\mathbf{r}, \mathbf{k}, t)$ ，它除了取决于电子波矢  $\mathbf{k}$ ，同样也取决于电子的空间坐标  $\mathbf{r}$  和时间  $t$ 。通过能带中载流子的半经典动力学，一个在时间  $t$  处  $(\mathbf{r}, \mathbf{k})$  点的电子在时间  $t + dt$  时运动到  $(\mathbf{r} + \mathbf{v}_\mathbf{k} dt, \mathbf{k} + \mathbf{F} dt/\hbar)$  点处，同时有

$$\mathbf{v}_\mathbf{k} = \frac{1}{\hbar} \frac{\partial E(\mathbf{k})}{\partial \mathbf{k}}; \frac{\hbar \mathbf{k}}{dt} = \mathbf{F}, \quad (2.2)$$

其中  $\mathbf{F}$  表示外场作用在载流子上的力。在运动过程中，碰撞过程可能造成在相空间中电子数量变化的净速率  $[\partial f / \partial t]_{\text{coll}}$ 。根据 Liouville 定理，可以得到如下的分布函数

$$f(\mathbf{r} + \mathbf{v}_\mathbf{k} dt, \mathbf{k} + (\mathbf{F}/\hbar) dt, t + dt) \equiv f(\mathbf{r}, \mathbf{k}, t) + \left[ \frac{\partial f}{\partial t} \right]_{\text{coll}} dt. \quad (2.3)$$

对上式的左边部分做一级泰勒级数展开，可以得到玻尔兹曼输运方程<sup>[1, 66]</sup>

$$\frac{\partial f}{\partial \mathbf{r}} \cdot \mathbf{v} + \frac{\partial f}{\partial \mathbf{k}} \cdot \frac{\mathbf{F}}{\hbar} + \frac{\partial f}{\partial t} = \left[ \frac{\partial f}{\partial t} \right]_{\text{coll}}, \quad (2.4)$$

其中  $\partial f / \partial \mathbf{r}$  和  $\partial f / \partial \mathbf{k}$  分别表示  $\nabla_{\mathbf{r}} f$  和  $\nabla_{\mathbf{k}} f$ 。

输运理论中一个关键的方面是碰撞项。当  $f$  离热平衡分布  $f_0$  的偏移很小的时候，通常可以假设由碰撞所导致  $f$  的改变率正比于偏移项本身

$$\left[ \frac{\partial f}{\partial t} \right]_{\text{coll}} = -\frac{f - f_0}{\tau}, \quad (2.5)$$

其中  $\tau$  是比率系数并被称作弛豫时间。一般来说  $\tau = \tau(\mathbf{k}, \mathbf{r})$  取决于能量  $E(\mathbf{k})$  和位置  $\mathbf{r}$ ，通常被看作是一个半经验的参数。在能量弛豫近似中，公式 (2.4) 可以写成

$$\frac{\partial f}{\partial \mathbf{r}} \cdot \mathbf{v} + \frac{\partial f}{\partial \mathbf{k}} \cdot \frac{\mathbf{F}}{\hbar} + \frac{\partial f}{\partial t} = -\frac{f - f_0}{\tau}. \quad (2.6)$$

### 2.1.2 费米黄金定律

考虑一个周期性的电子系统，单粒子的哈密量为  $H_0(\mathbf{k})$ ，电子系统的能量本征值和本征波函数分别为  $\psi_\lambda(\mathbf{k})$  和  $E_\lambda(\mathbf{k})$ ，其中  $\lambda$  是能带指数表示导带和价带。当系统在外加的电磁场中，系统的哈密量可以从无外场下的哈密量  $H_0$  通过将动量  $\hbar\mathbf{k}$  替换为  $\hbar\mathbf{k} + e\mathbf{A}(t)$  得到，其中  $\mathbf{A}(t)$  是光场的矢势。在库仑规范下，在外加电磁场中系统的哈密顿量可以写为

$$H(\mathbf{k}) = H_0(\mathbf{k} + e\mathbf{A}(t)/\hbar). \quad (2.7)$$

在弱外加电磁场微扰的作用下，通常可以忽略上式中非线性的电磁场高次项。考虑横波平面电磁波的频率为  $\omega$ ，电磁场的矢势为

$$\mathbf{A}(t) = A_0 e^{-i\omega t} + A_0 e^{i\omega t}, \quad (2.8)$$

其中  $A_0 = E_0/\omega$ ， $E_0$  是光场的电场强度。哈密顿量中的微扰项可以写为

$$H'(t) = H'(e^{-i\omega t} + e^{i\omega t}), \quad (2.9)$$

其中  $H'$  是去掉  $\mathbf{A}(t)$  的高次项后含时微扰项的不含时系数。通过费米黄金定律，可以得到电子从  $|\lambda, \mathbf{k}\rangle$  态通过电子-光子相互作用散射到  $|\lambda', \mathbf{k}'\rangle$  态的电子跃迁概率为<sup>[67, 68]</sup>

$$W_{\lambda\lambda'}^\mp(\mathbf{k}, \mathbf{k}') = \frac{2\pi}{\hbar} |\langle \lambda', \mathbf{k}' | H' | \lambda, \mathbf{k} \rangle|^2 \delta(E_{\lambda'}(\mathbf{k}') - E_\lambda(\mathbf{k}) \mp \hbar\omega), \quad (2.10)$$

其中 delta 函数中的  $\mp$  分别代表吸收/发射一个能量为  $\hbar\omega$  的光子。

### 2.1.3 光电导的能量平衡方程

在外加电磁场的作用下，费米-狄拉克分布函数与空间无关且电子受到外场的作用已经在碰撞项中考虑。在只考虑光吸收的情况下，公式(2.4)中的玻尔兹曼方程可以写为

$$\frac{\partial f_\lambda}{\partial t} = \left[ \frac{\partial f_\lambda}{\partial t} \right]_{\text{coll}} = \sum_{\lambda', \mathbf{k}'} [W_{\lambda' \lambda}^-(\mathbf{k}', \mathbf{k}) f_{\lambda'}(\mathbf{k}') (1 - f_\lambda(\mathbf{k})) - W_{\lambda \lambda'}^-(\mathbf{k}, \mathbf{k}') f_\lambda(\mathbf{k}) (1 - f_{\lambda'}(\mathbf{k}'))], \quad (2.11)$$

对上式两边乘以  $g_s \sum_{\lambda, \mathbf{k}} E_\lambda(\mathbf{k})$  可以得到吸收光子的能量吸收功率

$$\begin{aligned} P_- &= g_s \sum_{\lambda, \lambda'} \sum_{\mathbf{k}, \mathbf{k}'} [E_{\lambda'}(\mathbf{k}') - E_\lambda(\mathbf{k})] W_{\lambda \lambda'}^-(\mathbf{k}, \mathbf{k}') f_\lambda(\mathbf{k}) (1 - f_{\lambda'}(\mathbf{k}')) \\ &= g_s \hbar \omega \sum_{\lambda, \lambda'} \sum_{\mathbf{k}, \mathbf{k}'} W_{\lambda \lambda'}^-(\mathbf{k}, \mathbf{k}') f_\lambda(\mathbf{k}) (1 - f_{\lambda'}(\mathbf{k}')), \end{aligned} \quad (2.12)$$

其中  $g_s$  是自旋简并指数。由能量吸收功率和电场强度的关系<sup>[66, 69, 70]</sup>可以得到光电导

$$\sigma(\omega) = P_-(\omega) / (2E_0^2). \quad (2.13)$$

这个时候的光电导可以写作

$$\sigma(\omega) = \frac{g_s \hbar \omega}{2E_0^2} \sum_{\lambda, \lambda'} \sum_{\mathbf{k}, \mathbf{k}'} W_{\lambda \lambda'}^-(\mathbf{k}, \mathbf{k}') f_\lambda(E_\lambda(\mathbf{k})) [1 - f_{\lambda'}(E_{\lambda'}(\mathbf{k}'))]. \quad (2.14)$$

其中  $f_\lambda(E_\lambda(\mathbf{k})) = (e^{(E_\lambda(\mathbf{k}) - \mu_\lambda)/k_B T} + 1)^{-1}$  为导带或价带中的费米-狄拉克分布函数， $\mu_\lambda$  为系统中电子或空穴的化学势。

如果同时考虑系统在外加电磁场中的光子发射，方程(2.11)中应该加上光子发射项写作

$$\begin{aligned} \frac{\partial f_\lambda}{\partial t} &= \sum_{\lambda', \mathbf{k}'} [W_{\lambda' \lambda}^-(\mathbf{k}', \mathbf{k}) f_{\lambda'}(\mathbf{k}') (1 - f_\lambda(\mathbf{k})) - W_{\lambda \lambda'}^-(\mathbf{k}, \mathbf{k}') f_\lambda(\mathbf{k}) (1 - f_{\lambda'}(\mathbf{k}'))] \\ &\quad + W_{\lambda' \lambda}^+(\mathbf{k}', \mathbf{k}) f_{\lambda'}(\mathbf{k}') (1 - f_\lambda(\mathbf{k})) - W_{\lambda \lambda'}^+(\mathbf{k}, \mathbf{k}') f_\lambda(\mathbf{k}) (1 - f_{\lambda'}(\mathbf{k}'))]. \end{aligned} \quad (2.15)$$

通过关系  $W_{\lambda \lambda'}^-(\mathbf{k}, \mathbf{k}') = W_{\lambda' \lambda}^+(\mathbf{k}', \mathbf{k})$ ，总的能量吸收功率可以写为

$$P = P_- + P_+ = g_s \hbar \omega \sum_{\lambda, \lambda'} \sum_{\mathbf{k}, \mathbf{k}'} W_{\lambda \lambda'}^-(\mathbf{k}, \mathbf{k}') (f_\lambda(\mathbf{k}) - f_{\lambda'}(\mathbf{k}')), \quad (2.16)$$

同时光电导可以写作

$$\sigma(\omega) = \frac{g_s \hbar \omega}{2E_0^2} \sum_{\lambda, \lambda'} \sum_{\mathbf{k}, \mathbf{k}'} W_{\lambda \lambda'}^-(\mathbf{k}, \mathbf{k}') [f_\lambda(E_\lambda(\mathbf{k})) - f_{\lambda'}(E_{\lambda'}(\mathbf{k}'))]. \quad (2.17)$$

由于自发辐射项通常是非常小的，公式 (2.17) 和公式 (2.14) 通常是等价的。这里需要指出的是，在计算一个不考虑光生载流子的纯电子或空穴系统，可以任意使用公式 (2.14) 或公式 (2.17) 并去掉费米-狄拉克分布函数的下角标统一使用整个系统电子的费米-狄拉克分布函数。如果在计算的过程中考虑光生载流子的浓度，则系统中同时存在电子和空穴两种载流子。导带和价带中电子的费米-狄拉克分布分别基于导带中电子的化学势和价带中空穴的化学势来分别描述。在给定的光生载流子浓度下，通常应不考虑自发辐射项并使用公式 (2.14) 进行光电导的计算。如果使用公式 (2.17)，则在计算过程中会出现光子能量与载流子浓度的不匹配，在计算过程中光电导会出现较小的负值情况。

如果全面的考虑光生载流子的浓度和辐射场的频率和强度，可以近似的通过一个给定的弛豫时间并使用能量弛豫近似来描述光生载流子的通过电子-声子、电子-光子等相互作用的弛豫过程。在此时，如下玻尔兹曼输运方程的右边将包括两个部分并有

$$\frac{\partial f_\lambda}{\partial t} = \sum_{\lambda', \mathbf{k}'} [W_{\lambda'\lambda}^-(\mathbf{k}', \mathbf{k}) + W_{\lambda\lambda'}^-(\mathbf{k}, \mathbf{k}')](f_{\lambda'}(\mathbf{k}') - f_\lambda(\mathbf{k})) - \frac{f_\lambda(\mathbf{k}) - f_{\lambda 0}(\mathbf{k})}{\tau}, \quad (2.18)$$

上式右边第一项为光生载流子产生率和第二项为光生载流子弛豫散射率。在系统达到稳定的准平衡态时，且带内跃迁对导带和价带内的载流子数不做贡献，对上式两边乘以  $g_s \sum_{\mathbf{k}}$ ，经过整理后可以得到

$$\frac{\partial n_e}{\partial t} = \frac{\partial n_h}{\partial t} = g_s \sum_{\mathbf{k}, \mathbf{k}'} W_{-+}^-(\mathbf{k}, \mathbf{k}') [f_-(\mathbf{k}) - f_+(\mathbf{k}')] - \frac{\Delta n}{\tau} = 0. \quad (2.19)$$

通过上式，可以得到辐射场的强度和频率与光生载流子浓度的关系。整个系统电子和空穴的浓度的关系为

$$n_{e/h} = n_{e/h}^0 + \Delta n. \quad (2.20)$$

然后通过载流子守恒定理

$$n_{e/h} = \frac{1}{(2\pi)^2} \sum_s \int d\mathbf{k}^2 \delta_{\lambda, -1} + \lambda [e^{(E_\lambda(\mathbf{k}) - \mu_\lambda)/k_B T} + 1]^{-1}, \quad (2.21)$$

可以得到载流子浓度和电子/空穴化学势的关系。将公式 (2.19) 和公式 (2.21) 联立进行自治求解，便可得到光生载流子浓度。公式 (2.19) 中右边的第一部分是光生载流子的产生速率，因而乘以每个光生载流子产生时吸收的能量  $\hbar\omega$  后便是系统的光吸收功率。于是带间跃迁所贡献的光电导为

$$\sigma(\omega) = \frac{g_s \hbar \omega}{2E_0^2} \sum_{\mathbf{k}, \mathbf{k}'} W_{-+}^-(\mathbf{k}, \mathbf{k}') [f_-(E_-(\mathbf{k})) - f_+(E_+(\mathbf{k}'))]. \quad (2.22)$$

上式的结果与公式 (2.17) 中相同。

## 2.2 线性响应理论

线性响应理论的基本原理，是由久保亮伍 (R. Kubo) 于 1964 年首先给出<sup>[71]</sup>，被广泛的使用于多粒子系统中输运特性的理论计算。

一般的为了了解系统的物理特性，通常采用外加某种外加扰动系统，然后观测系统的物理量随着外加扰动的变化<sup>[72, 73]</sup>。人们通过研究外加扰动和物理响应的关系可以得到系统的物理特性。设所考虑系统的哈密顿量为  $H$  且其能量本征值和本征波函数分别为  $E_n$  和  $\phi_n$ 。令外场微小的扰动所贡献的附加哈密顿量项为  $H'(t)$ 。

在外场微扰下的薛定谔方程为

$$i\hbar \frac{\partial \psi}{\partial t} = [H + H'(t)]\psi, \quad (2.23)$$

令含时波函数  $\psi = e^{-iHt/\hbar}\varphi(t)$ ，再将  $\psi$  带入上式，可以得到

$$\frac{\partial \varphi}{\partial t} = \frac{1}{i\hbar} e^{iHt/\hbar} H'(t) e^{-iHt/\hbar} \varphi. \quad (2.24)$$

由于系统必须满足  $\varphi_{t \rightarrow -\infty} = \phi_m$ ，则可得到  $\varphi(t) = \phi_m + \frac{1}{i\hbar} \int_{-\infty}^t e^{iHt'/\hbar} H'(t') e^{-iHt'/\hbar} \varphi dt'$ 。

若在系统中通过物理量  $A$  来观测外场的响应，则算符  $A$  在时间  $t$  时刻的期望值

$$\bar{A} = \int \psi^\dagger A \psi d\tau = \int \varphi^\dagger e^{iHt/\hbar} A e^{-iHt/\hbar} \varphi d\tau \quad (2.25)$$

通过对  $\varphi(t)$  进行自我迭代的方法，可以求得其精确至  $H'(t')$  一次线性项的解为  $\varphi(t) = \phi_m + \frac{1}{i\hbar} \int_{-\infty}^t e^{iHt'/\hbar} H'(t') e^{-iHt'/\hbar} \phi_m dt'$ 。带入上式并略去  $H'(t')$  的二次项可以得到

$$\bar{A} = \langle m | A | m \rangle + \frac{1}{i\hbar} \int_{-\infty}^t dt' \langle m | [\tilde{A}(t), \tilde{H}'(t')] | m \rangle, \quad (2.26)$$

其中  $\tilde{A}(t) = e^{iHt/\hbar} A e^{-iHt/\hbar}$  同时  $\tilde{H}'(t') = e^{iHt'/\hbar} H'(t') e^{-iHt'/\hbar}$ 。

在观测上的响应应该是  $\bar{A}$  的统计平均值，计为  $\langle A \rangle_t = \sum_m W_m \bar{A}$ ，其中  $W_m$  是在  $\phi_m$  态的概率。因而系统力学量  $A$  统计平均值的改变为

$$\Delta A = \langle A \rangle_t - \langle A \rangle_{t=-\infty} = \frac{1}{i\hbar} \int_{-\infty}^t dt' \langle [\tilde{A}(t), \tilde{H}'(t')] \rangle, \quad (2.27)$$

其中  $\Delta A$  是外场的响应，而  $\langle A \rangle_{t=-\infty}$  是无外场时  $A$  的统计平均值。

如果外场的震荡频率为  $\omega$  且有一个很小的衰减率  $\eta$ ，则外场附加的哈密顿量可以假设为

$$H'(t) = B e^{(-i\omega+\eta)t}, \quad (2.28)$$

其中  $B$  为算符。可以得到在外场下的响应可以写作

$$\Delta A = \frac{1}{i\hbar} \int_{-\infty}^{\infty} dt' \theta(t-t') \langle [\tilde{A}(t), \tilde{B}(t')] \rangle e^{(-i\omega+\eta)t'}, \quad (2.29)$$

其中  $\tilde{B}(t') = e^{iHt/\hbar}Be^{-iHt/\hbar}$  且  $\theta(t - t')$  是阶梯函数。从上式可以知道外场的响应和外场扰动成线性关系。

如果定义推迟格林函数  $G_R(t - t') = \frac{1}{i\hbar}\theta(t - t')\langle[\tilde{A}(t), \tilde{B}(t')]\rangle$ , 上式可以写作

$$\Delta A = \int_{-\infty}^{\infty} dt' G_R(t - t') e^{(-i\omega + \eta)t'}. \quad (2.30)$$

对  $G_R(t)$  作傅里叶变换之后

$$G_R(\omega) = \int_{-\infty}^{\infty} dt G_R(t) e^{(i\omega - \eta)t}, \quad (2.31)$$

其中  $\eta \rightarrow 0^+$  是无穷小量。通过与公式 (2.29) 的对比, 可以得到

$$\Delta A = G_R(\omega) e^{(-i\omega + \eta)t}. \quad (2.32)$$

上式说明在线性范围内外场的响应  $\Delta A$  和外场扰动  $H'(t)$  有着相同的时间依赖变化关系。系统的有关物理量会随着外加扰动以相同频率变化。

有些物理量如电子气中的电流密度算符以及密度起伏算符在无外场情况下的统计平均值为零。因而对于这些物理量有如下关系

$$i\langle \dot{A} \rangle_t = (i\omega + \eta)\langle A \rangle_t. \quad (2.33)$$

### 2.3 电导的 Kubo 公式

考虑在带电粒子系统在外加电磁场中, 电磁场将会产生一个电流, 而电导则是电流对电场的线性响应系数。通常来说电导在时间和空间上是非局域的, 譬如在  $\mathbf{r}$  点时间  $t$  处电流  $\mathbf{j}$  取决于在  $\mathbf{r}'$  点的电场强度

$$j_{\alpha}(\mathbf{r}, t) = \int d\mathbf{r}' \sum_{\beta} \sigma_{\alpha\beta}(\mathbf{r}, \mathbf{r}'; \omega) E_{\beta}(\mathbf{r}') e^{-i\omega t}, \quad (2.34)$$

其中  $\sigma_{\alpha\beta}(\mathbf{r}, \mathbf{r}'; \omega)$  是描述在  $\hat{e}_{\alpha}$  方向的电流对  $\hat{e}_{\beta}$  方向外加交流电场响应的电导张量。通常我们对体材料或者晶体材料的均匀电导感兴趣。此时的电导是一个标量。这里我们先省去张量的下角标, 电流密度算符可以写成

$$\hat{j}_{\text{tot}}(\mathbf{r}) = \hat{j}(\mathbf{r}) + \hat{j}_{\text{dia}}(\mathbf{r}) \quad (2.35)$$

其中

$$\begin{aligned} \hat{j}(\mathbf{r}) &= -\frac{e}{2m} \sum_i [p_i \delta(\mathbf{r} - \mathbf{r}_i) + \delta(\mathbf{r} - \mathbf{r}_i)p_i], \\ \hat{j}_{\text{dia}}(\mathbf{r}) &= -\frac{n(\mathbf{r})e^2}{m} \mathbf{A}(\mathbf{r}); n(\mathbf{r}) = \sum_i \delta(\mathbf{r} - \mathbf{r}_i). \end{aligned} \quad (2.36)$$

在库仑规范下，电磁场的电场强度  $\mathbf{E}$  和矢势  $\mathbf{A}$  有如下关系

$$E(\mathbf{r}, t) = -\frac{\partial \mathbf{A}(\mathbf{r}, t)}{\partial t} = i\omega A(\mathbf{r}, t). \quad (2.37)$$

由外加电磁场所引起的哈密顿量中的附加微扰项近似到外加电磁场的线性项为

$$H'(t) = - \int d\mathbf{r} \hat{j}(\mathbf{r}) \cdot \mathbf{A}(\mathbf{r}) e^{-i\omega t} = \frac{i}{\omega} \int d\mathbf{r} \hat{j}(\mathbf{r}) \cdot \mathbf{E}(\mathbf{r}) e^{-i\omega t}. \quad (2.38)$$

因而系统的电导可以写为

$$\sigma_{\alpha\beta}(\mathbf{r}, \mathbf{r}'; \omega) = \frac{ie^2 n(\mathbf{r})}{m\omega} \delta(\mathbf{r} - \mathbf{r}') \delta_{\alpha\beta} + \frac{1}{\hbar\omega} \int_{-\infty}^t dt' e^{i(\omega+i\eta)(t-t')} \langle [\hat{j}_\alpha(\mathbf{r}, t), \hat{j}_\beta(\mathbf{r}', t')] \rangle \quad (2.39)$$

其中  $\eta \rightarrow 0$  是为了保证  $t = -\infty$  时外场微扰为零的无穷小量。

上式中只是关于时间差异  $t - t'$  的函数。如果用这个时间差异来做时间积分的替换后  $t - t' \rightarrow t$ , 可以得到

$$\sigma_{\alpha\beta}(\mathbf{r}, \mathbf{r}'; \omega) = \frac{ie^2 n(\mathbf{r})}{m\omega} \delta(\mathbf{r} - \mathbf{r}') \delta_{\alpha\beta} + \frac{1}{\hbar\omega} \int_0^\infty dt e^{i(\omega+i\eta)t} \langle [\hat{j}_\alpha(\mathbf{r}, t), \hat{j}_\beta(\mathbf{r}', 0)] \rangle \quad (2.40)$$

对上式做空间傅里叶变换之后，可以得到

$$\sigma_{\alpha\beta}(\mathbf{q}, \omega) = \frac{ie^2 n(\mathbf{r})}{m\omega} \delta_{\alpha\beta} + \frac{1}{\hbar\omega} \int_0^\infty dt e^{i(\omega+i\eta)t} \langle [\hat{j}_\alpha^\dagger(\mathbf{q}, t), \hat{j}_\beta(\mathbf{q}, 0)] \rangle \quad (2.41)$$

上式即为常用电导的 Kubo 公式<sup>[74, 75]</sup>。

在均匀材料的情况下，电导公式 (2.40) 可以写为

$$\sigma_{\alpha\beta}(\omega) = \frac{ie^2 n}{m\omega} \delta_{\alpha\beta} + \frac{1}{\hbar\omega} \int_0^\infty dt e^{i(\omega+i\eta)t} \langle [\hat{j}_\alpha(t), \hat{j}_\beta(0)] \rangle. \quad (2.42)$$

金属或者半导体材料通常可以非常好的用无相互作用的费米系统来近似描述。系统总的哈密顿量是各个电子的单粒子哈密顿量之和  $\sum_i H_0(i)$ 。单粒子本征态为  $H_0|n\rangle = E_n|n\rangle$  作为便利的基元，同时电流算符可以写作

$$\hat{j}_\alpha(t) = \sum_{nm} \langle n | \hat{j}_\alpha | m \rangle c_n^\dagger c_m e^{i(E_n - E_m)t/\hbar}, \quad (2.43)$$

对于相互作用系统使用相同的本征态基元，同时在  $t = 0$  的时候仍然有着相同的算符表达形式，但是海森堡时间电流算符没办法继续明确的给出。为了求解 Kubo 公式，在无相互作用近似下的公式中，需要如下关系<sup>[75]</sup>

$$\begin{aligned} \text{tr}\hat{\rho}([c_n^\dagger c_p, c_q^\dagger c_m]) &= \delta_{mp} \delta_{nq} (f_n - f_m), \\ \text{tr}\hat{\rho}(c_n^\dagger c_m c_p^\dagger c_q) &= \delta_{mp} \delta_{nq} f_n (1 - f_m) + \delta_{nm} \delta_{pq} f_n f_p, \end{aligned} \quad (2.44)$$

其中  $\text{tr}$  是求迹运算符且  $f_n = (e^{(E_n - \mu)/k_B T} + 1)^{-1}$  是费米-狄拉克分布函数。通过上式，可以得到 Kubo-Greenwood 电导公式<sup>[75, 76]</sup>

$$\begin{aligned}\sigma_{\alpha\beta}(\omega) &= \frac{ie^2 n}{m\omega} \delta_{\alpha\beta} + i\hbar \sum_{nm} \frac{f_n - f_m}{E_m - E_n} \frac{\langle n | \hat{j}_\alpha | m \rangle \langle m | \hat{j}_\beta | n \rangle}{\hbar(\omega + i\eta) + E_n - E_m} \\ &= \frac{ie^2 n}{m\omega} \delta_{\alpha\beta} + \frac{ie^2}{\omega} \sum_{nm} \frac{f_n - f_m}{\hbar(\omega + i\eta) + E_n - E_m} \langle n | \hat{v}_\alpha | m \rangle \langle m | \hat{v}_\beta | n \rangle,\end{aligned}\quad (2.45)$$

其中速度算符  $\hat{v}_\alpha = \hbar^{-1} \partial H / \partial k_\alpha$ 。

## 2.4 无规则相近似 (RPA)

无规则相近似通常有两种推导方式<sup>[74, 77]</sup>：一种是通过自治的动力学方程方法<sup>[78]</sup>，另一种则是格林函数和费曼图法<sup>[79]</sup>。下面给出了动力学方程法的基本推导流程<sup>[72, 73]</sup>。

在凝胶模型下相互作用电子气在二次量子化哈密顿量可以表示为：

$$H = \sum_{\mathbf{k}s} E_{\mathbf{k}} C_{\mathbf{k}s}^+ C_{\mathbf{k}s} + \frac{1}{2} \sum_{\mathbf{q}(\mathbf{q} \neq 0)} \sum_{\mathbf{k}\mathbf{k}'} \sum_{ss'} V(\mathbf{q}) C_{\mathbf{k}+\mathbf{q},s}^+ C_{\mathbf{k}'-\mathbf{q},s'}^+ C_{\mathbf{k}',s'} C_{\mathbf{k},s}, \quad (2.46)$$

其中  $C_{\mathbf{k}}^+$  和  $C_{\mathbf{k}}$  分别为产生和湮灭算符， $V(\mathbf{q})$  是库仑相互作用的傅里叶变换系数。

定义单个电子-空穴对的激发算符

$$\rho_{\mathbf{k}\mathbf{q}}^+ \equiv C_{\mathbf{k}+\mathbf{q}}^+ C_{\mathbf{k}}, \quad (2.47)$$

表示将  $\mathbf{k}$  态上的一个电子激发到  $\mathbf{k} + \mathbf{q}$  态上同时产生一个电子-空穴对。相互作用电子系统中的个别电子-空穴对的激发是相互耦合的，算符  $\rho_{\mathbf{k}\mathbf{q}}^+$  和  $\rho_{\mathbf{k}\mathbf{q}}$  的海森堡运动方程为

$$-i\dot{\rho}_{\mathbf{k}\mathbf{q}}^+ = [H, \rho_{\mathbf{k}\mathbf{q}}^+]; \quad -i\dot{\rho}_{\mathbf{k}\mathbf{q}} = [H, \rho_{\mathbf{k}\mathbf{q}}]. \quad (2.48)$$

密度起伏算符  $\rho_{\mathbf{q}}^+ = \sum_{\mathbf{k}} \rho_{\mathbf{k}\mathbf{q}}^+$  是总动量为  $\hbar\mathbf{q}$  的所有电子-空穴对的叠加。

在无相互作用的情况下  $V(\mathbf{q}) = 0$ ，这时候  $\rho_{\mathbf{k}\mathbf{q}}^+$  的本征方程为

$$-i\dot{\rho}_{\mathbf{k}\mathbf{q}}^+ = [H, \rho_{\mathbf{k}\mathbf{q}}^+] = \hbar\omega_{\mathbf{k}\mathbf{q}} \rho_{\mathbf{k}\mathbf{q}}^+, \quad (2.49)$$

其中  $\hbar\omega_{\mathbf{k}\mathbf{q}} = E_{\mathbf{k}+\mathbf{q}} - E_{\mathbf{k}}$  是能量本征值。在相互作用的电子系统下，则有

$$[H, \rho_{\mathbf{k}\mathbf{q}}^+] = (E_{\mathbf{k}+\mathbf{q}} - E_{\mathbf{k}})\omega \rho_{\mathbf{k}\mathbf{q}}^+ + \frac{1}{2} \sum_{\mathbf{q}'(\mathbf{q}' \neq 0)} V(\mathbf{q}') \{ [\rho_{\mathbf{q}'}, \rho_{\mathbf{k}\mathbf{q}}^+] \rho_{\mathbf{q}'} + \rho_{\mathbf{q}'}^+ [\rho_{\mathbf{q}'}, \rho_{\mathbf{k}\mathbf{q}}^+] \}, \quad (2.50)$$

其中  $[\rho_{\mathbf{q}'}, \rho_{\mathbf{k}\mathbf{q}}^+] = C_{\mathbf{k}+\mathbf{q}-\mathbf{q}'}^+ C_{\mathbf{k}} - C_{\mathbf{k}+\mathbf{q}}^+ C_{\mathbf{k}+\mathbf{q}'}^+$ 。整理后将  $\mathbf{q}' = \mathbf{q}$  和  $\mathbf{q}' \neq \mathbf{q}$  项分离开来，上式可以写作

$$\begin{aligned} [H, \rho_{\mathbf{k}\mathbf{q}}^+] &= (E_{\mathbf{k}+\mathbf{q}} - E_{\mathbf{k}}) \rho_{\mathbf{k}\mathbf{q}}^+ \\ &\quad + \frac{1}{2} V(\mathbf{q}) \left\{ \sum_{\mathbf{k}'} \rho_{\mathbf{k}'\mathbf{q}}^+ (C_{\mathbf{k}}^+ C_{\mathbf{k}} - C_{\mathbf{k}+\mathbf{q}}^+ C_{\mathbf{k}+\mathbf{q}}) \right. \\ &\quad \left. + (C_{\mathbf{k}}^+ C_{\mathbf{k}} - C_{\mathbf{k}+\mathbf{q}}^+ C_{\mathbf{k}+\mathbf{q}}) \sum_{\mathbf{k}'} \rho_{\mathbf{k}'\mathbf{q}}^+ \right\} \\ &\quad + \frac{1}{2} \sum_{\mathbf{q}' (\mathbf{q}' \neq \mathbf{q})} V(\mathbf{q}') \left\{ \rho_{\mathbf{q}'}^+ (C_{\mathbf{k}+\mathbf{q}-\mathbf{q}'}^+ C_{\mathbf{k}} - C_{\mathbf{k}+\mathbf{q}}^+ C_{\mathbf{k}+\mathbf{q}'}) \right. \\ &\quad \left. + (C_{\mathbf{k}+\mathbf{q}-\mathbf{q}'}^+ C_{\mathbf{k}} - C_{\mathbf{k}+\mathbf{q}}^+ C_{\mathbf{k}+\mathbf{q}'}) \sum_{\mathbf{k}'} \rho_{\mathbf{q}'}^+ \right\}, \end{aligned} \quad (2.51)$$

其中第一项代表自由运动，第二项代表所有具有相同  $\mathbf{q}$  的电子–空穴耦合项，第三项则是具有不同  $\mathbf{q}$  的电子–空穴耦合非线性项。为了将上式近似求解，将  $[\rho_{\mathbf{q}'}, \rho_{\mathbf{k}\mathbf{q}}^+]$  的值用基态的平均值代替可以得到

$$[\rho_{\mathbf{q}'}, \rho_{\mathbf{k}\mathbf{q}}^+] = \langle 0 | C_{\mathbf{k}+\mathbf{q}-\mathbf{q}'}^+ C_{\mathbf{k}} | 0 \rangle - \langle 0 | C_{\mathbf{k}+\mathbf{q}}^+ C_{\mathbf{k}+\mathbf{q}'} | 0 \rangle = (f_{\mathbf{k}} - f_{\mathbf{k}+\mathbf{q}}) \delta_{\mathbf{q}\mathbf{q}'} \quad (2.52)$$

将上述结果带入公式 (2.51)，可以得到量子运动方程在无规则相近似 (Random Phase Approximation; RPA) 下的解为<sup>[72, 73]</sup>

$$[H, \rho_{\mathbf{k}\mathbf{q}}^+] = (E_{\mathbf{k}+\mathbf{q}} - E_{\mathbf{k}}) \rho_{\mathbf{k}\mathbf{q}}^+ + V(\mathbf{q}) (f_{\mathbf{k}} - f_{\mathbf{k}+\mathbf{q}}) \rho_{\mathbf{q}}^+. \quad (2.53)$$

## 2.5 RPA 介电函数

在考虑电子系统对外场响应的时候，外场的附加哈密顿量可以写成

$$H'(t) = \sum_i V_{\text{ex}}(\mathbf{r}_i) e^{(-i\omega+\eta)t} = \sum_{\mathbf{q}} V_{\text{ex}}(\mathbf{q}) \sum_i e^{i\mathbf{q} \cdot \mathbf{r}_i} e^{(-i\omega+\eta)t} = \sum_{\mathbf{q}} V_{\text{ex}}(\mathbf{q}) \rho_{\mathbf{q}}^+ e^{(-i\omega+\eta)t}. \quad (2.54)$$

这时候  $\rho_{\mathbf{k}\mathbf{q}}^+$  的量子运动方程应写成

$$-i\dot{\rho}_{\mathbf{k}\mathbf{q}}^+ = [H, \rho_{\mathbf{k}\mathbf{q}}^+] + [H'(t), \rho_{\mathbf{k}\mathbf{q}}^+]. \quad (2.55)$$

在无规则相近似 (RPA) 下

$$[H'(t), \rho_{\mathbf{k}\mathbf{q}}^+] = \sum_{\mathbf{q}'} V_{\text{ex}}(\mathbf{q}') [\rho_{-\mathbf{q}'}, \rho_{\mathbf{k}\mathbf{q}}^+] = V_{\text{ex}}(-\mathbf{q}) (f_{\mathbf{k}} - f_{\mathbf{k}+\mathbf{q}}) e^{(-i\omega+\eta)t}. \quad (2.56)$$

将公式 (2.56) 带入公式 (2.55) 可以得到

$$-i\dot{\rho}_{\mathbf{k}\mathbf{q}}^+ = \hbar\omega_{\mathbf{k}\mathbf{q}} \rho_{\mathbf{k}\mathbf{q}}^+ + (f_{\mathbf{k}} - f_{\mathbf{k}+\mathbf{q}}) [V_{\text{ex}}(-\mathbf{q}) e^{(-i\omega+\eta)t} + V(\mathbf{q}) \rho_{\mathbf{q}}^+]. \quad (2.57)$$

利用线性响应的结论  $i\langle\rho_{\mathbf{k}\mathbf{q}}^+\rangle_t = (\hbar\omega + i\eta)\langle\rho_{\mathbf{k}\mathbf{q}}^+\rangle_t$  以及  $\langle\rho_{\mathbf{q}}^+\rangle_t = \sum_{\mathbf{k}}\langle\rho_{\mathbf{k}\mathbf{q}}^+\rangle_t$  对上式进行统计平均可以得到

$$\langle\rho_{\mathbf{q}}^+\rangle_t = \sum_{\mathbf{k}}\langle\rho_{\mathbf{k}\mathbf{q}}^+\rangle_t = \sum_{\mathbf{k}}\frac{f_{\mathbf{k}+\mathbf{q}} - f_{\mathbf{k}}}{\hbar\omega + E_{\mathbf{k}+\mathbf{q}} - E_{\mathbf{k}} + i\eta}[V_{\text{ex}}(-\mathbf{q})e^{(-i\omega+\eta)t} + V(\mathbf{q})\langle\rho_{\mathbf{q}}^+\rangle_t]. \quad (2.58)$$

由于  $\langle\rho_{\mathbf{q}}^+\rangle_t = \langle\rho_{-\mathbf{q}}^+\rangle_t$ , 可以得到

$$\langle\rho_{\mathbf{q}}\rangle_t = \sum_{\mathbf{k}}\frac{f_{\mathbf{k}-\mathbf{q}} - f_{\mathbf{k}}}{\hbar\omega + E_{\mathbf{k}-\mathbf{q}} - E_{\mathbf{k}} + i\eta}[V_{\text{ex}}(\mathbf{q})e^{(-i\omega+\eta)t} + V(-\mathbf{q})\langle\rho_{\mathbf{q}}\rangle_t]. \quad (2.59)$$

系统总势能的傅里叶变换为外场势能和对应的感生屏蔽势之和

$$V_{\text{all}}(\mathbf{q}, t) = V_{\text{ex}}(\mathbf{q})e^{(-i\omega+\eta)t} + V(\mathbf{q})\langle\rho_{\mathbf{q}}\rangle_t. \quad (2.60)$$

因而可以得到

$$\langle\rho_{\mathbf{q}}\rangle_t = \sum_{\mathbf{k}}\frac{f_{\mathbf{k}-\mathbf{q}} - f_{\mathbf{k}}}{\hbar\omega + E_{\mathbf{k}-\mathbf{q}} - E_{\mathbf{k}} + i\eta}V_{\text{all}}(\mathbf{q}, t). \quad (2.61)$$

将上两式合并可以得到

$$\frac{V_{\text{ex}}(\mathbf{q}, t)}{V_{\text{all}}(\mathbf{q}, t)} = 1 - V(\mathbf{q})\sum_{\mathbf{k}}\frac{f_{\mathbf{k}-\mathbf{q}} - f_{\mathbf{k}}}{\hbar\omega + E_{\mathbf{k}-\mathbf{q}} - E_{\mathbf{k}} + i\eta}, \quad (2.62)$$

其中  $V_{\text{ex}}(\mathbf{q}, t) = V_{\text{ex}}(\mathbf{q})e^{(-i\omega+\eta)t}$ 。

根据外场势和总势能的关系, 可以得到所定义的 RPA 介电函数<sup>[6, 74]</sup>

$$\epsilon_{\text{RPA}}(\mathbf{q}, \omega) = 1 - V(\mathbf{q})\Pi(\mathbf{q}, \omega), \quad (2.63)$$

其中

$$\Pi(\mathbf{q}, \omega) = \sum_{\mathbf{k}}\frac{f_{\mathbf{k}+\mathbf{q}} - f_{\mathbf{k}}}{\hbar\omega + E_{\mathbf{k}+\mathbf{q}} - E_{\mathbf{k}} + i\eta}, \quad (2.64)$$

是密度-密度关联函数。

在通常的导带和价带的二带模型中并考虑自旋, 可以得到系统的 RPA 介电函数为

$$\epsilon_{\text{RPA}}(\mathbf{q}, \omega) = 1 - v_q \sum_s \sum_{\lambda\lambda'} \sum_{\mathbf{k}} \frac{f_{\lambda'\mathbf{k}+\mathbf{q}}^s - f_{\lambda\mathbf{k}}^s}{\hbar\omega + E_{\lambda\mathbf{k}+\mathbf{q}}^s - E_{\lambda\mathbf{k}}^s + i\eta} C_{\lambda\mathbf{k}, \lambda'\mathbf{k}+\mathbf{q}}^s, \quad (2.65)$$

其中  $v_q$  是裸库仑势的傅里叶变化系数并且  $C_{\lambda\mathbf{k}, \lambda'\mathbf{k}+\mathbf{q}}^s = |\langle\mathbf{k} + \mathbf{q}, \lambda's|\mathbf{k}, \lambda s\rangle|^2$  是不同电子跃迁通道中库仑势的形状因子。

### 第三章 单层和多层石墨烯系统的红外到太赫兹光吸收窗口

自从 2004 年石墨烯的突破性的发现之后<sup>[7]</sup>，由于其具备非常优异的物理性质，譬如非常高的电子迁移率，非常高的力学强度，非常优异的热导率，光电性质等，使得基于石墨烯的新奇器件的研究成为了迅速发展的领域。当前，基于石墨烯器件的透明柔性电子学是十分受瞩目的技术并有着从可折叠显示、电子纸到透明太阳能电池的重要应用。空气/石墨烯/介电衬底结构已经被证实在紫外到近红外频段具有比较高的光透射系数。这使得石墨烯可以替代通常用到的铟锡氧化物 (ITO) 透明电极<sup>[80, 81]</sup> 来制作更好且更便宜的 LED，LCD 等器件。石墨烯系统中受调控的光透射率可以用来制作新型的具有宽阔的光和电调制带宽的光调制器<sup>[82-84]</sup>。同时，基于石墨烯的光探测器也因为其具有的较宽的光谱带宽和超快的响应时间<sup>[85-87]</sup> 而受到广泛的关注。石墨烯作为一种内禀的二维材料，已经表明在石墨烯表面附近的光生载流子能够引起极其灵敏的静电微电导。通过利用光门效应<sup>[88]</sup>，使得石墨烯成为特别具有前景的高增益光探测材料。另外，由于具有无带隙的态密度和高量子效率，石墨烯被认为是应用于光敏太赫兹 ( $10^{12}$  Hz 或 THz) 器件的杰出候选材料。实验上已经证实石墨烯在太赫兹波段范围的光电导可以很好的通过 Drude 模型进行描述，说明石墨烯是类金属性的太赫兹材料<sup>[89]</sup>。最后，单层和双层石墨烯系统在太赫兹到远红外频段具有的较强的非线性光响应，使得其成为可应用于非线性光子学和光电子学器件的优异材料<sup>[90, 91]</sup>。

众所周知，单层和双层石墨烯具有无带隙的二维电子结构，而 ABC-堆垛的三层石墨烯则是有着可调控原始带隙的半导体。对于多层石墨烯薄膜，它的电子结构受到石墨烯层数和堆垛顺序的强烈影响。因而，电子能带结构的特性将能直接影响不同层数石墨烯系统的电学和光学性质。目前，低成本和可靠的高质量大面积石墨烯薄膜的生长主要是通过化学气相沉积技术 (chemical vapor deposition; CVD) 来实现<sup>[92]</sup>。而通过化学气相沉积方法所得到的主要是多层石墨烯样品。近些年来，不同石墨烯系统的光学和光电性质被广泛的进行了研究。在理论上，不同层数石墨烯的电子能带结构已经被人们所研究<sup>[22, 93-97]</sup>。低温下单层和 AB-堆垛多层石墨烯的光电导已经通过久保公式得到<sup>[98]</sup>，其中不同石墨烯系统光学性质的研究范围主要集中在紫外到远红外区域。实验上，分子束外延 (molecular beam epitaxy; MBE) 生长的石墨烯在紫外到太赫兹范围内的光学性质已经被实验测量。同时多层石墨烯系统在红外和太赫兹区域的高透射率窗口已经被观测到<sup>[100]</sup>。已经证实石墨烯在可见光频段每层石墨烯的普适光电导为  $\sigma_0 = \pi e^2 / (2h)$ <sup>[101, 102]</sup>。单层、双层和三层石墨烯相对应的光透射系数分别大约为 97.7%，95.4% 和 93.1%，且每层之间的间距大约为 2.3%<sup>[21]</sup>。与此同时，单层石墨烯在室温下能观测到一个在中红外到太赫兹范围的光吸收窗口<sup>[101, 102]</sup>。这个单层石墨烯中光吸收窗口的宽度和深度，特别是在吸收窗口的低频率边缘，受到温度和载流子浓度强烈的影响。这些发现表明石墨烯系统可以应用于外界环境中的红外或者太赫兹

辐射探测。我们之前的理论工作<sup>[103]</sup> 表明在双层石墨烯中也可以获得太赫兹光吸收窗口。

当前，单层和双层石墨烯系统的光学性质已经得到较好的研究。但是对于层数  $N \geq 3$  的石墨烯系统则研究得较少。大多数研究多层石墨烯系统光学性质的理论工作主要集中在紫外到红外波段的吸收峰和在可见光范围内的普适光电导<sup>[98]</sup>。在这项研究中，我们通过低能有效的能带模型来研究单层和多层石墨烯系统对辐射场的光响应。可以定性的知道，在红外到太赫兹范围内，石墨烯的层数一定会对石墨烯系统的光学性质产生影响。因此，给出单层和多层石墨烯系统的光电性质如何受到石墨烯层数和堆垛次序变化定量的答案是非常重要并且十分有意义的<sup>[99]</sup>。这是我们开展这项理论研究的主要目的。

### 3.1 单层和多层石墨烯系统的光电导

我们考虑在介电衬底如在  $\text{SiO}_2$  衬底上  $x-y$  平面上的石墨烯在沿  $x$ -方向偏振的线偏振弱光场下。光场的矢势为  $A(t) = F_0 \sin(2\pi\nu t)/(2\pi\nu)$ ，其中  $F_0$  和  $\nu$  分别为光场的电场强度和光场的光子频率。在这种情况下石墨烯的光电响应可以通过半经典玻尔兹曼方程推导出的平衡方程得到<sup>[104]</sup>。通过这种方法，可以得到总的能量转移率： $P = \sum_{\lambda,\lambda'} P_{\lambda\lambda'}$ ，其中  $\lambda = +1$  代表导带同时  $\lambda = -1$  代表价带， $P_{\lambda\lambda'} = 4h\nu \sum_{\mathbf{k}',\mathbf{k}} f_\lambda(\mathbf{k}) [1 - f_{\lambda'}(\mathbf{k}')] W_{\lambda\lambda'}(\mathbf{k}, \mathbf{k}')$  是不同跃迁通道所引起能量转化率， $W_{\lambda\lambda'}(\mathbf{k}, \mathbf{k}')$  是由费米黄金定律所得到的电子跃迁概率， $f_\lambda(\mathbf{k}) \simeq f_\lambda[E_\lambda(\mathbf{k})]$  是石墨烯系统中载流子的费米-狄拉克分布函数。对于相对较弱的光场下，光电导可以通过  $\sigma(\nu) = 2P/F_0^2 = \sum_{\lambda,\lambda'} \sigma_{\lambda\lambda'}(\nu)$  计算得到。与此同时，空气/石墨烯/介电衬底系统的光透射系数可以通过如下公式得到<sup>[105]</sup>

$$T^i(\nu) = \sqrt{\frac{\epsilon_2^i}{\epsilon_1}} \frac{4(\epsilon_1 \epsilon_0)^2}{[(\epsilon_1 \epsilon_2^i)^{1/2} + \epsilon_1] \epsilon_0 + \sqrt{\epsilon_1} \sigma^i(\nu)/c^2}, \quad (3.1)$$

其中  $\sigma^i(\nu)$  是  $i$  层石墨烯系统在辐射场频率  $\nu$  下的光电导， $\epsilon_1 = 1$  和  $\epsilon_2^i = \epsilon_\infty^i$  分别是空气的介电常数和不同系统中衬底的高频有效介电函数， $c$  是真空中的光速。

#### 3.1.1 单层石墨烯

单层石墨烯中在  $\pi$  带  $\mathbf{K}$ -点附近载流子（电子或空穴）的无质量的狄拉克-外尔准粒子可以通过  $\mathbf{k} \cdot \mathbf{p}$  哈密顿量来描述

$$H_0^m = \begin{pmatrix} 0 & \hbar v_0 k_- \\ \hbar v_0 k_+ & 0 \end{pmatrix}, \quad (3.2)$$

其中  $k_\pm = k_x \pm ik_y = ke^{\pm i\phi}$  并且  $v_0 = 10^6$  m/s 是费米速度， $\mathbf{k} = (k_x, k_y)$  是载流子的波矢， $\phi$  是  $\mathbf{k}$  和  $x$ -坐标轴之间的夹角。单层石墨烯的本征波函数和能量本征值分别为  $\psi_{\lambda\mathbf{k}}^m(\mathbf{r}) = 2^{1/2}[e^{i\phi}, \lambda]e^{i\mathbf{k}\cdot\mathbf{r}}$  和  $E_\lambda^m(\mathbf{k}) = \lambda \hbar v_0 k$ ，其中  $\lambda = +1$  代表电子和  $\lambda = -1$  代表空穴，在这里本征波函数表示成行矢量的形式。

表 3.1: 不同层数石墨烯系统的能带结构参数

单层	AB 双层 <sup>[106]</sup>	ABC 三层 <sup>[95]</sup>	AB 多层 <sup>[97, 106]</sup>	ABC 多层
$v_0 = 10^6 \text{ m/s}$	$a = 2.46 \text{ \AA}$	$a = 2.46 \text{ \AA}$	$a = 2.46 \text{ \AA}$	$v_0 = 10^6 \text{ m/s}$
	$\xi_0 = 3.16 \text{ eV}$	$\gamma_0 = 3.16 \text{ eV}$	$\xi_0 = 3.16 \text{ eV}$	$\gamma_1 = 0.502 \text{ eV}$
	$\xi_1 = 0.39 \text{ eV}$	$\gamma_1 = 0.502 \text{ eV}$	$\xi_1 = 0.39 \text{ eV}$	
	$\xi_3 = 0.315 \text{ eV}$	$\gamma_2 = -0.0171 \text{ eV}$	$\xi_3 = 0.315 \text{ eV}$	
		$\gamma_3 = -0.377 \text{ eV}$	$\eta_2 = -0.02 \text{ eV}$	
		$\gamma_4 = -0.099 \text{ eV}$	$\eta_5 = 0.04 \text{ eV}$	
		$\gamma_5 = -0.0014 \text{ eV}$		

对于导带和价带内的带内跃迁，可以得到

$$\sigma_{\lambda\lambda}^m(\nu) = \frac{2\sigma_0 v_0^2}{\pi^2 \nu} \frac{\tau}{(2\pi\nu\tau)^2 + 1} \int_0^\infty dk k f_\lambda[E_\lambda^m(\mathbf{k})] \{1 - f_\lambda[E_\lambda^m(\mathbf{k})]\}, \quad (3.3)$$

其中  $\tau$  是能量弛豫时间， $E_\tau = \hbar/\tau$  是电子态的能量展宽，且  $\sigma_0 = \pi e^2/(2h)$ 。

对于价带和导带之间的带间跃迁，我们有  $\sigma_{+-}^m(\nu) \simeq 0$  并且

$$\sigma_{-+}^m(\nu) = \sigma_0 f_-(-h\nu/2) [1 - f_+(h\nu/2)]. \quad (3.4)$$

### 3.1.2 AB-堆垛双层石墨烯

在考虑了不同的层间耦合作用如最近邻和次近邻相互作用下，双层石墨烯中载流子（电子或空穴）在  $\pi$  带  $\mathbf{K}$  点附近的有效哈密顿量可以写作<sup>[113]</sup>

$$H_0^b = \begin{pmatrix} 0 & \hbar^2 k_-^2 / (2m^*) - \hbar u_3 k_+ \\ \hbar^2 k_+^2 / (2m^*) - \hbar u_3 k_- & 0 \end{pmatrix}, \quad (3.5)$$

其中  $m^* = \xi_1/(2u_0^2)$ ,  $u_i = \sqrt{3}a\xi_i/2\hbar$ ,  $p = \hbar k$  且  $a=2.46 \text{ \AA}$ 。如表 3.1 所示，我们取  $\xi_0 = 3.16 \text{ eV}$ ,  $\xi_1 = 0.39 \text{ eV}$ ,  $\xi_3 = 0.315 \text{ eV}$  作为双层石墨烯中典型的耦合常数<sup>[96, 106]</sup>。对应的薛定谔方程可以通过解析解得到并且本征值为  $E_\lambda^b(\mathbf{k}) = \lambda A$ , 其中  $A = [h_a^2 + h_b^2 - 2\cos(3\phi)h_a h_b]^{1/2}$ ,  $h_a = p^2/(2m^*)$  且  $h_b = pu_3$ 。对应的双层石墨烯的本征波函数可以写作行矢量的形式  $\psi_{\lambda\mathbf{k}}^b(\mathbf{r}) = 2^{-1/2}[(h_a e^{-2i\phi} - h_b e^{i\phi})/A, \lambda]e^{i\mathbf{k}\cdot\mathbf{r}}$ , 其中  $\mathbf{r} = (x, y)$ 。

对于导带和价带内的带内跃迁，我们可以得到

$$\begin{aligned} \sigma_{\lambda\lambda}^b(\nu) &= \frac{4\sigma_0}{\pi^3 \nu (m^*)^2} \frac{\tau}{(2\pi\nu\tau)^2 + 1} \int_0^\pi d\phi \int_0^\infty \frac{dk k}{A^2} \\ &\times f_\lambda[E_\lambda^b(\mathbf{k})] \{1 - f_\lambda[E_\lambda^b(\mathbf{k})]\} G_{\lambda\lambda}^b(k, \phi), \end{aligned} \quad (3.6)$$

其中  $G_{\lambda\lambda}^b(k, \phi) = [m^* u_3 (h_a \cos 2\phi - h_b \cos \phi) + \hbar k (h_b \cos 2\phi - h_a \cos \phi)]^2$ 。

对于带间跃迁通道，我们有  $\sigma_{+-}^b(\nu) \simeq 0$  和

$$\begin{aligned}\sigma_{-+}^b(\nu) = & \frac{4\sigma_0}{\pi^3\nu(m^*)^2} \int_0^\pi d\phi \int_0^\infty \frac{dkk}{A^2} [1 - f_+(h\nu/2)] \\ & \times f_-(-h\nu/2) \frac{\tau G_{-+}^b(k, \phi)}{4\tau^2(\pi\nu - A/\hbar)^2 + 1},\end{aligned}\quad (3.7)$$

其中  $G_{-+}^b(k, \phi) = [m^*u_3(-h_a \sin 2\phi - h_b \sin \phi) + \hbar k(h_b \sin 2\phi + h_a \sin \phi)]^2$ 。

### 3.1.3 ABC-堆垛三层石墨烯

ABC-堆垛三层石墨烯中载流子(电子或空穴)在  $\pi$ -带  $\mathbf{K}$ -点附近的低能量有效哈密顿量为<sup>[95]</sup>

$$H_0^t = \begin{pmatrix} S_1 & S_0\hbar^3k_-^3 + S_2 \\ S_0\hbar^3k_+^3 + S_2 & S_1 \end{pmatrix}, \quad (3.8)$$

其中  $S_0 = 3^{3/2}a^3\gamma_0^3/(8\hbar^3\gamma_1^2)$ ,  $S_1 = \gamma_5 - 3\gamma_0\gamma_4k^2a^2/(2\gamma_1)$  和  $S_2 = \gamma_2/2 - 3\gamma_0\gamma_3k^2a^2/(2\gamma_1)$ 。如表 3.1 所示，通用的跳跃能量参数  $\gamma_0 = 3.16$  eV<sup>[95]</sup>,  $\gamma_1 = 0.502$  eV,  $\gamma_2 = -0.0171$  eV,  $\gamma_3 = -0.377$  eV,  $\gamma_4 = -0.099$  eV,  $\gamma_5 = -0.0014$  eV。通过解薛定谔方程可以得到能量本征值  $E_\lambda(\mathbf{k}) = S_1 + \lambda B$  其中  $B = [S_0^2\hbar^6k^6 + S_2^2 + 2\cos(3\phi)S_0S_2\hbar^3k^3]^{1/2}$ 。对应的本征波函数可以写作行矢量的形式  $\psi_{\lambda\mathbf{k}}^t(\mathbf{r}) = 2^{1/2}[e^{i\psi}, \lambda]e^{i\mathbf{k}\cdot\mathbf{r}}$ , 其中  $e^{i\psi} = (S_0\hbar^3k^3e^{-3i\phi} + S_2)/B$  和  $\mathbf{r} = (x, y)$ 。

通过玻尔兹曼方程得到的平衡方程及费米黄金定律，导带内带内跃迁对光电导的贡献为

$$\begin{aligned}\sigma_{++}^t(\nu) = & \frac{4\sigma_0}{\pi^3\hbar^2\nu} \frac{\tau}{(2\pi\nu\tau)^2 + 1} \int_0^\pi d\phi \int_0^\infty \frac{dkk}{B^2} f_+[E_+^t(\mathbf{k})] \\ & \times \{1 - f_+[E_+^t(\mathbf{k})]\} G_{++}^t(k, \phi),\end{aligned}\quad (3.9)$$

其中  $G_{++}^t(k, \phi) = [Q_1B - 3S_0\hbar^3k^2(S_0\hbar^3k^3\cos\phi + S_2\cos 2\phi) + (S_0\hbar^3k^3\cos 3\phi + S_2)Q_2]^2$ 。对于价带内的带内跃迁

$$\begin{aligned}\sigma_{--}^t(\nu) = & \frac{4\sigma_0}{\pi^3\hbar^2\nu} \frac{\tau}{(2\pi\nu\tau)^2 + 1} \int_0^\pi d\phi \int_0^\infty \frac{dkk}{B^2} f_-[E_-^t(\mathbf{k})] \\ & \times \{1 - f_-[E_-^t(\mathbf{k})]\} G_{--}^t(k, \phi),\end{aligned}\quad (3.10)$$

其中  $G_{--}^t(k, \phi) = [3S_0\hbar^3k^2(S_0\hbar^3k^3\cos\phi + S_2\cos 2\phi) - (S_0\hbar^3k^3\cos 3\phi + S_2)Q_2 + Q_1B]^2$ 。

对于带间跃迁，可以得到  $\sigma_{+-}^t(\nu) \simeq 0$  和

$$\begin{aligned}\sigma_{-+}^t(\nu) = & \frac{2\sigma_0\tau}{\pi^2\hbar^2\nu} \int_0^\pi d\phi \int_0^\infty \frac{dkk}{B^2} e^{-|\tau(2\pi\nu - 2B/\hbar)|} \\ & \times f_-[E_-^t(\mathbf{k})] \{1 - f_+[E_+^t(\mathbf{k})]\} G_{-+}^t(k, \phi),\end{aligned}\quad (3.11)$$

其中  $G_{-+}^t(k, \phi) = [3S_0\hbar^3k^2(S_0\hbar^3k^3\sin\phi - S_2\sin 2\phi) - S_0Q_2\hbar^3k^3\sin 3\phi]^2$ 。

### 3.1.4 AB-堆垛多层石墨烯

对于 AB-堆垛  $N$ -层石墨烯且层数  $N \geq 3$ , 其电子结构的哈密顿量可以近似的分解成由单层和 AB-堆垛双层石墨烯组成的子系统并且系统总的光电导可以看做是各个子系统的叠加<sup>[96, 98, 106]</sup>。奇数层的多层石墨烯包含一个单层石墨烯型和  $(N - 1)/2$  个双层石墨烯型的子系统, 而对于偶数层的多层石墨烯则只由  $N/2$  个双层石墨烯子系统组成<sup>[97]</sup>。当我们只关注在长波长范围的光响应时, 对于单层和双层子系统有效的低能量约化哈密顿量可以写作<sup>[22, 97]</sup>

$$H_{AB}^M = \begin{pmatrix} q\eta_2 & v_0\hbar k_- \\ v_0\hbar k_+ & q\eta_5 \end{pmatrix}, \quad (3.12)$$

和

$$H_{AB}^{Bj} = \begin{pmatrix} \alpha_j\eta_2 & -v_0^2\hbar^2k_-^2/(\mu_j\xi_1) \\ -v_0^2\hbar^2k_+^2/(\mu_j\xi_1) & \beta_j\eta_2 \end{pmatrix}, \quad (3.13)$$

其中  $\eta_2 = -0.02$  eV,  $\eta_5 = 0.04$  eV,  $q = (1 - N)/(N + 1)$ ,  $u_j = 2\cos(\kappa_j)$ ,  $\kappa_j = \pi/2 - j\pi/(2N + 2)$  且  $j$  表示双层系统在不同条件下的指数,

$$j = \begin{cases} 1, 3, 5, \dots, N - 1, N = \text{even}, \\ 2, 4, 6, \dots, N - 1, N = \text{odd}. \end{cases} \quad (3.14)$$

另外, 对于偶数  $N$  有  $\alpha_j = \beta_j = [N\cos(2\kappa_j) + 1]/(N + 1)$ 。对于奇数  $N$  则有  $\alpha_j = [(N - 1)\cos(2\kappa_j) + 2]/(N + 1)$  和  $\beta_j = \cos(2\kappa_j)$ <sup>[96]</sup>。

对于单层石墨烯子系统, 对应的能量本征值和本征波函数可以分别写为

$$E_{N\lambda}^M(\mathbf{k}) = \frac{q(\eta_2 + \eta_5)}{2} + \lambda\sqrt{\frac{q^2(\eta_2 - \eta_5)^2}{4} + v_0^2\hbar^2k^2}, \quad (3.15)$$

和

$$\psi_{N\lambda\mathbf{k}}^M(\mathbf{r}) = \mathbb{N}_{N\lambda}^M[R_{N\lambda}^M e^{-i\phi}, 1]e^{i\mathbf{k}\cdot\mathbf{r}}, \quad (3.16)$$

其中  $R_{N\lambda}^M = v_0\hbar k/(E_{N\lambda}^M(\mathbf{k}) - q\eta_2)$  和  $\mathbb{N}_{N\lambda}^M = [1 + (R_{N\lambda}^M)^2]^{-1/2}$ 。对于双层石墨烯子系统  $B_j$ , 对应的能量本征值和本征波函数可以写作

$$E_{N\lambda}^{B_j}(\mathbf{k}) = \frac{\eta_2(\alpha_j + \beta_j)}{2} + \lambda\sqrt{\frac{\eta_2^2(\alpha_j - \beta_j)^2}{4} + v_0^4\hbar^4k^4/\mu_j^2\xi_1^2}, \quad (3.17)$$

和

$$\psi_{N\lambda\mathbf{k}}^{B_j}(\mathbf{r}) = \mathbb{N}_{N\lambda}^{B_j}[R_{N\lambda}^{B_j} e^{-2i\phi}, 1]e^{i\mathbf{k}\cdot\mathbf{r}}, \quad (3.18)$$

其中  $R_{N\lambda}^{B_j} = v_0^2\hbar^2k^2/[\mu_j\xi_1(\alpha_j\eta_2 - E_{N\lambda}^{B_j}(\mathbf{k}))]$  和  $\mathbb{N}_{N\lambda}^{B_j} = [1 + (R_{N\lambda}^{B_j})^2]^{-1/2}$ 。在相对较弱的线偏振光场下, 载流子-光子相互作用下吸收散射所导致的单层和双层石墨烯子系统的一级近似下定态电子跃迁概率分别为

$$W_{N\lambda\lambda'}^M(\mathbf{k}, \mathbf{k}') = \frac{2\pi}{\hbar} \left( \frac{eF_0v_0}{4\pi\nu} \right)^2 |U_{N\lambda\lambda'}^M(\mathbf{k})|^2 \delta_{\mathbf{k}', \mathbf{k}} \delta[E_{N\lambda'}^M(\mathbf{k}') - E_{N\lambda}^M(\mathbf{k}) - h\nu], \quad (3.19)$$

其中  $|U_{N\lambda\lambda'}^M(\mathbf{k})|^2 = (\mathbb{N}_{N\lambda}^M \mathbb{N}_{N\lambda'}^M)^2 [(R_{N\lambda}^M)^2 + (R_{N\lambda'}^M)^2 + 2 \cos(2\phi) R_{N\lambda}^M R_{N\lambda'}^M]$ , 和

$$W_{N\lambda\lambda'}^{B_j}(\mathbf{k}, \mathbf{k}') = \frac{2\pi}{\hbar} \left( \frac{eF_0 v_0^2 \hbar k}{2\pi\nu\mu_j\xi_1} \right)^2 |U_{N\lambda\lambda'}^{B_j}(\mathbf{k})|^2 \delta_{\mathbf{k}', \mathbf{k}} \\ \times \delta[E_{N\lambda'}^{B_j}(\mathbf{k}') - E_{N\lambda}^{B_j}(\mathbf{k}) - h\nu], \quad (3.20)$$

其中  $|U_{N\lambda\lambda'}^{B_j}(\mathbf{k})|^2 = (\mathbb{N}_{N\lambda}^{B_j} \mathbb{N}_{N\lambda'}^{B_j})^2 [(R_{N\lambda}^{B_j})^2 + (R_{N\lambda'}^{B_j})^2 + 2 \cos(2\phi) R_{N\lambda}^{B_j} R_{N\lambda'}^{B_j}]$ 。

对于奇数层 AB-堆垛多层石墨烯, 单层石墨烯子系统在导带和价带内的带内跃迁光电导为

$$\sigma_{N\lambda\lambda}^M(\nu) = \frac{8\sigma_0 v_0^2}{\pi^2 \nu} \frac{\tau}{(2\pi\nu\tau)^2 + 1} \int_0^\infty dk k \{1 - f_\lambda[E_{N\lambda}^M(\mathbf{k})]\} \\ \times f_\lambda[E_{N\lambda}^M(\mathbf{k})] (\mathbb{N}_{N\lambda}^M)^4 (R_{N\lambda}^M)^2. \quad (3.21)$$

对于带间跃迁通道, 则有  $\sigma_{N+-}^M(\nu) \simeq 0$  和

$$\sigma_{N-+}^M(\nu) = 2\sigma_0 (\mathbb{N}_{N-}^M \mathbb{N}_{N+}^M)^2 [(R_{N-}^M)^2 + (R_{N+}^M)^2] f_- [E_{N-}^M(\mathbf{k})] \\ \times \{1 - f_+[E_{N+}^M(\mathbf{k})]\}, \quad (3.22)$$

其中对于单层石墨烯子系统中入射频率为  $\nu$  时有  $k = [h^2\nu^2 - q^2(\eta_2 - \eta_5)^2]^{1/2}/(2v_0\hbar)$ 。

对于 AB-堆垛多层石墨烯中的  $B_j$  子系统, 导带和价带内带内跃迁的光电导为

$$\sigma_{N\lambda\lambda}^{B_j}(\nu) = \frac{32\sigma_0 v_0^4 \hbar^2}{\pi^2 \nu \mu_j^2 \xi_1^2} \frac{\tau}{(2\pi\nu\tau)^2 + 1} \int_0^\infty dk k^3 f_\lambda[E_{N\lambda}^{B_j}(\mathbf{k})] \\ \times \{1 - f_\lambda[E_{N\lambda}^{B_j}(\mathbf{k})]\} (\mathbb{N}_{N\lambda}^{B_j})^4 (R_{N\lambda}^{B_j})^2. \quad (3.23)$$

对于带间跃迁通道, 则有  $\sigma_{N+-}^{B_j}(\nu) \simeq 0$  和

$$\sigma_{N-+}^{B_j}(\nu) = 4\sigma_0 (\mathbb{N}_{N-}^{B_j} \mathbb{N}_{N+}^{B_j})^2 [(R_{N-}^{B_j})^2 + (R_{N+}^{B_j})^2] f_- [E_{N-}^{B_j}(\mathbf{k})] \\ \times \{1 - f_+[E_{N+}^{B_j}(\mathbf{k})]\}, \quad (3.24)$$

其中在  $B_j$  双层石墨烯子系统中入射光子频率为  $\nu$  的时候有  $k = \{[h^2\nu^2 - \eta_2^2(\alpha_i - \beta_i)^2] \mu_j^2 \xi_1^2\}^{1/4}/(2^{1/2}v_0\hbar)$ 。

在将各个子系统的贡献合并之后,  $N$ -层 AB-堆垛多层石墨烯系统总的光电导为

$$\sigma_N^{AB}(\nu) = \delta_{N,\text{odd}} \sum_{\lambda, \lambda'} \sigma_{N\lambda\lambda'}^M(\nu) + \sum_j \sum_{\lambda, \lambda'} \sigma_{N\lambda\lambda'}^{B_j}(\nu). \quad (3.25)$$

### 3.1.5 ABC-堆垛多层石墨烯

ABC-堆垛  $N$ -层石墨烯系统在  $N \geq 3$  时可以看作物理上实现的手性二维电子气且有效的低能量哈密顿量为<sup>[22, 95]</sup>

$$H_{ABC}^N = \frac{v_0^N}{\gamma_1^{N-1}} \begin{pmatrix} 0 & (\hbar k_-)^N \\ (\hbar k_+)^N & 0 \end{pmatrix}. \quad (3.26)$$

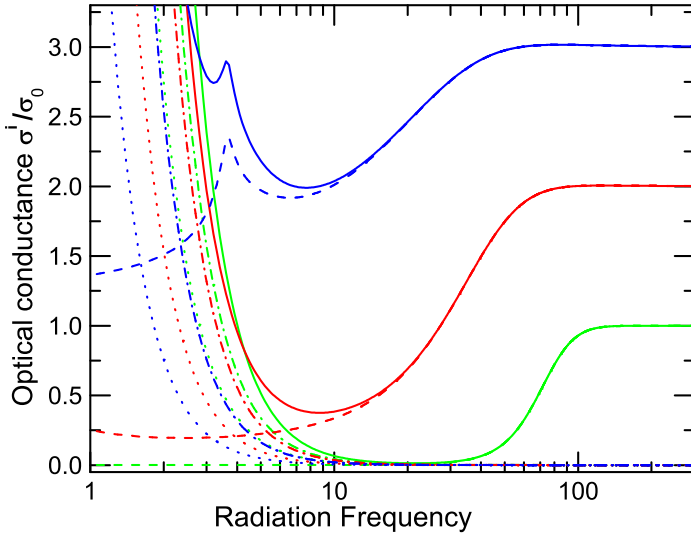


图 3.1: 在温度  $T=300$  K, 电子浓度  $n_e = 1.5 \times 10^{12}$  cm<sup>-2</sup> 和空穴浓度  $n_h = 5 \times 10^{11}$  cm<sup>-2</sup> 下, 不同跃迁通道对光电导的贡献。单层, 双层和 ABC-堆垛三层石墨烯的结果分别用绿色, 红色和蓝色曲线表示。这里,  $\sigma_{++}^i$  (点虚线),  $\sigma_{--}^i$  (点划线) 和  $\sigma_{+-}^i$  (短划线) 分别是导带内带内跃迁贡献的光电导, 价带内带内跃迁贡献的光电导以及从价带到导带带间跃迁所贡献的光电导。实曲线表示总的光电导同时  $\sigma_0 = \pi e^2 / (2h)$

ABC-堆垛  $N$ -层石墨烯手性指数为  $J = N$  对应的本征能量和本征波函数分别为  $E_\lambda^J(\mathbf{k}) = \lambda(v_0 \hbar k)^N / \gamma_1^{N-1}$  和  $\psi_{\lambda\mathbf{k}}^J(\mathbf{r}) = 2^{1/2}[\lambda, e^{iN\phi}]e^{i\mathbf{k}\cdot\mathbf{r}}$ 。在线偏振弱光场下, 载流子-光子相互作用下吸收散射过程中一级近似下定态电子跃迁概率为

$$W_{\lambda\lambda'}^J(\mathbf{k}, \mathbf{k}') = \frac{2\pi}{\hbar} \left( \frac{eF_0 N v_0^N (\hbar k)^{N-1}}{4\pi\nu\gamma_1^{N-1}} \right)^2 \frac{1 + \lambda\lambda' \cos(2\phi)}{2} \times \delta_{\mathbf{k}', \mathbf{k}} \delta[E_{\lambda'}^J(\mathbf{k}') - E_\lambda^J(\mathbf{k}) - h\nu]. \quad (3.27)$$

遵照同样的理论方法计算光电导, 对于 ABC-堆垛  $N$ -层石墨烯导带和价带内带内跃迁的光电导为

$$\begin{aligned} \sigma_{\lambda\lambda}^J(\nu) &= \frac{2\sigma_0 N^2 v_0^{2N} \hbar^{2N-2}}{\pi^2 \nu \gamma_1^{2N-2}} \frac{\tau}{(2\pi\nu\tau)^2 + 1} \int_0^\infty dk k^{2N-1} \\ &\times f_\lambda[E_\lambda^J(\mathbf{k})] \{1 - f_\lambda[E_\lambda^J(\mathbf{k})]\}. \end{aligned} \quad (3.28)$$

对于带间跃迁通道, 则有  $\sigma_{+-}^J(\nu) \simeq 0$  和

$$\sigma_{-+}^J(\nu) = N\sigma_0 f_-(-h\nu/2) [1 - f_+(h\nu/2)]. \quad (3.29)$$

## 3.2 结果和讨论

在这项研究中, 我们考虑在暗场下的导电载流子为电子且暗场下的电子浓度为  $n_0$ 。在辐射光场下, 总的电子浓度为  $n_e = n_0 + \Delta n_e$ , 其中  $\Delta n_e$  是光生电子浓度, 同时通

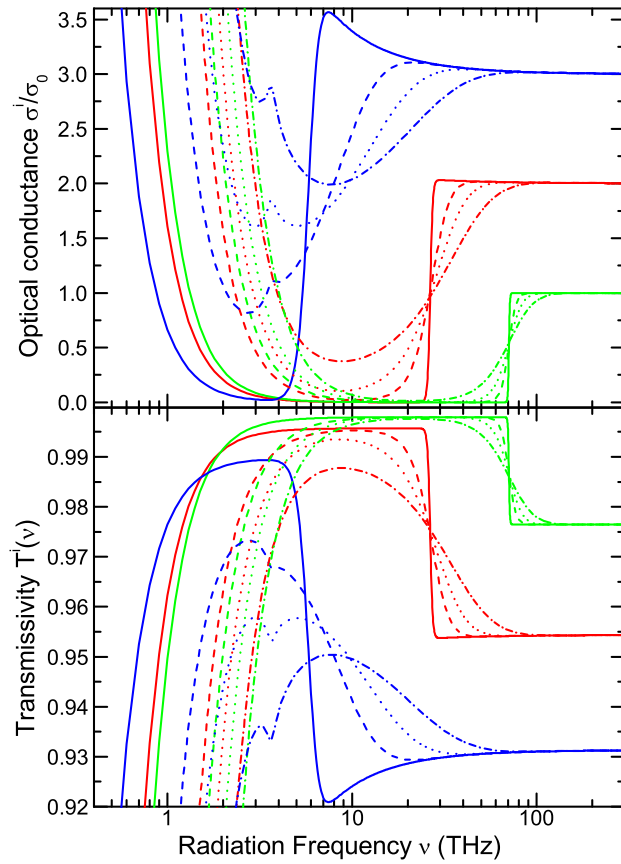


图 3.2: 在给定载流子浓度  $n_e = 1.5 \times 10^{12} \text{ cm}^{-2}$  和  $n_h = 5 \times 10^{11} \text{ cm}^{-2}$  不同温度  $T=10 \text{ K}$  (实曲线),  $77 \text{ K}$  (短划线曲线),  $150 \text{ K}$  (虚曲线), 和  $300 \text{ K}$  (点缀中曲线) 下, 光电导 (上面板) 和光透射系数 (下面板) 随辐射场频率的变化。单层、双层和 ABC-堆垛三层石墨烯系统的结果分别用绿色、红色和蓝色曲线表示

过电荷数守恒定理可以得到空穴的浓度为  $n_h = \Delta n_e$ 。单层、双层、和 ABC-堆垛多层石墨烯的导带中电子或价带中空穴的化学势  $\mu_\lambda^i$  可以通过  $n_e^i = g \sum_{\mathbf{k}} f_+[E_+^i(\mathbf{k})]$  和  $n_h^i = g \sum_{\mathbf{k}} \{1 - f_-[E_-^i(\mathbf{k})]\}$  分别得到, 其中  $g = 4$  是自旋和谷简并因子。对于 AB-堆垛多层石墨烯, 电子和空穴的化学势可以通过  $n_e^N = g \sum_{\mathbf{k}} \{f_+[E_{N+}^M(\mathbf{k})] \delta_{N,\text{odd}} + \sum_j f_+[E_{N+}^{B_j}(\mathbf{k})]\}$  和  $n_h^N = g \sum_{\mathbf{k}} \{\{1 - f_-[E_{N-}^M(\mathbf{k})]\} \delta_{N,\text{odd}} + \sum_j \{1 - f_-[E_{N-}^{B_j}(\mathbf{k})]\}\}$  分别得到。

在计算光透射系数的过程中, 我们取用单层, 双层和 ABC-堆垛三层石墨烯系统的高频介电常数分别为  $\epsilon_2^m = 1.2$ ,  $\epsilon_2^b = 1.3$  和  $\epsilon_2^t = 1.5$ , 其中计入了石墨烯薄膜和介电衬底介电常数的不匹配所产生的影响<sup>[107]</sup>。另外, 高载流子浓度石墨烯器件中的能量弛豫时间大约为  $\tau \sim 1 \text{ ps}$ <sup>[108]</sup>。因而我们在数值计算中采用这个弛豫时间值。在数值计算中, 我们在技术上可行的载流子浓度  $1 \times 10^{12} \text{ cm}^{-2}$  量级上选取石墨烯的载流子浓度<sup>[109]</sup>。

在图 3.1 中, 我们给出了在给定电子浓度  $n_e^i$  和空穴浓度  $n_h^i$  下, 在温度  $T=300 \text{ K}$  时, 单层、双层和 ABC-堆垛三层石墨烯中不同电子跃迁通道对光电导的贡献。可以

得到如下的特性。 (i) 在三种石墨烯系统中，从导带到价带的带间跃迁对  $\nu > 20$  THz 频段的光吸收作主要贡献，而带内跃迁则会造成低频段区域的光吸收。 (ii) 对于单层、双层和 ABC-堆垛三层石墨烯系统，分别在  $\nu > 130$  THz,  $\nu > 100$  THz 和  $\nu > 70$  THz 区域内的光电导受辐射场频率  $\nu$  的影响很小，然而分别在  $\nu < 130$  THz,  $\nu < 100$  THz 和  $\nu < 70$  THz 频率区域则受到频率  $\nu$  强烈的影响。可以看到，在 ABC-堆垛三层石墨烯中在频率 3.6 THz 处可以看到一个较小的吸收峰。这个小吸收峰是由 ABC-堆垛三层石墨烯中导带和价带之间的不对称性引起的。 (iii) 可以发现在高频率段，三种石墨烯系统的光电导分别是为  $\sigma_0^m = \pi e^2/(2h)$ ,  $\sigma_0^b = \pi e^2/h$  和  $\sigma_0^t = 3\pi e^2/(2h)$  的普适常数。这证实多层石墨烯系统中每层石墨烯的普适光电导为  $\pi e^2/(2h)$ 。 (iv) 更重要的是，在 1–100 THz 频率范围内，可以在三种石墨烯系统中看到光吸收窗口。如图 3.1 所示，这些光吸收窗口是由需要不同能量的带间跃迁和带内跃迁吸收通道的共同作用引起的。 (v) 随着石墨烯层数的增加，光吸收窗口会出现红移并且能看到更窄和更高的光吸收窗口。

图 3.2 给出了三种石墨烯系统中光电导和光透射系数在给定载流子浓度并在不同温度下随着辐射场频率的变化。可以看到，在高频区域  $\sigma^i(\nu)$  和  $T^i(\nu)$  几乎不随频率  $\nu$  和温度的变化而变化。这些特征和单层石墨烯在实验上的发现一致<sup>[21]</sup>。在远红外和太赫兹频段区域可以看到光吸收窗口并且  $\sigma^i(\nu)$  和  $T^i(\nu)$  同时受到温度很大的影响。这也和实验上单层石墨烯<sup>[101]</sup> 和双层石墨烯<sup>[110]</sup> 的结果相一致。在给定的电子/空穴浓度下，我们知道电子系统中电子/空穴的化学势能随着温度的增加而减小/增加。因此，如图 3.2 所示，在 Moss-Burstein 效应<sup>[111]</sup> 的影响下，光吸收窗口的吸收边将随着温度的增加而向高频区域蓝移。对于单层石墨烯，光吸收窗口的宽度随着温度的升高而减小。在双层和 ABC-堆垛三层石墨烯系统中，光吸收窗口的高度和宽度随着温度的增加而减小。在更低的温度下，能看到更宽和更深的光吸收窗口并且在光吸收的边缘有着更明显的截断。这与单层石墨烯系统的实验结果相符<sup>[101]</sup>。在 ABC-堆垛三层石墨烯在 3.6 THz 处的小吸收峰的位置不随温度变化并且吸收峰的强度随着温度的增加而减弱。

图 3.3 给出了在给定温度为  $T=300$  K 和空穴浓度为  $n_h$  时，不同电子浓度  $n_e$  下三种石墨烯系统的光电导和与之相对应的光透射系数随着频率的变化关系。对于在介电衬底上的石墨烯，加一个正(负)的偏压能将介电衬底内的电子(空穴)挤压出并注入到石墨烯层中。于是石墨烯层中的电子浓度可以通过门电压来进行调节<sup>[112]</sup>。外加门电压对石墨烯系统电子结构性质的影响已经在理论上进行了研究<sup>[113, 114]</sup>。通过图 3.3 我们发现在高频区域，三种石墨烯系统中的光电导不受频率  $\nu$  的影响并且受电子浓度的影响也同样很小。在 2–150 THz 的频率范围内可以观看到光吸收窗口。ABC-堆垛三层石墨烯中在 3.6 THz 处小吸收峰的位置不随电子浓度而改变并且吸收峰的强度随着电子浓度的增加而减弱。通常来说，导带中电子的化学势能随电子浓度的增加而增加。因此，如图 3.3 所示，随着电子浓度的增加光吸收窗口将蓝移到高能量区域。可以看到不同石墨烯系统光吸收窗口的深度随着电子浓度增加而增加。在较高的电子浓度下可以

看到光吸收窗口的边缘具有更尖锐的截断。这些研究结果表明单层、双层和 ABC-堆垛三层石墨烯系统光吸收窗口的宽度和高度可以通过外加门电压的形式被电子浓度进行有效的调节。

图 3.4 给出了在给定载流子浓度和不同温度下，AB-堆垛多层石墨烯系统光电导随辐射场频率的变化。可以看到在可见光频段内的普适光电导是由不同有效低能量子系统所贡献的并且 AB-堆垛多层石墨烯中的每层对光电导的贡献为  $\pi e^2/(2h)$ 。在三层、四层和五层 AB-堆垛石墨烯中可以看到红外到太赫兹频段的光吸收窗口。在更低的温度下可以得到更宽和更深的光吸收窗口并且光吸收窗口会随着石墨烯层数的增加而红移。随着温度的降低，光吸收窗口也会发生红移。

在图 3.4(a) 和 (c) 中，可以在 AB-堆垛五层和三层石墨烯中看到两个吸收边。这些吸收边是由 AB-堆垛奇数层石墨烯中的迷你带隙造成的。在图 3.4(b) 中没有吸收边是因为偶数层 AB-堆积多层石墨烯的子系统是无带隙的。这些特性可以从公式 (3.15)

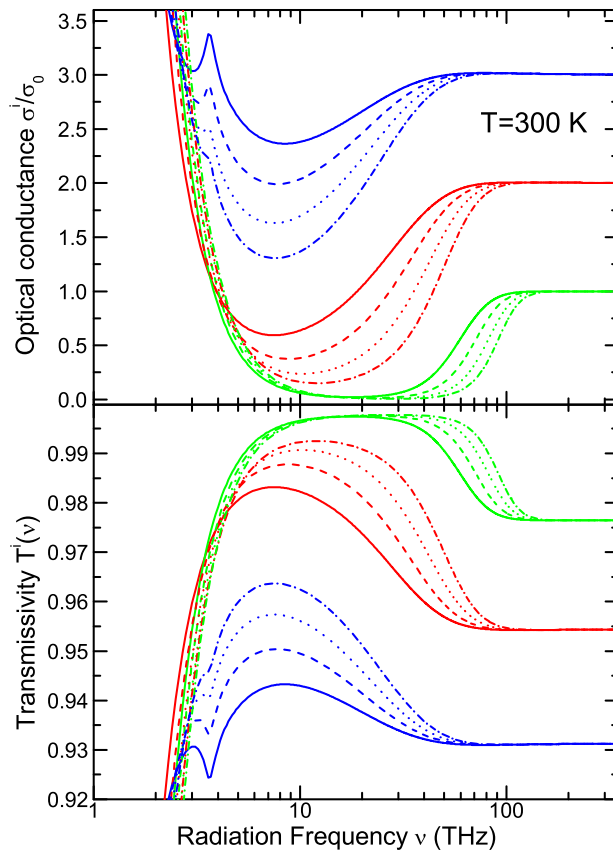


图 3.3: 光电导 (上面板) 和光透射系数 (下面板) 在给定温度  $T=300\text{ K}$  和空穴浓度  $n_h = 5 \times 10^{11}\text{ cm}^{-2}$  不同电子浓度  $n_e = 1 \times 10^{12}\text{ cm}^{-2}$  (实曲线),  $n_e = 1.5 \times 10^{12}\text{ cm}^{-2}$  (短划线曲线),  $n_e = 2 \times 10^{12}\text{ cm}^{-2}$  (虚曲线), 和  $n_e = 2.5 \times 10^{12}\text{ cm}^{-2}$  (点缀中曲线) 下随着辐射场频率  $\nu$  的变化。单层、双层和 ABC-堆垛三层石墨烯的结果分别用绿色、红色和蓝色的曲线表示

和公式 (3.17) 中看出。AB-堆垛三层石墨有两个迷你带隙  $E_{g1}^3 = 0.03$  eV 和  $E_{g2}^3 = 0.01$  eV 分别对应两个在 7.3 THz 和 2.4 THz 处的吸收边。对于 AB-堆垛五层石墨则有三个迷你带隙  $E_{g1}^5 = 0.04$  eV,  $E_{g2}^5 = 0.01$  eV 和  $E_{g3}^5 = 3.33$ 。前两个迷你带隙分别对应 9.7 THz 和 2.4 THz 处的吸收边。在低频率范围  $\nu < 1$  THz, 带间跃迁所做的贡献非常小因而在图 3.4(a)中看不到第三个迷你带隙所导致的吸收边。这里同样发现光吸收边的高度随着温度增加而上升。另外, 需要指出的是带隙的吸收边和光吸收窗口的吸收边不同。光吸收窗口的吸收边是由费米能级附近的电子跃迁所导致的。从图 3.4 中, 我们可以看到 AB-堆垛多层石墨烯中迷你带隙引起的光吸收边处在光吸收窗口的范围内。

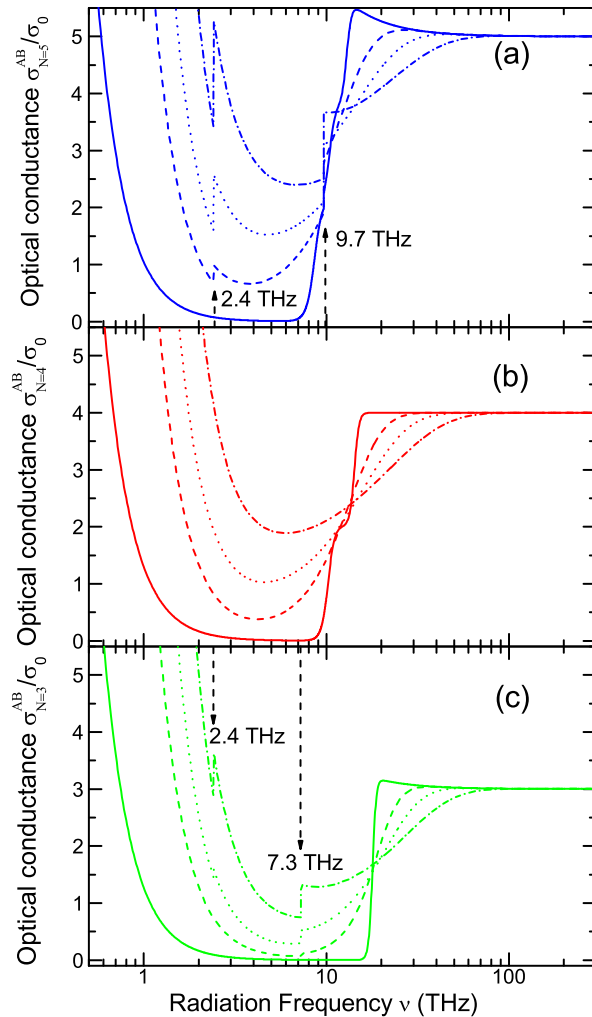


图 3.4: 在给定载流子浓度  $n_e = 1.5 \times 10^{12} \text{ cm}^{-2}$  和  $n_h = 5 \times 10^{11} \text{ cm}^{-2}$ , 不同温度  $T = 10 \text{ K}$  (实曲线),  $77 \text{ K}$  (短划线曲线),  $150 \text{ K}$  (虚曲线), 和  $300 \text{ K}$  (点缀中曲线) 下, AB-堆垛多层石墨烯中光电导随辐射频率  $\nu$  的变化。图中分别为 AB-堆积五层 (a, 蓝色曲线), 四层 (b, 红色曲线), 和三层 (c, 绿色曲线) 的结果

在最近的一项工作中, Hao<sup>[98]</sup> 计算了 AB-堆垛多层石墨烯在整个光谱范围内的光电导。这里需要指出的是文献 [98] 的研究基于全能带的哈密顿量模型并且报道了石墨烯的层数如何影响近红外到紫外区间吸收峰的数量。在文献 [98] 中, 近红外范围内的吸收峰是由 **K** 点附近低能量子系统到高能量子系统之间的光吸收跃迁所导致的。而紫外范围内的吸收峰则和 **M** 点附近的范霍夫奇点有关。在本项研究中, 我们通过有效的低能量哈密顿量模型来研究石墨烯系统对辐射场的光响应, 同时也可以得到红外到太赫兹范围内的光学性质。另外, 我们证实了 AB-堆积多层石墨烯系统中在可见光范围内的普适光电导是由低能量子系统所贡献的。我们发现石墨烯的层数能够有效的影响图 3.4 中 AB-堆积多层石墨烯中的光吸收窗口的形状、位置和宽度及深度。

图 3.5 给出了 ABC-堆垛多层石墨烯系统中光电导在给定载流子浓度不同温度下随着频率的变化关系。ABC-堆垛  $N$ -层石墨烯在高频段的普适光电导为  $N\pi e^2/(2h)$ 。ABC-堆垛多层石墨烯在低频段同样存在光吸收窗口。在图 3.5 中, 可以看到随着石墨烯层数  $N$  的增加或者温度的降低, 光吸收窗口将向低频段红移。同时, 光吸收窗口的宽度和深度随着石墨烯层数  $N$  的增加而减小。另外, 我们发现图 3.5 中的光吸收窗口与图 3.4 中的光吸收窗口有不同的特征。i) 不同于 AB-堆垛多层石墨烯有着多样的低能量子系统, ABC-堆垛多层石墨烯只有一个有效低能量子系统。因而, 与 ABC-堆垛多层石墨烯相比, 在 AB-堆垛多层石墨烯中可以看到相对更加丰富的光吸收窗口结构。ii) 与 AB-堆垛多层石墨烯相比, 在相同的石墨烯层数下 ABC-堆垛多层石墨有着更窄的光吸收窗口。AB-堆垛多层石墨烯中光吸收窗口的深度比 ABC-堆垛多层石墨烯中的更深。iv) 在低温下, 在 ABC-堆垛多层石墨烯中有着受温度和石墨烯层数发生移动更加明显的光吸收窗口。这些结果表明多层石墨烯系统的堆垛次序同样对红外到太赫兹带宽范围内的光电特性有着重要的影响。

这项研究的结果表明在整个光谱范围内, 多层石墨烯系统的光吸收强度随着石墨烯的层数增加而增加。在红外至太赫兹区域, 在 AB- 和 ABC-堆垛的单层和多层石墨烯系统中可以看到光吸收窗口。随着石墨烯层数的增加可以看到光吸收窗口的红移。这些有趣性质的背后主要的物理原因是单层和多层石墨烯系统有着不同的电子能带结构。这能导致不同石墨烯系统具有满足动量和能量守恒定律光吸收跃迁散射的不同的态密度。这些理论发现表明石墨烯系统的光电特性可以被调节并且不仅可以通过改变温度和电子浓度来调节同样能通过选择不同的石墨烯层数和堆垛次序来进行调节。

### 3.3 本章小结

在这项研究中, 我们用一套简单的理论方法来研究单层和多层石墨烯系统在 AB- 和 ABC-堆垛顺序下的光电性质。我们研究了空气/石墨烯/介电衬底系统中温度、电子浓度、堆垛次序和石墨烯层数对光电导/光透射系数的影响。从理论上证实了  $N$ -层石墨烯系统在高频范围内的光电导是一个普适的常数  $\sigma_0^N = N\pi e^2/(2h)$ , 且几乎不受温度、电子浓度和堆垛顺序的影响。这表明每层石墨烯对高频段光电导的贡献是一个

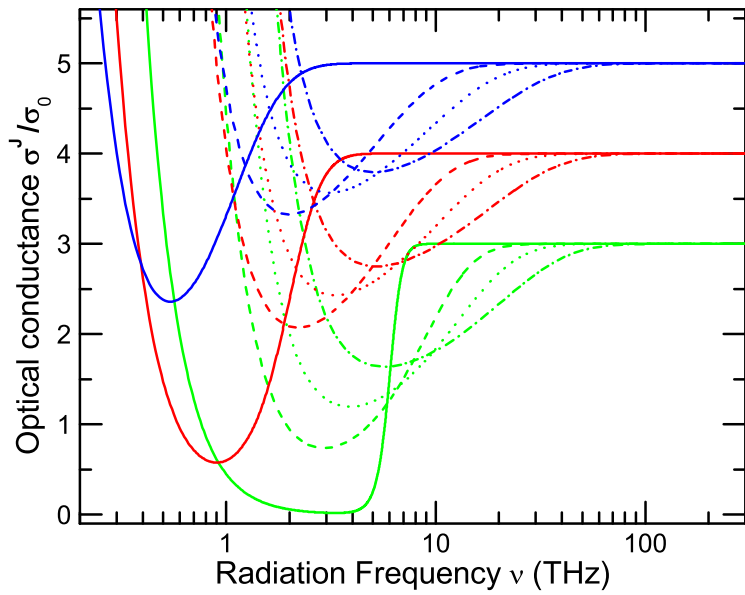


图 3.5: ABC-堆垛多层石墨烯系统在给定的载流子浓度  $n_e = 1.5 \times 10^{12} \text{ cm}^{-2}$  和  $n_h = 5 \times 10^{11} \text{ cm}^{-2}$  不同温度  $T=10 \text{ K}$  (实曲线),  $77 \text{ K}$  (短划线曲线),  $150 \text{ K}$  (虚曲线), 和  $300 \text{ K}$  (点缀中曲线) 下光电导随频率的变化关系。图中分别为三层 (绿色曲线), 四层 (红色曲线) 和五层 (蓝色曲线) 石墨烯的结果

普适值  $\sigma_0 = \pi e^2 / (2h)$ 。在高频段, 单层、双层和 ABC-堆垛三层石墨烯对应的光透射系数分别大约为 97.7%, 95.4% 和 93.1%, 这与实验结果相符<sup>[21]</sup>。我们的研究结果表明在 AB- 和 ABC-堆垛的单层和多层石墨烯系统中存在在 0.2–150 THz 辐射频率范围内的光吸收窗口。在红外到太赫兹区域类 Drude 模型的光电导和相对应的高透射系数窗口已经在实验上得到证实<sup>[89, 100]</sup>。少数层石墨烯系统中的光吸收窗口是由带间跃迁和带内跃迁通道所需要的不同跃迁能量而引起的。这些光吸收窗口的深度和宽度, 尤其是在低频率区域的吸收边, 受到温度、电子浓度、堆垛顺序和石墨烯层数的强烈影响。在 ABC-堆垛三层石墨烯中存在一个在 3.6 THz 处的小吸收峰。这个小吸收峰的位置不随温度和电子浓度的变化而改变, 但是它的强度随着温度的降低或者电子浓度的增加而减小。对于有着奇数层的 AB-堆垛多层石墨烯, 存在由迷你带隙所引起的吸收边。吸收边的数量和位置取决于石墨烯的层数  $N$  并且受温度的影响很小, 但是吸收边的强度随着温度的增加而增强。在更低的温度和/或者更大的电子浓度下, 我们可以在石墨烯系统中的光吸收窗口边缘看到光吸收明显的截止。AB-堆垛  $N$ -层石墨烯中的光吸收窗口比 ABC-堆垛  $N$ -层石墨烯中的光吸收窗口更宽和更深。随着石墨烯层数的增加, 光吸收窗口发生红移并且光吸收窗口的宽度减小。这些理论研究结果表明 AB- 和 ABC-堆垛的单层和多层石墨烯在红外至太赫兹频段有着许多独特的性质。这些独特的性质可以被用来应用在红外或者太赫兹光电器件上。

This chapter corresponds to the published paper “Infrared to terahertz absorption window in mono- and multi-layer graphene systems” in Appendix D.

## 第四章 Rashba 自旋-轨道耦合下单层二硫化钼红外到太赫兹波段的光电导

原子层厚度二维材料的发现开创了全新的研究领域。这类材料能十分具有前景的应用于下一代高性能纳米电子器件上<sup>[7]</sup>。最近，新型二维材料如单层过渡金属硫化物  $\text{MX}_2$  ( $\text{M}=\text{Mo, W, Nb, Ta, Ti}$ , 和  $\text{X}=\text{S, Se, Te}$ ) 已经被制备出来。这类二维材料是金属原子层夹在两个硫族原子层平面中间通过  $\text{X}-\text{M}-\text{X}$  形式构建出的层状结构材料<sup>[115–117]</sup>。过渡金属硫化物 (TMDCs) 有着相当可观的带隙。同时它的带隙由多层结构的间接带隙变为单层结构的直接带隙<sup>[11]</sup>。例如，二硫化钼在块体材料中具有 1.29 eV 的间接带隙而在单层结构中不相等的高对称点  $\mathbf{K}$  和  $\mathbf{K}'$  处则有着大约 1.90 eV 的直接带隙<sup>[116, 118]</sup>。

自从单层二硫化钼首次从实验上通过机械分离制备出来<sup>[116, 119]</sup>，由于其具备十分有趣的和重要的电子学和光学性质而被人们进行了广泛的研究。最近，基于单层二硫化钼的场效应晶体管被证实在常温下具有高达  $10^8$  的开关比并且具有大于  $200 \text{ cm}^2/(\text{Vs})$  的电子迁移率<sup>[42, 120, 121]</sup>。其它基于二硫化钼的电子元件如气敏探测器<sup>[122]</sup>，光电晶体管，高响应度的光探测器<sup>[123]</sup>，甚至发光二极管 (LEDs)<sup>[124]</sup> 已经在实验上被实现。当前，对单层二硫化钼的研究已经成为在电子学、光学和光电子学上极具潜力并迅速发展的研究领域。

单层二硫化钼的电子能带结构可以通过  $\mathbf{k}\cdot\mathbf{p}$  理论来计算<sup>[125, 126]</sup>。不同于石墨烯中的无质量的狄拉克-费米子 (MDF)，单层过渡金属硫化物的电子态可以被描述为有质量的狄拉克-费米子。此外，人们发现单层二硫化钼中存在内禀自旋-轨道耦合 (SOC) 使单层二硫化钼中导带和价带内产生自旋劈裂并有着相反的自旋取向<sup>[125, 127]</sup>。在最近的一项研究工作中 Li 等<sup>[128]</sup> 计算了单层二硫化钼内由从价带到导带带间跃迁所贡献的在可见光范围内的光电导。单层二硫化钼中的集体激发，例如，等离激元和库仑屏蔽同样已经被研究和讨论<sup>[129]</sup>。单层过渡金属硫化物中较强的内禀自旋-轨道耦合使得自旋和谷的自由度发生耦合，这表明单层过渡金属硫化物能成为应用于谷电子学和自旋电子学极具前景的材料<sup>[38, 39, 130, 131]</sup>。

对半导体纳米结构中载流子自旋动力学的调控是自旋电子学研究中的重要课题并且其可以由 Rashba 效应通过垂直电场对自旋-轨道耦合的调控来实现<sup>[132, 133]</sup>。传统二维半导体的光学性质如集体激发<sup>[134, 135]</sup>和光电导<sup>[136, 138–140]</sup> 已经被研究并且展示了 Rashba 效应如何影响基于传统二维半导体材料自旋电子学器件的光学性质。这些研究表明 Rashba 效应能强烈的影响等离激元模式和低频率波段的光谱。

当一个电场垂直作用于单层二硫化钼薄膜片上时，空间反演对称被打破，同时根据 Kane-Mele 模型<sup>[141]</sup>，哈密顿量中将增加一个 Rashba 自旋-轨道耦合项。因此，自

旋量子数  $\hat{s}_z$  将不再是一个好量子数<sup>[141–143]</sup> 并且自旋劈裂电子态之间的电子跃迁变得可能。这将使我们能观测到之前已经在传统二维电子气中发现的自旋相关的光学现象<sup>[134–140]</sup>。在单层二硫化钼中，两种自旋耦合机制同时发生作用，同时可以预期在其中能发现有趣的自旋光学效应。另外，归功于 Rashba 自旋-轨道耦合受外加电场的可调性，也使得可以对这些效应进行开和关的调控。另外，也可以通过在二硫化钼表面沉积不同原子的方法来增强 Rashba 自旋-轨道耦合强度，这种方法已经在掺杂金的石墨烯<sup>[144]</sup>和 Bi<sub>2</sub>Se<sub>3</sub>(001)<sup>[145]</sup> 表面被证实。

Rashba 自旋-轨道耦合对石墨烯光学性质的影响已经被研究<sup>[146–149]</sup>。研究表明 Rashba 效应能强烈的影响石墨烯的光学性质。在 Rashba 自旋-轨道耦合的作用下，石墨烯的光电导曲线表现出吸收峰和扭曲，这是由不同自旋劈裂态之间的带间光吸收跃迁所导致的<sup>[148, 149]</sup>。单层二硫化钼在低能量范围有着抛物线型的能带这与有着线性色散关系的石墨烯不同。为了对单层二硫化钼材料系统有更深入的了解并探索它们将来在工作在低能量频段实际器件中的应用，研究 Rashba 效应在影响单层二硫化钼光电性质中起到的作用是非常有必要的。

除了大量对二硫化钼的理论研究之外，二硫化钼的光学和输运性质同样在实验上被广泛的研究<sup>[38, 39, 42, 116, 118, 120, 121, 131]</sup>。但是这些工作主要集中在研究由导带和价带之间的带间跃迁所导致的在可见光范围电磁谱的光电性质。在这项研究中，我们可以预测由 Rashba 效应所导致的自旋-翻转跃迁能对单层二硫化钼在红外到太赫兹波段的光电响应有着重要的影响。据我们所知，目前在此波段光谱范围内对单层二硫化钼的光电性质的研究非常少。在这个区域，内禀自旋-轨道耦合和 Rashba 自旋-轨道耦合能对光电响应性质起到非常重要的作用。因而我们想要研究单层二硫化钼在 Rashba 自旋-轨道耦合作用下在线偏振和圆偏振辐射场下的光电导特性。通过计算带内跃迁和带间跃迁的贡献，我们研究了 *n*-型和 *p*-型掺杂（通过化学掺杂或加一个偏压来改变载流子浓度）、温度和 Rashba 自旋轨道耦合强度对二硫化钼光电导的影响。我们通过加上了 Kane-Mele 自旋-轨道耦合项后的  $4 \times 4$  矩阵哈密顿来计算单层二硫化钼的电子能带结构。

## 4.1 单层二硫化钼在 Rashba 自旋-轨道耦合下的电子结构

在这项研究中，我们考虑在 x-y 平面介电衬底如氧化硅上的单层二硫化钼<sup>[150, 151]</sup>。在低能区域，单层二硫化钼中带电荷载流子（电子或空穴）在  $\mathbf{K}(\mathbf{K}')$  点附近在 Rashba 自旋-轨道耦合下的有效  $\mathbf{k} \cdot \mathbf{p}$  哈密顿量可以写作<sup>[125, 127, 128, 142, 143]</sup>

$$\begin{aligned} \hat{H}^s = & [at(\varsigma k_x \hat{\sigma}_x + k_y \hat{\sigma}_y) + \frac{\Delta}{2} \hat{\sigma}_z] \otimes \hat{I} + \varsigma \gamma_v \frac{\hat{I} - \hat{\sigma}_z}{2} \otimes \hat{s}_z \\ & + \gamma_R (\varsigma \hat{\sigma}_x \otimes \hat{s}_y - \hat{\sigma}_y \otimes \hat{s}_x), \end{aligned} \quad (4.1)$$

其中  $\hat{\sigma}_i$  和  $\hat{s}_i$  是分别表示赝自旋和自旋的泡利矩阵。 $\hat{I}$  是  $2 \times 2$  的单位矩阵并且  $\varsigma = \pm$  是表示  $\mathbf{K}(\mathbf{K}')$ -谷的谷指数。上述哈密顿量在基于波函数  $\Psi^+ = \{\psi_{A\uparrow}, \psi_{A\downarrow}, \psi_{B\uparrow}, \psi_{B\downarrow}\}^T$

表 4.1: 由第一性原理计算得到不同单层过渡金属硫化物材料的能带结构参数<sup>[125]</sup>

	晶格常数 $a$	带隙 $\Delta$	跃迁常数 $t$	自旋-轨道耦合常数 $2\gamma_v$
MoS <sub>2</sub>	3.193 Å	1.66 eV	1.10 eV	150 meV
WS <sub>2</sub>	3.197 Å	1.79 eV	1.37 eV	430 meV
MoSe <sub>2</sub>	3.313 Å	1.47 eV	1.94 eV	180 meV
WSe <sub>2</sub>	3.110 Å	1.60 eV	1.19 eV	460 meV

和  $\Psi^- = \{\psi_{A\downarrow}, \psi_{A\uparrow}, \psi_{B\downarrow}, \psi_{B\uparrow}\}^T$  下两个谷的哈密顿量可以分别写作

$$\hat{H}^s = \begin{pmatrix} \Delta/2 & 0 & \varsigma atk_{-\varsigma} & 0 \\ 0 & \Delta/2 & 2i\gamma_R & \varsigma atk_{-\varsigma} \\ \varsigma atk_\varsigma & -2i\gamma_R & \gamma_v - \Delta/2 & 0 \\ 0 & \varsigma atk_\varsigma & 0 & -\gamma_v - \Delta/2 \end{pmatrix}, \quad (4.2)$$

其中  $\mathbf{k} = (k_x, k_y)$  是波矢,  $k_\pm = k_x \pm ik_y = ke^{\pm i\phi}$ 。表 4.1 给出了单层过渡金属硫化物的能带结构参数, 对于单层二硫化钼,  $a = 3.193$  Å 是晶格常数,  $t = 1.1$  eV 是跳跃参数<sup>[125]</sup>, 内禀自旋-轨道耦合参数  $2\gamma_v = 150$  meV 是在没有 Rashba 自旋-轨道耦合下价带顶的自旋劈裂<sup>[125, 152]</sup>,  $\Delta = 1.66$  eV 是我们在计算中取用的导带和价带间的直接带隙<sup>[125, 127, 128]</sup>,  $\gamma_R$  是可以被电场调控的 Rashba 自旋-轨道耦合参数并且能通过 *ab initio* 计算或者实验拟合得到。Kormányos 等<sup>[153]</sup> 估算了两带模型中单层二硫化钼的 Rashba 参数  $\alpha_R = 0.033$  eÅ<sup>2</sup> $E_z$ [V/Å]。对应到我们的四带模型则是  $\gamma_R = 0.0078$  eÅ $E_z$ [V/Å], 其中不同模型下 Rashba 参数的对应关系  $\gamma_R = \alpha_R \Delta / (2at)$  可以通过文献 [154] 中得到并且这里  $E_z$  是垂直电场强度。在这里特别指出 Rashba 效应不仅可以通过一个门电压调控, 而且能通过掺杂原子的手段增强并且已经在石墨烯中实现<sup>[144]</sup>。例如, 较大的 Rashba 耦合强度 72 meV 已经在 EuO 衬底上的单层二碲化钼中发现<sup>[155]</sup>。

通过上述的哈密顿量可以同时描述出导带和价带在 Rashba 效应下的自旋态。单层二硫化钼在谷  $\mathbf{K}(\mathbf{K}')$  附近对应的薛定谔方程可以通过解析法得到并且本征能量是对角化方程

$$\varepsilon^4 - A_2 \varepsilon^2 + A_1 \varepsilon + A_0 = 0, \quad (4.3)$$

的根, 其中

$$A_0 = (\Delta^2/4 + a^2 t^2 k^2)^2 + \gamma_R^2 \Delta (\Delta + 2\gamma_v) - \Delta^2 \gamma_v^2 / 4,$$

$$A_1 = \Delta \gamma_v^2 - 4\gamma_v \gamma_R^2,$$

和

$$A_2 = \Delta^2/2 + 2a^2 t^2 k^2 + 4\gamma_R^2 + \gamma_v^2.$$

能量色散关系  $\varepsilon_{\mathbf{k},\xi} = \varepsilon_{\mathbf{k},\lambda v}$  可以通过上式四次方程的通用解析解得到<sup>[156]</sup>。这里我们定义总量子数  $\xi = (\varsigma, \lambda, s)$ , 其中  $\lambda = \pm$  表示导带/价带,  $s = \pm$  是自旋指数同时  $\varsigma$  表示谷指数。我们通常来用指数  $v = \varsigma s = \pm$  来表示谷/自旋的对称性。

对于一个在  $\mathbf{K}(\mathbf{K}')$  谷附近电子态对应的能量本征函数为

$$|\mathbf{k}, \xi\rangle = \psi_\xi(\mathbf{k}, \mathbf{r}) = \mathcal{N}_{\lambda v}(k)[c_1^\xi, c_2^\xi, c_3^\xi, c_4^\xi]e^{i\mathbf{k}\cdot\mathbf{r}}. \quad (4.4)$$

公式 (4.4) 表示为行矢量的形式且其中本征函数各个单元的值为

$$\begin{aligned} c_1^\xi &= -2i\gamma_R a^2 t^2 k_{-\varsigma}^2, & c_2^\xi &= \varsigma at k_{-\varsigma} b_1^{\lambda v}, \\ c_3^\xi &= -2i\varsigma\gamma_R at k_{-\varsigma} b_0^{\lambda v}, & c_4^\xi &= b_0^{\lambda v} b_2^{\lambda v}, \end{aligned}$$

并且

$$\begin{aligned} b_1^{\lambda v} &= \varepsilon_{\mathbf{k},\lambda v}^2 - \gamma_v \varepsilon_{\mathbf{k},\lambda v} + \Delta(2\gamma_v - \Delta)/4 - a^2 t^2 k^2, \\ b_2^{\lambda v} &= b_1^{\lambda v} - 4\gamma_R^2, & b_0^{\lambda v} &= \varepsilon_{\mathbf{k},\lambda v} - \Delta/2. \end{aligned}$$

归一化系数  $\mathcal{N}_{\lambda v}(k)$  写作  $\mathcal{N}_{\lambda v}(k) = 1/\sqrt{h^{\lambda v}}$ , 其中  $h^{\lambda v} = 4\gamma_R^2 a^2 t^2 k^2 [a^2 t^2 k^2 + (b_0^{\lambda v})^2] + a^2 t^2 k^2 (b_1^{\lambda v})^2 + (b_0^{\lambda v} b_2^{\lambda v})^2$ 。

## 4.2 单层二硫化钼在 Rashba 效应下的光电导

在这项研究中, 我们通过标准的久保公式 (Kubo formula) 来计算单层二硫化钼的光电导<sup>[74, 157]</sup>

$$\sigma_{\alpha\beta}(\mathbf{q}, \omega) = i \frac{e^2 n_i}{m\omega} \delta_{\alpha\beta} + \frac{1}{\omega} \int_0^\infty dt e^{i\tilde{\omega}t} \langle [j_\alpha^\dagger(\mathbf{q}, t), j_\beta(\mathbf{q}, 0)] \rangle, \quad (4.5)$$

其中对于二维系统  $(\alpha, \beta) = (x, y)$ ,  $j_\alpha(\mathbf{q}, t)$  是电流密度算符,  $\tilde{\omega} = \omega + i\eta$  ( $\eta \rightarrow 0^+$ ) 并且  $n_i$  是导带中电子或价带中空穴的电荷密度。在这里必须指出公式 (4.5) 中的第一项是逆磁项<sup>[157]</sup>。在这里我们主要计算光电导的实部, 然而这项不做贡献因为在有限光频率下这项是纯粹的虚部。

在光学极限  $\mathbf{q} \rightarrow 0$  下, 在入射光子频率为  $\omega$  下单层二硫化钼系统的动态光电导可以写成 Kubo-Greenwood 的形式<sup>[76, 157]</sup>

$$\sigma_{\alpha\beta}(\omega) = \frac{ie^2}{\omega} \sum_{\xi', \xi} \sum_{\mathbf{k}', \mathbf{k}} \langle \mathbf{k}, \xi | \hat{v}_\alpha^\xi | \mathbf{k}', \xi' \rangle \langle \mathbf{k}', \xi' | \hat{v}_\beta^\xi | \mathbf{k}, \xi \rangle \frac{f(\varepsilon_{\mathbf{k}, \xi}) - f(\varepsilon_{\mathbf{k}', \xi'})}{\varepsilon_{\mathbf{k}, \xi} - \varepsilon_{\mathbf{k}', \xi'} + \hbar(\omega + i\eta)}, \quad (4.6)$$

其中速度算符  $\hat{v}_\alpha^\xi = \hbar^{-1} \partial \hat{H}^\xi / \partial k_\alpha$ ,  $\eta = \tau^{-1}$ ,  $\tau$  是输运弛豫时间,  $f(\varepsilon_{\mathbf{k}, \xi}) = f(\varepsilon_{\mathbf{k}, \lambda v}) = \{\exp[(\varepsilon_{\mathbf{k}, \lambda v} - \mu_\lambda)/(k_B T)] + 1\}^{-1}$  是费米-狄拉克分布函数且  $\mu_\lambda$  是电子或空穴的化学势,  $T$  表示温度。需要指出的是我们使用一个弛豫时间常数来进行接下来的计算, 在这里

并没有具体考虑特定的散射机制。最近，单层二硫化钼的带内跃迁光电导也同样被计算<sup>[158]</sup>，文献 [159] 中讨论了杂质散射对弛豫时间的影响。

在谷  $\zeta$  的纵向光电导可以写作

$$\sigma_{xx}^{\zeta}(\omega) = \frac{ie^2}{\omega} \sum_{\lambda'v',\lambda v} \sum_{\mathbf{k}',\mathbf{k}} w_{\lambda'v',\lambda v}^{xx}(\mathbf{k}', \mathbf{k}) \frac{f(\varepsilon_{\mathbf{k},\lambda v}) - f(\varepsilon_{\mathbf{k}',\lambda'v'})}{\varepsilon_{\mathbf{k},\lambda v} - \varepsilon_{\mathbf{k}',\lambda'v'} + \hbar(\omega + i\eta)}, \quad (4.7)$$

其中

$$w_{\lambda'v',\lambda v}^{xx}(\mathbf{k}', \mathbf{k}) = \frac{a^4 t^4 k^2 [p^2 + r^2 + 2pr \cos(2\phi)]}{\hbar^2 h^{\lambda v} h^{\lambda'v'}} \delta_{\mathbf{k},\mathbf{k}'},$$

且

$$\begin{aligned} p &= b_0^{\lambda'v'} (4\gamma_R^2 a^2 t^2 k^2 + b_1^{\lambda v} b_2^{\lambda'v'}), \\ r &= b_0^{\lambda v} (4\gamma_R^2 a^2 t^2 k^2 + b_1^{\lambda'v'} b_2^{\lambda v}). \end{aligned}$$

同时，在  $\zeta$  谷的横向或“霍尔”光电导是

$$\sigma_{xy}^{\zeta}(\omega) = \frac{i\zeta e^2}{\omega} \sum_{\lambda'v',\lambda v} \sum_{\mathbf{k}',\mathbf{k}} w_{\lambda'v',\lambda v}^{xy,\zeta}(\mathbf{k}', \mathbf{k}) \frac{f(\varepsilon_{\mathbf{k},\lambda v}) - f(\varepsilon_{\mathbf{k}',\lambda'v'})}{\varepsilon_{\mathbf{k},\lambda v} - \varepsilon_{\mathbf{k}',\lambda'v'} + \hbar(\omega + i\eta)}, \quad (4.8)$$

其中

$$w_{\lambda'v',\lambda v}^{xy,\zeta}(\mathbf{k}', \mathbf{k}) = \frac{a^4 t^4 k^2}{\hbar^2} \frac{i(p^2 - r^2) + 2\zeta pr \sin(2\phi)}{h^{\lambda v} h^{\lambda'v'}} \delta_{\mathbf{k},\mathbf{k}'}$$

在  $\eta \rightarrow 0^+$  极限下，上述公式中的主值项 ( $\mathcal{P}$ ) 和狄拉克-德尔塔项可以完全分离通过借助于狄拉克等式

$$\lim_{\eta \rightarrow 0^+} \frac{1}{x + i\eta} = \mathcal{P}\left(\frac{1}{x}\right) - i\pi\delta(x). \quad (4.9)$$

因此，单层二硫化钼的光电导可以被分成实部和虚部。在  $\zeta$  谷，纵向光电导的实部和霍尔光电导的虚部分别表示为如下形式

$$\text{Re } \sigma_{xx}^{\zeta}(\omega) = \sum_{\lambda'v',\lambda v} \text{Re } \sigma_{xx,\zeta}^{\lambda v \lambda'v'}(\omega), \quad (4.10)$$

其中

$$\text{Re } \sigma_{xx,\zeta}^{\lambda v \lambda'v'}(\omega) = \int_0^{\infty} dk \frac{e^2 a^4 t^4 k^3}{2\hbar^3 \omega} \frac{(p^2 + r^2)}{h^{\lambda v} h^{\lambda'v'}} [f(\varepsilon_{k,\lambda v}) - f(\varepsilon_{k,\lambda v} + \hbar\omega)] \delta[\omega - \omega_{\lambda v}^{\lambda'v'}(k)],$$

同时

$$\text{Im } \sigma_{xy}^{\zeta}(\omega) = \sum_{\lambda'v',\lambda v} \text{Im } \sigma_{xy,\zeta}^{\lambda v \lambda'v'}(\omega), \quad (4.11)$$

其中

$$\text{Im } \sigma_{xy,\varsigma}^{\lambda\nu\lambda'\nu'}(\omega) = \varsigma \int_0^\infty dk \frac{e^2 a^4 t^4 k^3}{2\hbar^3 \omega} \frac{(p^2 - r^2)}{h^{\lambda\nu} h^{\lambda'\nu'}} [f(\varepsilon_{k,\lambda\nu}) - f(\varepsilon_{k,\lambda\nu} + \hbar\omega)] \delta[\omega - \omega_{\lambda\nu}^{\lambda'\nu'}(k)],$$

其中公式 (4.7)–(4.8) 中  $\cos(2\phi)$  和  $\sin(2\phi)$  对角度  $\phi$  的积分分别为零，同时  $\omega_{\lambda\nu}^{\lambda'\nu'}(k) = (\varepsilon_{k,\lambda'\nu'} - \varepsilon_{k,\lambda\nu})/\hbar$  是跃迁过程中初态和末态和能量频率之差。

系统总的光电导是两个谷贡献的和

$$\sigma_{\alpha\beta}(\omega) = \sum_{\varsigma=\pm} \sigma_{\alpha\beta}^{\varsigma}(\omega). \quad (4.12)$$

公式 (4.10) 表明对于不同谷纵向光电导的实部是相等的。这意味着纵向光电导的实部可以写作  $\text{Re } \sigma_{xx}(\omega) = g_v \text{Re } \sigma_{xx}^{\varsigma}(\omega)$ ，其中  $g_v = 2$  是简并因子。对于横向电导的虚部，公式 (4.11) 显示其在不同谷的值只是受符号  $\varsigma$  改变的影响。例如， $\text{Im } \sigma_{xy,+}^{\lambda\nu\lambda'\nu'}(\omega) = -\text{Im } \sigma_{xy,-}^{\lambda\nu\lambda'\nu'}(\omega)$ ，表明系统是谷反对称的。这表明系统总的霍尔电导的虚部为零，因为两个谷的贡献相互抵消了。

通常来说，对于入射线偏振光的吸收一般可以由纵向电导的实部来表示。对于给定光频率下系统对于右旋圆偏振光 (+) 和左旋圆偏振光 (-) 的光响应，在圆偏振光场下  $\varsigma$  谷中光电导中的光吸收部分可以表示为<sup>[128]</sup>

$$\text{Re } \sigma_{\pm}^{\varsigma}(\omega) = \text{Re } \sigma_{xx}^{\varsigma}(\omega) \mp \text{Im } \sigma_{xy}^{\varsigma}(\omega). \quad (4.13)$$

因此，为了计算对辐射场的光吸收，我们仅需要计算公式 (4.10) 中纵向光电导的实部和公式 (4.11) 中霍尔电导的虚部。

### 4.3 结果与讨论

在这项研究中，我们考虑  $n$ -型和  $p$ -型单层二硫化钼在相对较弱的红外至太赫兹辐射场下的光电响应，因而所用到的线性响应理论是有效的<sup>[6, 74]</sup>。同时在辐射场下电子或空穴的浓度不会有较大的变化。这是因为单层二硫化钼中较大的带隙抑制了光激发电子-空穴对的产生。这表明在目前的研究中只需要考虑导带或价带内的带内电子跃迁，例如 ( $\lambda = \lambda'$ ) 的情况下。 $n$ -型样品中电子或  $p$ -型样品中空穴的化学势  $\mu_\lambda$  可以分别通过载流子数守恒定理来决定

$$n_e = g_v \sum_{\lambda=+, v=\pm} \sum_{\mathbf{k}} f(\varepsilon_{\mathbf{k},\lambda\nu}), \quad (4.14)$$

和

$$n_h = g_v \sum_{\lambda=-, v=\pm} \sum_{\mathbf{k}} [1 - f(\varepsilon_{\mathbf{k},\lambda\nu})]. \quad (4.15)$$

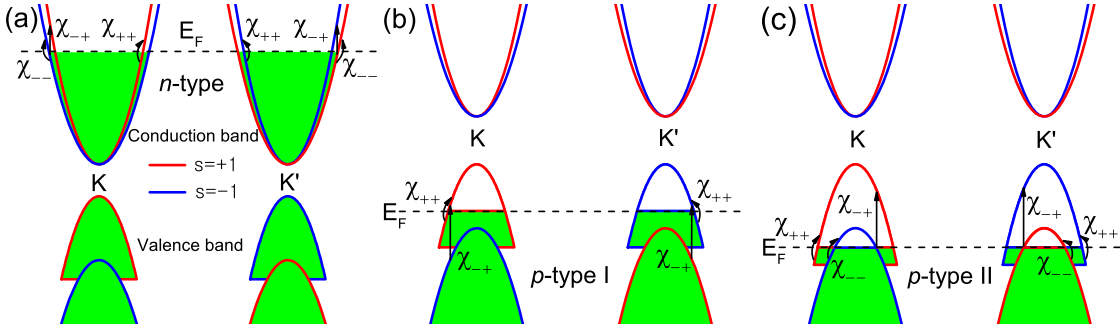


图 4.1: 单层二硫化钼能带结构的示意图和在两个谷可能的光跃迁通道。(a)  $n$ -型样品, (b)  $p$ -型 I 单层二硫化钼样品其中费米能级  $E_F$  在两个自旋劈裂价带顶点的中间, (c)  $p$ -型 II 单层二硫化钼样品其中费米能级  $E_F$  在  $v = -$  自旋劈裂价带子带顶点之下。可能的光吸收跃迁通道由  $\chi_{vv'}$  表示

为了完成光电导的数值计算, 我们在计算自旋-翻转跃迁贡献的过程中采用电子的自旋弛豫时间  $\tau_{\text{spin}}^e = 3 \text{ ps}$  和空穴的自旋弛豫时间  $\tau_{\text{spin}}^h = 200 \text{ ps}$ <sup>[160]</sup>。对于自旋不变的自由载流子吸收, 能量弛豫时间约为  $\tau_c = 0.5 \text{ ps}$ <sup>[161]</sup>。在能量驰豫近似下, 可以使用洛伦兹分布函数:  $\delta(E) \rightarrow (E_\tau/\pi)/(E^2 + E_\tau^2)$  来替换公式 (4.10) 和 (4.11) 中的德尔塔函数, 其中  $E_\tau = \hbar/\tau$  是电子态的延展宽度<sup>[162]</sup>。这里需要指出的是能量驰豫时间是一个随频率变化的参数但是在数值计算中通常设定为一个常数<sup>[163]</sup>。公式 (4.10) 和 (4.11) 表示的光电导可以通过标准的 Gauss-Kronrod 积分算法进行一重积分的数值计算<sup>[164]</sup> 得到, 同时积分是天然收敛的因为其中的费米-狄拉克函数分布特性和能量守恒德尔塔函数的洛伦兹分布特性。

在图 4.1 中, 给出了单层二硫化钼在  $\mathbf{K}$  和  $\mathbf{K}'$  谷的低能量电子能带结构和对应的光跃迁通道  $\chi_{vv'}$ 。在单层二硫化钼中, 如图 4.1 所示, 内禀的自旋-轨道耦合在导带中造成较小的自旋劈裂但是引起了价带中较大的自旋劈裂。另外, 此时系统中的自旋上和自旋下部分是完全不耦合的, 从而使得相反自旋方向子带间的电子跃迁是不可能的。在考虑了 Rashba 效应后, 体系的能谱只是被轻微的影响, 但是使得不同能带的电子态是一种自旋混合态。从而使得图 4.1 中所示的不同自旋-劈裂子带间的电子跃迁变得可能。从前面的讨论可知, 纵向霍尔光电导的绝对值是不受谷指数影响的。于是我们用符号  $\chi_{vv'}$  来表示从  $v$  带到  $v'$  带的光吸收跃迁。在这里我们定义在能量可分辨的自旋劈裂能带中, 能量低的子带用  $v = -$  表示, 同时能量较高的子带用  $v = +$  表示。

单层二硫化钼是半导体并且可以通过化学掺杂或加一个门电压的手段进行掺杂浓度的调控<sup>[121, 167]</sup>。如果系统是电子掺杂的, 例如,  $n$ -型单层二硫化钼, 系统的光电导可以分开表示为在导带内源于自旋不变和自旋翻转跃迁的贡献。因此, 光电导是图 4.1(a) 中所示跃迁通道所做贡献的和。得益于价带顶较大的自旋劈裂,  $p$ -型单层二硫化钼的光吸收跃迁强烈的取决于掺杂的浓度。对于低掺杂的情况, 在价带中能量较低的自旋劈裂带完全由电子占据。因而, 如图 4.1(b) 所示, 在这个子带中的自由载流子吸收是完全禁止的。如果  $p$ -型掺杂的浓度更大一些, 如图 4.1(c) 所示, 这个能量较低的子带

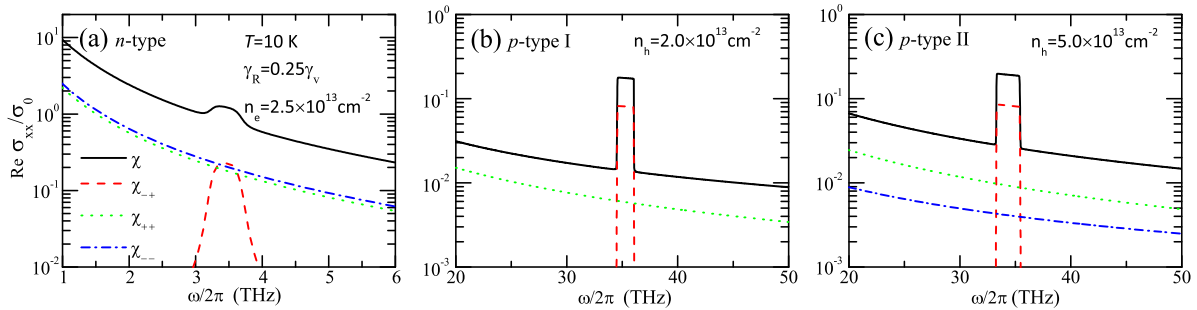


图 4.2: 在有限温度不同掺杂类型和掺杂浓度下, 不同跃迁通道对纵向光电导实部的贡献。在图 (a)-(c) 中不同跃迁通道对光电导的贡献对应于图 3.1 中的跃迁通道。同时, 黑色实线  $\chi$  所表示的是所有跃迁通道所做贡献的和。这里,  $\sigma_0 = e^2/(4\hbar)$ , 图中取用对数坐标系

内则可以有带内跃迁的贡献部分。为了确定系统的光吸收, 如在前一个小节中所提到, 需要计算光电导的实部。因而, 通过实验上对不同掺杂浓度下系统光吸收的测量, 同样能够确定公式 (4.12)-(4.13) 中所定义的光电导。

在图 4.2 中, 给出了给定电子浓度  $n_e$  下  $n$ -型单层二硫化钼和给定空穴浓度  $n_h$  下  $p$ -型 I/II 单层二硫化钼在温度  $T = 10$  K 且  $\gamma_R = 0.25\gamma_v$  时不同电子跃迁通道对光电导的贡献。可以看到  $n$ -型 ( $p$ -型) 单层二硫化钼的光电导由图 4.1 中所示的自旋不变跃迁和自旋翻转跃迁同时贡献。由于  $\mathbf{K}$  和  $\mathbf{K}'$  谷间的对称关系, 图 4.2 中不同谷对光电导的贡献是相同的除了不同谷中能量较高和较低的子带分别有着不同的自旋指数。在图 4.2(b) 中, 自由载流子吸收只存在于能量最高的自旋分辨子带中, 而能量最低的自旋分辨子带中则是如图 4.1(b) 中所示被完全占据。因此, 在  $p$ -型 II 单层二硫化钼中的带内跃迁比与之相对应的  $p$ -型 II 样品对光电导有着更多的贡献。这一点可以从图 4.2(b)-(c) 中很清楚的看到。同时, 我们可以看到  $p$ -型样品中在  $v = +$  子带中的自由载流子吸收对光电导的贡献比在  $v = -$  子带中的贡献大。与此同时, 在  $n$ -型样品中则情况相反。对于带内跃迁, 主要发生在低频率的区域, 能量弛豫时间随频率的变化不是很强。研究表明在 InP 中, 低频段内自由载流子弛豫时间随光频率的变化很小<sup>[165]</sup>。同时 Rashba 效应对自由载流子弛豫时间的影响也很小这是因为 Rashba 效应几乎不参与到带内跃迁散射机制。通常来说, 用单一能量弛豫时间的 Drude 模型能较好的描述带内跃迁光电导<sup>[166]</sup>。

自旋守恒的带内跃迁会引起低频段的太赫兹光吸收, 而自旋翻转跃迁则会导致图 4.2(a) 中较宽的吸收峰和图 4.2(b)-(c) 中近似矩形的吸收光谱。在图 4.2(a) 中, 总的光电导在低频段有一个宽的吸收峰, 同时总光电导在低频段随着频率的减小而增强, 表现出类似于通常的 Drude 模型的性质。在 3 – 3.8 THz 范围内较宽的吸收峰是由导带中较小的自旋劈裂所造成的。吸收峰的形状是由  $n$ -型样品中跃迁能量的范围较小而导致的。在图 4.2(b)-(c) 中, 总的光电导曲线在高频区域有一个吸收窗口同时在低频段的

总光电导同样随频率减小而增加。同时在图 4.2(b)-(c) 中近似矩形的吸收窗口在频率范围  $34.5 - 36 \text{ THz}$  和  $33.3 - 35.5 \text{ THz}$  是由价带中较大的自旋劈裂所导致的。

图 4.3 给出了单层二硫化钼中两个谷在圆偏振和线偏振光场下对光吸收的贡献。光电导包含由自旋守恒带内跃迁所贡献的类 Drude 部分和自旋翻转带间跃迁所贡献的较小的光吸收窗口。在线偏振和圆偏振光辐射下，类 Drude 部分是相同的，因为从公式 (4.8) 可以看到带内跃迁对霍尔电导虚部的贡献为零。如在第 4.2 节中所阐述，对线偏振光的光吸收与纵向光电导的实部  $\text{Re } \sigma_{xx}^S$  成正比，并且在两个谷是相等的。然而，对圆偏振光的吸收同时受到霍尔光电导虚部  $\text{Im } \sigma_{xy}^S$  的影响，并且霍尔光电导的虚部在两个谷是  $\pm$  相反的。因此，不同谷对圆偏振光的吸收是受谷指数影响的。对于系统对左旋和右旋圆偏振光总的吸收响应， $\sigma_-$  主要探测  $\mathbf{K}$  谷而  $\sigma_+$  主要探测  $\mathbf{K}'$  谷。另外，在两个谷的平均值则等于纵向光电导。这些有趣的发现与硅稀中的发现一致<sup>[162]</sup>。

图 4.4 给出了在给定载流子浓度和  $\gamma_R$  参数，不同温度下  $n$ -型和  $p$ -型 II 单层二硫化钼光电导随辐射场频率的变化关系。对于 Rashba 参数  $\gamma_R = 0.25\gamma_v$  和温度  $T = 10 \text{ K}$  时， $p$ -型掺杂样品可以被认为是  $p$ -型 I 当  $n_h < 3.36 \times 10^{13} \text{ cm}^{-2}$ ，同时会变成是  $p$ -型 II 当  $n_h > 3.36 \times 10^{13} \text{ cm}^{-2}$ 。在图 4.4(a) 中，我们发现宽吸收峰的强度随着温度增加而减小并且在常温下会消失。图 4.4(b) 中的光电导曲线在常温下有一个吸收峰并且在低温下有一个光吸收窗口。在低温  $T=10 \text{ K}$  时，光吸收窗口的边缘处有一个强烈的截断。我们注意到在  $36.1 \text{ THz}$  处的截断在温度较高的情形下一直存在。在较高的温度

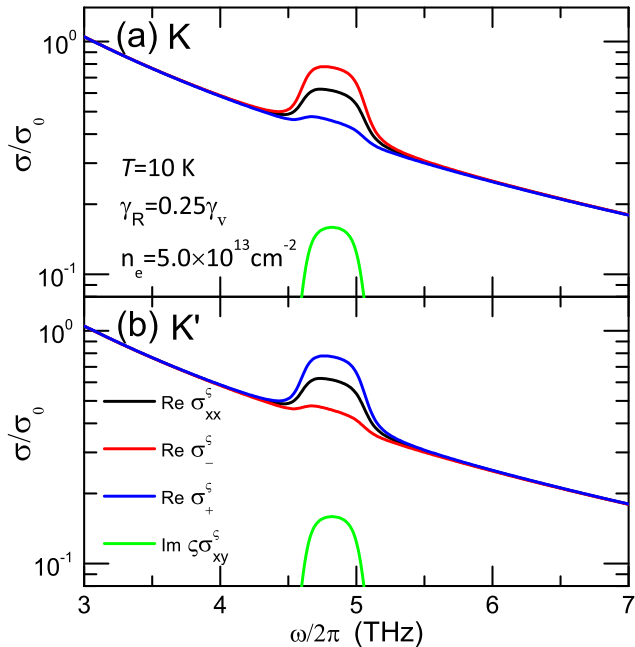


图 4.3: 在温度  $T=10 \text{ K}$ ，电子浓度  $n_e = 5 \times 10^{13} \text{ cm}^{-2}$  和 Rashba 参数  $\gamma_R = 0.25\gamma_v$  时，圆偏振光场下  $n$ -型单层  $\text{MoS}_2$  中光电导的吸收部分。(a)  $\mathbf{K}$  谷和 (b)  $\mathbf{K}'$  谷的结果。图中取用对数坐标系

下, 由于费米-狄拉克分布的平滑作用, 图 4.1(c) 中所示的一些电子重新分布到费米能级以上的电子态上。因而, 电子可以占据  $v = -$  子带顶部的一些电子态并且可以发生由  $v = -$  带到  $v = +$  带的电子跃迁。然而, 当  $\gamma_R = 0.25\gamma_v$  时两个价带子带顶的能量差对应的辐射频率为 36.1 THz。因此, 36.1 THz 是所允许的自旋翻转跃迁的最大光跃迁频率。类 Drude 部分随温度发生变化很小是因为在数值计算中取用了相同的能力弛豫时间。通常来说, 我们可以在较低的温度下在光电导谱中得到更强的吸收峰和更尖锐的吸收窗口。无论如何, 我们发现在  $p$ -型样品中的自旋翻转跃迁产生的光吸收仍然可以在室温下观测到。

图 4.5 中给出了在给定 Rashba 参数  $\gamma_R = 0.25\gamma_v$  和温度  $T = 10$  K, 不同载流子浓度下  $n$ -型和  $p$ -型单层二硫化钼光电导随辐射场频率的变化。对于单层二硫化钼,  $n$ -型和  $p$ -型掺杂的样品可以通过场效应并通过不同的源极和漏极来实现<sup>[121, 168]</sup>且掺杂浓度可以通过门电压来调控。通常, 可以在二硫化钼中得到较高的载流子浓度<sup>[121, 169]</sup>。于是我们在数值计算中取载流子浓度的数量级为  $10^{13} \text{ cm}^{-2}$ 。如图 4.5 中所示,  $n$ -型和  $p$ -型样品中带内跃迁所贡献的光电导随着载流子浓度的增加而增加。更加有趣的是, 我们发现随着载流子浓度的增加, 图 4.5(a) 中的宽吸收峰蓝移到高频率段, 图 4.5(b) 中

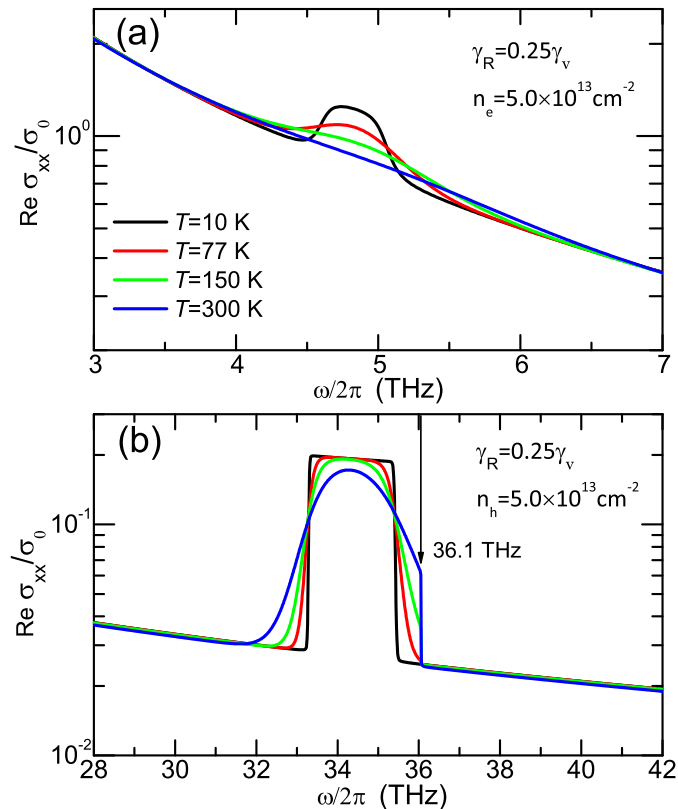


图 4.4: 给定的载流子浓度和 Rashba 参数在不同温度下纵向光电导的实部随辐射频率的变化。  
(a)  $n$ -型和 (b)  $p$ -型单层二硫化钼。图中取用对数坐标系

的光吸收窗口红移到低频率段。在给定的 Rashba 参数和温度下，电子/空穴在  $n/p$ -型样品中的化学势随载流子浓度的增加而增加/减小。因此，由于泡利阻塞效应<sup>[170]</sup>，直接自旋翻转跃迁所需要的能量随着  $n/p$ -型样品中电子/空穴浓度的增加而增加/减小。这就是为什么随着载流子浓度的增加， $n$ -型样品中的吸收峰会蓝移而  $p$ -型样品中光吸收窗口会红移。在图 4.5(b) 中，我们看到光吸收在右边的边界在 36.1 THz 位置处，这里 36.1 THz 是这些情况下允许的最大光跃迁频率。除去带内跃迁的贡献，我们发现  $n$ -型样品中的吸收峰和  $p$ -型样品中光吸收窗口的高度受到载流子浓度的影响很小。而且， $n$ -型样品中吸收峰的宽度随着电子浓度发生轻微的变化并且  $p$ -型样品中光吸收窗口的宽度随空穴浓度的变换有着显著的变化。这些理论研究的结果表明单层二硫化钼从太赫兹到红外区域的光吸收可以通过改变载流子浓度的方法来进行有效的调节。

在图 4.6 中，我们给出了单层二硫化钼在 Rashba 自旋-轨道耦合作用下取不同 Rashba 参数在  $\mathbf{K}$  谷中的低能有效能带结构以及导带和价带中自旋劈裂子带之间的能量差随波矢的变化。通常来说，半导体中的 Rashba 自旋-轨道耦合强度可以被电场调节<sup>[50, 132, 133]</sup>。在图 4.6(b) 中的  $\mathbf{K}$  点附近，导带中的两个自旋劈裂子带之间的能

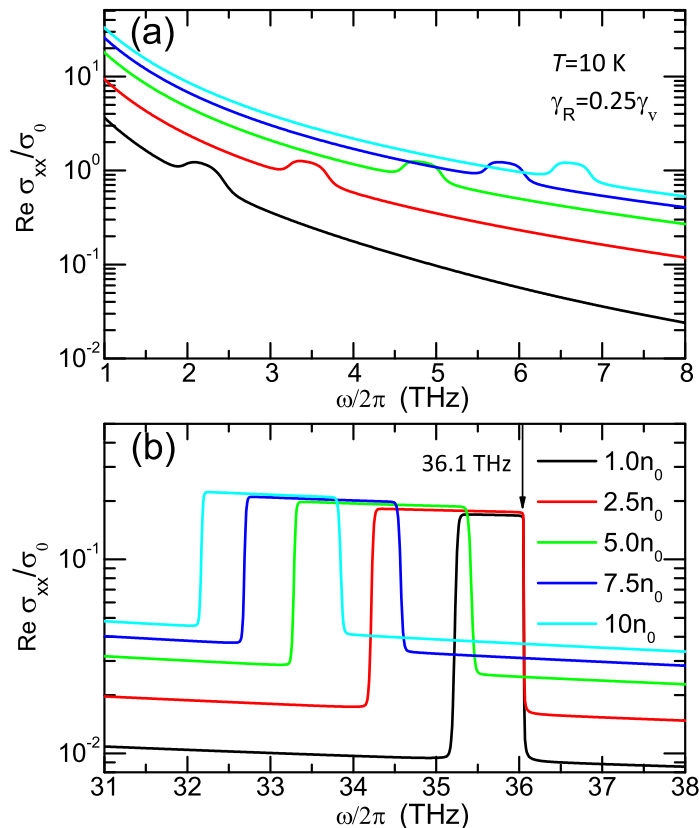


图 4.5: 在 Rashba 参数  $\gamma_R = 0.25\gamma_v$  和温度  $T = 10$  K 时，不同载流子浓度下纵向光电导的实部随辐射场频率的变化，其中  $n_0 = 1 \times 10^{13} \text{ cm}^{-2}$ 。 (a)  $n$ -型和 (b)  $n$ -型单层二硫化钼的结果。图中取用对数坐标系

级差随着波矢或 Rashba 参数的增加而增加。随着 Rashba 参数的增加，能级之间的能量差由近似的抛物线曲线变成近似的线性曲线。并且在较大的 Rashba 参数下，可以发现在  $ka = 0$  处的自旋-轨道分裂的带隙。在图 4.6(c) 中，当  $\gamma_R = 0.1\gamma_v, 0.25\gamma_v$ , 和  $0.5\gamma_v$  时，可以看到两个自旋劈裂价带子带间的能量差随着波矢的增加而减小。当  $\gamma_R = 0.75\gamma_v$  时，自旋劈裂价带子带之间能量差随着波矢的增加先增加后稍微的减小。而当  $\gamma_R = \gamma_v$  时，自旋劈裂价带子带之间能量差随着波矢的增加而增加。我们发现单层二硫化钼的能带结构可以通过 Rashba 效应得到轻微的调节。不同的 Rashba 参数下，在价带中可以得到更加复杂的自旋劈裂子能带结构。

图 4.7 给出了  $n$ -型和  $p$ -型单层二硫化钼在不同 Rashba 参数下光电导随频率的变化。在较大的载流子浓度下(例如  $5 \times 10^{13} \text{ cm}^{-2}$ )，我们发现价带  $v = -$  子带顶点的位置和  $n$ -/ $p$ -型单层二硫化钼中电子/空穴的化学势能不随 Rashba 参数的变化而变化。因此，对于  $p$ -型单层二硫化钼且空穴浓度为  $n_h = 5 \times 10^{13} \text{ cm}^{-2}$ ，在不同参数  $\gamma_R$  下可以一直被看作是  $p$ -型 II 单层二硫化钼。在较大的载流子浓度下，我们发现 Rashba 参数对费米能级的影响是可以忽略的。当载流子浓度较小时，我们发现在  $n$ -型样品

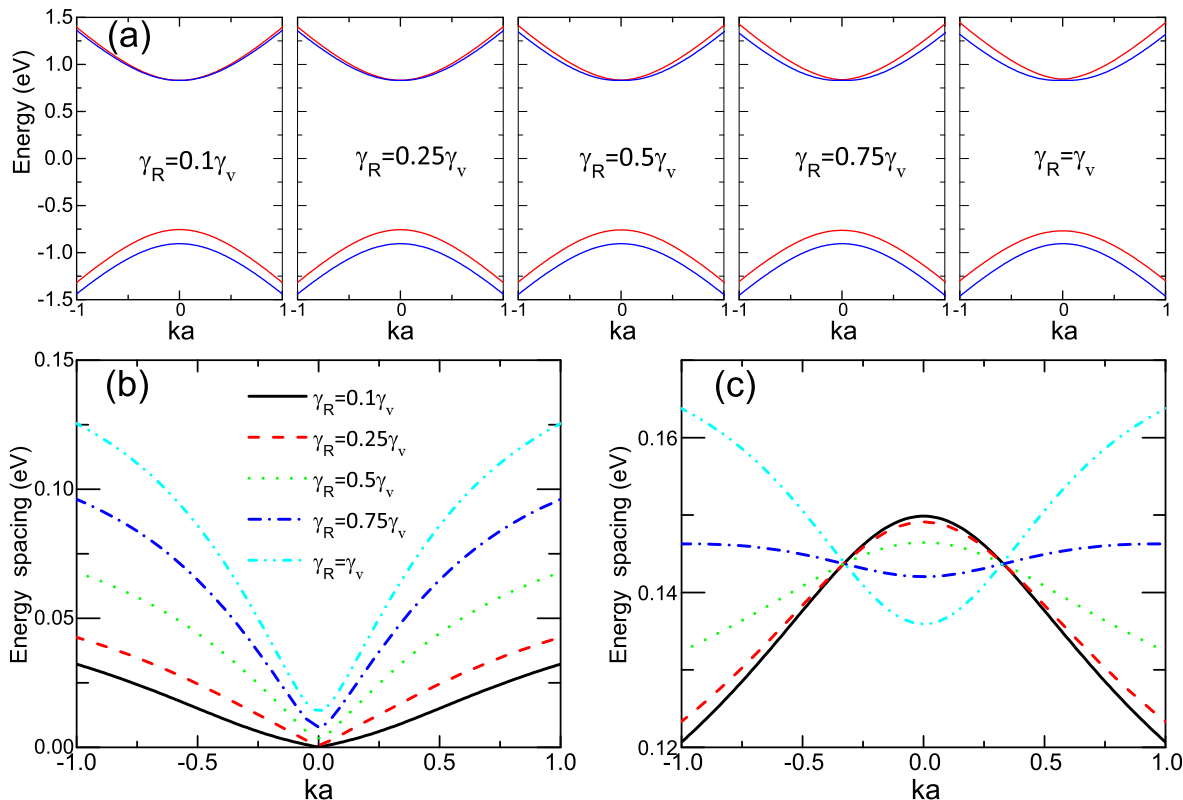


图 4.6: (a) 在不同 Rashba 参数下，单层二硫化钼在 K 谷的低能量有效能带结构。自旋上 ( $s = 1$ ) 和自旋下 ( $s = -1$ ) 的子带分别用红色和蓝色的曲线表示。(b) 导带中和 (c) 价带中自旋劈裂子带之间的能量差

中当 Rashba 耦合强度较小的时候费米能级随 Rashba 耦合强度的增加保持不变。随着 Rashba 耦合强度的继续增加，费米能级稍微的减小。而在  $p$ -型低载流子浓度样品中，费米能级一直随着  $\gamma_R$  的增加而缓慢的减小。

在图 4.7(a)-(b) 中，我们可以看到  $n$ -/ $p$ -型单层二硫化钼光电导的类 Drude 部分不受  $\gamma_R$  取值的影响。随着  $\gamma_R$  的增加，在图 4.7(a) 中的宽吸收峰发生蓝移并且吸收峰的形状转变为吸收窗口。同时，光吸收窗口的宽度随着  $\gamma_R$  的增加而增加并且光吸收窗口的高度随  $\gamma_R$  的变化也很小。在图 4.7(b) 中同样可以看到在不同 Rashba 参数下的光电导曲线中存在光吸收窗口但是光吸收窗口的宽度和高度受到  $\gamma_R$  的影响很大。从图 4.7(b) 中的五组数据可以看到，当  $\gamma_R = \gamma_v$  时有着最宽的光吸收窗口，当  $\gamma_R = 0.75\gamma_v$  时有着最窄的光吸收窗口。这种特性可以从图 4.6(c) 中得到。我们可以看到在图 4.7(b) 中这些光吸收窗口的边界与图 4.6(c) 中  $ka = 0$  处的自旋劈裂价带子带间的能级差并不相符。这意味着在较大空穴浓度和较低温度下，允许自旋翻转跃迁的光子能量边界主要由在费米能级附近受到费米狄拉克分布所限制空穴的光吸收跃迁所决定。当  $\gamma_R = 0.75\gamma_v$  时，图 4.6(c) 中较窄的能级差导致了图 4.7(b) 中最窄的光吸收窗口并且光吸收窗口有着刀锋型的顶端。

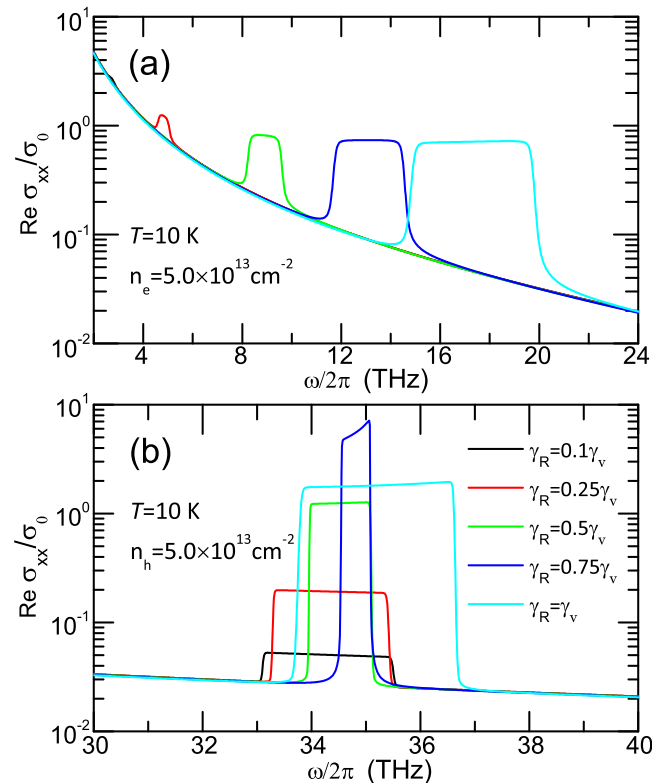


图 4.7: 在给定温度  $T = 10$  K 和载流子浓度  $5 \times 10^{13} \text{ cm}^{-2}$  下，不同 Rashba 自旋-轨道耦合参数下光电导的实部随着辐射频率的变化。(a)  $n$ -型单层二硫化钼和 (b)  $p$ -型 II 单层二硫化钼的结果。图中取用对数坐标系

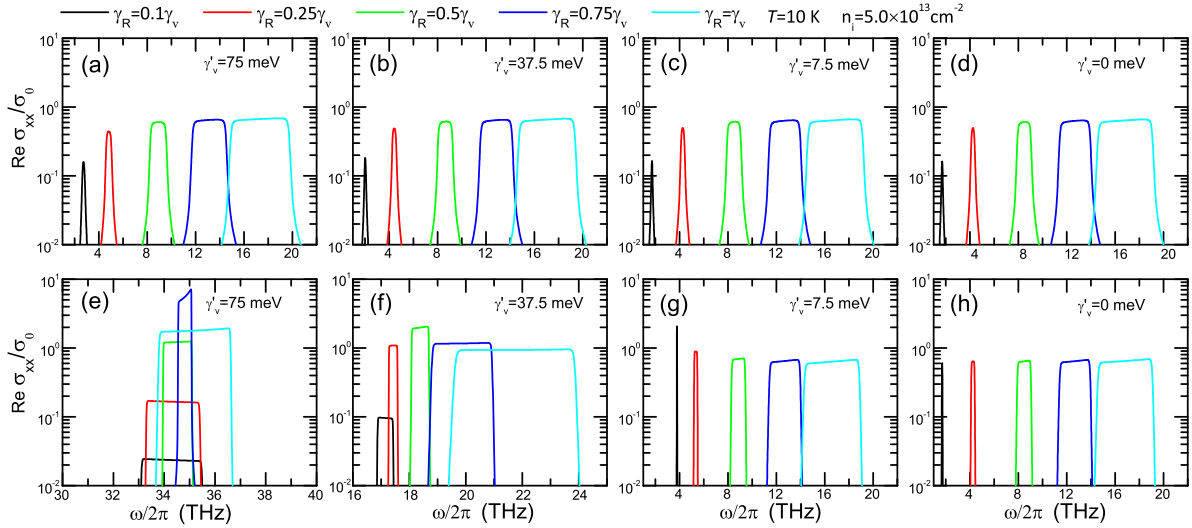


图 4.8: 在给定温度和载流子浓度, 不同 Rashba 系数下自旋翻转跃迁所贡献的纵向光电导的实部随辐射场频率的变化。这里我们用  $\gamma'_v$  来代替  $\gamma_v$  作为内禀自旋-轨道耦合参数。不同内禀自旋-轨道耦合参数  $\gamma'_v$  下 (a-d)  $n$ -型和 (e-h)  $p$ -型单层二硫化钼样品的结果。图中取用对数坐标系

另外, 在 Rashba 效应下单层二硫化钼中自旋劈裂的导带和传统二维电子气系统类似。因此, 图 4.7(a) 中的结果和传统二维电子气中的结果类似<sup>[136–138]</sup>。由于自旋-轨道劈裂价带结构的复杂性, 图 4.7(b) 中光吸收窗口的高度随 Rashba 参数的变化很大, 这一点和传统二维电子系统有很大的区别。因此, 可以总结得到不同掺杂类型单层二硫化钼的光电性质可以通过 Rashba 效应进行有效的调制。

为了更好的理解在 Rashba 效应下  $p$ -型样品的光电导中的光吸收窗口的高度随 Rashba 参数的影响很大这种特殊的现象, 我们将研究内禀自旋-轨道耦合所起到的作用。虽然内禀自旋-轨道耦合参数  $\gamma_v$  是一个常数且不受外加电场而改变, 我们将通过选择不同的内禀自旋-轨道耦合参数的方式来研究内禀自旋-轨道耦合如何决定单层二硫化钼的光学性质。在图 4.8 中, 我们给出了在给定温度和载流子浓度下,  $n$ -/ $p$ -型二硫化钼样品中自旋翻转跃迁对光电导贡献随辐射场频率的变化。这里, 我们重新定义  $\gamma'_v$  为内禀自旋-轨道耦合参数。图 4.8(a) 给出了图 4.7(a) 中自旋翻转所贡献的光电导部分。当 Rashba 耦合很弱时, 我们可以看到  $n$ -型系统中电子自旋翻转跃迁所贡献部分的宽度和高度随着 Rashba 耦合强度的减小而减小。从图 4.8(a)-(d) 中可以看出, 在不同  $\gamma_R$  参数下, 光电导曲线的特性受内禀自旋-轨道耦合的影响非常小。这点微小的差异是由不同  $\gamma'_v$  下自旋劈裂导带的微小变化所造成的。从图 4.8(e)-(h), 我们可以发现如下的特征: (i) 在较大的内禀自旋-轨道耦合下(例如  $\gamma'_v = 75$  meV, 37.5 meV), 光吸收窗口的高度随 Rashba 参数的变化很强。(ii) 在较小的  $\gamma'_v$  下, 光吸收窗口的高度随着 Rashba 参数的变化稍稍的变化并且这些光电导曲线的形状和与之对应的  $n$ -型情况下类似。(iii) 在没有内禀自旋轨道耦合的作用下 ( $\gamma'_v = 0$  meV), 图 4.8(h) 中的光电

导曲线和图 4.8(d) 中的光电导曲线几乎相等。其中细微的差异是由计算中所选择的电子和空穴不同的弛豫散射时间所造成的。Rashba 效应的确可以影响带间跃迁的弛豫时间。但是从图 4.8(d) 和 (h) 可以看到，能量弛豫近似中用到的不同弛豫时间只会稍微影响光吸收窗口的边界同时不会对整个自旋翻转跃迁所贡献的光电导曲线有较大的影响。较大的弛豫散射时间意味着较小的散射态的延展，自旋翻转光电导将接近于长波光学极限下的结果。在这项研究中，我们对在高频段区域的自旋翻转跃迁所贡献的光吸收部分更加感兴趣。在这个区域，带内跃迁的贡献很微弱。于是，我们可以很放心的认为在本研究数值计算中用到的能量弛豫时间能够很好的描述在所研究频段范围的光吸收特性。因此，我们可以看到内禀自旋-轨道耦合能在影响不同 Rashba 自旋-轨道耦合参数下  $p$ -型单层二硫化钼随的光吸收谱起到很重要的作用。在单层  $\text{MX}_2$  中，内禀自旋-轨道耦合参数和公式 (4.1) 中其它的参数随着不同 M 和 X 元素变化。因而在红外到太赫兹范围内有着不同频段范围和形状的吸收窗口也同样可以在 Rashba 效应下其它的单层过渡金属硫化物中观看到。

#### 4.4 本章小结

在这项研究中，我们探索了在 Rashba 效应下  $n$ - 和  $p$ -型单层二硫化钼红外至太赫兹波段的光电特性。光电导通过标准的久保公式计算得到。研究了辐射场的偏振方向，温度，载流子浓度和 Rashba 参数对光电导的影响。系统总的光电导包含不同自旋态之间不同跃迁通道的贡献。我们同样研究了内禀自旋-轨道耦合作用在 Rashba 效应下对单层二硫化钼光电性质的影响。本研究主要的结论如下。

在单层二硫化钼中，自由载流子吸收存在于整个红外到太赫兹范围。自旋翻转跃迁所导致的宽吸收峰和吸收窗口处在红外到太赫兹频段。自由载流子吸收受到辐射场偏振方向、温度和 Rashba 参数的影响很弱但是强烈的受到载流子浓度的影响。在圆偏振光下，自旋翻转跃迁表现出谷指数选择性的光吸收。然而，不同谷之间光电导之和等于纵向光电导。在更低的温度下，可以看到更强的吸收峰或者更清晰的光吸收窗口。光吸收峰和光吸收窗口的位置和宽度可以有效的被载流子浓度和 Rashba 参数调节。这表明单层二硫化钼在红外到太赫兹区域有着较宽的光频响应范围。

在 Rashba 效应下， $n$ -型单层二硫化钼光电导的特征与传统二维电子气类似并且内禀自旋-轨道耦合对  $p$ -型单层二硫化钼的光电性质有着较强烈的影响。

我们发现  $n$ - 和  $p$ -型单层二硫化钼的光电特性可以被载流子浓度和 Rashba 参数进行有效的调节，这使得单层二硫化钼能成为应用于光学和光电子学非常有潜力的红外和太赫兹材料。本研究所得到理论结果有助于理解单层二硫化钼的光学性质。我们期望本理论研究中的预测能够被实验所证实。

This chapter corresponds to the published paper “Infrared to terahertz optical conductivity of *n*-type and *p*-type monolayer MoS<sub>2</sub> in the presence of Rashba spin-orbit coupling” in Appendix D.

## 第五章 Rashba 自旋-轨道耦合下单层二硫化钼在可见光波段范围的光吸收

在上一章中，我们讨论了单层二硫化钼系统在 Rashba 自旋-轨道耦合下基于  $4 \times 4$  矩阵哈密顿量计算得到的光电导。通过计算结果，我们了解到 Rashba 自旋-轨道耦合对单层二硫化钼在低频率红外到太赫兹频段内的光电导/光吸收有着非常重要的影响。由 Rashba 效应引起了  $n$ -型样品中与传统二维电子系统在 Rashba 效应下相类似的独特光吸收特性。Rashba 效应对自旋态的耦合效应能使不同非简并自旋子带中的电子发生光吸收带间跃迁，因而 Rashba 效应同样会对单层二硫化钼在高频段区域的光吸收特性产生影响。通过上一章中  $4 \times 4$  矩阵哈密顿量模型和在不考虑 Rashba 效应下  $2 \times 2$  矩阵哈密顿量模型，在这一章中我们研究和对比了 Rashba 效应在可见光区域对单层二硫化钼光的吸收及相对应的跃迁通道的影响。

### 5.1 单层二硫化钼在零 Rashba 自旋-轨道耦合下的电子结构

在这项研究中，我们考虑在 x-y 平面上的单层二硫化钼，单层二硫化钼中载流子（电子或空穴）在  $\mathbf{K}(\mathbf{K}')$ -点附近的有效哈密顿量可以写作<sup>[125, 127]</sup>

$$\hat{H}_0^\varsigma = \begin{pmatrix} \Delta/2 & \varsigma atk_{-\varsigma} \\ \varsigma atk_\varsigma & -\Delta/2 + \varsigma s\gamma \end{pmatrix}, \quad (5.1)$$

其中  $\mathbf{k} = (k_x, k_y)$  是载流子的波矢， $k_\pm = k_x \pm ik_y = ke^{\pm i\phi}$ ，且  $\phi$  是  $\mathbf{k}$  和  $x$ -轴之间的夹角， $\varsigma = \pm$  是  $\mathbf{K}(\mathbf{K}')$  谷的谷指数，自旋指数  $s = \pm$  代表自旋上和自旋下的电子态，晶格常数  $a = 3.193 \text{ \AA}$ ，跳跃参数  $t = 1.1 \text{ eV}$ ，内禀自旋-轨道耦合参数  $\gamma = 75 \text{ meV}$ ， $\Delta$  等于  $1.66 \text{ eV}$  是导带和价带之间的带隙。这里我们也使用  $v = \varsigma s$  来描述谷和自旋在能带结构中的对称性。单层二硫化钼在  $\mathbf{K}(\mathbf{K}')$  谷相对应的薛定谔方程可以有解析解且能量本征值为

$$E_{\lambda\mathbf{k}}^{\varsigma s} = E_{\lambda\mathbf{k}}^v = v\gamma/2 + \lambda[a^2t^2k^2 + \Delta_v^2]^{1/2}, \quad (5.2)$$

其中  $\Delta_v = (\Delta - v\gamma)/2$  且  $\lambda = \pm$  代表导带和价带。与之相对应的在导带或价带中载流子在  $\mathbf{K}(\mathbf{K}')$  谷的本征波函数为  $|\mathbf{k}, \lambda\varsigma s\rangle$  可以分别写做行矢量的形式

$$\begin{aligned} |\mathbf{k}, +\varsigma s\rangle &= [\cos(\vartheta_{\mathbf{k}}^v/2), \varsigma \sin(\vartheta_{\mathbf{k}}^v/2)e^{i\varsigma\phi}]e^{i\mathbf{k}\cdot\mathbf{r}}, \\ |\mathbf{k}, -\varsigma s\rangle &= [-\sin(\vartheta_{\mathbf{k}}^v/2), \varsigma \cos(\vartheta_{\mathbf{k}}^v/2)e^{i\varsigma\phi}]e^{i\mathbf{k}\cdot\mathbf{r}}, \end{aligned} \quad (5.3)$$

其中

$$\cos \vartheta_{\mathbf{k}}^v = \frac{\Delta_v}{\sqrt{a^2t^2k^2 + \Delta_v^2}}, \sin \vartheta_{\mathbf{k}}^v = \frac{atk}{\sqrt{a^2t^2k^2 + \Delta_v^2}}.$$

## 5.2 单层二硫化钼在无 Rashba 自旋-轨道耦合下的光电导

考虑在弱光场下并且带内跃迁对光生载流子浓度的贡献非常小，因而在此处仅考虑在纯  $n$ -型 ( $p$ -型) 掺杂情况下的单层二硫化钼。在单层二硫化钼中导带和价带中载流子的分布可以用同一个费米-狄拉克分布函数来描述。通过上一章中的公式可以得到单层二硫化钼在没有 Rashba 效应下的光电导为

$$\sigma_{\alpha\beta}(\omega) = \frac{ig_v e^2}{\omega} \sum_{v=\pm} \sum_{\lambda\lambda'} \sum_{\mathbf{k}',\mathbf{k}} \langle \mathbf{k}, \lambda\zeta s | \hat{v}_\alpha^\zeta | \mathbf{k}', \lambda'\zeta s \rangle \langle \mathbf{k}', \lambda'\zeta s | \hat{v}_\beta^\zeta | \mathbf{k}, \lambda\zeta s \rangle \frac{f(E_{\lambda\mathbf{k}}^v) - f(E_{\lambda'\mathbf{k}'}^v)}{E_{\lambda\mathbf{k}}^v - E_{\lambda'\mathbf{k}'}^v + \hbar(\omega + i\eta)}, \quad (5.4)$$

其中速度算符  $\hat{v}_\alpha^\zeta = \hbar^{-1} \partial \hat{H}_0^\zeta / \partial k_\alpha$ ,  $g_v = 2$  是谷简并因子,  $f(E_{\lambda\mathbf{k}}^v) = [e^{(E_{\lambda\mathbf{k}}^v - \mu_\lambda)/k_B T} + 1]^{-1}$  为费米-狄拉克分布函数。

谷和自旋指数为  $v$  的子系统的纵向光电导可以写作

$$\sigma_{xx,\varsigma}^{\lambda v \lambda' v}(\omega) = \frac{ie^2}{\omega} \sum_{\lambda',\lambda} \sum_{\mathbf{k}',\mathbf{k}} w_{\lambda' v, \lambda v}^{xx,\varsigma}(\mathbf{k}', \mathbf{k}) \frac{f(E_{\lambda\mathbf{k}}^v) - f(E_{\lambda'\mathbf{k}'}^v)}{E_{\lambda\mathbf{k}}^v - E_{\lambda'\mathbf{k}'}^v + \hbar(\omega + i\eta)}, \quad (5.5)$$

其中

$$w_{\lambda' v, \lambda v}^{xx,\varsigma}(\mathbf{k}', \mathbf{k}) = a^2 t^2 [\cos^4(\vartheta_{\mathbf{k}}^v/2) + \sin^4(\vartheta_{\mathbf{k}}^v/2) - \sin^2(\vartheta_{\mathbf{k}}^v) \cos(2\phi)/2]/\hbar^2 \delta_{\mathbf{k},\mathbf{k}'}.$$

同时，在谷和自旋指数为  $v$  的子系统的横向或“霍尔”光电导为

$$\sigma_{xy,\varsigma}^{\lambda v \lambda' v}(\omega) = \frac{i\varsigma e^2}{\omega} \sum_{\lambda',\lambda} \sum_{\mathbf{k}',\mathbf{k}} w_{\lambda' v, \lambda v}^{xy,\varsigma}(\mathbf{k}', \mathbf{k}) \frac{f(E_{\lambda\mathbf{k}}^v) - f(E_{\lambda'\mathbf{k}'}^v)}{E_{\lambda\mathbf{k}}^v - E_{\lambda'\mathbf{k}'}^v + \hbar(\omega + i\eta)}, \quad (5.6)$$

其中

$$w_{\lambda' v, \lambda v}^{xy,\varsigma}(\mathbf{k}', \mathbf{k}) = ia^2 t^2 [i\varsigma \sin^2(\vartheta_{\mathbf{k}}^v) \sin(2\phi)/2 + \sin^4(\vartheta_{\mathbf{k}}^v/2) - \cos^4(\vartheta_{\mathbf{k}}^v/2)]/\hbar^2 \delta_{\mathbf{k},\mathbf{k}'}.$$

在这里，我们只考虑在可见光范围内的光吸收。带内跃迁在低频率范围所贡献的光吸收为零因而不在考虑的范围之内。对于由价带到导带的带间电子跃迁，在谷和自旋指数为  $v$  的子系统，单层二硫化钼中纵向光电导的实部和霍尔光电导的虚部分别写为如下形式

$$\text{Re } \sigma_{xx,\varsigma}^{-v+v}(\omega) = \frac{e^2}{16\hbar} \left[ 1 + \frac{4\Delta_v^2}{\hbar^2 \omega^2} \right] \theta(\hbar\omega - 2\Delta_v) \left[ f\left(\frac{v\gamma - \hbar\omega}{2}\right) - f\left(\frac{v\gamma + \hbar\omega}{2}\right) \right], \quad (5.7)$$

和

$$\text{Im } \sigma_{xy,\varsigma}^{-v+v}(\omega) = -\frac{e^2}{16\hbar} \frac{4\varsigma\Delta_v}{\hbar\omega} \theta(\hbar\omega - 2\Delta_v) \left[ f\left(\frac{v\gamma - \hbar\omega}{2}\right) - f\left(\frac{v\gamma + \hbar\omega}{2}\right) \right]. \quad (5.8)$$

在圆偏振光场 ( $\rho = \pm$  分别表示右旋/左旋圆偏振) 下，可得到单层二硫化钼的光电导为

$$\text{Re } \sigma_{\rho,\varsigma}^{-v+v}(\omega) = \frac{e^2}{16\hbar} \left[ 1 + \varsigma\rho \frac{2\Delta_v}{\hbar\omega} \right]^2 \theta(\hbar\omega - 2\Delta_v) \left[ f\left(\frac{v\gamma - \hbar\omega}{2}\right) - f\left(\frac{v\gamma + \hbar\omega}{2}\right) \right]. \quad (5.9)$$

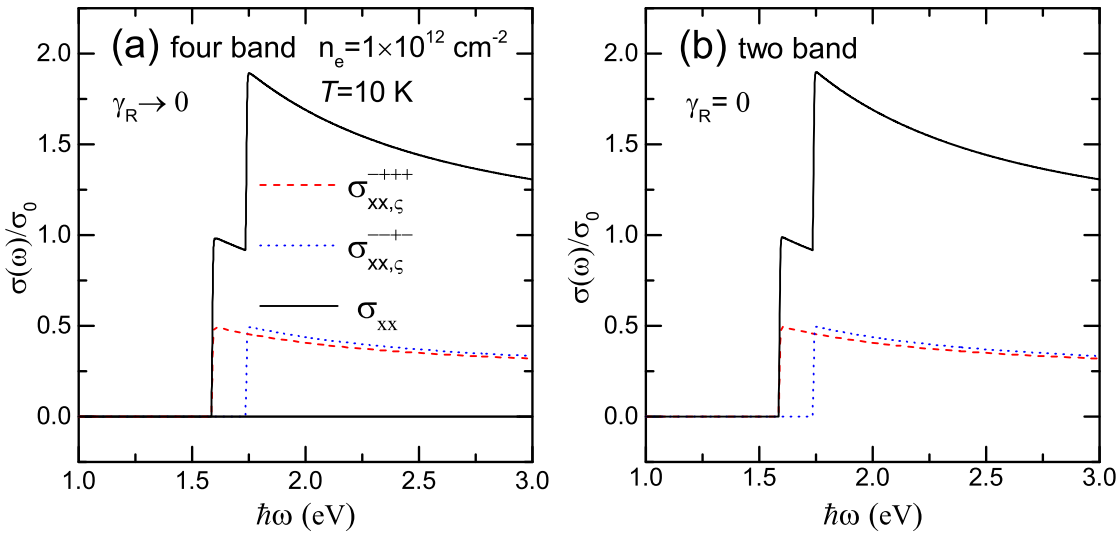


图 5.1: 在给定温度  $T = 10 \text{ K}$  和电子浓度  $1 \times 10^{12} \text{ cm}^{-2}$  下, 带间跃迁所贡献光电导  $\sigma_{xx,\zeta}^{\lambda v \lambda' v'}$  随着辐射频率的变化。 (a) 在四带模型中  $\gamma_R \rightarrow 0$  时和 (b) 二带模型中  $\gamma_R = 0$  时的结果。 $\sigma_{xx}$  为单层二硫化钼中不同子系统光电导的贡献之和。这里,  $\sigma_0 = e^2/(16\hbar)$

### 5.3 结果与讨论

上一节中的理论公式表明单层二硫化钼系统中的纵向光电导不受光场偏振方向的影响。因此,在线偏振光场的激发下,单层二硫化钼系统的谷简并不会被打破。同时在这里我们考虑单层二硫化钼在较弱光场下的光响应同时系统中光生载流子浓度在计算光电导的时候可以忽略。系统中导带中电子或价带中空穴的化学势  $\mu_\lambda$  可以通过载流子数守恒定理来决定

$$n_{e/h} = g_v \sum_{v=\pm} \sum_{\mathbf{k}} \{ \delta_{\lambda,-1} + \lambda [e^{(E_{\lambda\mathbf{k}}^v - \mu_\lambda)/k_B T} + 1]^{-1} \}. \quad (5.10)$$

同时在数值计算中在能量弛豫近似下在考虑带间跃迁过程中取能量弛豫时间  $\tau = 5 \text{ ps}$  来替换上一章中公式 (4.10) 中的  $\delta$  函数。

图 5.1 给出了四带哈密顿模型在 Rashba 耦合参数趋于零情况下和没有 Rashba 效应下二带哈密顿量模型计算得到的带间跃迁所贡献的光电导。可以看到图 5.1(a) 和图 5.1(b) 中的结果是相等的。在没有 Rashba 效应下, 只有自旋相同的子带之间能发生光吸收跃迁。同时可以看到在线偏振光下, 光电导在不同谷中的贡献可以被看作是简并的。在  $\mathbf{K}$  谷, 自旋向上子带和自旋向下子带所贡献的光电导随着能量的增加而减小。由于价带内较大的自旋劈裂, 在总的光电导曲线中会出现一个由不同自旋系统在  $ka = 0$  处的不同带隙所导致的光吸收台阶。

图 5.2 中给出了在电子浓度  $n_e = 1 \times 10^{12} \text{ cm}^{-2}$ 、Rashba 自旋-轨道耦合参数  $\gamma_R = 0.25\gamma_v$ 、温度  $T = 10 \text{ K}$  下, 单层二硫化钼系统的不同带间跃迁通道所贡献的光电导。

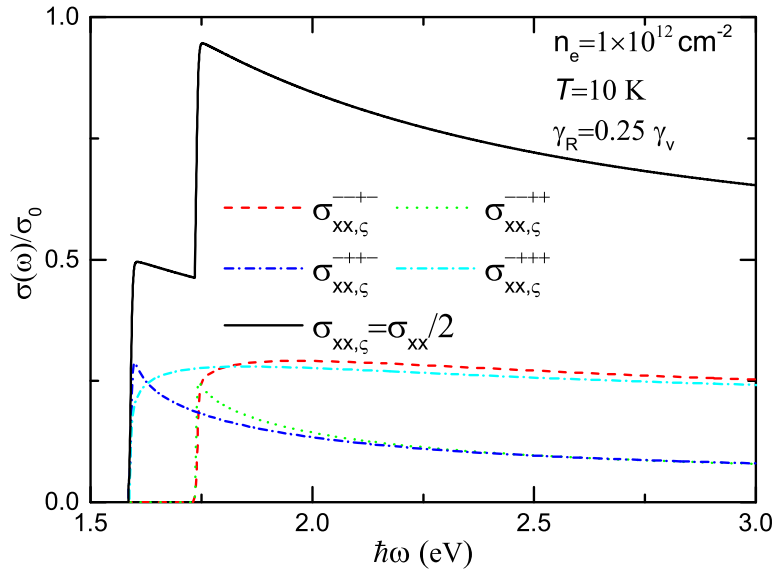


图 5.2: 在给定温度  $T=10\text{ K}$ 、电子浓度  $1\times 10^{12}\text{ cm}^{-2}$  以及 Rashba 自旋-轨道耦合参数  $\gamma_R=0.25\gamma_v$  下, 带间跃迁所贡献光电导  $\sigma_{xx,\zeta}^{\lambda\nu\lambda'\nu'}$  随着辐射频率的变化。 $\sigma_{xx,\zeta}$  为  $\zeta$  谷不同子系统所贡献光电导之和

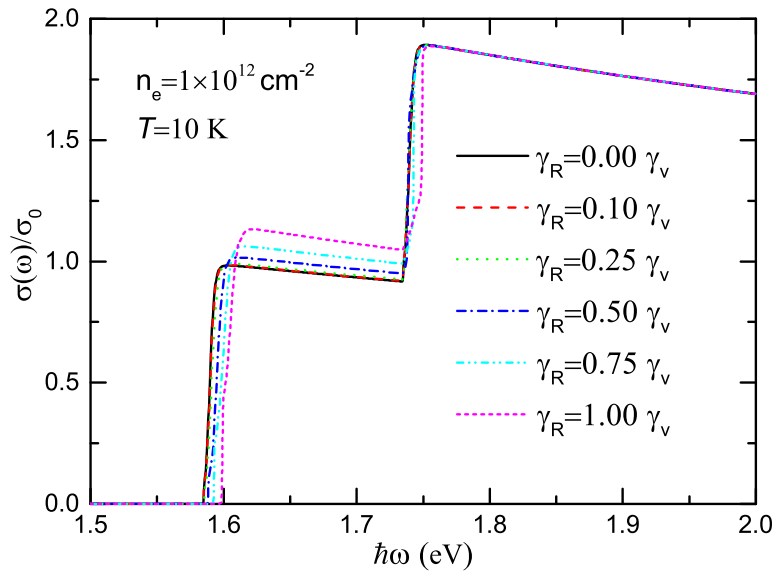


图 5.3: 在给定温度  $T=10\text{ K}$  和电子浓度  $1\times 10^{12}\text{ cm}^{-2}$  下, 不同 Rashba 参数下带间跃迁所贡献的光电导  $\sigma_{xx}$  随着辐射频率的变化

可以看到在 Rashba 效应的作用下, 从价带到导带有四个光吸收电子跃迁通道。这是由于 Rashba 效应对自旋态的耦合作用, 使得在不同自旋分裂子带间的电子跃迁成为了可能。由于价带内较大的自旋分裂, 由  $v=-1$  价带子带到  $v=+1$  导带子带的跃迁通道在有着更大的光子能量时才开始做贡献。对于由相同自旋指数能带直接跃迁所贡献

的光电导  $\sigma_{xx,\varsigma}^{--++}$  和  $\sigma_{xx,\varsigma}^{-+++}$ , 光电导随着能量的增加而增加。而对于电子跃迁过程中具有相反自旋指数的跃迁通道, 光电导  $\sigma_{xx,\varsigma}^{-++-}$  和  $\sigma_{xx,\varsigma}^{--++}$  在带隙处具有最大值然后随着能量的增加而减小。系统总的光电导曲线仍有着由价带内较大自旋分裂所导致的台阶形状。

图 5.3 给出了在给定温度和电子浓度下, 不同 Rashba 自旋-轨道耦合参数下系统总的光电导随着辐射场能量的变化。从图中可以看到, Rashba 效应对带隙附近的光吸收有着十分重要的影响。在 Rashba 参数很小的情况下, Rashba 效应对整个系统光电导曲线的影响非常小。随着 Rashba 参数的增加, 总的光电导曲线会出现向右的蓝移。而且第一个台阶的光电导曲线的高度会随着 Rashba 参数的增加而上升。在较大的 Rashba 参数下, 光电导曲线的形状也受到 Rashba 效应的影响。在高能量区域, Rashba 效应对总的光电导曲线几乎没有影响。这表明, 利用 Rashba 效应同样能对单层二硫化钼带隙附近的光学性质进行有效的调节。

## 5.4 本章小结

Rashba 效应不仅十分强烈的影响单层二硫化钼系统在低频率区域的光吸收, 同样会对可见光范围的带间跃迁光吸收造成影响。Rashba 效应对自旋态的耦合作用增加了光吸收跃迁通道的数量。在 Rashba 系数较小的情况下, Rashba 效应只影响不同光吸收跃迁通道对光电导的贡献而对总的光吸收/光电导没有明显的影响。在 Rashba 系数较大时, 随着 Rashba 系数的增加, 总的光电导曲线会发生蓝移且光电导曲线中第一个台阶的高度会增加。这项研究表明 Rashba 效应对单层二硫化钼在带隙附近的光学性质有着有效的调控作用。



## 第六章 圆偏振光场泵浦下单层二硫化钼中的多组份等离激元

最近，已经在实验上成功的制备出单层过渡金属硫化物  $\text{MX}_2$  ( $\text{M}=\text{Mo}, \text{W}, \text{Nb}, \text{Ta}, \text{Ti}$ , 和  $\text{X}=\text{S}, \text{Se}, \text{Te}$ )<sup>[116, 118]</sup> 并且其新颖的物理性质引起了人们极大的研究兴趣。ML-MX<sub>2</sub> 是有着 X-M-X 结构构成的三层结构并且金属原子层被夹在硫族原子层的中间<sup>[115]</sup>。过渡金属硫化物在多层次结构的时候具有间接带隙而在单层结构的时候具有直接带隙<sup>[115, 116, 118]</sup>。实验上证实单层二硫化钼场效应晶体管具有常温下  $10^8$  的开光比，迁移率大于  $200 \text{ cm}^2/(\text{Vs})$ <sup>[41, 42, 120]</sup>。单层二硫化钼有着超薄的层状结构和可观的直接带隙，这使得它在纳米电子学<sup>[42]</sup>，光电子学<sup>[171, 172]</sup>，自旋电子学和谷电子学<sup>[38, 39, 130, 131, 174]</sup> 上的应用极具潜力。

对单层 MX<sub>2</sub> 独特的光子-物质相互作用所产生光学性质如光荧光<sup>[38, 39]</sup>、光电导<sup>[128, 158, 173]</sup>，以及激子<sup>[175]</sup> 和三激子<sup>[176]</sup> 丰富了我们对单层 MX<sub>2</sub> 物理性质的认知。为了更好的了解单层过渡金属硫化物的潜在应用，它的等离激元特性的研究也同样十分重要。等离激元是振荡电荷的集体激发。他们在电子系统的动态响应中起到最基本的作用并且是构建光学超材料<sup>[177, 178]</sup> 研究的基础。自从原子层二维材料石墨烯的发现<sup>[7]</sup>，研究表明二维材料在等离激元学器件<sup>[64]</sup> 上有着巨大的应用前景。近年来石墨烯等离激元光子学的研究尤其受到关注因为它们具有独特的可调性<sup>[178]</sup>，较长的等离激元寿命<sup>[179]</sup>，和高度的电磁局域性<sup>[180]</sup>，并且石墨烯的等离激元色散关系能有效的从中红外到太赫兹频段进行调节<sup>[181]</sup>。石墨烯和有带隙石墨烯的介电函数和等离激元已经被研究并且它们的极化函数有解析解<sup>[182-184]</sup>。硅稀在无外场和有外场下的等离激元同样被研究<sup>[185, 186]</sup>。无外场下单层二硫化钼的集体激发性质也已被人们所研究和讨论<sup>[129, 187]</sup>。

由于它们的能带结构，无质量狄拉克-费米子、有质量狄拉克-费米子和二维电子气有着由粒子间库仑相互作用所产生的不同的集体激发响应特性<sup>[182-184, 188]</sup>。不同于石墨烯中无质量的狄拉克-费米子，单层二硫化钼可以被描述为有着很强内禀自旋-轨道耦合的有质量狄拉克-费米子。并且自旋-轨道耦合作用使自旋带发生劈裂并有着相反的自旋取向<sup>[125, 127]</sup>。较强的自旋-轨道耦合能保护平面外的自旋部分使自旋指数成为好量子数。另外，有质量狄拉克-费米子中较大的带隙能够使单层二硫化钼的低能量能带结构中的导带和价带同样能被有着不同谷和自旋指数的二维抛物线带模型来进行描述<sup>[153]</sup>。这项有趣的特征使得单层二硫化钼的等离激元色散关系和石墨烯有着很大的不同<sup>[129, 182, 183]</sup>。实际上，单层二硫化钼中的等离激元色散关系为  $\omega_q \propto q^{1/2}n^{1/2}$ <sup>[129]</sup> 与传统二维电子气的结果类似，而石墨烯中的等离激元色散关系为  $\omega_q \propto q^{1/2}n^{1/4}$ ，其中  $n$  是载流子浓度。

单层二硫化钼的光学响应主要由倒格矢空间中狄拉克点附近带电粒子所决定，例如，处于能谱中两个能谷中之一的带电粒子。近期的理论预测和实验研究已经表明单

层二硫化钼对圆偏振光具有关键性的谷选择性吸收<sup>[38, 39, 125, 131]</sup>，这使得我们可以在单个谷上调控电子。这项重要的性质可以被利用来实现谷霍尔效应<sup>[174]</sup>。因此，单层二硫化钼在单个谷中的载流子浓度可以通过光泵浦的方法被有效的调节<sup>[174]</sup>。

通过这种手段，一个光泵浦的过程能够使得单层二硫化钼的电子系统成为一个如图 6.1 所示的多组份系统。事实上，通过从价带到导带泵浦一个谷中的电子，人们可以得到图 6.1(d)-(e) 中所示的由两种相互作用电子液体所构成的系统。通过对系统外加偏压的方式来改变系统的费米能级进而进一步填充或清空导带或价带，使得在图 6.1(a) 和 (c) 中出现额外的一个组份。由于单层二硫化钼中自旋带是劈裂的，一个额外的自由度将出现。如图 6.1(b)-(c)，这是因为可以使费米能级只穿过每个谷中两个自旋价带子带的一个或者同时穿过两个自旋价带子带。在这项工作中，我们研究这些不同多组份系统的等离激元响应，力图了解在什么情况下新型等离激元模式能出现并描述他们的性质。

单层二硫化钼中的多组份费米系统被证实是产生不同集体激发效应的研究平台。除了本质上存在于相互作用二维费米子液体中通常的等离子激元模式之外<sup>[6, 188]</sup>，我们还发现在长波极限下  $n$ -组份系统能够支持  $n - 1$  个弱衰减的声学模式。这些模式对应于不同组份系统中有着不同相位振幅的振荡。另外，对于较大的波矢，我们同样发现在吸收谱区域存在新的等离激元模式。并且，朗道阻尼发生在其中一些组份系统中，这使得这些等离激元模式具有较高的衰减率。

这项工作的结构如下。第 6.1 节中给出了描述多组份系统等离激元特性的理论。在第 6.1.1 节中，我们给出了单层二硫化钼在有质量狄拉克费米子和二维抛物带模型下的低能量能带结构并且指出了它们的相同和差异性。在第 6.1.2 节中，我们给出了谷相关光吸收度并且计算了在圆偏振光场下光激发系统的载流子浓度。在第 6.1.3 节中，我们阐述了在有限温度下极化函数的计算和如何在无规则相近似下计算多组份系统的等离激元。在第 6.2 节我们报告和讨论了不同多组份系统的数值计算结果。单层二硫化钼在圆偏振光场下的光吸收在第 6.2.1 节中给出。在第 6.2.2 节中，我们比较了  $n$ -型单层二硫化钼在有效质量和双曲线模型下的结果。在第 6.2.3 节讨论了有限温度下的自旋极化二组份系统。谷极化的三组份和四组份系统的结果在第 6.2.4 节和第 6.2.5 节分别给出。最后，主要的结论在第 6.3 节中进行了归纳。

## 6.1 理论方法

### 6.1.1 电子能带结构和载流子浓度

与上一章的哈密顿量模型一样，在这项研究中，我们考虑在 x-y 平面上的单层二硫化钼，单层二硫化钼中载流子（电子或空穴）在  $\mathbf{K}(\mathbf{K}')$ -点附近的有效哈密顿量可以写作<sup>[125, 127]</sup>

$$\hat{H}_0^\zeta = \begin{pmatrix} \Delta/2 & \zeta atk_{-\zeta} \\ \zeta atk_\zeta & -\Delta/2 + \zeta s\gamma \end{pmatrix}, \quad (6.1)$$

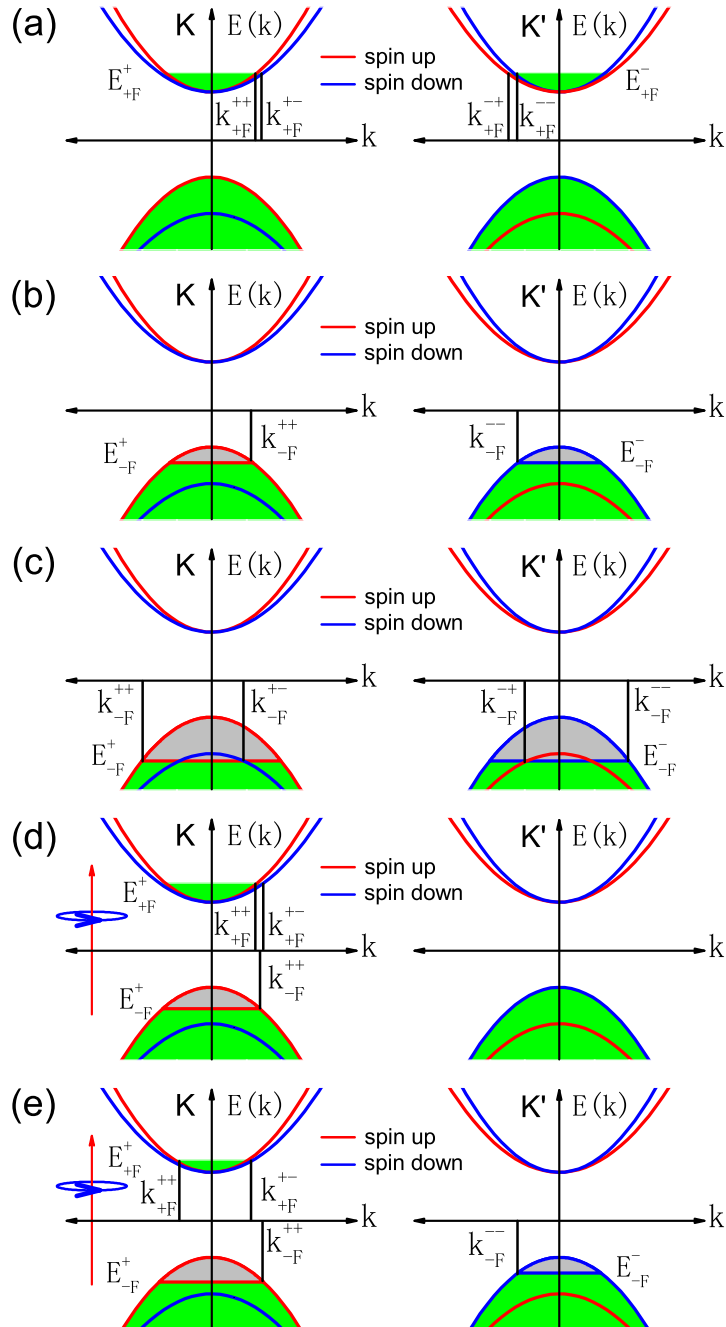


图 6.1: 这项研究中考虑的不同单层二硫化钼系统在  $\mathbf{K}$  谷(左图)和  $\mathbf{K}'$  谷(右图)的能带结构示意图。不同颜色的子带代表不同的自旋指数。绿色阴影表示电子占据而灰色阴影表示空穴占据。在面板 (a)-(c) 中仅仅通过静电偏压来改变系统的费米能级。在面板 (d)-(e) 中, 右旋圆偏振光场被加在系统上进而将电子从价带泵浦到导带。费米波矢  $k_{\lambda F}^{\varsigma s}$  和费米能级  $E_{\lambda F}$  由公式 (6.6), (6.8)-(6.9) 和 (6.14)-(6.15) 给出

其中  $\mathbf{k} = (k_x, k_y)$  是载流子的波矢,  $k_{\pm} = k_x \pm ik_y = ke^{\pm i\phi}$ , 且  $\phi$  是  $\mathbf{k}$  和  $x$ -轴之间的夹角,  $\varsigma = \pm$  是  $\mathbf{K}(\mathbf{K}')$  谷的谷指数, 自旋指数  $s = \pm$  代表自旋上和自旋下的电子态, 晶格常数  $a = 3.193 \text{ \AA}$ , 跳跃参数  $t = 1.1 \text{ eV}$ , 内禀自旋轨道耦合参数  $\gamma = 75 \text{ meV}$ ,

$\Delta = 1.66$  eV 是导带和价带之间的带隙。单层二硫化钼在  $\mathbf{K}(\mathbf{K}')$  谷相对应的薛定谔方程可以有解析解且能量本征值为

$$E_{\lambda\mathbf{k}}^{\varsigma s} = \varsigma s \gamma / 2 + \lambda \Lambda^{\varsigma s}(\mathbf{k}), \quad (6.2)$$

其中  $\Lambda^{\varsigma s}(\mathbf{k}) = [a^2 t^2 \mathbf{k}^2 + \Delta_{\varsigma s}^2]^{1/2}$ ,  $\Delta_{\varsigma s} = (\Delta - \varsigma s \gamma) / 2$  且  $\lambda = \pm$  代表导带和价带。与之对应在导带或价带中载流子在  $\mathbf{K}(\mathbf{K}')$  谷的本征波函数为  $|\mathbf{k}, \lambda \varsigma s\rangle$  可以分别写做行矢量的形式

$$\begin{aligned} |\mathbf{k}, +\varsigma s\rangle &= [\cos(\vartheta_{\mathbf{k}}^{\varsigma s}/2), \varsigma \sin(\vartheta_{\mathbf{k}}^{\varsigma s}/2) e^{i\varsigma\phi}] e^{i\mathbf{k}\cdot\mathbf{r}}, \\ |\mathbf{k}, -\varsigma s\rangle &= [-\sin(\vartheta_{\mathbf{k}}^{\varsigma s}/2), \varsigma \cos(\vartheta_{\mathbf{k}}^{\varsigma s}/2) e^{i\varsigma\phi}] e^{i\mathbf{k}\cdot\mathbf{r}}, \end{aligned} \quad (6.3)$$

且

$$\cos \vartheta_{\mathbf{k}}^{\varsigma s} = \frac{\Delta_{\varsigma s}}{\sqrt{a^2 t^2 k^2 + \Delta_{\varsigma s}^2}}, \sin \vartheta_{\mathbf{k}}^{\varsigma s} = \frac{at k}{\sqrt{a^2 t^2 k^2 + \Delta_{\varsigma s}^2}}.$$

单层二硫化在  $\varsigma$  谷的电子(空穴)的浓度  $n_{\lambda}^{\varsigma}$  ( $\lambda = +$  表示导带和  $\lambda = -$  表示价带)可以写作

$$n_{\lambda}^{\varsigma} = \frac{1}{(2\pi)^2} \sum_{s=\pm} \int d\mathbf{k}^2 [\delta_{\lambda, -1} + \lambda f_{\lambda}(E_{\lambda\mathbf{k}}^{\varsigma s})], \quad (6.4)$$

其中  $f_{\lambda}(E_{\lambda\mathbf{k}}^{\varsigma s}) = [e^{(E_{\lambda\mathbf{k}}^{\varsigma s} - \mu_{\lambda}^{\varsigma})/k_B T} + 1]^{-1}$  是导带/价带中电子的费米-狄拉克分布函数并且  $\mu_{\lambda}^{\varsigma}$  是我们当前研究中光泵浦准平衡系统中在  $\varsigma$  谷导带中电子或价带中空穴的化学势(或者是在零温下的费米能级  $E_{\lambda F}^{\varsigma}$ )。

在温度  $T=0$  K 时, 公式 (6.4) 可以写成常见的载流子浓度和费米波矢的关系

$$n_{\lambda}^{\varsigma} = \sum_{s=\pm} [k_{\lambda F}^{\varsigma s}]^2 / (4\pi), \quad (6.5)$$

其中  $k_{\lambda F}^{\varsigma s}$  是有着特定自旋指数  $s$  和谷指数  $\varsigma$  导带/价带子带的费米波矢。

如图 6.1 所示, 可以利用费米能级来产生具有不同自旋的载流子液体。如图 6.1(b) 所示, 在  $p$ -型单层二硫化钼中当费米能级处在能量最低的自旋分裂子带的顶点之上时, 能量较低的价带子带完全被电子占据同时空穴只在第一个能量较高的价带子带中进行分布。能量较高的价带子带的空穴浓度为  $n_{-}^{\varsigma}$ 。当费米能级满足  $E_{-F}^{\varsigma} \geq -\Delta/2 - \gamma$  时, 对应的在  $\varsigma$  谷的空穴浓度将满足  $n_{-}^{\varsigma} \leq (\gamma^2 + \Delta\gamma)/(2\pi a^2 t^2) = 1.679 \times 10^{13} \text{ cm}^{-2}$ 。此时, 在  $\varsigma$  谷能量较高的第一个价带子带的费米波矢和费米能级分别为

$$\begin{aligned} [k_{-F}^{\varsigma s}]^2 &= 4\pi n_{-}^{\varsigma} (\varsigma s = 1), \\ E_{-F}^{\varsigma} &= \gamma/2 - [4\pi a^2 t^2 n_{-}^{\varsigma} + (\Delta - \gamma)^2/4]^{1/2}. \end{aligned} \quad (6.6)$$

接下来我们将考虑在图 6.1(a) 和图 6.1(c) 中所表示的情形。利用自旋向上和自旋向下子带费米波矢相对应的费米能级必须相等的关系, 我们可以得到

$$\Lambda^{\varsigma-}(k_{\lambda F}^{\varsigma-}) - \Lambda^{\varsigma+}(k_{\lambda F}^{\varsigma+}) = \varsigma \lambda \gamma. \quad (6.7)$$

在通过将公式 (6.5) 和公式 (6.7) 联立之后，可以解出  $[k_{\lambda F}^{\zeta s}]^2$  的解为

$$[k_{\lambda F}^{\zeta s}]^2 = 2\pi n_{\lambda}^{\zeta} + \zeta s \left[ \frac{\Delta\gamma}{2a^2 t^2} - \lambda \frac{[\Delta^2\gamma^2 + 8\pi n_{\lambda}^{\zeta} a^2 t^2 \gamma^2]^{1/2}}{2a^2 t^2} \right]. \quad (6.8)$$

因此，在零温下  $\zeta$  谷载流子浓度为  $n_{\lambda}^{\zeta}$  时的费米能级为

$$E_{\lambda F}^{\zeta} = \zeta s \gamma / 2 + \lambda \Lambda^{\zeta s}(k_{\lambda F}^{\zeta s}). \quad (6.9)$$

在特定的电子能带分支的载流子浓度同时也可以写为

$$n_{\lambda}^{\zeta s} = \frac{n_{\lambda}^{\zeta}}{2} + \zeta s \left[ \frac{\Delta\gamma}{8\pi a^2 t^2} - \frac{\lambda [\Delta^2\gamma^2 + 8\pi n_{\lambda}^{\zeta} \gamma^2 a^2 t^2]^{1/2}}{8\pi a^2 t^2} \right]. \quad (6.10)$$

同时，单层二硫化钼系统的态密度 (density of states, DOS) 可以通过格林函数的虚部得到

$$D_{\lambda}(E) = \sum_{\zeta s} \frac{|E| - \lambda \zeta s \gamma / 2}{2\pi a^2 t^2} \theta[|E| - \lambda \zeta s \gamma / 2 - \Delta_{\zeta s}]. \quad (6.11)$$

当载流子浓度很低时，可以对公式 (6.2) 在  $\mathbf{K}$  和  $\mathbf{K}'$  点进行较小的展开。在这种情况下，单层二硫化钼的低能量电子能带结构可以写成自由二维电子/空穴气的二维抛物带形式

$$\tilde{E}_{\lambda \mathbf{k}}^{\zeta s} = \lambda \frac{a^2 t^2 \mathbf{k}^2}{2\Delta_{\zeta s}} + \lambda \Delta_{\zeta s} + \frac{\zeta s \gamma}{2}. \quad (6.12)$$

并且二维抛物带模型的态密度 (DOS) 为

$$\tilde{D}_{\lambda}(E) = \sum_{\zeta s} \frac{\Delta_{\zeta s}}{2\pi a^2 t^2} \theta[|E| - \lambda \zeta s \gamma / 2 - \Delta_{\zeta s}]. \quad (6.13)$$

当  $p$ -型单层二硫化钼样品在  $\zeta$  谷的空穴浓度为  $n_{\zeta}^{-} \leq (\Delta - \gamma)\gamma / (2\pi a^2 t^2)$  时，能量较高的价带子带的费米波矢和费米能级为

$$\begin{aligned} [\tilde{k}_{-F}^{\zeta s}]^2 &= 4\pi n_{\lambda}^{\zeta} (\zeta s = 1), \\ \tilde{E}_{-F}^{\zeta} &= -4\pi a^2 t^2 n_{\lambda}^{\zeta} / (\Delta - \gamma) - \Delta / 2 + \gamma. \end{aligned} \quad (6.14)$$

对于其它情况下的  $n$ -型或  $p$ -型掺杂样品，在给定自旋和谷指数的子带中的费米波矢和费米能级可以分别写成

$$\begin{aligned} [\tilde{k}_{\lambda F}^{\zeta s}]^2 &= 2\pi n_{\lambda}^{\zeta} - \zeta s \left[ \frac{2\pi n_{\lambda}^{\zeta} \gamma}{\Delta} - \frac{(\Delta^2 - \gamma^2)\gamma}{a^2 t^2 \Delta} \delta_{\lambda, -1} \right], \\ \tilde{E}_{\lambda F}^{\zeta} &= \lambda \frac{a^2 t^2 [\tilde{k}_{\lambda F}^{\zeta s}]^2}{2\Delta_{\zeta s}} + \lambda \Delta_{\zeta s} + \frac{\zeta s \gamma}{2}. \end{aligned} \quad (6.15)$$

### 6.1.2 光泵浦下准平衡系统

在这项研究中，我们考虑单层二硫化钼对圆偏振泵浦光的光响应。在库仑规范下，左旋 ( $\rho = -$ )/右旋 ( $\rho = +$ ) 圆偏振光场的矢势为<sup>[192]</sup>

$$A_{\nu=\pm}(t) = \frac{F_0}{\sqrt{2}\omega} \sin(\omega t)(\hat{\mathbf{x}} + \rho i\hat{\mathbf{y}}). \quad (6.16)$$

利用一级近似下的微扰理论，在载流子-光子相互作用下导带和价带之间电子跃迁的定态电子跃迁概率可以由费米黄金定律得到并写作

$$\begin{aligned} W_{\rho,\lambda\lambda'}^{ss,\mp}(\mathbf{k}, \mathbf{k}') = & \frac{2\pi}{\hbar} \left( \frac{e at F_0}{\sqrt{2}\hbar\omega} \right)^2 \delta_{\mathbf{k}, \mathbf{k}'} \delta(E_{\lambda'\mathbf{k}'}^{ss} - E_{\lambda\mathbf{k}}^{ss} \mp \hbar\omega) \\ & \times [\cos^4(\vartheta_{\mathbf{k}}^{ss}/2)\delta_{\varsigma\rho, +1} + \sin^4(\vartheta_{\mathbf{k}}^{ss}/2)\delta_{\varsigma\rho, -1}], \end{aligned} \quad (6.17)$$

其中  $\lambda' = -\lambda$ ，德尔塔函数  $\delta_{\varsigma\rho, \pm 1}$  表示了单层二硫化钼在圆偏振光场下光吸收跃迁的谷选择性吸收定律，同时在能量守恒德尔塔函数中的  $\pm$  符号分别表示对能量为  $\hbar\omega$  光子的吸收 (-) 和发射 (+)。

由于单层二硫化钼中有着比光激发载流子寿命更快的导带内的自旋弛豫时间<sup>[160, 174, 193]</sup>，因而这项研究中的光泵浦系统在很短的一段时间之后可以被看作是一个准平衡的系统，其中导带和价带内载流子的分布可以分别近似的由有着导带内电子化学势和价带内空穴化学势的费米-狄拉克函数来描述。在非简并的统计下，各个谷和自旋子系统的玻尔兹曼方程 (BE) 有着如下的形式

$$\frac{\partial f_{\lambda}^{ss}(\mathbf{k})}{\partial t} = \sum_{\mathbf{k}'} F_{\rho}^{ss}(\mathbf{k}, \mathbf{k}') - \frac{f_{\lambda}^{ss}(\mathbf{k}) - f_{\lambda 0}^{ss}(\mathbf{k})}{\tau}, \quad (6.18)$$

其中  $F_{\rho}^{ss}(\mathbf{k}', \mathbf{k}) = [W_{\rho, \lambda'\lambda}^{ss, -}(\mathbf{k}', \mathbf{k}) + W_{\rho, \lambda'\lambda}^{ss, +}(\mathbf{k}', \mathbf{k})][f_{\lambda'}^{ss}(\mathbf{k}') - f_{\lambda}^{ss}(\mathbf{k})]$ ，且  $f_{\lambda}^{ss}(\mathbf{k}) \simeq f_{\lambda}(E_{\lambda\mathbf{k}}^{ss})$  是载流子电子态的动量分布函数同时  $f_{\lambda 0}^{ss}(\mathbf{k})$  表示暗系统中的初始态。

首先，质量平衡方程 (或者速率方程) 可以通过在玻尔兹曼方程两边作用上  $\sum_{s\mathbf{k}}$  得到

$$\frac{\partial n_{+}^{\varsigma}}{\partial t} = \frac{\partial n_{-}^{\varsigma}}{\partial t} = \sum_s G_{\rho}^{ss} - \frac{\Delta n^{\varsigma}}{\tau}, \quad (6.19)$$

其中各个子系统的光生载流子产生率为

$$G_{\rho}^{ss} = \frac{e^2 F_0^2}{32\hbar^2\omega} \left[ 1 + \rho \varsigma \frac{2\Delta_{ss}}{\hbar\omega} \right]^2 \theta(\hbar\omega - 2\Delta_{ss}) \left[ f_{-} \left( \frac{\varsigma s\gamma - \hbar\omega}{2} \right) - f_{+} \left( \frac{\varsigma s\gamma + \hbar\omega}{2} \right) \right], \quad (6.20)$$

$\Delta n^{\varsigma}$  是光激发载流子的浓度， $\tau$  是光激发载流子的寿命并通过实验上的测量得到<sup>[193]</sup>。当系统为定态准平衡态的时候，例如，在  $dn_{+}^{\varsigma}/dt = dn_{-}^{\varsigma}/dt = 0$  时，在  $\varsigma$  谷的质量平衡方程变为

$$\Delta n^{\varsigma} = \tau \sum_s G_{\rho}^{ss}. \quad (6.21)$$

当光场作用于单层二硫化钼上时，价带内的电子被激发到导带之中同时产生光激发载流子。与此同时，在各个谷导带/价带内电子/空穴的化学势可以通过如下公式得到

$$n_\lambda^\varsigma = n_{\lambda 0}^\varsigma + \Delta n^\varsigma. \quad (6.22)$$

通过上式也能得到光激发载流子的浓度，这里  $n_{\lambda 0}^\varsigma$  是导带或价带内的初始载流子浓度。

与此同时，光激发下单层二硫化钼的光电导也可以通过下式得到

$$\begin{aligned} \sigma_\rho^{\varsigma s}(\omega) &= \frac{2\hbar\omega G_\rho^{\varsigma s}}{F_0^2} = \frac{e^2}{16\hbar} \left[ 1 + \varsigma\rho \frac{2\Delta_{\varsigma s}}{\hbar\omega} \right]^2 \theta(\hbar\omega - 2\Delta_{\varsigma s}) \\ &\times \left[ f_- \left( \frac{\varsigma s\gamma - \hbar\omega}{2} \right) - f_+ \left( \frac{\varsigma s\gamma + \hbar\omega}{2} \right) \right], \end{aligned} \quad (6.23)$$

同时我们定义系统对偏振方向为  $\rho$  的圆偏振光的谷相关吸收度 (valley-dependent absorption, VA) 为

$$P_\rho(\omega) = \frac{\sum_s [\sigma_\rho^{+s}(\omega) - \sigma_\rho^{-s}(\omega)]}{\sum_s [\sigma_\rho^{+s}(\omega) + \sigma_\rho^{-s}(\omega)]}. \quad (6.24)$$

这项物理量描述了在圆偏振光下  $\mathbf{K}$  和  $\mathbf{K}'$  谷中光吸收 (或光激发载流子浓度) 的差异。

### 6.1.3 无规则相近似 (RPA) 下的极化函数和等离激元

在这一节中，我们建立了计算多组份系统等离激元的理论框架。我们在无规则相近似下开展我们的研究。当电子/空穴气系统的自旋或者谷简并被打破之后，这时的系统可以看作是一个多组份的系统。对于一个多组份系统，相互作用电子气的组份/密度可分辨的响应函数  $\Pi^{i,i'}(\mathbf{q}, \omega)$  可以通过无规则相近似由如下矩阵方程得到<sup>[6, 189]</sup>:

$$[\Pi^{i,i'}(\mathbf{q}, \omega)]^{-1} = \{\Pi^i(\mathbf{q}, \omega)\}^{-1} \delta_{i,i'} - v_q, \quad (6.25)$$

其中  $\Pi^i(\mathbf{q}, \omega)$  是无相互作用下第  $i$ -个组份系统的响应函数， $v_q = e^2/(2\epsilon_r\epsilon_0 q)$  是裸库仑势相互作用的傅里叶变换， $\epsilon_r = 5$  是单层二硫化钼系统的背景介电常数<sup>[129, 191]</sup>。在无规则相近似下总的密度-密度关联函数可以写作

$$\Pi^{\text{RPA}}(\mathbf{q}, \omega) = \sum_{ii'} \Pi_{i,i'} = \sum_i \Pi^i(\mathbf{q}, \omega)/\epsilon_{\text{RPA}}(\mathbf{q}, \omega), \quad (6.26)$$

其中 RPA 介电函数被定义为

$$\epsilon_{\text{RPA}}(\mathbf{q}, \omega) = 1 - v_q \sum_i \Pi^i(\mathbf{q}, \omega). \quad (6.27)$$

在无规则相近似下等离激元可以通过求解介电函数  $\epsilon_{\text{RPA}}(\mathbf{q}, \omega(q) - i\eta)$  为零的根得到，其中  $\omega(q)$  是等离激元频率且  $\eta$  是等离激元衰减率<sup>[184]</sup>。通常来讲，等离激元可以

近似的通过介电函数的实部为零得到  $\text{Re}[\epsilon_{\text{RPA}}(\mathbf{q}, \omega)] = 0$ <sup>[185, 186]</sup>, 同时也需要在能量损失函数  $\text{Los}(\mathbf{q}, \omega) = -\text{Im}[\epsilon_{\text{RPA}}]^{-1}$  中观看到共振吸收峰。能量损失函数可以通过电子能量损失谱 (Electron energy loss spectroscopy, EELS) 来测量<sup>[194]</sup>。弱阻尼等离激元的衰减率 (等离激元寿命的倒数) 为

$$\eta = \frac{\text{Im}[\Pi(\mathbf{q}, \omega(q))]}{\{(\partial/\partial\omega)\text{Re}[\Pi(\mathbf{q}, \omega)]\}_{\omega=\omega(q)}}. \quad (6.28)$$

在无阻尼等离激元模式附近的动态 RPA 极化函数的虚部可以写成<sup>[6, 185]</sup>

$$\text{Im}[\Pi^{\text{RPA}}(\mathbf{q}, \omega(q))] = -O(\omega(q))\delta(\omega - \omega(q)), \quad (6.29)$$

同时无阻尼等离激元的振荡强度被定义为

$$O(\omega(q)) = \frac{-\pi}{v_q} \frac{\text{Re}[\Pi(\mathbf{q}, \omega(q))]}{\{(\partial/\partial\omega)\text{Re}[\Pi(\mathbf{q}, \omega)]\}_{\omega=\omega(q)}}. \quad (6.30)$$

我们用吸收谱函数  $A(\mathbf{q}, \omega) = -\text{Im}[\Pi^{\text{RPA}}(\mathbf{q}, \omega)]$ <sup>[191]</sup> 的强度来定义在粒子-空穴激发区 ( $\text{Im}[\Pi(\mathbf{q}, \omega)] \neq 0$ ) 内阻尼振荡等离激元模式的振荡强度。

对于无阻尼和有阻尼的等离激元模式，各个组份的等离激元振荡强度  $N(i)$  可以通过计算矩阵公式 (6.25) 实部的本征模式<sup>[189]</sup> 得到

$$[\{\text{Re}[\Pi^i(\mathbf{q}, \omega(q))]\}]^{-1}\delta_{i,i'} - v_q]N(i) = 0, \quad (6.31)$$

通过上述公式我们可以得到不同组份等离激元振荡强度的比例关系

$$N(i)/N(i') = \text{Re}[\Pi^i(\mathbf{q}, \omega(q))]/\text{Re}[\Pi^{i'}(\mathbf{q}, \omega(q))]. \quad (6.32)$$

我们现在来计算各个组份系统无相互作用的关联函数  $\Pi^i(\mathbf{q}, \omega)$ 。我用用自旋和谷指教来代表各个组份系统，例如  $i = \varsigma, s$ , 并且可以得到

$$\Pi^{\varsigma s}(\mathbf{q}, \omega) = \sum_{\lambda\lambda'\mathbf{k}} \frac{f(E_{\lambda\mathbf{k}}^{\varsigma s}) - f(E_{\lambda'\mathbf{k}+\mathbf{q}}^{\varsigma s})}{\hbar\omega + E_{\lambda\mathbf{k}}^{\varsigma s} - E_{\lambda'\mathbf{k}+\mathbf{q}}^{\varsigma s} + i\delta} C_{\lambda\mathbf{k}, \lambda'\mathbf{k}+\mathbf{q}}^{\varsigma s}, \quad (6.33)$$

其中形状因子

$$C_{\lambda\mathbf{k}, \lambda'\mathbf{k}+\mathbf{q}}^{\varsigma s} = \frac{1}{2} \left[ 1 + \lambda\lambda' \frac{\Delta_{\varsigma s}^2 + a^2 t^2 \mathbf{k}(\mathbf{k} + \mathbf{q})}{\Lambda^{\varsigma s}(\mathbf{k})\Lambda^{\varsigma s}(\mathbf{k} + \mathbf{q})} \right], \quad (6.34)$$

其中  $\varphi$  是  $\mathbf{k}$  和  $\mathbf{k} + \mathbf{q}$  之间的夹角且  $\cos\varphi = (k + q \cos\theta)/|\mathbf{k} + \mathbf{q}|$ ,  $\theta$  是  $\mathbf{k}$  和  $\mathbf{q}$  之间的夹角,  $f(E_{\lambda\mathbf{k}}^{\varsigma s}) = f_\lambda(E_{\lambda\mathbf{k}}^{\varsigma s})$  是电子的费米-狄拉克分布函数。

在长波极限 ( $\mathbf{q} \rightarrow 0$ ) 和低温极限 ( $T \rightarrow 0$  K) 下, 我们可以将公式 (6.34) 展开到  $q$  的二次项:

$$C_{\lambda\mathbf{k}, \lambda'\mathbf{k}+\mathbf{q}}^{\varsigma s} \simeq \delta_{\lambda, \lambda'} - \lambda\lambda' \sin^2(\vartheta_{\mathbf{k}}^{\varsigma s})q^2 \sin^2\theta/(4k^2). \quad (6.35)$$

对于带内跃迁 ( $\lambda' = \lambda$ ), 公式 (6.33) 中的 Lindhard 比值展开到  $q$  的二次项的结果为

$$\frac{f(E_{\lambda\mathbf{k}}^{\zeta s}) - f(E_{\lambda\mathbf{k}+\mathbf{q}}^{\zeta s})}{\hbar\omega + E_{\lambda\mathbf{k}}^{\zeta s} - E_{\lambda\mathbf{k}+\mathbf{q}}^{\zeta s}} = q \cos \theta \delta(E_{\lambda\mathbf{k}}^{\zeta s} - E_{\lambda\text{F}}^{\zeta}) \frac{\partial E_{\lambda\mathbf{k}}^{\zeta s}}{\partial k} \\ \times \left( \frac{1}{\hbar\omega} + \frac{q \cos \theta}{\hbar^2 \omega^2} \frac{\partial E_{\lambda\mathbf{k}}^{\zeta s}}{\partial k} \right), \quad (6.36)$$

因为在长波极限下  $C_{\lambda\mathbf{k}, \lambda'\mathbf{k}+\mathbf{q}}^{\zeta s} \simeq 1$ , 我们可以得到带内跃迁极化函数的实部为

$$\text{Re}[\Pi_{\text{intra}}(\mathbf{q}, \omega)] = \frac{q^2}{4\pi\hbar^2\omega^2} \sum_{\lambda\zeta s} (u_{\zeta s}^\lambda - \Delta_{\zeta s}^2/u_{\zeta s}^\lambda) \theta(u_{\zeta s}^\lambda - \Delta_{\zeta s}), \quad (6.37)$$

这里  $u_{\zeta s}^\lambda = |E_{\lambda\text{F}}^{\zeta}| - \lambda\zeta s\gamma/2$  其中  $E_{\lambda\text{F}}^{\zeta}$  是导带中电子 ( $\lambda = 1$ ) 或价带中空穴 ( $\lambda = -1$ ) 的费米能级。

对于带间跃迁 ( $\lambda' = -\lambda$ ), 极化函数的实部在  $q$  的二次项展开下为

$$\text{Re}[\Pi_{\text{inter}}(\mathbf{q}, \omega)] = \frac{-q^2}{32\pi\hbar\omega} \sum_{\lambda\zeta s} \ln \left| \frac{\hbar\omega + 2u_{\zeta s}^\lambda}{\hbar\omega - 2u_{\zeta s}^\lambda} \right| \theta(u_{\zeta s}^\lambda - \Delta_{\zeta s}). \quad (6.38)$$

这项在等离激元存在的低频区域通常对整个极化函数的贡献很小。

在对极化函数进行小  $q$  展开后并忽略掉对数项的修正, 可以得到单层二硫化钼的电荷等离激元色散关系为

$$\omega_0(q) = \left[ e^2 q \sum_{\lambda\zeta s} (u_{\zeta s}^\lambda - \Delta_{\zeta s}^2/u_{\zeta s}^\lambda) \theta(u_{\zeta s}^\lambda - \Delta_{\zeta s}) / (8\pi\epsilon_r\epsilon_0) \right]^{1/2}. \quad (6.39)$$

在全  $q$  计算下, 系统的极化函数是各个不相关谷和自旋子系统的叠加。这种特性与有带隙石墨烯或硅稀类似<sup>[184-186]</sup>。可以看到极化函数取决于  $u_{\zeta s}^\lambda$  的值, 同时  $u_{\zeta s}^\lambda$  是费米能级在  $\pm\gamma/2$  处的偏移。零温下, 在光泵浦系统中公式 (6.33) 在  $\zeta$  谷自旋为  $s$  子系统的极化函数可以写为

$$\Pi_{T=0}^{\zeta s}(\mathbf{q}, \omega) = \Pi_{0,T=0}^{\zeta s}(\mathbf{q}, \omega) [\tilde{\theta}(\Delta_{\zeta s} - u_{\zeta s}^-) \tilde{\theta}(\Delta_{\zeta s} - u_{\zeta s}^+) \\ - \theta(u_{\zeta s}^- - \Delta_{\zeta s}) \theta(u_{\zeta s}^+ - \Delta_{\zeta s})] \\ + \sum_{\lambda} \Pi_{1,T=0}^{\zeta s \lambda}(\mathbf{q}, \omega) \theta(u_{\zeta s}^\lambda - \Delta_{\zeta s}), \quad (6.40)$$

其中所定义的阶梯函数

$$\tilde{\theta}(x) = \begin{cases} 1, & x \geq 0 \\ 0, & x < 0 \end{cases}, \quad \theta(x) = \begin{cases} 1, & x > 0 \\ 0, & x \leq 0 \end{cases}. \quad (6.41)$$

极化函数在  $(q-\omega)$  平面的具体形式在附录 A 中给出。

在有限温度下, 可以利用如下的等式来表示费米-狄拉克分布函数<sup>[195]</sup>

$$\frac{4k_B T}{e^{(E-\mu)/k_B T} + 1} = \int_{-\infty}^{\infty} \frac{d\mu' \theta(\mu' - E)}{\cosh^2[(\mu' - \mu)/2k_B T]}. \quad (6.42)$$

因而，极化函数可以写成其对应的零温极化函数的积分变换形式<sup>[196]</sup>

$$\begin{aligned} \Pi_T^{\zeta s}(\mathbf{q}, \omega; \mu_+^\zeta, \mu_-^\zeta) &= \int_{\Delta/2}^{\infty} \frac{d\mu' \Pi_{1,T=0}^{\zeta s+}(\mathbf{q}, \omega)|_{E_{+F}^\zeta = \mu'}}{4k_B T \cosh^2[(\mu' - \mu_+^\zeta)/2k_B T]} \\ &+ \int_{-\infty}^C \frac{d\mu' \Pi_{1,T=0}^{\zeta s-}(\mathbf{q}, \omega)|_{E_{-F}^\zeta = \mu'}}{4k_B T \cosh^2[(\mu' - \mu_-^\zeta)/2k_B T]} + \Pi_{0,T=0}^{\zeta s}(\mathbf{q}, \omega) \\ &\times [\mathcal{F}_T(C - \mu_-^\zeta) - \mathcal{F}_T(\Delta/2 - \mu_+^\zeta)], \end{aligned} \quad (6.43)$$

其中  $C = \zeta s \gamma - \Delta/2$  和  $\mathcal{F}_T(x) = (e^{x/k_B T} + 1)^{-1}$ ，且  $\mu_\lambda^\zeta$  是在  $\zeta$  谷导带和价带的化学势并通过公式 (6.4) 求得。

对于在低载流子浓度下的单层二硫化钼系统，我们同样可以用一个自由二维抛物带模型来描述导带和价带中的电子能带结构。单层二硫化钼在二维抛物带模型中的极化函数和等离激元同样在附录 A 中给出。

## 6.2 结果与讨论

在这项研究中，我们考虑在有圆偏振光泵浦下和无圆偏振光泵浦下的  $n$ - 和  $p$ -型单层二硫化钼。我们可以很放心的忽略需要很强外加电场的 Rashba 自旋-轨道耦合效应<sup>[173]</sup>。因此，光场只和波函数的轨道项部分发生耦合而电子在光吸收跃迁过程中的自旋是保持不变的。在这里需要指出的是在第 6.1.2 节中我们讨论的圆偏振光场下光激发载流子浓度的计算只在相对较弱的光泵浦辐射场下有效。而在较高浓度的光泵浦下，光激发载流子的浓度可以通过实验上的数据来追溯<sup>[174]</sup>。在接下来的数值计算中，我们给出了等离激元色散关系、能量损失函数、等离激元衰减率、等离激元振荡强度、吸收谱函数和等离激元振荡比例来了解单层二硫化钼中的等离激元特性。

### 6.2.1 圆偏振光下的光吸收

在图 6.2 中，我们给出了在右旋圆偏振光( $\rho = +$ )泵浦下由不同谷和自旋子系统中电子产生的带间跃迁光电导。相对应的，谷相关的光吸收在图 6.2(b) 给出。这里，电子浓度为  $n_e = 1 \times 10^{12} \text{ cm}^{-2}$ ，假定系统在较低温度  $T = 4 \text{ K}$  下且光激发载流子寿命为  $\tau = 5 \text{ ps}$ <sup>[193]</sup>。图 6.2(a) 表明在右旋圆偏振光场下在  $\mathbf{K}$  谷有着最大的光电导以及光吸收。当右旋圆偏振光的光子能量接近带隙边缘的时候，在  $\mathbf{K}$  谷自旋向上子带中的带间吸收占主导地位而自旋向下子带中的光吸收因为较大的内禀自旋-轨道分裂而被抑制。由于更多的光吸收跃迁成为可能，图 6.2(b) 中的谷相关吸收度随着光子能量的增加而减小。随着光子能量的增加，可以看到在谷相关吸收度曲线中有一个突然的增加，这是因为这时候  $\mathbf{K}$  谷中自旋向下子带系统的带间跃迁开始对光吸收做贡献。当圆偏振光的光子频率在带隙附近时，我们可以得到接近 100% 的谷相关吸收度<sup>[197]</sup>。

在图 6.2(c) 中，我们给出了在给定光电场强度的右旋圆偏振光泵浦下  $\mathbf{K}$  谷中光激发载流子浓度随着光子频率的变化。图 6.2(c) 中的光激发载流子浓度和图 6.2(a) 中  $\mathbf{K}$

谷中自旋上和自旋下子系统的光电导之和成正比关系。图 6.2(d) 给出了在给定光子能量的右旋圆偏振光泵浦下 **K** 谷中光激发载流子浓度随着光场强度的变化。在光子能量  $\hbar\omega = 1.6 \text{ eV}$  的圆偏振光场下，谷相关吸收度可以达到接近 100%。这说明只有 **K** 谷价带中的电子被激发到导带。在相对较弱的光场下，我们可以看到光激发载流子浓度与光场强度成线性关系。而在温度  $T = 180 \text{ K}$  时，载流子浓度和光场强度有着平方根的对应关系。需要注意的是光激发载流子的寿命随着温度的变化而变化<sup>[193]</sup>。从公式 (6.21) 和图 6.2(d) 可以看到在较高温度下能得到较大的光激发载流子浓度。

这些结果表明为了更有效的在单个谷来激发带电荷载流子，应该使用能量在带隙附近的圆偏振泵浦光。这将打破单层二硫化钼的谷简并且使其成为一个多组份的系统。这些系统的等离激元响应将在接下来的讨论中给出。

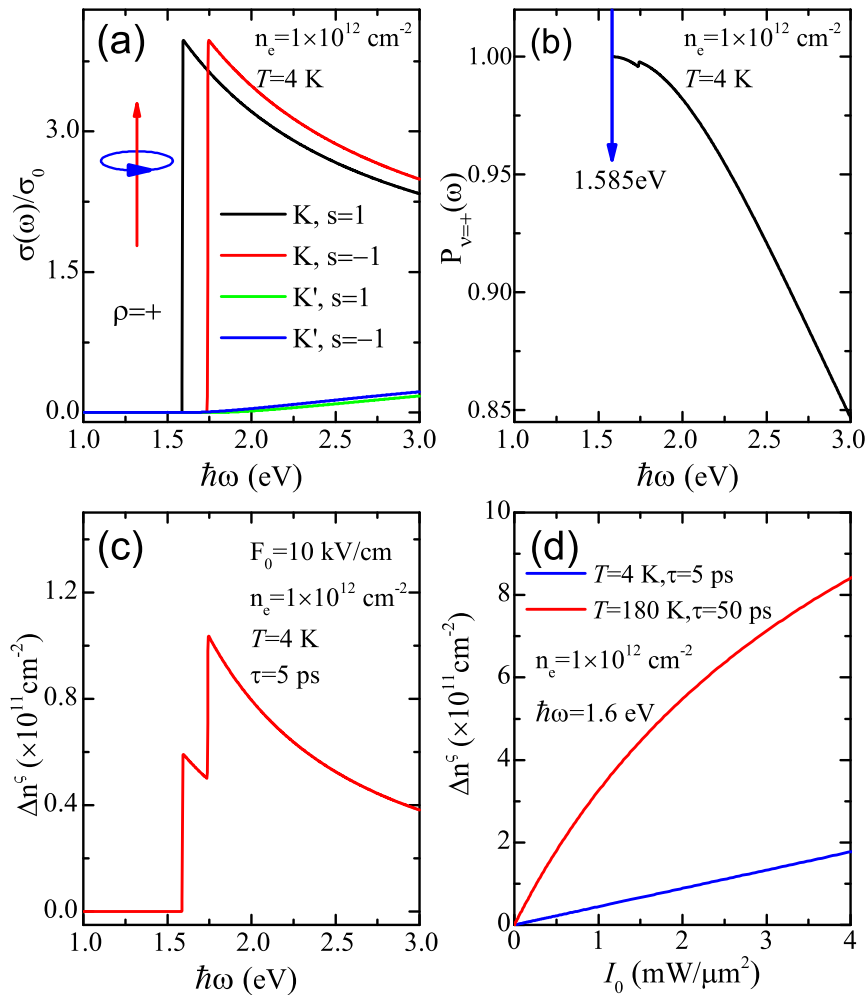


图 6.2: (a) 在右旋 ( $\rho = +1$ ) 圆偏振光场下，单层二硫化钼不同谷和自旋子带系统中带间跃迁光电导  $\sigma_{\rho}^{\zeta s}(\omega)$  和 (b) 单层二硫化钼在右旋圆偏振光辐射下谷相关吸收度随着光子频率的变化曲线。(c) 在右旋圆偏振光场下 **K** 谷的光激发载流子浓度随光子频率的变化。(d) 在给定的光子频率下，右旋圆偏振光场下 **K** 谷光激发载流子浓度随光场强度  $I_0 \sim F_0^2$  的变化。这里， $F_0$  是光场的电场强度

### 6.2.2 有效质量模型和双曲线模型的比较

通常，单层二硫化钼的能带结构可以有效的表示为有质量狄拉克-费米子模型<sup>[125]</sup>。由于单层二硫化钼或者其它过渡金属硫化物有着较大的带隙，当能带中的载流子浓度不是很大的时候，有质量狄拉克-费米子模型的有效能带结构同样能够用二维电子/空穴来描述。两个模型之间的关系在前面的公式 (6.12) 中给出。在这一节中，我们将说明两个模型在描述单层二硫化钼光学响应时是等价的。

在图 6.3 中，我们分别画出了单层二硫化钼在有质量狄拉克-费米子和二维抛物带模型下的电子态密度。在导带/价带的底部/顶部的低能量区域，两个模型的态密度非常接近。随着能量的增加，两个模型的差异性将不断增大。这表明我们可以利用二维抛物带模型来描述低载流子浓度单层二硫化钼的电子结构。

在图 6.4 中，我们比较了由两个模型所给出  $n$ -型单层二硫化钼的等离激元光学性质同时系统的能带结构和载流子分布由图 6.1(a) 所给出。在零温和室温下，我们给出了  $(q-\omega)$  平面上的能量损失函数以及等离激元色散关系，这些模式的等离激元衰减率。这里电子浓度为  $n_e = 1 \times 10^{12} \text{ cm}^{-2}$  且等量的分布在两个谷之间。在图 6.4(a) 和 (e) 中，我们比较了零温下两个模型的能量损失函数。等离激元在长波极限下表现出强烈的吸收曲线。在较大的波矢处，等离激元支进入带内电子-空穴激发区并且造成吸收的增强。需要指出的是两个模型给出了定性上相同的结果并且在定量上也十分接近。

图 6.4(b) 和 (f) 中给出了室温时的能量损失函数。结果表明一定的温度会使等离激元模式减弱并且会抑制在较大能量和波矢区域的集体激发。需要注意这里两个模型在定性和定量上都有着非常接近的结果。

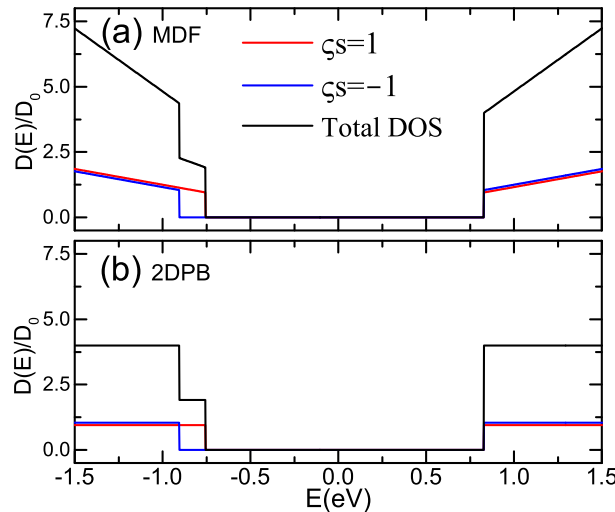


图 6.3: 单层二硫化钼在 (a) 有质量狄拉克-费米子 (massive Dirac fermions; MDF) 模型和 (b) 二维抛物带 (two dimensional parabolic band; 2DPB) 模型中的电子态密度。这里  $D_0 = \Delta/(4\pi a^2 t^2)$

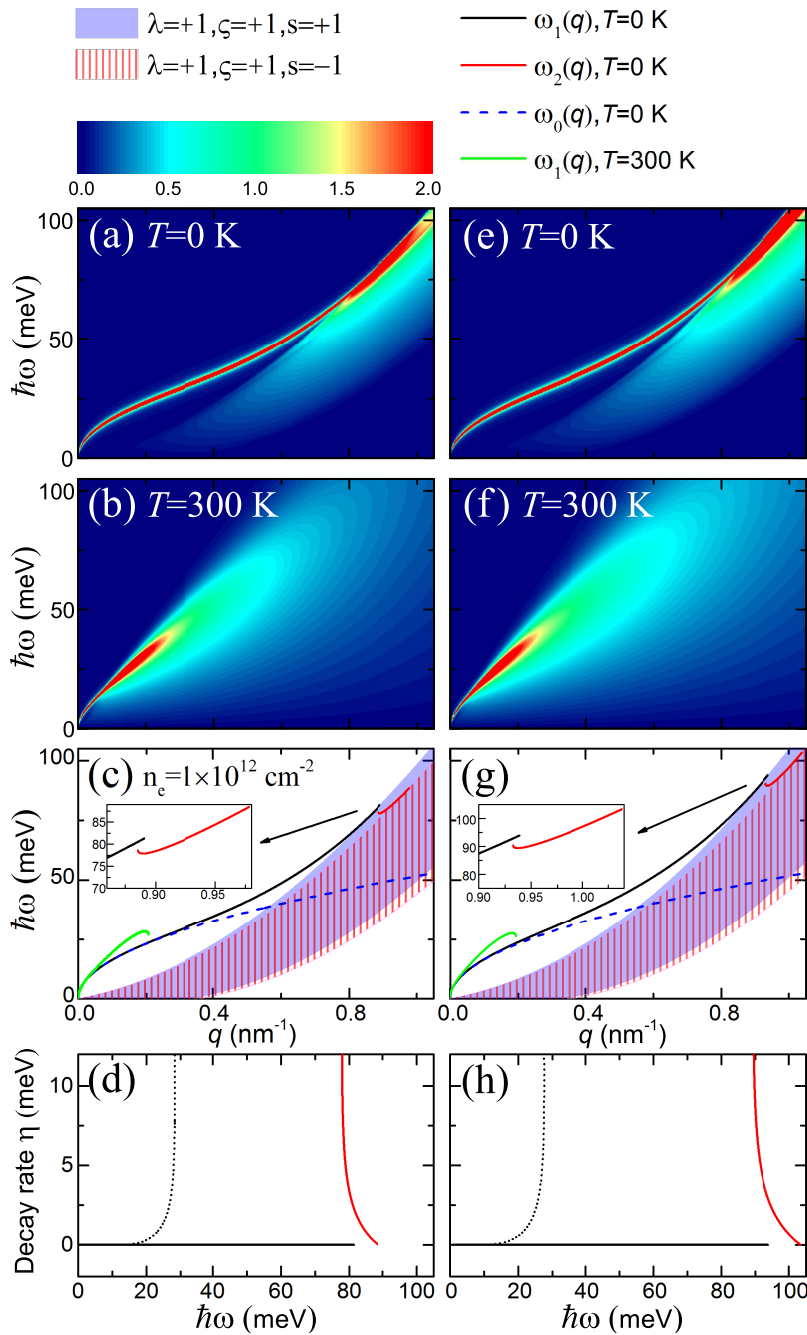


图 6.4: 在 (a)  $T = 0$  K 和 (b)  $T = 300$  K 时  $n$ -型单层二硫化钼在有质量狄拉克-费米子模型下的能量损失函数。等离激元色散关系和等离激元衰减率分别在 (c) 和 (d) 中给出。 (e)-(h) 是 (a)-(e) 中相对应的二维抛物带模型的结果。 (c) 和 (g) 中的内插图是箭头标识的大  $q$  区域的放大。蓝色的虚曲线表示对应的小  $q$  近似下的零温电荷等离激元模式

在图 6.4 中的面板 (c) 和 (g)，我们用实曲线给出了介电函数  $\epsilon_{\text{RPA}}(\mathbf{q}, \omega)$  实部为零的根。黑色的曲线是二维电荷等离激元模式并且与之前面板中的吸收增强线相对应。如蓝色的曲线所示，在长波极限下，这一支等离激元模式与公式 (6.39) 中的  $\sqrt{q}$  型等

离激元模式相吻合。在这些面板中绿色的曲线表示在有限温度下的等离激元模式。结果表明在室温下这只等离激元模式仅仅局限在长波区域。特别值得注意的是，在两个面板中，在  $\mathbf{K}/\mathbf{K}'$  谷中自旋上/自旋下带电粒子所产出的带内电子-空穴激发区内有一支由红色实曲线表示的新型等离激元模式。这个新的模式会导致面板 (a) 和 (e) 中能量损失函数中的吸收增加并且这个模式的出现并不是仅仅因为系统的自旋简并被打开。

在面板 (d) 和 (h) 中我们给出了两个模型下等离激元衰减率随着光子能量的变化关系。在面板底端的黑色曲线对应于普通的电荷等离激元模式。这支模式的等离激元衰减率为零这是因为这支模式处于粒子-空穴激发谱外。而由红色曲线所表示的一支新发现的等离激元模式，是部分朗道阻尼的并且有着一定的等离激元衰减率。需要指出的是这支等离激元的衰减率随着能量的增加而减小，并且和图 6.4 (d) 和 (h) 中绿色曲线所表示的室温下普通电荷等离激元模式的衰减率处在相同数量级。

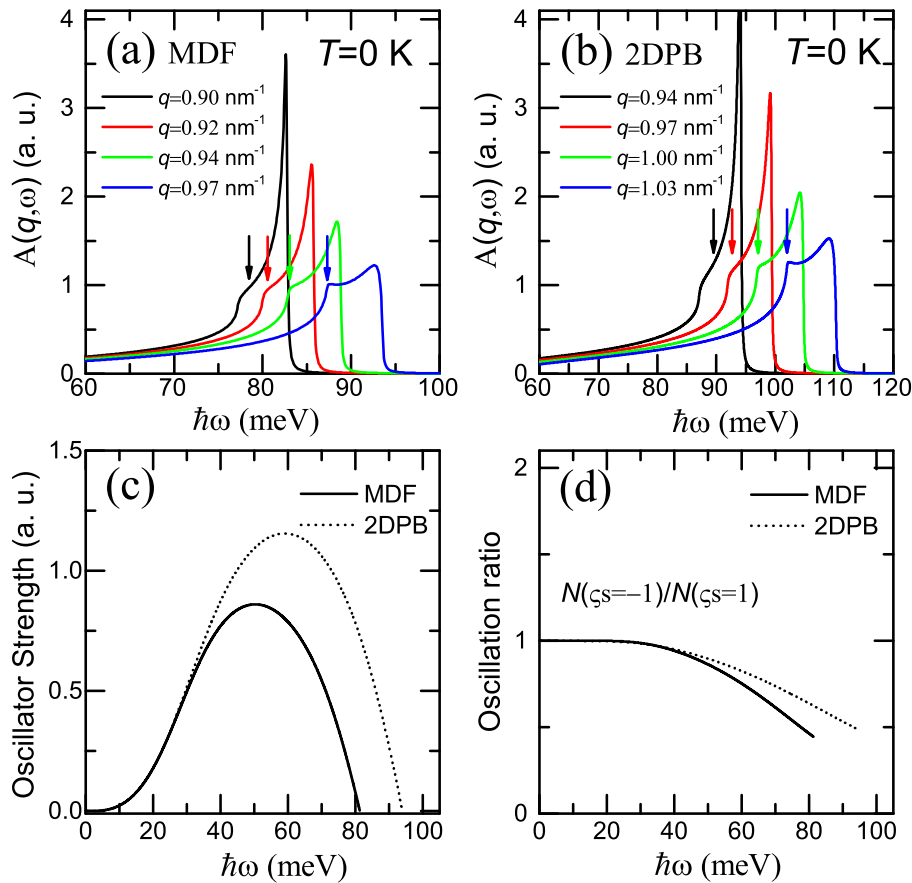


图 6.5: 在与图 6.4 中相同条件下  $n$ -型单层二硫化钼中零温下的吸收谱函数在不同的给定波矢下随着能量的变化。(a) 有质量狄拉克-费米子模型 (MDF) 和 (b) 二维抛物带模型 (2DPB)。(c) 零温下两个模型中无阻尼等离激元的振荡强度。(d)  $n$ -型单层二硫化钼中两种模型下无阻尼等离激元振荡中不同组份的振荡幅度比例。(a)-(b) 中的箭头标明了给定波矢下在带内粒子-空穴激发谱中的第二支等离激元  $\omega_2(q)$  对应的等离激元能量

为了更进一步描述这个新的弱阻尼等离激元模式，在图 6.5 中，我们给出了不同给定波矢下的吸收谱函数  $A(q, \omega)$ 。我们可以看到这支新的等离激元模式出现在吸收谱函数中的肩部并且要和吸收谱函数中粒子-空穴激发谱边缘的峰加以区别。图 6.5 中的 (a) 和 (b) 面板表明有质量狄拉克费米子模型和二维抛物带模型的结果在定性上是相一致的，而在定量上则有一些细微的差异。在分别计算等离激元振荡强度 (图 6.5(c)) 和两个谷中不同组份的等离激元振幅比 (图 6.5(d)) 的时候，这种差异同样会出现。结果表明，在给定的波矢下，二维抛物带模型会高估电荷等离激元的振荡强度和等离激元频率。但是，在定性的特性是相似的。因此，我们可以很放心的使用二维抛物带模型来研究单层二硫化钼的等离激元光子学特性。同时需要记住的是，利用二维抛物带模型所得到的结果可能与实际情况在定量上有着稍微的差异。

### 6.2.3 有限温度下的自旋极化二组份系统

接下来我们将讨论两个组份由不同自旋指数所描述的二组份系统。通过调节费米能级，可以得到如图 6.1(c) 所示的在价带中两个自旋态可分辨的空穴系统。需要注意的是，由于不同谷中价带子带有着相反的自旋取向，因而整个系统没有宏观层面上的自旋不平衡。尽管如此，在单个谷中自旋不平衡仍会对光学和等离激元光子学性质产生影响。这一点将会在接下来的讨论中给出。

图 6.6 给出了固定空穴浓度  $n_h = 5 \times 10^{13} \text{ cm}^{-2}$  三个温度下 MDF 模型  $p$ -型单层二硫化钼的能量损失函数、等离激元色散关系和等离激元衰减率。在各个温度下的能量损失函数和等离激元色散关系表明在小  $q$  区域存在一支电荷等离激元模式。需要指出的是，与上一节中的  $n$ -型系统相比，图 6.6(d) 中的等离激元模式受温度的影响不大。在面板 (e) 中，我们给出了在各个温度下等离激元模式的衰减率并且发现在有限温度下仍有着可观的等离激元寿命，这一点和上一节中的  $n$ -型单层二硫化钼有着很大的区别。

图 6.6(d) 中的等离激元模式同样揭示了在长波极限下的一个额外的特征。在两个自旋劈裂价带子带的带内粒子-空穴激发谱的上边界之间的小  $q$  区域实际存在一个弱阻尼的线性声学等离激元模式。在这个区域，粒子-空穴激发谱函数有着较小的值因而可以预期这只等离激元模式具有一定的稳定性。这支新的声学模式与自旋极化的二维电子气<sup>[189, 190]</sup>中所讨论的情况类似。与之不同的是，我们所讨论的情况中没有宏观上的自旋不平衡。

图 6.7(a) 给出了在图 6.6(d) 中零温下在给定空穴浓度  $n_h = 5 \times 10^{13} \text{ cm}^{-2}$  时  $p$ -型单层二硫化钼的等离激元模式随着波矢变化的色散关系。在图中可以清晰的看到通常的电荷等离激元模式  $\omega_1(q)$  和新发现的声学模式  $\omega_2(q)$ 。图 6.7(b) 给出了在给定的波矢下的吸收谱函数。需要注意的是这支线性声学等离激元模式表现出在粒子-空穴激发谱背景上的吸收峰，因而，可以预期它将没有较明显的等离激元模式  $\omega_1(q)$  那样清晰。在图 6.7(c) 中给出了等离激元模式  $\omega_1(q)$  的振荡强度并表现出与之前相似的性质。

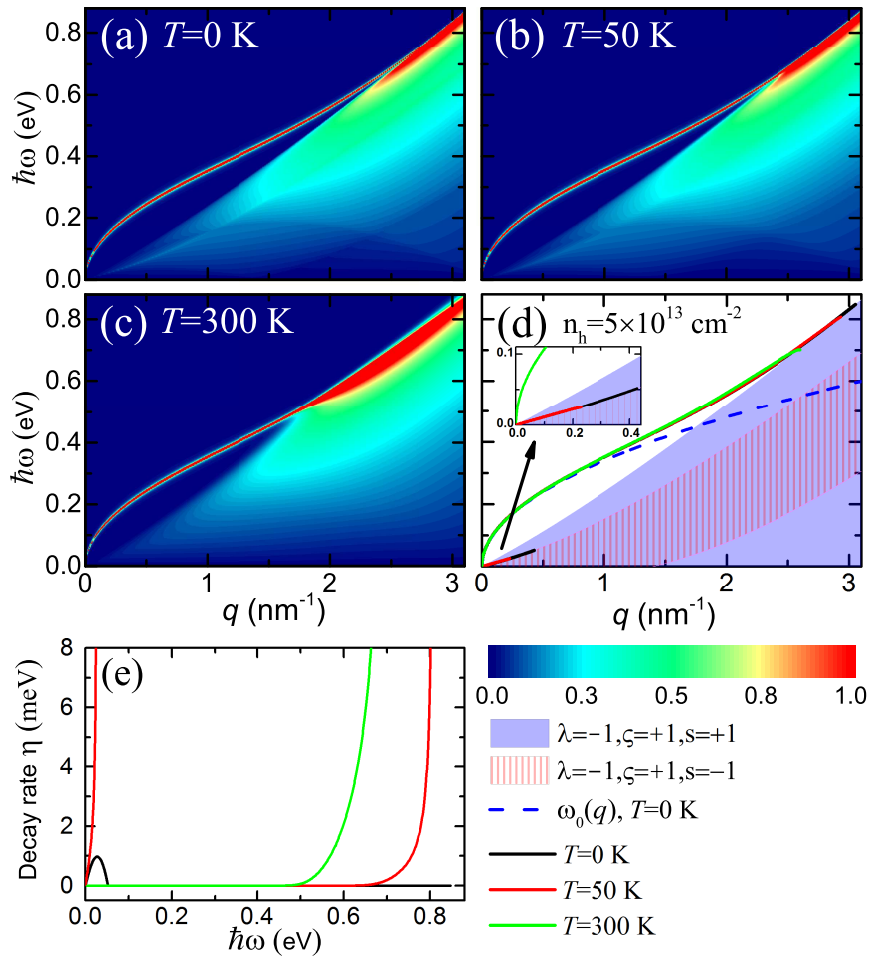


图 6.6: (a)-(c)  $p$ -型掺杂单层二硫化钼在不同温度下  $(q, \omega)$  平面上的能量损失函数。(d) 不同温度下等离激元色散关系随着波矢的变化。(e) 在面板 (d) 中等离激元模式的等离激元衰减率随着等离激元能量的变化。在面板 (d) 中的插图是箭头示意的小  $q$  和  $\omega$  区域的放大

为了弄清楚这支新发现声学等离激元模式的特性，在图 6.7(d) 中给出了在等离激元振荡下两个自旋劈裂组份的振荡振幅比。我们可以看到对于这支红色曲线表示的新模式，两个自旋劈裂组份的振荡强度在长波极限时趋于  $-1$ 。这表明两个自旋劈裂组份有着相反的振荡相。因此，这支等离激元模式即是之前已经被定义的自旋等离激元<sup>[189]</sup>。由于各个自旋组份的载流子密度振荡是反相的，因而这支模式是近乎电中性的。在图 6.7(d) 中  $\omega_1(q)$  模式在较小的能量下自旋组份表现出同相的振荡。随着能量的增加进而转变成反相的振荡。在这个转变的交叉点，自旋能量较低子带中空穴液体的振幅为零。因而此时等离激元模式是自旋极化的。

#### 6.2.4 自旋极化的三组份系统

在图 6.8 中，我们给出了零温下未掺杂单层二硫化钼在右旋圆偏振光泵浦下光激发载流子浓度为  $\Delta n^+ = 5 \times 10^{11} \text{ cm}^{-2}$  时的等离激元特性。能带结构的示意图和载流子占

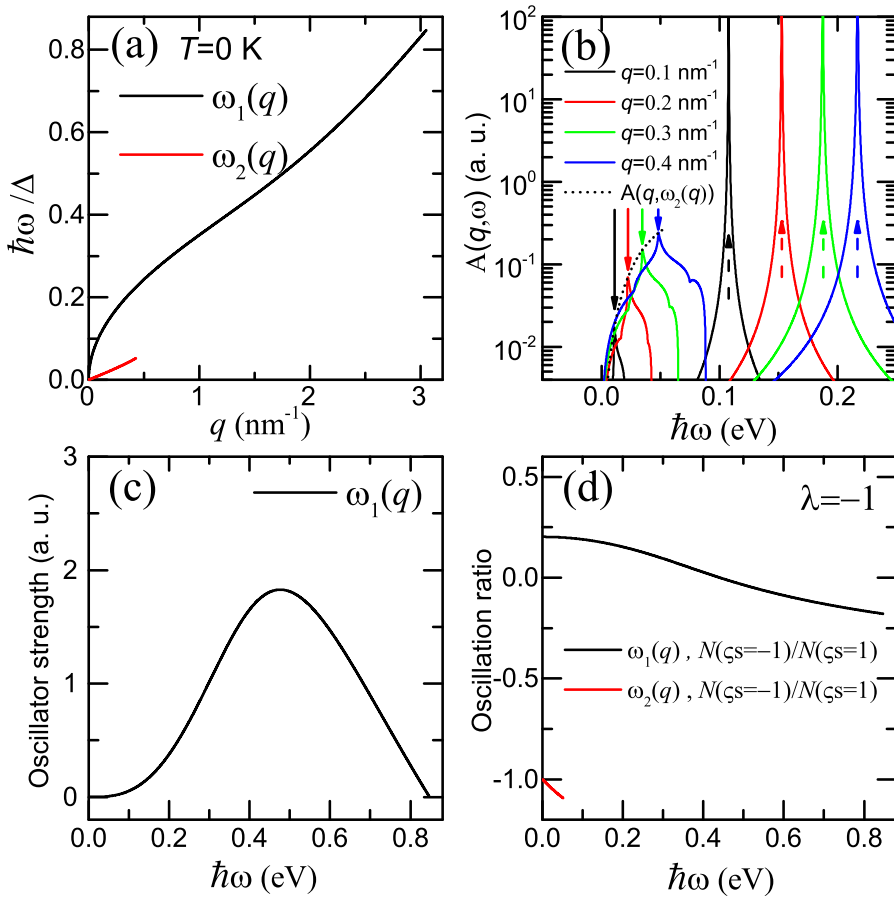


图 6.7: (a) 图 6.6(d) 中  $p$ -型单层二硫化钼在温度  $T = 0$  K 时等离激元随着波矢变化的色散关系。(b) 在给定波矢下的吸收谱函数随着能量  $\omega$  的变化和线性声学等离激元模式  $\omega_2(q)$  的吸收谱函数  $A(q, \omega_2(q))$  (虚曲线)。实线箭头和短划线箭头分别对应给定波矢下弱阻尼线性声学等离激元模式和无阻尼电荷等离激元模式的能量。(c) 无阻尼等离激元模式  $\omega_1(q)$  的等离激元振荡强度。(d) 两个等离激元模式振荡中自旋劈裂两个组份的等离激元振荡振幅比

据情况在图 6.1(d) 中给出。在这个系统中, 由于谷相关的光生载流子激发, 自由载流子仅存在于  $\mathbf{K}$  谷。而在  $\mathbf{K}'$  谷由于没有自由载流子存在, 因而等离激元不能在此处传播。

这个系统可以被看作是一个三组份的系统。由于只有一个自旋价带被光激发, 因而只产生一个空穴液体。但是在导带中有着非常快的自旋弛豫, 因而两个自旋子带都被占据。这将产生两个独立的自由载流子液体。对于这个系统中, 在  $(q-\omega)$  平面的能量损失函数在图 6.8(a) 中给出。同时, 等离激元色散关系随着波矢  $q$  的变化在图 6.8(b) 中给出。在图 6.8(a) 中可以清晰看到的等离激元支对应于无阻尼的电荷等离激元模式。从图 6.8(b) 中我们可以看到在三个子系统带内粒子-空穴激发谱上边界分隔的三个区域内存在三支等离激元模式。额外出现的等离激元模式会造成这些区域内能量损失的增加。图 6.8(c) 中给出了对应的等离激元衰减率并且可以看到新型等离激元模式确实存

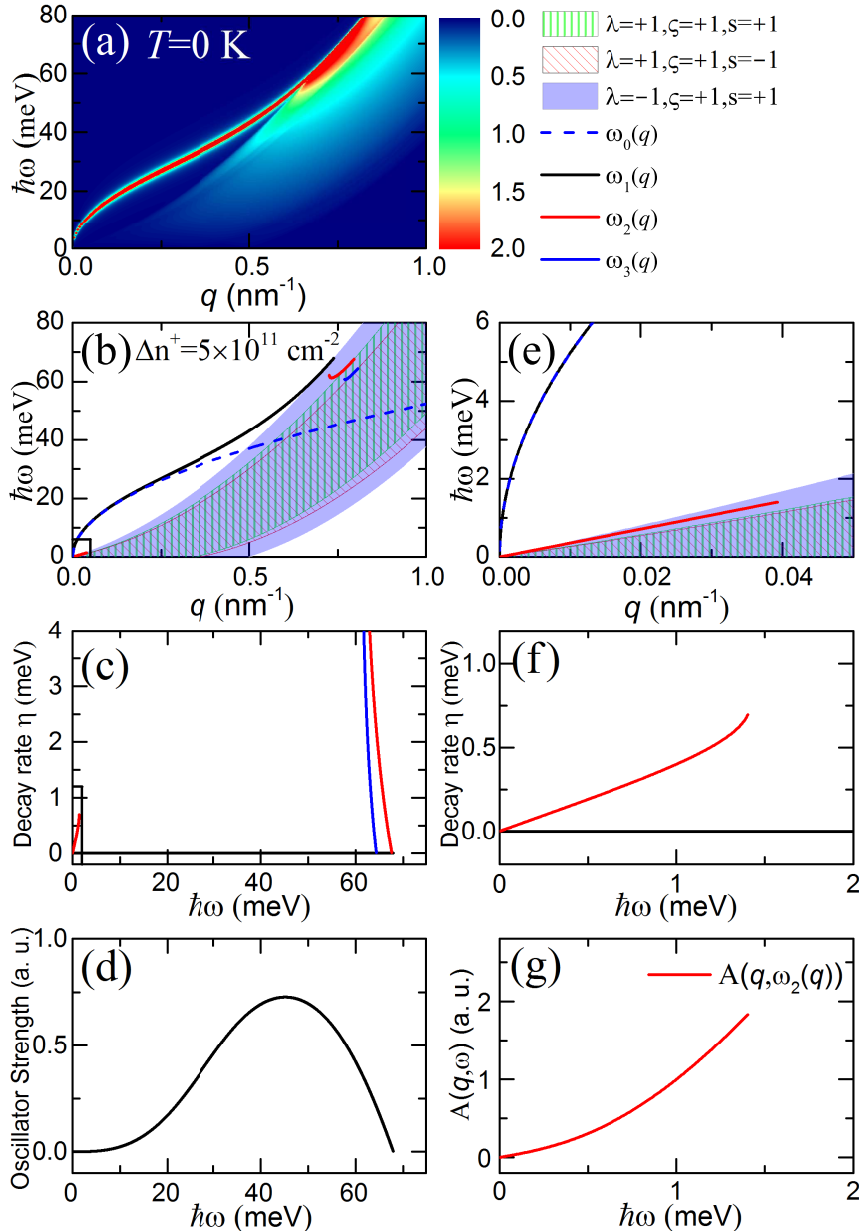


图 6.8: 未掺杂单层二硫化钼在右旋圆偏振光泵浦下光激发载流子浓度为  $\Delta n^+ = 5 \times 10^{11} \text{ cm}^{-2}$  时的 (a) 能量损失函数和 (b) 等离激元色散关系随着波矢的变化。 (c) 对应的等离激元衰减率随着等离激元能量的变化。 (e)-(f) 是 (b)-(c) 中黑色方框区域的放大。 (d) 无阻尼等离激元模式  $\omega_1(q)$  振荡强度随等离激元能量的变化。 (g) 弱阻尼线性声学等离激元模式  $\omega_2(q)$  的吸收谱函数

在有限的寿命。对于无阻尼的电荷等离激元模式  $\omega_1(q)$ ，其等离激元衰减率为零。

在小  $q$  区域，存在一个弱衰减的线性声学等离激元模式  $\omega_2(q)$ 。为了更好的看到这个模式，图 6.8(e)-(f) 是图 6.8(b)-(c) 中黑色方框内小  $q$  区域的放大。通过图 6.8(d)，可以看到等离激元模式  $\omega_1(q)$  的衰减率也是先增大然后减小到零。对于在小  $q$  区域的弱阻尼的线性声学等离激元模式  $\omega_2(q)$ ，其等离激元衰减率和其吸收谱函数随着等离激元能量的增加而增加。

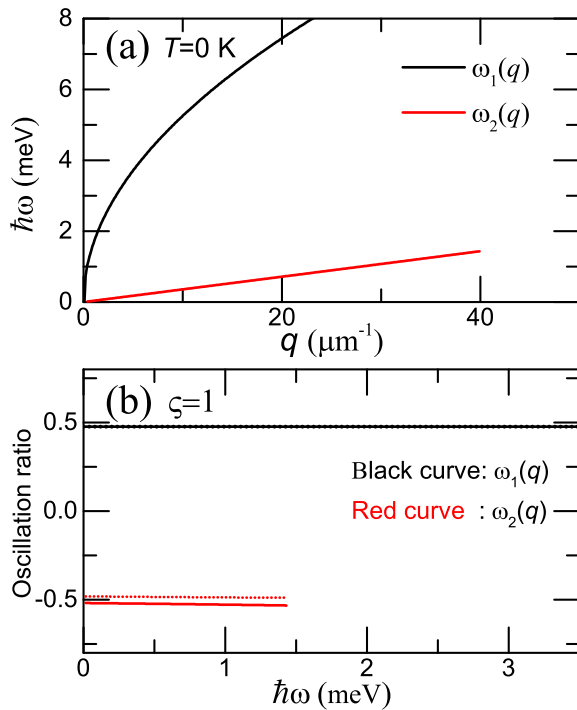


图 6.9: (a) 二维抛物带模型下，在右旋圆偏振光泵浦下且光激发载流子浓度为  $\Delta n^+ = 5 \times 10^{11} \text{ cm}^{-2}$  时未掺杂单层二硫化钼系统的等离激元色散关系。 (b) 在  $\mathbf{K}$  谷自旋向上导带子带和在  $\mathbf{K}$  谷自旋向上价带子带的等离激元振荡振幅比 (实曲线) 和在  $\mathbf{K}$  谷自旋向下导带子带和在  $\mathbf{K}$  谷自旋向上价带子带的等离激元振荡振幅比 (短划线)。黑色和红色的曲线分别对应等离激元模式  $\omega_1(q)$  和  $\omega_2(q)$  的结果

在第 6.1.3 节中，我们所得到的在各个谷和自旋子系统在有质量狄拉克-费米子模型下的极化函数同时包含导带和价带内的带内跃迁以及导带和价带之间的带间跃迁。因此，对于光泵浦系统在 MDF 模型下的极化函数，我们不能直接用公式 (6.32) 来计算不同子带组份的等离激元振荡振幅比。取而代之，我们用二维抛物带模型来描述这个系统。

图 6.9 中，我们给出了与图 6.8 相对应的在 2DPB 模型下小  $q$  区域的等离激元色散关系和等离激元振荡振幅比例。通过二维抛物带模型，我们可以计算我们所考虑的三组份系统中三个不同组份的振荡振幅。在图 6.9(b) 中，我们给出了这些振荡振幅比随着光子频率的变化关系。在计算中，等离激元振荡振幅通过和价带组份的振荡幅度进行对照来得到。对于无阻尼等离激元模式  $\omega_1(q)$ ，在  $\mathbf{K}$  谷中，导带中自旋上和自旋下的组份和价带中自旋上的组份有着同相的振荡振幅。两个电子组份系统有着相同大小的振荡振幅。对于线性的等离激元模式  $\omega_2(q)$ ，导带和价带的等离激元振荡振幅比是负的因而这个模式的振荡是反相的。在小  $q$  极限下，等离激元模式  $\omega_2(q)$  在导带自旋上和自旋下子带的等离激元振荡振幅比例之和为  $-1$ 。这意味着两个电子组份系统的振荡振幅是近似相等的，但是与空穴的振荡振幅是反相的。这种类型的反相振荡特性在自旋

极化二维电子系统中得到过<sup>[189]</sup>。此时，这个弱阻尼的线性等离激元模式不是电中性的。这是由于这里的反相振荡是发生在电子和空穴构成的相反电荷液体之间。

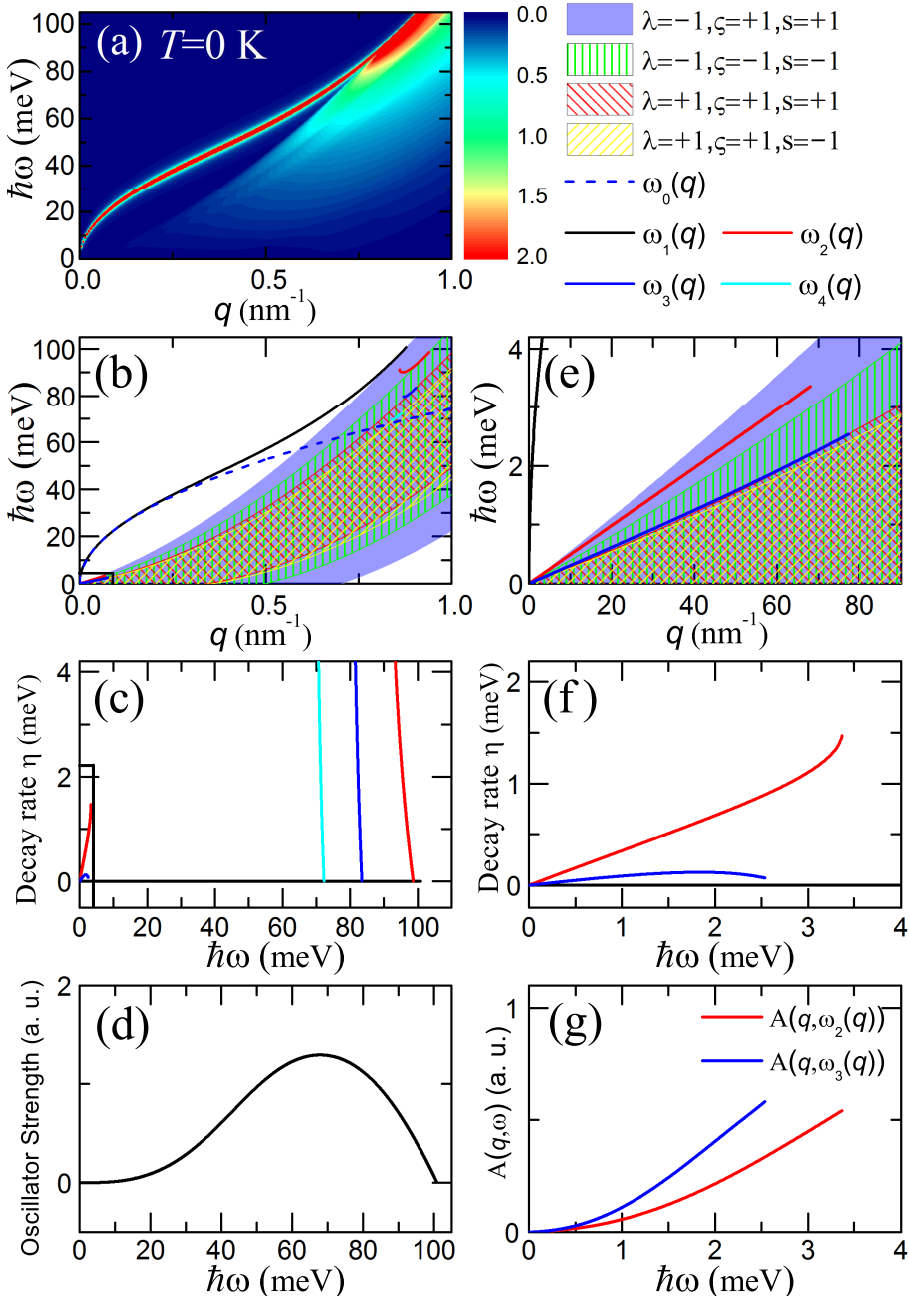


图 6.10: 在右旋圆偏振光泵浦下  $p$ -型单层二硫化钼在初始空穴浓度  $n_h = 1 \times 10^{12} \text{ cm}^{-2}$  和光激发载流子浓度  $\Delta n^+ = 5 \times 10^{11} \text{ cm}^{-2}$  下的 (a) 能量损失函数和 (b) 等离激元随着波矢的变化。 (c) 相对应的等离激元衰减率随着能量的变化。 (e) 和 (f) 是 (b) 和 (c) 中黑色方框区域的放大。 (d) 无阻尼等离激元模式  $\omega_1(q)$  的等离激元振荡强度随着能量的变化。 (g) 两支弱阻尼线性声学等离激元模式的吸收谱函数

### 6.2.5 四组份系统

最后我们来分析和讨论一个四组份系统。如图 6.1(e) 所示，这样一个系统可以通过光泵浦一个  $p$ -型的单层二硫化钼产生。这将激发电子到单个谷中的导带。由于自旋弛豫的时间非常小<sup>[160, 174]</sup>，所构建的准平衡系统包含在一个谷内有着同一个费米能级两种自旋态的电子袋和在两个谷有着不同费米能级的两个空穴袋。

我们假定一个有着初始空穴浓度  $n_h = 1 \times 10^{12} \text{ cm}^{-2}$  的  $p$ -型单层二硫化钼在右旋圆偏振光泵浦激发下光激发载流子浓度为  $\Delta n^+ = 5 \times 10^{11} \text{ cm}^{-2}$ 。图 6.10(b) 中能量损失函数中的红色极点分支对应于之前系统中的无阻尼的电荷等离激元模式  $\omega_1(q)$ 。从图 6.10(b) 和 (e) 可以看到系统在较大的光子能量下存在三支新的等离激元模式，而在长波极限下存在两支新的声学等离激元模式。和之前所讨论的一样，这些新的等离激元模式处于带内粒子-空穴激发区内并且其中只有一部分的组份系统对应于朗道阻尼。对朗道阻尼重要性的量化由面板 (c) 和 (f) 中的衰减率来给出。从中可以看到即使是处在带内电子-空穴激发区的更深处，声学等离激元模式  $\omega_3(q)$  仍比声学等离激元模式  $\omega_2(q)$  更加稳定。此外，如面板 (g) 所示， $\omega_3(q)$  的等离激元吸收谱函数强度比  $\omega_2(q)$

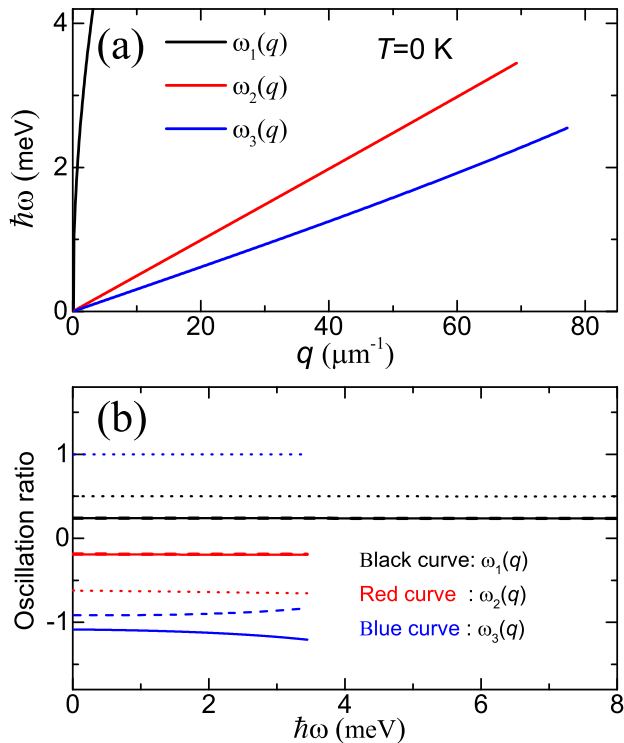


图 6.11: (a) 零温时在 2DPB 模型下右旋圆偏振光泵浦下  $p$ -型单层二硫化钼初始空穴浓度为  $n_h = 1 \times 10^{12} \text{ cm}^{-2}$  同时光激发载流子浓度  $\Delta n^+ = 5 \times 10^{11} \text{ cm}^{-2}$  时系统的等离激元色散关系。(b) 在  $\mathbf{K}$  谷自旋上导带子带和自旋上价带子带的振荡振幅比 (实线)，在  $\mathbf{K}$  谷自旋下导带子带和自旋上价带子带的振荡振幅比 (短划线) 和在  $\mathbf{K}'$  谷自旋下导带子带和在  $\mathbf{K}$  谷自旋上价带子带的振荡振幅比 (虚线)。黑色，红色和蓝色的曲线分别对应等离激元模式  $\omega_1(q)$ ,  $\omega_2(q)$  和  $\omega_3(q)$

更加明显。因而前者可以被认为更加容易被激发。最后，由于在带内粒子-空穴激发区内存在新的模式，图 6.10(d) 中等离激元模式  $\omega_1(q)$  的等离激元振荡强度与之前几种情况没有明显的定性上的差异。这意味着这些新模式是由带内粒子激发区中谱权重的重新分布所导致，而不是从通常的这支等离激元模式中获得。

在图 6.11 中，我们画出了前一个图中讨论的光泵浦下  $p$ -型掺杂单层二硫化钼在长波极限区域的等离激元色散关系和不同组份的等离激元振荡振幅比。得到的结果是通过二维抛物带模型计算得到。我们发现面板 (a) 中长波极限下的等离激元模式和之前的结果相一致。

在面板 (b) 中我们计算了三个等离激元模式中不同组份系统的等离激元振荡振幅比。实曲线代表在  $\mathbf{K}$  谷自旋上电子袋和自旋上空穴袋的等离激元振荡振幅比。从中可以看到， $\omega_1(q)$  模式由同相振荡构成，而另外两种模式的等离激元振荡是反相的。面板内的短划线代表在  $\mathbf{K}$  谷内自旋下电子袋和自旋上空穴带之间的等离激元振荡振幅比。对于这个的结果，我们发现与前面相似的结果， $\omega_1(q)$  模式同相振荡而  $\omega_2(q)$  和  $\omega_3(q)$  模式则是反相振荡的。需要注意的是，由于我们考虑的是电荷相反的电荷粒子的密度振荡，同相振荡的等离激元模式抵消了各自的电荷振荡。最后图中的虚线表示两个谷间空穴袋之间的等离激元振荡振幅比。需要注意的是， $\omega_3(q)$  模式是完全的同相振荡而且两个组份的振荡幅度在这种情况下是相同的。与之前一样， $\omega_1(q)$  模式是同相振荡，同时  $\omega_2(q)$  模式是反相振荡。

### 6.3 本章小结

在这项研究中，我们研究了多组份系统的等离激元特性。我们采用圆偏振光场下的单层二硫化钼系统作为研究平台。我们发现这个系统能够支持多组份的等离激元模式同时我们也在玻尔兹曼方程的框架下量化的给出了圆偏振光泵浦光所产生的影响。

我们发现所有的平台系统都能支持在零温时长波极限下的  $\sqrt{q}$  等离激元模式支。由于载流子浓度的关系，随着温度的增加，我们发现电子掺杂的系统内的等离激元模式受到较强的影响而空穴掺杂的系统则更加稳定。

多组份系统对等离激元特性最主要的影响是新的等离激元模式的产生并且这些新模式是部分阻尼的。我们发现对于一个  $n$  组份系统， $n - 1$  个等离激元模式将会出现。这些新出现的模式在长波极限下表现出有着线性色散关系的声学模式并且它们处在带内粒子-空穴激发区内较小的限制区域内。为了了解它们的稳定性，我们计算了各个等离激元模式的衰减率并且发现即使它们处于带内粒子激发区，它们的寿命仍然是可观的。对于较大的波矢，我们发现多组份系统同样支持新的等离激元模式且其中只有部分的组份系统对应与集体振荡中的朗道阻尼。

我们通过计算集体密度振荡中不同组份系统的振幅比来了解新型等离激元模式的性质。我们发现通常的  $\sqrt{q}$ -模式的振荡是同相的，而对于其它新的声学模式，反相的

振荡则变得可能。最后，我们给出了吸收谱函数并展示了如何来表征这些声学等离激元模式。

单层二硫化钼等离激元模式的特征能量范围不仅包含红外区域也包含太赫兹频段，尤其是低能量的弱阻尼线性声学等离激元模式。这些性质使得单层二硫化钼成为可以应用在红外和太赫兹区域等离激元光子学极具前景的材料平台。本项理论研究能够帮助指引实验上寻找单层二硫化钼系统中的新型等离激元模式。

This chapter corresponds to the preprint “Multi-component plasmons in monolayer MoS<sub>2</sub> with circularly polarized optical pumping” in Appendix D.



# 第七章 单层二硫化钼在二氧化硅衬底上耦合的等离激元-声子模式

单层二硫化钼具有点群  $D_3h$  的对称性，并有着九支声子（三支声学声子和六支光学声子）<sup>[198]</sup>。在单层二硫化钼中，两个占主导作用的光学声子（极性光学声子和单极性光学声子）与电子有着强烈的耦合作用。通常来讲，极性材料中的载流子与  $\Gamma$  点附近的纵向光学（longitudinal optical; LO）声子通过长程的 Fröhlich（弗洛里希）相互作用发生耦合并产生有着较大电极化的宏观电场。单极性光学声子对应于材料层厚度的改变并且这支声子模式不会产生宏观电场<sup>[199, 200]</sup>。为了更好的研究单层二硫化钼中的集体激发性质，极性纵向光学（LO）声子的耦合作用是需要被进一步考虑的。

实验制备出的单层二维材料通常不是独立悬空的样品。它们通常被制备在衬底如  $\text{SiO}_2$ ,  $\text{SiC}$ ,  $\text{HfO}_2$  或者六方氮化硼（h-BN）上。因此，基底材料对材料内部电子的集体激发的影响也需要被考虑。实验上已经证实，高质量、均匀覆盖的单层二硫化钼原子层已经在  $\text{SiO}_2$  基底上通过化学气相沉积（CVD）的方法成功制备<sup>[201, 202]</sup>。单层二维材料中的载流子可以和薄膜下层晶格中的表面光学（surface optical; SO）声子发生长程极化 Fröhlich 耦合。因此，我们对单层二硫化钼系统中考虑了电子-电子相互作用、以及内禀纵向光学声子和  $\text{SiO}_2$  中表面光学声子的电子-声子相互作用下的集体激发特性开展了研究。

## 7.1 LO 声子和 SO 声子参与下耦合的等离激元-声子模式

我们考虑单层二硫化钼中由二维电子或者空穴与无色散的 LO 声子和 SO 声子通过 Fröhlich 相互作用的等离激元-声子耦合模型。在这种情况下，电子和其余的电子通过库仑相互作用和产生虚声子交换的 Fröhlich 电子-声子（e-p）相互作用发生耦合。Fröhlich 相互作用哈密顿量由下式给出

$$H_{\text{ep}} = \sum_{\chi} [W_{\chi\mathbf{q}} a_{\mathbf{q}} e^{i(\mathbf{q}\cdot\mathbf{r} + \omega_{\chi} t)} + W_{\chi\mathbf{q}}^* a_{\mathbf{q}}^\dagger e^{-i(\mathbf{q}\cdot\mathbf{r} + \omega_{\chi} t)}], \quad (7.1)$$

其中  $\mathbf{q} = (q_x, q_y)$  是 x-y 平面上声子的波矢， $(a_{\mathbf{q}}^\dagger, a_{\mathbf{q}})$  是声子系统的正则共轭坐标， $W_{\chi\mathbf{q}}$  是电子-声子相互作用系数同时  $\omega_{\chi}$  是第  $\chi$  种光学声子的声子频率。

此外，光学声子参与下的有效电子-电子相互作用的空间傅里叶变换可以写作

$$V_{\text{ep}}^{\lambda\lambda'}(\varsigma s, \mathbf{k}, \mathbf{q}; \omega) = \sum_{\chi} D_0^{\chi}(\omega_{\chi}, \omega) |U_{\lambda\lambda'}^{\chi, \varsigma s}(\mathbf{k}, \mathbf{q})|^2, \quad (7.2)$$

其中  $|U_{\lambda\lambda'}^{\chi, \varsigma s}(\mathbf{k}, \mathbf{q})|^2 = |\langle \mathbf{k} + \mathbf{q}, \lambda' \varsigma s | W_{\chi\mathbf{q}} | \mathbf{k}, \lambda \varsigma s \rangle|^2$ ,  $\omega$  是激发频率且  $D_0^{\chi}(\omega_{\chi}, \omega) = 2\omega_{\chi}/[\omega^2 - \omega_{\chi}^2]$  是声子频率为  $\omega_{\chi}$  的第  $\chi$ -种声子不受干扰的光学声子传播子。对于单层二硫

化钼以及附着在极性基底上的单层二硫化钼，电子-声子相互作用矩阵元可以写作  $|\langle \mathbf{k} + \mathbf{q}, \lambda' \zeta s | W_{\chi \mathbf{q}} | \mathbf{k}, \lambda \zeta s \rangle|^2 = g_\chi^2(q) C_{\lambda \mathbf{k}, \lambda' \mathbf{k} + \mathbf{q}}^{\zeta s}$ ，其中  $g_\chi(q)$  是第  $\chi$  种光学声子参与下电子-电子相互作用的耦合强度。因而光学声子参与下的电子-电子相互作用可以写作  $V_{\text{ep}}^{\lambda \lambda'}(\zeta s, \mathbf{k}, \mathbf{q}; \omega) = V_{\text{ep}}(\mathbf{q}, \omega) C_{\lambda \mathbf{k}, \lambda' \mathbf{k} + \mathbf{q}}^{\zeta s}$ 。

总的有效电子-电子相互作用可以通过在图解自治场理论下将所有的裸泡泡图叠加的无规则相近得到<sup>[203]</sup>

$$V_{\text{eff}}(\mathbf{q}, \omega) = \frac{v_q + V_{\text{ep}}(\mathbf{q}, \omega)}{1 - [v_q + V_{\text{ep}}(\mathbf{q}, \omega)] \Pi(\mathbf{q}, \omega)} = \frac{v_q}{\epsilon_{\text{RPA}}(\mathbf{q}, \omega)}, \quad (7.3)$$

其中  $V_{\text{ep}}(\mathbf{q}, \omega) = \sum_\chi D_0^\chi(\omega_\chi, \omega) g_\chi^2(q)$  且  $\Pi(\mathbf{q}, \omega)$  是动量空间中自由极化函数。因而声子耦合下单层二硫化钼系统在无规则相近似 (RPA) 下的介电函数被定义为

$$\epsilon_{\text{RPA}}(\mathbf{q}, \omega) = 1 - v_q \Pi(\mathbf{q}, \omega) - \frac{\sum_\chi D_0^\chi(\omega_\chi, \omega) g_\chi^2(q)}{v_q + \sum_\chi D_0^\chi(\omega_\chi, \omega) g_\chi^2(q)}. \quad (7.4)$$

同时，耦合等离激元-声子激发模式由介电函数的实部为零  $\text{Re}[\epsilon_{\text{RPA}}] \rightarrow 0$  决定。

在考虑了电子-电子相互作用和电子-内禀声子相互作用后，单层二硫化钼层中的电子与极性 LO 声子通过 Fröhlich 相互作用发生耦合并且极性 LO 声子的能量为  $\omega_{\text{op}} = 48$  meV，耦合强度为  $g_{\text{op}}(q) = g_{\text{Fr}} \text{erfc}(qd/2)$  其中耦合常数  $g_{\text{Fr}} = 286$  meV Å,  $d = 5.41$  Å 是电子布洛赫态的有效宽度，erfc 是余误差函数<sup>[204, 205]</sup>。于是，内禀 LO 声子参与下耦合的等离激元-声子模式为

$$\omega_\pm = \frac{1}{\sqrt{2}} \left[ \omega_q^2 + \omega_{\text{op}}^2 \pm \sqrt{(\omega_q^2 - \omega_{\text{op}}^2)^2 + 4\alpha \omega_q^2 \omega_{\text{op}}^2} \right]^{1/2}, \quad (7.5)$$

其中  $\alpha = 2g_{\text{op}}^2(q)/(\omega_{\text{op}} v_q)$ ,  $\omega_q$  是上一章中在零温时长波极限下的电荷等离激元模式。

对于在极性衬底上的单层二硫化钼，电子不仅和内禀极性 LO 声子发生耦合同时也和极性衬底层中的 Fuchs-Kliewer 表面光学 (SO) 声子发生耦合。在  $\text{SiO}_2$  衬底层中，两个主要的表面声子模式  $\omega_{\text{sp1}} = 59$  meV 和  $\omega_{\text{sp2}} = 156$  meV 通过长程相互作用和单层二硫化钼中的电子发生耦合因而对系统的光学性质产生了重要的影响。 $\text{SiO}_2$  衬底中 Fuchs-Kliewer 声子的耦合强度为<sup>[206, 207]</sup>

$$\begin{aligned} g_{\text{sp1}}^2(q) &= \frac{2\pi e^2}{q} e^{-2qd_0} \frac{\omega_{\text{sp1}}}{2} \left[ \frac{1}{\epsilon_i^{\text{sub}} + \epsilon^{\text{env}}} - \frac{1}{\epsilon_0^{\text{sub}} + \epsilon^{\text{env}}} \right], \\ g_{\text{sp2}}^2(q) &= \frac{2\pi e^2}{q} e^{-2qd_0} \frac{\omega_{\text{sp2}}}{2} \left[ \frac{1}{\epsilon_\infty^{\text{sub}} + \epsilon^{\text{env}}} - \frac{1}{\epsilon_i^{\text{sub}} + \epsilon^{\text{env}}} \right], \end{aligned} \quad (7.6)$$

其中  $\epsilon_\infty^{\text{sub}} = 2.4$ ,  $\epsilon_i^{\text{sub}} = 3.36$  和  $\epsilon_0^{\text{sub}} = 3.9$  分别是  $\text{SiO}_2$  衬底中的光学，中间和定态介电常数。 $d_0 \approx 3$  Å 是单层二硫化钼层和  $\text{SiO}_2$  衬底之间的间距<sup>[151, 208, 209]</sup>，背景环境介电常数  $\epsilon^{\text{env}} = (\epsilon_t + \epsilon_0^{\text{sub}})/2 = \epsilon_r$ <sup>[209–211]</sup>，其中  $\epsilon_t$  是顶端介电门电极的介电常数。对于在极性衬底上单层二硫化钼内禀光学声子和表面光学声子参与耦合的等离激元-声子模式同样也可以通过  $\text{Re}[\epsilon_{\text{RPA}}] \rightarrow 0$  得到，这将得到  $\omega^2$  的四次方程

$$\omega^8 - A_3 \omega^6 + A_2 \omega^4 - A_1 \omega^2 + A_0 = 0, \quad (7.7)$$

其中

$$\begin{aligned}
 A_3 &= \omega_{\text{op}}^2 + \omega_{\text{sp1}}^2 + \omega_{\text{sp2}}^2 + \omega_q^2, \\
 A_2 &= \omega_q^2 [(1 - \beta_{\text{op}})\omega_{\text{op}}^2 + (1 - \beta_{\text{sp1}})\omega_{\text{sp1}}^2 + (1 - \beta_{\text{sp2}})\omega_{\text{sp2}}^2] \\
 &\quad + \omega_{\text{op}}^2 \omega_{\text{sp1}}^2 + \omega_{\text{op}}^2 \omega_{\text{sp2}}^2 + \omega_{\text{sp1}}^2 \omega_{\text{sp2}}^2, \\
 A_1 &= [(1 - \beta_{\text{op}} - \beta_{\text{sp1}})\omega_{\text{op}}^2 \omega_{\text{sp1}}^2 + (1 - \beta_{\text{op}} - \beta_{\text{sp2}})\omega_{\text{op}}^2 \omega_{\text{sp2}}^2 \\
 &\quad + (1 - \beta_{\text{sp1}} - \beta_{\text{sp2}})\omega_{\text{sp1}}^2 \omega_{\text{sp2}}^2] \omega_q^2 + \omega_{\text{op}}^2 \omega_{\text{sp1}}^2 \omega_{\text{sp2}}^2, \\
 A_0 &= (1 - \beta_{\text{op}} - \beta_{\text{sp1}} - \beta_{\text{sp2}})\omega_{\text{op}}^2 \omega_{\text{sp1}}^2 \omega_{\text{sp2}}^2 \omega_q^2,
 \end{aligned}$$

其中  $\omega_q$  是  $n$ -/ $p$ -型单层二硫化钼样品中的电荷等离激元能量且  $\beta_{\text{op}} = 2g_{\text{op}}^2(q)/(\omega_{\text{op}} v_q)$ ,  $\beta_{\text{sp1}} = 2g_{\text{sp1}}^2(q)/(\omega_{\text{sp1}} v_q)$  和  $\beta_{\text{sp2}} = 2g_{\text{sp2}}^2(q)/(\omega_{\text{sp2}} v_q)$ 。因此，系统中会有四支声子耦合的等离激元-声子模式且分别由公式 (7.7) 中的四个正实数根得到。

## 7.2 结果与讨论

对于在测量电学和等离激元光子学特性的实际实验器件中，单层二硫化钼样品通常被制备成场效应晶体管的器件结构并能通过不同的源极材料实现  $n$ -/ $p$ -型掺杂器件并且载流子的浓度可以通过改变门电压来调控。通常来说，二氧化硅被用作单层二维材料晶体管的底部栅极并且单层二硫化钼晶体管有着较高介电常数的顶部栅极如  $\text{HfO}_2$ , 聚合物电解质 (polymer electrolyte; PE) 等。因此，作为理论上的模型，在整个计算中我们采用一个常用的背景环境介电函数  $\epsilon^{\text{env}} = 5$ 。

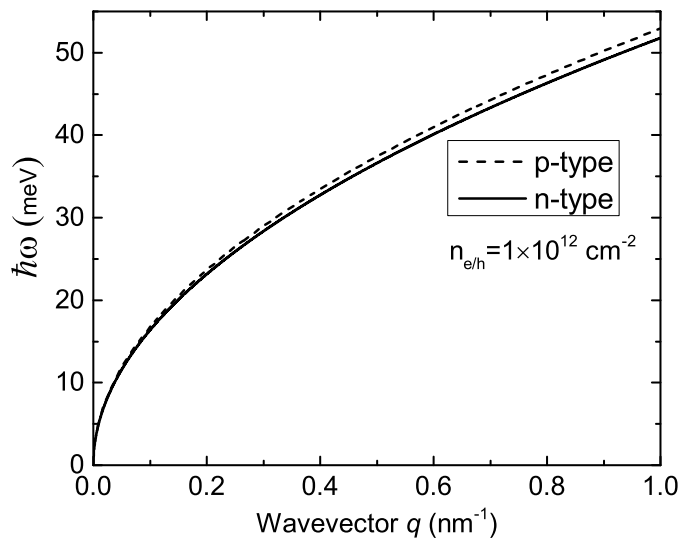


图 7.1: 载流子浓度为  $n_{e/h} = 1 \times 10^{12} \text{ cm}^{-2}$  时  $n$ - 和  $p$ -型单层二硫化钼的电荷等离激元模式  $\omega_q$  随着波矢  $q$  的变化。实线和短划线分别是  $n$ - 和  $p$ -型单层二硫化钼的结果

图 7.1 给出了给定载流子浓度下  $n$ - 和  $p$ -型单层二硫化钼的等离激元模式随着波矢的变化。从上一章中可以知道，单层二硫化钼中的等离激元模式  $\omega_q \propto q^{1/2}n^{1/2}$  是与传统二维电子气类似的声学支并受到波矢和载流子浓度的强烈影响。从图 7.1 中可以看到，在低载流子浓度下， $n$ - 和  $p$ -型单层二硫化钼的等离激元色散关系非常接近并且  $p$ -型样品中的等离激元色散曲线比  $n$ -型样品的稍微高一点。这一点差异是由单层二硫化钼中的导带和价带的能带结构差异所导致的。

在图 7.2 中，给出了零温下  $n$ - 和  $p$ -型单层二硫化钼样品中由公式 (7.5) 给出的内禀光学声子参与下两支耦合的等离激元-声子模式在不同载流子浓度下的色散关系  $\omega_{\pm}$ 。内禀光学声子参与下耦合的等离激元-声子模式  $\omega_-$  在小  $q$  区域是声学型的并具有较低的能量而在大  $q$  区域是光学型的并且等离激元频率接近于内禀光学声子频率。与之相反，耦合的等离激元-声子模式  $\omega_+$  在小  $q$  区域是光学型的且能量趋于内禀光学声子频率而在大  $q$  区域是声学型的并有着较大的能量。可以看到，最强的等离激元-声子耦合发生在非耦合的等离激元模式和内禀光学声子模式的交点之上。从图 7.1 中可以得到在较低载流子浓度下， $n$ - 和  $p$ -型单层二硫化钼有着非常接近的等离激元色散关系。因而

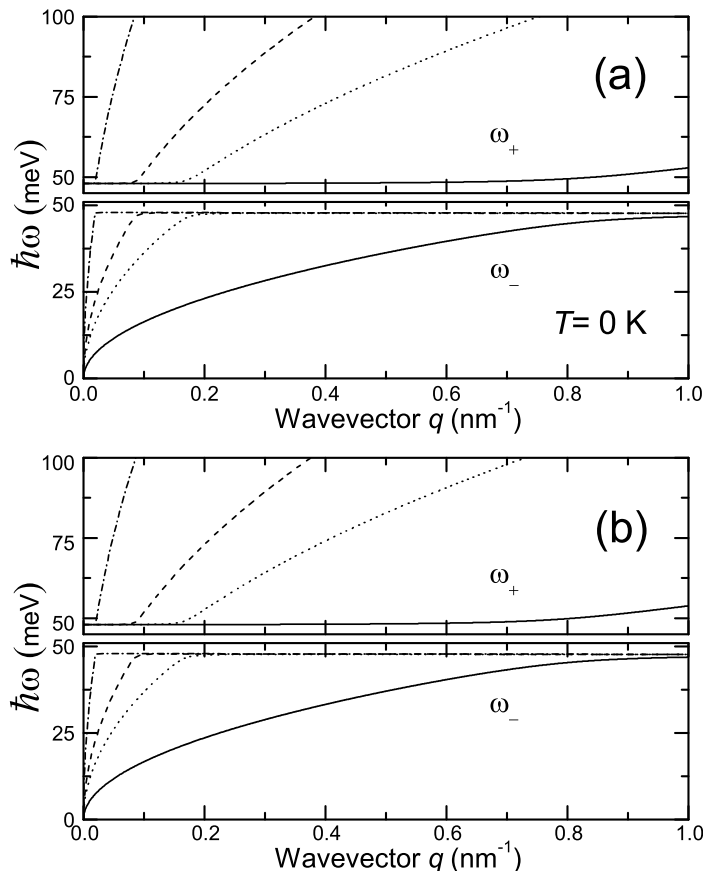


图 7.2: 单层二硫化钼中内禀光学声子参与下耦合的等离激元-声子模式在不同载流子浓度  $n = 1 \times 10^{12} \text{ cm}^{-2}$  (实曲线),  $n = 5 \times 10^{12} \text{ cm}^{-2}$  (短划线曲线),  $n = 1 \times 10^{13} \text{ cm}^{-2}$  (虚曲线), 和  $n = 5 \times 10^{13} \text{ cm}^{-2}$  (点缀中曲线) 下随着波矢  $q$  的变化。 (a)  $n$ -型和 (b)  $p$ -型样品的结果

图 7.2(a)-(b) 中耦合的等离激元-声子模式色散关系十分接近。从图 7.2 中我们可以得到内禀光学声子参与下耦合的等离激元-声子模式可以通过一个外加偏压改变载流子浓度进行有效的调节。在较小的载流子浓度下，在大  $q$  区域能看到更清晰的等离激元-声子耦合现象。由于单层二硫化钼中内禀光学声子与电子的耦合强度较弱，因而在高载流子浓度下，耦合的等离激元-声子模式的耦合效应不是很明显。

图 7.3 给出了在给定电子浓度下  $n$ -型单层二硫化钼中内禀光学声子和二氧化硅衬底中表面光学声子参与下耦合的等离激元-声子模式。由于图 7.1 和图 7.2 中  $n$ -型和  $p$ -型样品中的相似性，这里只讨论  $n$ -型掺杂的情形。单层二硫化钼样品通常被制备在二氧化硅薄膜衬底上因而二氧化硅中的表面光学声子模式将在基于单层二硫化钼器件的光学性质尤其是等离激元性质中扮演着重要的角色。由内禀光学声子和基底表面光学声子参与的单层二硫化钼/二氧化硅结构系统中存在四支耦合的等离激元-声子模

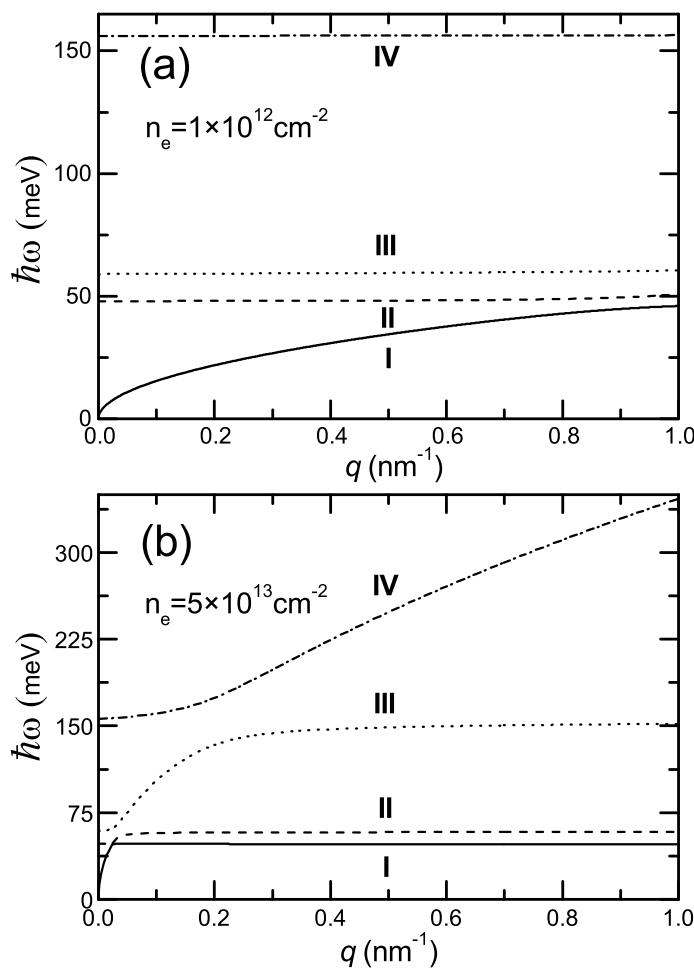


图 7.3:  $n$ -型单层二硫化钼样品中稟光学声子和表面光学声子参与下耦合的等离激元-声子模式 (分支 I, II, III, 和 IV) 在给定载流子浓度 (a)  $n_e = 1 \times 10^{12} \text{ cm}^{-2}$  和 (b)  $n_e = 5 \times 10^{13} \text{ cm}^{-2}$  下随着波矢  $q$  的变化

式。其中耦合的等离激元-声子模式是纯等离激元模式  $\omega_q$ , 光学声子  $\omega_{\text{op}}$ ,  $\omega_{\text{sp}1}$  和  $\omega_{\text{sp}2}$  相互耦合后的混杂化产物。在图 7.3(a) 中, 由于在低载流子浓度下的等离激元能量较低, 因而与光学声子的耦合作用较弱。在图 7.3(b) 中, 可以看到在波矢  $q$  趋于零的区域, 耦合的等离激元模式分支 I, II, III, 和 IV 分别渐进的收敛至纯的等离激元  $\omega_q$  和光学声子  $\omega_{\text{op}}$ ,  $\omega_{\text{sp}1}$  和  $\omega_{\text{sp}2}$  模式。在另一端的大  $q$  区域, 随着波矢的增加, 耦合等离激元模式分支 I, II, III, 和 IV 分别渐进的收敛至纯的光学声子  $\omega_{\text{op}}$ ,  $\omega_{\text{sp}1}$  和  $\omega_{\text{sp}2}$  和等离激元  $\omega_q$  模式。在波矢  $q$  较小的中间部分, 等离激元和表面光学声子具有较强的耦合作用而与内禀光学声子的耦合较弱。同时也可以看到在高载流子浓度下, 单层二硫化钼/二氧化硅结构系统中最强的等离激元-声子耦合发生在具有较小波矢的区域。由于在较大波矢情况下, 耦合的等离激元-声子模式将进入到粒子-空穴激发区因而我们在长波极限下的小  $q$  区域得到的结果是有效的。最近, 在石墨烯/衬底结构系统中较强的耦合的等离激元-声子模式在实验上被角分辨反射电子能量损失能谱、中红外透射谱和近场光学显微技术所测到<sup>[202, 212–215]</sup>。同时发现电子-声子的耦合作用在决定原子层材料/衬底混合系统的光学性质中起到了非常重要的作用。

本项研究表明基于单层二硫化钼的等离激元、内禀光学声子参与下耦合的等离激元-声子模式和内禀光学声子及表面光学声子参与下耦合的等离激元-声子模式的色散关系可以通过改变载流子的浓度进行有效的调节。等离激元和耦合的等离激元-声子模式的能量在红外到太赫兹频段范围内。在相同载流子浓度下, 不同掺杂类型单层二硫化钼的等离激元模式有着细微的差异。单层二硫化钼系统的载流子浓度可以通过外加偏压的方式进行调节。而实际二维材料器件中的波矢则由样品的几何结构决定。因此, 通过考虑电子-声子的耦合作用, 单层二硫化钼微纳结构中耦合的等离激元-声子模式的共振频率可以通过改变样品的几何结构以及载流子浓度进行调节, 从而得到高度受控的等离激元光子学器件。

### 7.3 本章小结

基于无规则相近似和自治场理论且在长波近似下, 我们对单层二硫化钼的集体激发性质(如等离激元、声子参与下耦合的等离激元-声子模式)进行了理论上的研究。单层二硫化钼中有着和传统二维电子气类似的由带内跃迁所导致声学等离激元模式  $\omega_q \propto q^{1/2} \sim n^{1/2}$ 。掺杂类型对等离激元模式及耦合的等离激元-声子模式的色散关系有着细微的影响。单层二硫化钼中等离激元与内禀光学声子的耦合产生了两支耦合的等离激元-声子模式。同时, 单层二硫化钼中等离激元和内禀光学声子以及二氧化硅中表面光学声子的耦合产了四支耦合的等离激元-声子模式。这些等离激元模式和耦合的等离激元-声子模式的能量范围在红外和太赫兹区域内并且可以受到载流子浓度的有效调节。这些特性使得单层二硫化钼能成为应用在红外及太赫兹频段等离激元光子学极具潜力的材料平台。我们希望本项理论研究能很快的在实验上通过基于单层二硫化钼的器件所证实。

## 第八章 论文总结与展望

### 8.1 论文总结

本学位论文是博士研究生阶段研究工作的系统性总结。主要在基于近年来发现的新型二维电子气材料多层石墨烯和单层二硫化钼，系统的研究了多层石墨烯和单层二硫化钼系统的光吸收/光电导，Rashba 效应对单层二硫化钼光电导的影响和在圆偏振光泵浦激发下单层二硫化钼的等离激元特性。通过理论上的模拟和计算研究了典型新型二维电子气系统的光电特性，主要的工作总结如下：

1. 通过由半经典玻尔兹曼方程得到的平衡方程法，计算了多层石墨烯系统的光电导和光透射系数。系统的研究了石墨烯层数和堆垛次序对光吸收窗口的影响。多层石墨烯系统中不同的层数和堆垛方式会导致不同的电子结构。 $N$  层石墨烯系统在可见光区域的普适光电导为  $\sigma_0^N = N\pi e^2/(2h)$  且不受层数和堆垛次序的影响。多层石墨烯系统中有一个从红外到太赫兹频段 (0.2-150 THz) 的光吸收窗口且能有效的受到温度、电子浓度、石墨烯的层数和堆垛次序的调节。特别的是，在奇数层 AB-堆垛多层石墨烯系统中有着由迷你带隙引起的特征吸收边。这项理论研究工作为如何利用多层石墨烯在红外和太赫兹频段的特殊光吸收特性提供了依据。譬如，少数层石墨烯可以用于透明电极，可以利用多层石墨烯中的特征吸收边来确定 AB 堆垛石墨烯的层数。石墨烯系统的独特的光吸收窗口特性能极具潜力的应用于红外及太赫兹探测器中。

2. 我们考虑 Rashba 效应对单层二硫化钼的影响，利用 Kubo-Greenwood 公式计算了在 Rashba 自旋-轨道耦合作用下单层二硫化钼的光电导。在单层二硫化钼中，自由载流子吸收存在于整个红外到太赫兹范围。自旋翻转跃迁所导致的宽吸收峰和吸收窗口处在红外到太赫兹频段。在长波长圆偏振光下，自旋翻转跃迁表现出谷指数选择性的光吸收。然而，不同谷间光电导之和等于纵向光电导。光吸收峰和光吸收窗口的位置和宽度可以有效的被载流子浓度和 Rashba 参数调节。研究结果揭示了 Rashba 效应可以有效的导致在红外和太赫兹范围光吸收窗口的产生，这一现象预示着单层二硫化钼将能很好的应用在低频率范围的光探测器或其它光电器件中。

3. 通过四带模型和二带模型研究了单层二硫化钼在可将光范围的光电导。Rashba 效应对自旋态的耦合增加了单层二硫化钼中带间跃迁光吸收跃迁通道的数量。在 Rashba 系数较小的情况下，Rashba 效应对总的光吸收没有明显的影响。在 Rashba 系数较大时，带隙附近的光吸收受到很明显的影响。这些理论结果预示着可以利用 Rashba 效应对单层二硫化钼在带隙附近的光吸收或者光荧光特性进行调节。

4. 利用无规则相近似 (RPA) 下的介电函数理论研究了光泵浦激发下单层二硫化钼的等离激元特性。单层二硫化钼中子系统的组份数量可以通过伴随着打破自旋和/或谷简并性的光泵浦手段来实现。带内粒子-空穴激发谱区域外存在无阻尼电荷等离激元模

式同时在带内粒子-空穴激发谱内可能存在弱阻尼线性声学等离激元模式。单层二硫化钼中无阻尼电荷等离激元模式与传统二维电子气类似。等离激元模式的数量和色散关系随着掺杂类型和掺杂浓度而改变并且可以通过调节泵浦光强度的光泵浦手段来实现。单层二硫化钼等离激元模式的能量不仅包含红外区域也包含太赫兹频段，尤其是低能量的弱阻尼线性声学等离激元模式。这意味着通过光调控和偏压调控的手段，单层二硫化钼可以成为响应频率在低频段绝佳的等离激元光子学材料。

5. 考虑电子-声子相互作用，利用介电函数理论研究了二硫化钼中等离激元和内禀光学声子和基底表面声子的耦合作用。掺杂类型对等离激元模式及光学声子参与下耦合的等离激元-声子模式的色散关系有着细微的影响。单层二硫化钼中等离激元与内禀光学声子的耦合产生了两支耦合的等离激元-声子模式。同时，单层二硫化钼中等离激元和内禀光学声子以及二氧化硅中表面光学声子的耦合产生了四支耦合的等离激元-声子模式。这些等离激元模式和耦合的等离激元-声子模式的能量在红外和太赫兹区域内并且可以受到载流子浓度的有效调节。在实验中，通常可以通过观测等离激元吸收共振峰的位置来确定等离激元-声子的耦合效应。本项理论研究能进一步为基于单层二硫化钼的器件在等离激元光子学中的应用提供理论支持。

总体上，本论文从理论上较为系统的研究了新型二维电气材料多层石墨烯和单层二硫化钼系统的光电特性。虽然石墨烯系统没有带隙或者在特定条件下的带隙较小，在目前难以较好的应用于电子器件中，但是石墨烯系统由于具有较好的光学特性和等离激元特性，特别是多层石墨烯系统中存在的光吸收窗口和在可见光范围内的均匀光吸收，使得其能极具潜力的应用在光学和等离激元光子学器件中。对于新型材料单层二硫化钼，其较大的带隙和自旋轨道耦合效应使得其在各个方面都十分具有潜力。本学位论文中采用有效的低能量能带结构模型对其光学特性和等离激元特性进行了理论上的模拟计算。得到的结果虽无法准确定量的符合实际样品的情况，但是能够很好的定性的得到相关的物理特性以及阐明其中的机理。对进一步的实验工作能起到理论支撑和启发作用。

在本学位论文中的研究表明多层石墨烯和单层二硫化钼能够较好的应用在红外和太赫兹频段范围的光学，光电子学和等离激元器件中。

## 8.2 下一步研究计划和展望

本论文中系统的研究了新型二维电子气的光吸收/光电导以及等离激元特性。在下一步的研究中，可以在基于目前的研究基础上对如下几个方面展开新的探索和研究：

1. 研究 Rashba 效应对单层二硫化钼中电子态自旋取向的影响。由于单层二硫化钼中具有较强的内禀自旋-轨道耦合作用，因而在 Rashba 效应下，单层二硫化钼中电子态的自旋取向不光有平面内的分量也会有平面外的分量。
2. 近年来兴起了对三维狄拉克半金属的研究，由于二维系统和三维系统具有本质上的差异，可以利用现有的理论研究三维狄拉克半金属系统的电子学、光学以及等离

激元特性。

3. 在目前的研究内容中进一步引入外加电场、磁场等外部条件，并考虑电子-声子的相互作用，进一步研究新型二维材料的光电性质。

在以后的科研工作中，将加大对新材料的跟进，进一步学习和掌握模拟和计算材料物理性质的理论和方法。



## 附录 A 单层二硫化钼极化函数的解析解表达式

### A.1 RPA 介电函数和自由极化函数

在电子-电子相互作用下，单层二硫化钼系统的无规则相近似(RPA)介电函数为

$$\epsilon_{\text{RPA}}(\mathbf{q}, \omega) = 1 - v_q \Pi(\mathbf{q}, \omega), \quad (\text{A.1})$$

其中  $\Pi(\mathbf{q}, \omega)$  是在二维动量空间中积分表示的自由极化函数，极化函数是由在不同谷的自旋系统的求和构成

$$\Pi(\mathbf{q}, \omega) = \sum_{\varsigma s} \Pi^{\varsigma s}(\mathbf{q}, \omega).$$

在  $\varsigma$  谷自旋为  $s$  带的极化函数  $\Pi^{\varsigma s}(\mathbf{q}, \omega)$  可以表示为在动量空间中的积分

$$\Pi^{\varsigma s}(\mathbf{q}, \omega) = \sum_{\lambda \lambda' \mathbf{k}} \frac{f(E_{\lambda \mathbf{k}}^{\varsigma s}) - f(E_{\lambda' \mathbf{k} + \mathbf{q}}^{\varsigma s})}{\hbar \omega + E_{\lambda \mathbf{k}}^{\varsigma s} - E_{\lambda' \mathbf{k} + \mathbf{q}}^{\varsigma s} + i\delta} C_{\lambda \mathbf{k}, \lambda' \mathbf{k} + \mathbf{q}}^{\varsigma s}, \quad (\text{A.2})$$

这里  $f(E_{\lambda \mathbf{k}}^{\varsigma s}) = [e^{(E_{\lambda \mathbf{k}}^{\varsigma s} - \mu_{\lambda}^{\varsigma})/k_B T} + 1]^{-1}$  是费米-狄拉克分布函数。

在进行了  $\mathbf{k} + \mathbf{q} \rightarrow -\mathbf{k}$  变换之后，在各个谷的自旋子带的极化函数为

$$\Pi^{\varsigma s}(\mathbf{q}, \omega) = \sum_{\lambda \lambda' \mathbf{k}} \left[ \frac{f(E_{\lambda \mathbf{k}}^{\varsigma s})}{\hbar \omega + E_{\lambda \mathbf{k}}^{\varsigma s} - E_{\lambda' \mathbf{k} + \mathbf{q}}^{\varsigma s} + i\delta} - \frac{f(E_{\lambda' \mathbf{k}}^{\varsigma s})}{\hbar \omega + E_{\lambda' \mathbf{k}}^{\varsigma s} - E_{\lambda \mathbf{k} + \mathbf{q}}^{\varsigma s} + i\delta} \right] C_{\lambda \mathbf{k}, \lambda' \mathbf{k} + \mathbf{q}}^{\varsigma s}, \quad (\text{A.3})$$

极化函数可以写作带内跃迁和带间跃迁部分的和，带间跃迁部分为

$$\begin{aligned} \Pi_{\text{inter}}^{\varsigma s}(\mathbf{q}, \omega) &= \sum_{\mathbf{k}} \left\{ \frac{f(E_{+ \mathbf{k}}^{\varsigma s})}{\hbar \omega + E_{+ \mathbf{k}}^{\varsigma s} - E_{- \mathbf{k} + \mathbf{q}}^{\varsigma s} + i\delta} - \frac{f(E_{+ \mathbf{k}}^{\varsigma s})}{\hbar \omega + E_{- \mathbf{k} + \mathbf{q}}^{\varsigma s} - E_{+ \mathbf{k}}^{\varsigma s} + i\delta} \right. \\ &\quad \left. + \frac{f(E_{- \mathbf{k}}^{\varsigma s})}{\hbar \omega + E_{- \mathbf{k}}^{\varsigma s} - E_{+ \mathbf{k} + \mathbf{q}}^{\varsigma s} + i\delta} - \frac{f(E_{- \mathbf{k}}^{\varsigma s})}{\hbar \omega + E_{+ \mathbf{k} + \mathbf{q}}^{\varsigma s} - E_{- \mathbf{k}}^{\varsigma s} + i\delta} \right\} C_{\lambda \mathbf{k}, \lambda' \mathbf{k} + \mathbf{q}}^{\varsigma s} \\ &= \frac{1}{2} \sum_{\mathbf{k}} \sum_{\alpha=\pm} \frac{\alpha[f(E_{+ \mathbf{k}}^{\varsigma s}) - f(E_{- \mathbf{k}}^{\varsigma s})]}{\hbar \omega + \alpha[\Lambda_{\mathbf{k}}^{\varsigma s} + \Lambda_{\mathbf{k} + \mathbf{q}}^{\varsigma s}] + i\delta} \left[ 1 - \frac{\Delta_{\varsigma s}^2 + \mathbf{k}(\mathbf{k} + \mathbf{q})}{\Lambda_{\mathbf{k} + \mathbf{q}}^{\varsigma s} \Lambda_{\mathbf{k}}^{\varsigma s}} \right], \end{aligned} \quad (\text{A.4})$$

其中  $\Lambda_{\mathbf{k}}^{\varsigma s} = \sqrt{a^2 t^2 \mathbf{k}^2 + \Delta_{\varsigma s}^2}$ ，同时带内跃迁部分为

$$\begin{aligned} \Pi_{\text{intra}}^{\varsigma s}(\mathbf{q}, \omega) &= \sum_{\lambda \mathbf{k}} \left\{ \frac{f(E_{\lambda \mathbf{k}}^{\varsigma s})}{\hbar \omega + E_{\lambda \mathbf{k}}^{\varsigma s} - E_{\lambda \mathbf{k} + \mathbf{q}}^{\varsigma s} + i\delta} - \frac{f(E_{\lambda \mathbf{k}}^{\varsigma s})}{\hbar \omega + E_{\lambda \mathbf{k} + \mathbf{q}}^{\varsigma s} - E_{\lambda \mathbf{k}}^{\varsigma s} + i\delta} \right\} C_{\lambda \mathbf{k}, \lambda \mathbf{k} + \mathbf{q}}^{\varsigma s} \\ &= \frac{1}{2} \sum_{\lambda} \sum_{\mathbf{k}} \sum_{\alpha=\pm} \frac{\alpha f(E_{\lambda \mathbf{k}}^{\varsigma s})}{\hbar \omega + \alpha[\Lambda_{\mathbf{k}}^{\varsigma s} - \Lambda_{\mathbf{k} + \mathbf{q}}^{\varsigma s}] + i\delta} \left[ 1 + \frac{\Delta_{\varsigma s}^2 + \mathbf{k}(\mathbf{k} + \mathbf{q})}{\Lambda_{\mathbf{k} + \mathbf{q}}^{\varsigma s} \Lambda_{\mathbf{k}}^{\varsigma s}} \right]. \end{aligned} \quad (\text{A.5})$$

包含了带内跃迁和带间跃迁后，总的来说，极化函数可以写作

$$\begin{aligned} \Pi^{\varsigma s}(\mathbf{q}, \omega) &= \frac{1}{2} \sum_{\lambda} \sum_{\mathbf{k}} \sum_{\beta=\pm} \sum_{\alpha=\pm} \frac{\alpha[\delta_{\lambda, -1} + \lambda f(E_{\lambda \mathbf{k}}^{\varsigma s})]}{\hbar \omega + \alpha[\Lambda_{\mathbf{k}}^{\varsigma s} - \beta \Lambda_{\mathbf{k} + \mathbf{q}}^{\varsigma s}] + i\delta} \left[ 1 + \frac{\Delta_{\varsigma s}^2 + \mathbf{k}(\mathbf{k} + \mathbf{q})}{\beta \Lambda_{\mathbf{k} + \mathbf{q}}^{\varsigma s} \Lambda_{\mathbf{k}}^{\varsigma s}} \right] \\ &\quad - \frac{1}{2} \sum_{\mathbf{k}} \sum_{\alpha=\pm} \frac{\alpha}{\hbar \omega + \alpha[\Lambda_{\mathbf{k}}^{\varsigma s} + \Lambda_{\mathbf{k} + \mathbf{q}}^{\varsigma s}] + i\delta} \left[ 1 - \frac{\Delta_{\varsigma s}^2 + \mathbf{k}(\mathbf{k} + \mathbf{q})}{\Lambda_{\mathbf{k} + \mathbf{q}}^{\varsigma s} \Lambda_{\mathbf{k}}^{\varsigma s}} \right], \end{aligned} \quad (\text{A.6})$$

其中第二部分为未掺杂情况下的极化函数。

## A.2 极化函数的相关解析表达式

在零温下，公式 (A.6) 中的费米狄拉克分布函数可以写作阶梯函数的形式

$$f(E_{\lambda\mathbf{k}}^{\varsigma s}) = \theta(\mu_{\lambda}^{\varsigma} - E_{\lambda\mathbf{k}}^{\varsigma s}). \quad (\text{A.7})$$

在这里定义推迟函数

$$\begin{aligned} \chi_{\varsigma s \lambda}^{\beta}(\mathbf{q}, \omega) &= \frac{1}{2} \sum_{\mathbf{k} \leq \mathbf{k}_{\lambda F}^{\varsigma s}} \sum_{\alpha=\pm} \frac{\alpha}{\hbar\omega + \alpha[\Lambda_{\mathbf{k}}^{\varsigma s} - \beta\Lambda_{\mathbf{k}+\mathbf{q}}^{\varsigma s}] + i\delta} \\ &\times \left[ 1 + \frac{\Delta_{\varsigma s}^2 + \mathbf{k}(\mathbf{k} + \mathbf{q})}{\beta\Lambda_{\mathbf{k}+\mathbf{q}}^{\varsigma s}\Lambda_{\mathbf{k}}^{\varsigma s}} \right], \end{aligned} \quad (\text{A.8})$$

其中  $\beta = \pm$  分别代表带内跃迁和带间跃迁。

在导带和价带同时掺杂的情况下，在  $\varsigma$  谷自旋为  $s$  子带系统零温下的极化函数可以写作

$$\Pi_{T=0}^{\varsigma s}(\mathbf{q}, \omega) = -\chi_{\varsigma s \infty}^{-}(\mathbf{q}, \omega) + \sum_{\lambda} \sum_{\beta=\pm} \chi_{\varsigma s \lambda}^{\beta}(\mathbf{q}, \omega) \theta(\mu_{\varsigma s \lambda} - \Delta_{\varsigma s}), \quad (\text{A.9})$$

其中  $\mu_{\varsigma s \lambda} = |E_{\lambda F}^{\varsigma}| - \lambda \varsigma s \gamma / 2$ ,  $E_{\lambda F}^{\varsigma}$  是在  $\varsigma$  谷导带和价带内电子/空穴的化学势。通过对上式进行积分，可以得到零温下的极化函数

$$\begin{aligned} \Pi_{T=0}^{\varsigma s}(q, \omega) &= \Pi_{0, T=0}^{\varsigma s}(q, \omega) [\tilde{\theta}(\Delta_{\varsigma s} - u_{\varsigma s-}) \tilde{\theta}(\Delta_{\varsigma s} - u_{\varsigma s+}) \\ &\quad - \theta(u_{\varsigma s-} - \Delta_{\varsigma s}) \theta(u_{\varsigma s+} - \Delta_{\varsigma s})] \\ &\quad + \sum_{\lambda} \Pi_{1, T=0}^{\varsigma s \lambda}(q, \omega) \theta(u_{\varsigma s \lambda} - \Delta_{\varsigma s}). \end{aligned} \quad (\text{A.10})$$

在接下来的表述中，为了简化起见，使用  $\omega$  和  $k$  来表示  $\hbar\omega$  和  $atk$ 。在未掺杂的情况下，在  $\varsigma$  谷自旋为  $s$  带的极化函数为<sup>[184]</sup>

$$\begin{aligned} \Pi_{0, T=0}^{\varsigma s}(\mathbf{q}, \omega) &= -\frac{q^2}{4\pi a^2 t^2} \left\{ \frac{\Delta_{\varsigma s}}{q^2 - \omega^2} + \frac{q^2 - \omega^2 - 4\Delta_{\varsigma s}^2}{4|q^2 - \omega^2|^{3/2}} \right. \\ &\quad \times \left[ \theta(q - \omega) \arccos \frac{\omega^2 - q^2 + 4\Delta_{\varsigma s}^2}{q^2 - \omega^2 + 4\Delta_{\varsigma s}^2} \right. \\ &\quad \left. - \theta(\omega - q) \ln \frac{(\sqrt{\omega^2 - q^2} + 2\Delta_{\varsigma s})^2}{|\omega^2 - q^2 - 4\Delta_{\varsigma s}^2|} \right] \left. \right\} \\ &\quad - i \frac{q^2 \tilde{x}_{\varsigma s}^2 \theta(\omega^2 - q^2 - 4\Delta_{\varsigma s}^2)}{16a^2 t^2 |\omega^2 - q^2|^{1/2}}, \end{aligned} \quad (\text{A.11})$$

其中  $\tilde{x}_{\varsigma s}^2 = 2 - x_{\varsigma s}^2$  和  $x_{\varsigma s} = \sqrt{|1 + 4\Delta_{\varsigma s}^2/(q^2 - \omega^2)|}$ 。

对于有限掺杂情况下 ( $\lambda = +$  对应导带掺杂、 $\lambda = -$  对应价带掺杂)，在  $\varsigma$  谷自旋

为  $s$  带的极化函数为

$$\Pi_{1,T=0}^{\varsigma s \lambda}(\mathbf{q}, \omega) = -\frac{u_{\varsigma s}^\lambda}{2\pi a^2 t^2} + \frac{q^2}{16\pi a^2 t^2 |q^2 - \omega^2|^{1/2}} \times \begin{cases} iG_>(y_-) - iG_>(y_+), & 1A \\ G_<(y_-) - iG_>(y_+), & 2A \\ G_<(y_+) + G_<(y_-), & 3A \\ G_<(y_-) - G_<(y_+), & 4A \\ G_>(y_+) - G_>(y_-), & 1B \\ G_>(y_+) + iG_<(y_-), & 2B \\ G_>(y_+) - G_>(-y_-) - i\pi\tilde{x}_{\varsigma s}^2, & 3B \\ G_>(y_+) + G_>(-y_-) - i\pi\tilde{x}_{\varsigma s}^2, & 4B \\ G_0(y_+) - G_0(y_-). & 5B \end{cases} \quad (A.12)$$

其中  $y_\pm = (2u_{\varsigma s}^\lambda \pm \omega)/q$ , 且

$$\begin{aligned} G_<(x) &= x(x_{\varsigma s}^2 - x^2)^{1/2} + (x_{\varsigma s}^2 - 2)\arccos(x/x_{\varsigma s}), \\ G_>(x) &= x(x^2 - x_{\varsigma s}^2)^{1/2} + (x_{\varsigma s}^2 - 2)\text{arccosh}(x/x_{\varsigma s}), \\ G_0(x) &= x(x^2 + x_{\varsigma s}^2)^{1/2} + (-x_{\varsigma s}^2 - 2)\text{arcsinh}(x/x_{\varsigma s}). \end{aligned} \quad (A.13)$$

公式 (A.12) 中所定义的极化函数对应不同的区域 (见图 A.1) 为

$$\begin{aligned} 1A : \omega &\leq u_{\varsigma s}^\lambda - [(k_{\lambda F}^{\varsigma s} - q)^2 + \Delta_{\varsigma s}^2]^{1/2}, \\ 2A : \mp u_{\varsigma s}^\lambda &\pm [(k_{\lambda F}^{\varsigma s} - q)^2 + \Delta_{\varsigma s}^2]^{1/2} < \omega \\ &\leq -u_{\varsigma s}^\lambda + [(k_{\lambda F}^{\varsigma s} + q)^2 + \Delta_{\varsigma s}^2]^{1/2}, \\ 3A : \omega &\leq -u_{\varsigma s}^\lambda + [(k_{\lambda F}^{\varsigma s} - q)^2 + \Delta_{\varsigma s}^2]^{1/2}, \\ 4A : -u_{\varsigma s}^\lambda &+ [(k_{\lambda F}^{\varsigma s} + q)^2 + \Delta_{\varsigma s}^2]^{1/2} < \omega < q, \\ 1B : q &\leq 2k_{\lambda F}^{\varsigma s}, [q^2 + 4\Delta_{\varsigma s}^2]^{1/2} < \omega \\ &\leq u_{\varsigma s}^\lambda + [(k_{\lambda F}^{\varsigma s} - q)^2 + \Delta_{\varsigma s}^2]^{1/2}, \\ 2B : u_{\varsigma s}^\lambda &+ [(k_{\lambda F}^{\varsigma s} - q)^2 + \Delta_{\varsigma s}^2]^{1/2} < \omega \\ &\leq u_{\varsigma s}^\lambda + [(k_{\lambda F}^{\varsigma s} + q)^2 + \Delta_{\varsigma s}^2]^{1/2}, \\ 3B : \omega &> u_{\varsigma s}^\lambda + [(k_{\lambda F}^{\varsigma s} + q)^2 + \Delta_{\varsigma s}^2]^{1/2}, \\ 4B : q &> 2k_{\lambda F}^{\varsigma s}, [q^2 + 4\Delta_{\varsigma s}^2]^{1/2} < \omega \\ &\leq u_{\varsigma s}^\lambda + [(k_{\lambda F}^{\varsigma s} - q)^2 + \Delta_{\varsigma s}^2]^{1/2}, \\ 5B : q &< \omega \leq [q^2 + 4\Delta_{\varsigma s}^2]^{1/2}. \end{aligned}$$

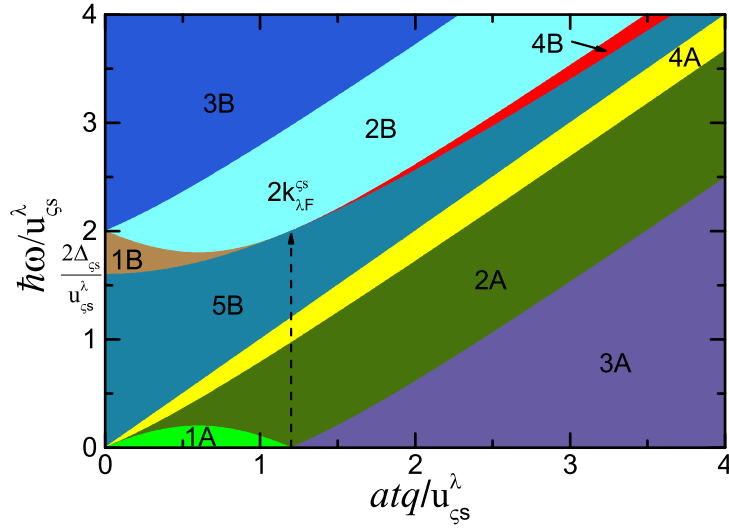


图 A.1: 公式 (A.12) 中极化函数不同表达形式的分割区域。这里取  $\Delta_{\zeta s} = 0.8u_{\zeta s}^\lambda$

其中费米波矢  $k_{\lambda F}^{\zeta s} = \sqrt{|u_{\zeta s}^\lambda|^2 - \Delta_{\zeta s}^2}$ 。

在公式 (6.12) 中单层二硫化钼在二维抛物带中的极化函数可以写作

$$\tilde{\Pi}(\mathbf{q}, \omega) = \sum_{\zeta s \lambda} \tilde{\Pi}_{\lambda}^{\zeta s}(\mathbf{q}, \omega), \quad (\text{A.14})$$

其中

$$\tilde{\Pi}_{\lambda}^{\zeta s}(\mathbf{q}, \omega) = \sum_{\mathbf{k}} \frac{f(\tilde{E}_{\lambda \mathbf{k}}^{\zeta s}) - f(\tilde{E}_{\lambda \mathbf{k} + \mathbf{q}}^{\zeta s})}{\omega + \tilde{E}_{\lambda \mathbf{k}}^{\zeta s} - \tilde{E}_{\lambda \mathbf{k} + \mathbf{q}}^{\zeta s} + i\delta}. \quad (\text{A.15})$$

在零温下, 极化函数  $\tilde{\Pi}_{\lambda, T=0}^{\zeta s}(\mathbf{q}, \omega)$  的实部和虚部分别写为<sup>[6, 188]</sup>

$$\begin{aligned} \text{Re}\tilde{\Pi}_{\lambda, T=0}^{\zeta s}(\mathbf{q}, \omega) = & -\frac{\Delta_{\zeta s}}{2\pi a^2 t^2} \left[ 1 + \sum_{\alpha=\pm} \frac{\alpha \tilde{k}_{\lambda F}^{\zeta s}}{q} \theta(|\nu_{\alpha}^{\zeta s}|^2 - 1) \right. \\ & \times \text{sgn}[\nu_{\alpha}^{\zeta s}] \sqrt{|\nu_{\alpha}^{\zeta s}|^2 - 1} \left. \right] \theta(\tilde{u}_{\zeta s}^{\lambda} - \Delta_{\zeta s}), \end{aligned}$$

和

$$\begin{aligned} \text{Im}\tilde{\Pi}_{\lambda, T=0}^{\zeta s}(\mathbf{q}, \omega) = & -\frac{\Delta_{\zeta s}}{2\pi a^2 t^2} \sum_{\alpha=\pm} \frac{\alpha \tilde{k}_{\lambda F}^{\zeta s}}{q} \theta(1 - |\nu_{\alpha}^{\zeta s}|^2) \\ & \times \sqrt{1 - |\nu_{\alpha}^{\zeta s}|^2} \theta(\tilde{u}_{\zeta s}^{\lambda} - \Delta_{\zeta s}), \end{aligned} \quad (\text{A.16})$$

其中  $\tilde{u}_{\zeta s}^{\lambda} = |\tilde{E}_{\lambda F}^{\zeta s}| - \lambda \zeta s \gamma / 2$ , 费米波矢  $\tilde{k}_{\lambda F}^{\zeta s} = \sqrt{2\Delta_{\zeta s}(\tilde{u}_{\zeta s}^{\lambda} - \Delta_{\zeta s})}$ , 且

$$\nu_{\alpha}^{\zeta s} = \frac{\omega \Delta_{\zeta s}}{q \tilde{k}_{\lambda F}^{\zeta s}} - \alpha \frac{q}{2 \tilde{k}_{\lambda F}^{\zeta s}}. \quad (\text{A.17})$$

在零温和小  $q$  近似下，单层二硫化钼在二维抛物带模型下电荷等离激元模式的色散关系为

$$\tilde{\omega}_q^0 = \left[ e^2 q \sum_{\lambda \varsigma s} (\tilde{u}_{\varsigma s}^\lambda - \Delta_{\varsigma s}) \theta(\tilde{u}_{\varsigma s}^\lambda - \Delta_{\varsigma s}) / (4\pi\epsilon_r\epsilon_0) \right]^{1/2}. \quad (\text{A.18})$$

在有限温度下，全  $q$  下的极化函数写作

$$\begin{aligned} \tilde{\Pi}_{\lambda,T}^{\varsigma s}(\mathbf{q}, \omega; \tilde{\mu}_\lambda^\varsigma) &= \int_{-\infty}^{\infty} \frac{d\mu' \tilde{\Pi}_{\lambda,T=0}^{\varsigma s}(\mathbf{q}, \omega)|_{\tilde{E}_{\lambda F}^\varsigma = \mu'}}{4k_B T \cosh^2[(\tilde{\mu}_\lambda^\varsigma - \mu')/2k_B T]} \\ &\times \theta(|u'| - \lambda \varsigma s \gamma/2 - \Delta_{\varsigma s}), \end{aligned} \quad (\text{A.19})$$

其中  $\tilde{\mu}_\lambda^\varsigma$  是从公式 (6.4) 中得到的导带和价带中的化学势。



## 附录 B 单层二硫化钼中电子-电子相互作用的形状因子

### B.1 电子-电子相互作用的形状因子

令公式 (6.3) 中单层二硫化钼的波函数为  $F_{\lambda\varsigma s\mathbf{k}} = |\mathbf{k}, \lambda\varsigma s\rangle$ , 则电子-电子相互作用的形状因子可以写作

$$C_{\lambda\mathbf{k}, \lambda'\mathbf{k}+\mathbf{q}}^{\varsigma s} = |F_{\lambda'\varsigma s\mathbf{k}}^\dagger \cdot F_{\lambda\varsigma s\mathbf{k}}|^2. \quad (\text{B.1})$$

通过将上述波函数带入进行计算, 带内跃迁和带间跃迁单层二硫化钼中的形状因子可以表示为

$$\begin{aligned} C_{\lambda\mathbf{k}, \lambda'\mathbf{k}+\mathbf{q}}^{\varsigma s} &= \frac{1}{2} [1 + \lambda\lambda' (\cos(\vartheta_{\mathbf{k}+\mathbf{q}}^{\varsigma s}) \cos(\vartheta_{\mathbf{k}}^{\varsigma s}) + \sin(\vartheta_{\mathbf{k}+\mathbf{q}}^{\varsigma s}) \sin(\vartheta_{\mathbf{k}}^{\varsigma s}) \cos \varphi)] \\ &= \frac{1}{2} \left[ 1 + \lambda\lambda' \frac{\Delta_{\varsigma s}^2 + a^2 t^2 \mathbf{k}(\mathbf{k} + \mathbf{q})}{\Lambda^{\varsigma s}(\mathbf{k}) \Lambda^{\varsigma s}(\mathbf{k} + \mathbf{q})} \right]. \end{aligned} \quad (\text{B.2})$$

### B.2 长波极限下电子-电子相互作用形状因子

通过图 B.1 可以得到, 波矢  $\mathbf{k}$  与  $\mathbf{k} + \mathbf{q}$  之间的夹角为  $\varphi$  并且可以得到

$$\cos \varphi = \frac{k + q \cos \theta}{|\mathbf{k} + \mathbf{q}|}. \quad (\text{B.3})$$

在长波极限近似下 ( $\mathbf{q} \rightarrow 0$ ), 可以得到电子-电子相互作用形状因子为

$$\begin{aligned} C_{\lambda\mathbf{k}, \lambda'\mathbf{k}+\mathbf{q}}^{\varsigma s} &= \frac{1}{2} [1 + \lambda\lambda' [\cos^2(\vartheta_{\mathbf{k}}^{\varsigma s}) + \sin^2(\vartheta_{\mathbf{k}}^{\varsigma s}) \cos \varphi]] \\ &= \frac{1}{2} [(1 + \lambda\lambda') - \lambda\lambda' [\sin^2(\vartheta_{\mathbf{k}}^{\varsigma s})(1 - \cos \varphi)]]. \end{aligned} \quad (\text{B.4})$$

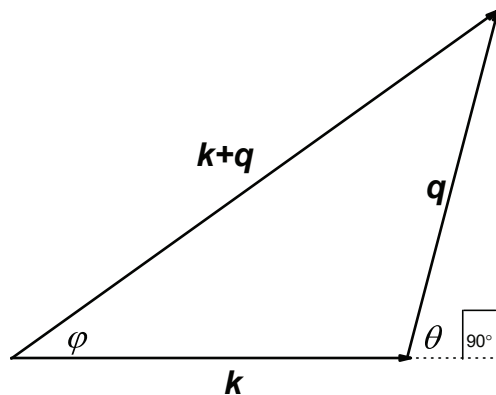


图 B.1: 波矢  $\mathbf{k}$  与  $\mathbf{k} + \mathbf{q}$  之间的夹角  $\varphi$  与波矢  $\mathbf{k}$  和  $\mathbf{q}$  之间的夹角  $\theta$  之间的关系

上式中有关角度  $\varphi$  的项可以写作

$$1 - \cos \varphi = 1 - \sqrt{1 - \frac{q^2 \sin^2 \theta}{k^2 + q^2 + 2kq \cos \theta}}. \quad (\text{B.5})$$

再利用如下关系

$$1 - \sqrt{1 - x} = \frac{x}{1 + \sqrt{1 - x}} \simeq \frac{x}{2}, \quad x \rightarrow 0 \quad (\text{B.6})$$

可以得到

$$1 - \cos \varphi \simeq \frac{q^2 \sin^2 \theta}{2k^2}. \quad (\text{B.7})$$

因而可以得到公式 (6.35) 中长波近似下电子-电子相互作用的形状因子为

$$C_{\lambda\mathbf{k},\lambda'\mathbf{k}+\mathbf{q}}^{\varsigma s} = \frac{1}{2} [(1 + \lambda\lambda') - \lambda\lambda' \sin^2(\vartheta_{\mathbf{k}}^{\varsigma s}) \frac{q^2 \sin^2 \theta}{2k^2}]. \quad (\text{B.8})$$

## 附录 C 计算中用到的重要公式

### C.1 直积

对于  $m \times n$  阶的矩阵 A 和  $p \times q$  阶的矩阵 B

$$A = \begin{pmatrix} a_{11} & a_{12} & \cdots & a_{1n} \\ a_{21} & a_{22} & \cdots & a_{2n} \\ \vdots & \vdots & \ddots & \vdots \\ a_{m1} & a_{m2} & \cdots & a_{mn} \end{pmatrix}, B = \begin{pmatrix} b_{11} & b_{12} & \cdots & b_{1q} \\ b_{21} & b_{22} & \cdots & b_{2q} \\ \vdots & \vdots & \ddots & \vdots \\ b_{p1} & b_{p2} & \cdots & b_{pq} \end{pmatrix}. \quad (\text{C.1})$$

他们的直积(克罗内克积)被定义为

$$A \otimes B = \begin{pmatrix} a_{11}b_{11} & a_{11}b_{12} & \cdots & a_{11}b_{1q} & \cdots & \cdots & a_{1n}b_{11} & a_{1n}b_{12} & \cdots & a_{1n}b_{1q} \\ a_{11}b_{21} & a_{11}b_{22} & \cdots & a_{11}b_{2q} & \cdots & \cdots & a_{1n}b_{21} & a_{1n}b_{22} & \cdots & a_{1n}b_{2q} \\ \vdots & \vdots & \ddots & \vdots & & & \vdots & \vdots & \ddots & \vdots \\ a_{11}b_{p1} & a_{11}b_{p2} & \cdots & a_{11}b_{pq} & \cdots & \cdots & a_{1n}b_{p1} & a_{1n}b_{p2} & \cdots & a_{1n}b_{pq} \\ \vdots & \vdots & & \vdots & \ddots & & \vdots & \vdots & & \vdots \\ \vdots & \vdots & & \vdots & & \ddots & \vdots & \vdots & & \vdots \\ a_{m1}b_{11} & a_{m1}b_{12} & \cdots & a_{m1}b_{1q} & \cdots & \cdots & a_{mn}b_{11} & a_{mn}b_{12} & \cdots & a_{mn}b_{1q} \\ a_{m1}b_{21} & a_{m1}b_{22} & \cdots & a_{m1}b_{2q} & \cdots & \cdots & a_{mn}b_{21} & a_{mn}b_{22} & \cdots & a_{mn}b_{2q} \\ \vdots & \vdots & \ddots & \vdots & & & \vdots & \vdots & \ddots & \vdots \\ a_{m1}b_{p1} & a_{m1}b_{p2} & \cdots & a_{m1}b_{pq} & \cdots & \cdots & a_{mn}b_{p1} & a_{mn}b_{p2} & \cdots & a_{mn}b_{pq} \end{pmatrix}. \quad (\text{C.2})$$

### C.2 泡利矩阵

泡利矩阵的定义为

$$\hat{\sigma}_x = \begin{pmatrix} 0 & 1 \\ 1 & 0 \end{pmatrix}, \hat{\sigma}_y = \begin{pmatrix} 0 & -i \\ i & 0 \end{pmatrix}, \hat{\sigma}_z = \begin{pmatrix} 1 & 0 \\ 0 & -1 \end{pmatrix}. \quad (\text{C.3})$$

### C.3 Kramers-Kronig (K-K) 关系

Kramers-Kronig (K-K) 关系最通用的形式写作

$$\begin{aligned} \operatorname{Re} \chi(\omega + i\delta) &= \frac{1}{\pi} \mathcal{P} \int_{-\infty}^{\infty} d\omega' \frac{\operatorname{Im} \chi(\omega' + i\delta)}{\omega' - \omega} = \frac{2}{\pi} \mathcal{P} \int_0^{\infty} d\omega' \frac{\omega' \operatorname{Im} \chi(\omega' + i\delta)}{\omega'^2 - \omega^2}, \\ \operatorname{Im} \chi(\omega + i\delta) &= \frac{-1}{\pi} \mathcal{P} \int_{-\infty}^{\infty} d\omega' \frac{\operatorname{Re} \chi(\omega' + i\delta)}{\omega' - \omega} = \frac{-2}{\pi} \mathcal{P} \int_0^{\infty} d\omega' \frac{\omega' \operatorname{Re} \chi(\omega' + i\delta)}{\omega'^2 - \omega^2}. \end{aligned} \quad (\text{C.4})$$

其中  $\mathcal{P}$  代表柯西主值.

## C.4 极化函数计算中用到的积分公式

在极化函数的计算过程中，需要处理许多复杂的定积分。下面给出在计算中所用到的一些重要定积分公式。

相关三角函数的积分：

$$\int_0^{2\pi} \frac{dx}{z - \cos x} = \begin{cases} 2\pi|z|/[z\sqrt{z^2 - 1}], & z^2 > 1 \\ 0, & z^2 \leq 1 \end{cases} \quad (\text{C.5})$$

和

$$\int_0^{2\pi} \frac{\cos x dx}{z - \cos x} = \begin{cases} 2\pi[|z|/\sqrt{z^2 - 1} - 1], & z^2 > 1 \\ 0, & z^2 \leq 1. \end{cases} \quad (\text{C.6})$$

在计算在根号内的二次项函数将用到

$$\begin{aligned} \int \sqrt{x^2 - x_0^2} dx &= \frac{1}{2} \{x\sqrt{x^2 - x_0^2} - x_0^2 \ln[(x/x_0) + \sqrt{(x/x_0)^2 - 1}]\} \\ &= \frac{1}{2} [x\sqrt{x^2 - x_0^2} - x_0^2 \operatorname{arccosh}(x/x_0)], \quad |x| > x_0 \\ \int \frac{dx}{\sqrt{x^2 - x_0^2}} &= \ln[(x/x_0) + \sqrt{(x/x_0)^2 - 1}] \\ &= \operatorname{arccosh}(x/x_0), \quad |x| > x_0 \\ \int \sqrt{x_0^2 - x^2} dx &= \frac{1}{2} [x\sqrt{x_0^2 - x^2} + x_0^2 \arcsin(x/x_0)], \quad |x| < x_0 \\ \int \frac{dx}{\sqrt{x_0^2 - x^2}} &= \arcsin(x/x_0) = \frac{\pi}{2} - \arccos(x/x_0), \quad |x| < x_0. \end{aligned} \quad (\text{C.7})$$

对于普通的分母中带有二次项函数的积分有

$$\begin{aligned} \int \frac{dx}{x^2 + a^2} &= \frac{1}{a} \arctan \frac{x}{a} = \frac{1}{a} \arccos \frac{a}{\sqrt{a^2 + x^2}} \\ &= \frac{1}{2a} \arccos \left[ 2 \left( \frac{a}{\sqrt{a^2 + x^2}} \right)^2 - 1 \right] = \frac{1}{2a} \arccos \frac{a^2 - x^2}{a^2 + x^2}, \quad a > 0 \\ \int \frac{dx}{x^2 - a^2} &= \frac{1}{2a} \ln \left| \frac{x-a}{x+a} \right|, \quad |x| > |a| \\ \int \frac{dx}{x^2 - a^2} &= \frac{1}{2a} \ln \left| \frac{a-x}{a+x} \right|, \quad |x| < |a|. \end{aligned} \quad (\text{C.8})$$

## **附录 D The published papers and preprint related to the thesis**

1. Infrared to terahertz absorption window in mono- and multi-layer graphene systems. Optics Communications, 2014, 328: 135-142.
2. Infrared to terahertz optical conductivity of *n*-type and *p*-type monolayer MoS<sub>2</sub> in the presence of Rashba spin-orbit coupling. Physical Review B, 2016, 94: 155432.
3. Multi-component plasmons in monolayer MoS<sub>2</sub> with circularly polarized optical pumping. (Submitted to PRB)



## Infrared to terahertz absorption window in mono- and multi-layer graphene systems



Y.M. Xiao <sup>a</sup>, W. Xu <sup>a,b,\*</sup>, F.M. Peeters <sup>c</sup>

<sup>a</sup> Department of Physics, Yunnan University, Kunming 650091, China

<sup>b</sup> Key Laboratory of Materials Physics, Institute of Solid State Physics, Chinese Academy of Sciences, Hefei 230031, China

<sup>c</sup> Department of Physics, University of Antwerp, Groenenborgerlaan 171, B-2020 Antwerpen, Belgium

### ARTICLE INFO

#### Article history:

Received 18 January 2014

Received in revised form

18 April 2014

Accepted 28 April 2014

Available online 13 May 2014

#### Keywords:

Graphene

AB-stacking

ABC-stacking

Light transmittance

Optical conductance

### ABSTRACT

We present a theoretical study on optical properties such as optical conductance and light transmission coefficient for mono- and multi-layer graphene systems with AB- and ABC-stacking. Considering an air/graphene/dielectric-wafer structure, the optical coefficients for those graphene systems are examined and compared. The universal optical conductance  $\sigma_0^N = N\pi e^2/(2h)$  for  $N$  layer graphene systems in the visible region is verified. For  $N \geq 3$  layer graphene, the mini-gap induced absorption edges can be observed in odd layers AB-stacked multilayer graphene, where the number and position of the absorption edges are decided by the layers number  $N$ . Meanwhile, we can observe the optical absorption windows for those graphene systems in the infrared to terahertz bandwidth (0.2–150 THz). The absorption window is induced by different transition energies required for inter- and intra-band optical absorption channels. We find that the depth and width of the absorption window can be tuned not only via varying temperature and electron density but also by changing the number of graphene layers and the stacking order. These theoretical findings demonstrate that mono- and multi-layer graphene systems can be applied as frequency tunable optoelectronic devices working in infrared to terahertz bandwidth.

© 2014 Elsevier B.V. All rights reserved.

## 1. Introduction

Since the breakthrough discovery of graphene in 2004 [1], the investigation into graphene based novel devices has become a fast-growing field of research due to their extremely useful physical properties, including very high electron mobility, high mechanical strength, excellent thermal conductivity, optoelectronic properties, etc. At present, transparent flexible electronics on the basis of graphene devices is a much sought technology with important applications that can range from foldable displays and electronic paper, to transparent solar cells. It has been found that an air/graphene/dielectric-wafer system has high light transmittance from UV to near-infrared bandwidth. This makes it possible to replace the conventional indium tin oxide (ITO) transparent electrodes [2,3] in producing better and cheaper LED, LCD, etc. The variable optical transmittance in graphene systems can make a new breed of optical modulators with broad optical and electrical bandwidths [4–6]. Meanwhile, graphene based photodetectors have also received considerable attention because of the broad spectral bandwidth and ultrafast response time [7–9]. It has been

shown that graphene is an intrinsically two-dimensional (2D) material with sensitive electrostatic perturbation conductance induced by photo-generated carriers close to the surface which makes graphene a particularly promising material for high gain photo-detection by employing the photo-gating effect [10]. Moreover, graphene has been considered as a promising candidate for photosensitive terahertz ( $10^{12}$  Hz or THz) devices, due to its gapless density of states and high quantum efficiency. It has been demonstrated experimentally that the optical conductivity of graphene in THz regime can be well described by the Drude model, implying that graphene is a metallic like THz material [11]. In addition, the strong nonlinear optical response in mono- and bi-layer graphene systems from THz to far-infrared regime makes graphene a preferred material for nonlinear photonics and optoelectronics devices [12,13].

It is known that mono- and bi-layer graphene systems are gapless 2D electronic structures, whereas the ABC-stacked tri-layer graphene becomes a semiconductor with tunable fundamental band gap. For multilayer graphene films, the electronic structures depend strongly on layers number and stacking order. Thus, the features of electronic band structure can directly affect the electronic and optical properties of graphene systems with different graphene layers. At present, the low-cost and reliable growth of high quality and large size graphene films are mainly

\* Corresponding author at: Department of Physics, Yunnan University, Kunming 650091, China.

E-mail address: [wexu\\_issp@aliyun.com](mailto:wexu_issp@aliyun.com) (W. Xu).

based on a chemical vapor deposition (CVD) technique [14]. Multi-layer graphene samples are the main products of the CVD growth. In recent years, the optical and optoelectronic properties of different graphene systems have been investigated intensively. Theoretically, the electronic band structures for systems with different graphene layers have been examined [15–17,27–29]. The low-temperature optical conductivity for both monolayer and AB-stacked multilayer graphene was calculated using the Kubo formula [18], where optical properties for different graphene systems were examined in UV to far-infrared regime. Experimentally, the optical properties of epitaxial graphene from visible to THz range were measured and the high transmittance windows were observed in infrared and THz regime for multilayer graphene systems [19]. It has been found that the optical conductance per graphene layer is a universal value  $\sigma_0 = \pi e^2/(2h)$  in visible bandwidth [20,21]. The corresponding light transmittances for mono-, bi- and tri-layer graphene are about 97.7%, 95.4% and 93.1%, respectively, and the opacity is about 2.3% per graphene layer [22]. Furthermore, it has been observed that there exists an optical absorption window in mono-layer graphene at room-temperature [20,21] in the mid-infrared to THz regime. The width and depth of this absorption window in monolayer graphene depend strongly on temperature and carrier density, especially at the lower frequency edge. These findings imply that graphene systems can be applied for infrared or THz detection in ambient condition. Our previous theoretical work [23] shown that the THz absorption window can also be achieved in bilayer graphene systems.

Currently, the major results for optical properties of mono- and bi-layer graphene systems have been well documented. However, less research work has been conducted for graphene systems with layer number  $N \geq 3$ . Most theoretical work on optical properties of multi-layer graphene has been focused mainly on ultraviolet to infrared absorption peaks and universal optical conductance observed in visual light regime [18]. In this paper, we employ the effective low-energy model to study the responses of mono- and multi-layer graphene systems to the radiation field. It is known qualitatively that in infrared to THz region, the number of graphene layers must have influence on optical properties of the graphene systems. It is of great importance and significance to provide a quantitative answer about how optoelectronic properties of mono- and multi-layer graphene systems vary with the number of graphene layers and with the stacking orders. This becomes a prime motivation of the present theoretical study.

## 2. Theoretical approaches

We consider that a graphene sheet is placed on the  $xy$ -plane on top of a dielectric wafer such as  $\text{SiO}_2$  substrate and a weak radiation field is applied with linear polarization along the  $x$ -direction. The vector potential of the light field is  $A(t) = F_0 \sin(2\pi\nu t)/(2\pi\nu)$ , where  $F_0$  and  $\nu$  are the electric field strength and the frequency of the light field, respectively. The optoelectronic response of the graphene system in such a situation can be studied through the balance equation approach [24] derived from the semiclassical Boltzmann equation. With this approach, the total energy transfer rate can be evaluated via  $P = \sum_{\lambda,\lambda'} P_{\lambda\lambda'}$ , where  $\lambda = +1$  for conduction band and  $\lambda = -1$  for valence band,  $P_{\lambda\lambda'} = 4h\nu \sum_{\mathbf{k},\mathbf{k}'} f_{\lambda}(\mathbf{k})[1 - f_{\lambda'}(\mathbf{k}')]W_{\lambda\lambda'}(\mathbf{k}, \mathbf{k}')$  is the energy transfer rate induced by different transition channels,  $W_{\lambda\lambda'}(\mathbf{k}, \mathbf{k}')$  is the electronic transition rate obtained from Fermi's golden rule, and  $f_{\lambda}(\mathbf{k}) \simeq f_{\lambda}[E_{\lambda}(\mathbf{k})]$  is the Fermi-Dirac distribution function for carriers in graphene. For a relatively weak radiation field, the optical conductivity can be calculated through  $\sigma(\nu) = 2P/F_0^2 = \sum_{\lambda,\lambda'} \sigma_{\lambda\lambda'}(\nu)$ . Furthermore, the optical transmission coefficient for an air/

graphene/dielectric-wafer system can be evaluated via [25]

$$T^i(\nu) = \sqrt{\frac{\epsilon_2^i}{\epsilon_1}} \frac{4(\epsilon_1 \epsilon_0)^2}{[(\epsilon_1 \epsilon_2^i)^{1/2} + \epsilon_1] \epsilon_0 + \sqrt{\epsilon_1} \sigma^i(\nu)/c]^2}, \quad (1)$$

where  $\sigma^i(\nu)$  is the optical conductivity for an  $i$ -layer graphene system at a radiation frequency  $\nu$ ,  $\epsilon_1 = 1$  and  $\epsilon_2^i = \epsilon_{\infty}^i$  are the dielectric constant of free space and the effective high-frequency dielectric constant of the substrate for different systems, respectively, and  $c$  is the speed of light in vacuum.

### 2.1. Monolayer graphene

The massless Dirac-Weyl quasiparticles of monolayer graphene for a carrier (an electron or a hole) in the monolayer graphene in the  $\pi$ -bands near the  $K$ -point can be described by a  $\mathbf{k} \cdot \mathbf{p}$  Hamiltonian

$$H_0^m = \begin{pmatrix} 0 & \hbar v_0 k_- \\ \hbar v_0 k_+ & 0 \end{pmatrix}, \quad (2)$$

where  $k_{\pm} = k_x \pm ik_y = ke^{\pm i\phi}$  with  $v_0 = 10^6$  m/s being the Fermi velocity,  $\mathbf{k} = (k_x, k_y)$  is the wavevector for a carrier, and  $\phi$  is the angle between  $\mathbf{k}$  and the  $x$ -axis. The eigenfunction and the energy eigenvalue are given by  $\psi_{\lambda\mathbf{k}}^m(\mathbf{r}) = 2^{1/2} [e^{-i\phi}, \lambda] e^{i\mathbf{k}\cdot\mathbf{r}}$  and  $E_{\lambda}^m(\mathbf{k}) = \lambda \hbar v_0 k$ , respectively, where  $\lambda = +1$  for electron and  $\lambda = -1$  for hole. Here, the eigenfunction is in a form of row matrix. In the presence of a weak light field applied perpendicular to the graphene sheet and polarized along the  $x$ -direction, the steady-state electronic transition rate induced by direct carrier-photon interaction can be obtained by using Fermi's golden rule, which reads

$$W_{\lambda\lambda'}^m(\mathbf{k}, \mathbf{k}') = \frac{2\pi}{\hbar} \left( \frac{eF_0v_0}{4\pi\nu} \right)^2 \frac{1 + \lambda\lambda' \cos(2\phi)}{2} \times \delta_{\mathbf{k}, \mathbf{k}'} \delta[E_{\lambda'}^m(\mathbf{k}') - E_{\lambda}^m(\mathbf{k}) - h\nu]. \quad (3)$$

It measures the probability for scattering of a carrier from a state  $|\mathbf{k}, \lambda\rangle$  to a state  $|\mathbf{k}', \lambda'\rangle$ . After considering the effect of the broadening of the scattering states due to energy relaxation through Poisson Kernel:  $\delta(E) \rightarrow (E_{\tau}/\pi)(E^2 + E_{\tau}^2)^{-1}$  to replace the  $\delta$  function for intra-band optical transition and using the identity  $\int_0^{\infty} f(x)\delta[g(x)] dx = f(x)/|g'(x)|$  in the case that  $g(x) = 0$  has only a single root for interband optical transition, we can obtain

$$\sigma_{\lambda\lambda'}^m(\nu) = \frac{2\sigma_0 v_0^2}{\pi^2 \nu} \frac{\tau}{(2\pi\nu\tau)^2 + 1} \int_0^{\infty} dk k f_{\lambda}^m(E_{\lambda}^m(\mathbf{k})) \times \{1 - f_{\lambda'}^m(E_{\lambda'}^m(\mathbf{k}))\}, \quad (4)$$

for transition within the conduction band and valence band, where  $\tau$  is the energy relaxation time,  $E_{\tau} = \hbar/\tau$  is the energy broadening of the states, and  $\sigma_0 = \pi e^2/(2h)$ .

For interband transition channels, we have  $\sigma_{+-}^m(\nu) \simeq 0$  and  $\sigma_{-+}^m(\nu) = \sigma_0 f_{-}(-h\nu/2)[1 - f_{+}(h\nu/2)]$ . (5)

### 2.2. Bilayer graphene

After including the various interlayer coupling such as the near-neighbor and the next-nearest neighbor interactions, the effective Hamiltonian for a carrier (an electron or a hole) in the bilayer graphene in the  $\pi$ -bands near the  $K$ -point can be written as [15]

$$H_0^b = \begin{pmatrix} 0 & \hbar^2 k_-^2 / (2m^*) - \hbar u_3 k_+ \\ \hbar^2 k_+^2 / (2m^*) - \hbar u_3 k_- & 0 \end{pmatrix}, \quad (6)$$

where  $m^* = \xi_1/(2u_0^2)$ ,  $u_i = \sqrt{3}a\xi_i/2\hbar$ ,  $p = \hbar k$  and  $a = 2.46$  Å. Moreover, we quote  $\xi_0 = 3.16$  eV,  $\xi_1 = 0.39$  eV,  $\xi_3 = 0.315$  eV for typical coupling values [26,27] in bilayer graphene. The corresponding Schodinger equation can be solved analytically and the eigenvalue is given as  $E_{\lambda}^b(\mathbf{k}) = \lambda A$ , where  $A = [h_a^2 + h_b^2 - 2 \cos(3\phi)h_a h_b]^{1/2}$ ,

$h_a = p^2/(2m^*)$ , and  $h_b = pu_3$ . The eigenfunction for a carrier in bilayer graphene is  $\psi_{\lambda\kappa}^b(\mathbf{r}) = 2^{-1/2}[(h_a e^{-2i\phi} - h_b e^{i\phi})/A, \lambda]e^{i\kappa\mathbf{r}}$ , in the form of a row matrix, with  $\mathbf{r} = (x, y)$ . In the presence of a weak light field applied perpendicular to the bilayer graphene sheet, the carrier-photon interaction Hamiltonian within the usual Coulomb gauge for bilayer graphene becomes

$$H_{cp}^b(t) = \frac{eA(t)}{m^*} \begin{pmatrix} 0 & m^* u_3 - \hbar k_- \\ m^* u_3 - \hbar k_+ & 0 \end{pmatrix}. \quad (7)$$

Here, the contribution from the  $F_0^2$  term has been neglected. Then the first-order contribution to the steady-state electronic transition rate induced by carrier-photon interaction via absorption scattering is obtained as

$$W_{\lambda\lambda'}^b(\mathbf{k}, \mathbf{k}') = \frac{2\pi}{\hbar} \left( \frac{eF_0}{4\pi m^*\nu} \right)^2 \frac{|U_{\lambda\lambda'}^b(\mathbf{k})|^2}{4A^2} \delta_{\mathbf{k}', \mathbf{k}} \times \delta[E_{\lambda'}^b(\mathbf{k}') - E_{\lambda}^b(\mathbf{k}) - \hbar\nu], \quad (8)$$

with  $|U_{\lambda\lambda'}^b(\mathbf{k})|^2 = |\lambda' (h_a e^{-2i\phi} - h_b e^{i\phi}) + \lambda(h_a e^{2i\phi} - h_b e^{-i\phi})| m^* u_3 + \hbar k[\lambda'(h_b e^{2i\phi} - h_a e^{-i\phi}) + \lambda(h_b e^{-2i\phi} - h_a e^{i\phi})]|^2$ . After considering the effect of the broadening of the scattering states due to energy relaxation through Poisson Kernel, we have

$$\sigma_{\lambda\lambda}^b(\nu) = \frac{4\sigma_0}{\pi^3 \nu (m^*)^2} \frac{\tau}{(2\pi\nu\tau)^2 + 1} \int_0^\pi d\phi \int_0^\infty \frac{dk}{A^2} f_+ [E_{\lambda}^b(\mathbf{k})] \{1 - f_+[E_{\lambda}^b(\mathbf{k})]\} G_{\lambda\lambda}^b(k, \phi), \quad (9)$$

for transition within the conduction band and valance band, where  $G_{\lambda\lambda}^b(k, \phi) = [m^* u_3 (h_a \cos 2\phi - h_b \cos \phi) + \hbar k (h_b \cos 2\phi - h_a \cos \phi)]^2$ .

For interband transition channels, we have  $\sigma_{+-}^b(\nu) \approx 0$  and

$$\sigma_{-+}^b(\nu) = \frac{4\sigma_0}{\pi^3 \nu (m^*)^2} \int_0^\pi d\phi \int_0^\infty \frac{dk}{A^2} [1 - f_+(\hbar\nu/2)] \times f_-(-\hbar\nu/2) \frac{\tau C_{-+}^b(k, \phi)}{4\tau^2 (\pi\nu - A/\hbar)^2 + 1}, \quad (10)$$

where  $G_{-+}^b(k, \phi) = [m^* u_3 (-h_a \sin 2\phi - h_b \sin \phi) + \hbar k (h_b \sin 2\phi + h_a \sin \phi)]^2$ .

### 2.3. ABC-stacked trilayer graphene

The effective Hamiltonian for a carrier (an electron or a hole) in low-energy regime in ABC-stacked tri-layer graphene (TLG) in the  $\pi$ -bands near the  $K$ -point is [17]

$$H_0^t = \begin{pmatrix} S_1 & S_0 \hbar^3 k_-^3 + S_2 \\ S_0 \hbar^3 k_+^3 + S_2 & S_1 \end{pmatrix}, \quad (11)$$

where  $S_0 = 3^{3/2} a^3 \gamma_0^3 / (8\hbar^3 \gamma_1^2)$ ,  $S_1 = \gamma_5 - 3\gamma_0 \gamma_4 k^2 a^2 / (2\gamma_1)$ , and  $S_2 = \gamma_2/2 - 3\gamma_0 \gamma_3 k^2 a^2 / (2\gamma_1)$ , with the typical hoping parameters [17]  $\gamma_0 = 3.16$  eV,  $\gamma_1 = 0.502$  eV,  $\gamma_2 = -0.0171$  eV,  $\gamma_3 = -0.377$  eV,  $\gamma_4 = -0.099$  eV,  $\gamma_5 = -0.0014$  eV. The corresponding Schodinger equation can be solved analytically and the eigenvalue is given as  $E_{\lambda}^t(\mathbf{k}) = S_1 + \lambda B$  with  $B = [S_0^2 \hbar^6 k^6 + S_2^2 + 2 \cos(3\phi) S_0 S_2 \hbar^3 k^3]^{1/2}$ . The corresponding eigenfunction for a carrier in ABC-stacked TLG is  $\psi_{\lambda\kappa}^t(\mathbf{r}) = 2^{1/2} [e^{i\kappa\mathbf{r}}, \lambda] e^{i\kappa\mathbf{r}}$ , in the form of a row matrix, with  $e^{i\kappa\mathbf{r}} = (S_0 \hbar^3 k^3 e^{-3i\phi} + S_2)/B$  and  $\mathbf{r} = (x, y)$ . The carrier-photon interaction Hamiltonian for a ABC-stacked TLG becomes

$$H_{cp}^t(t) = \frac{eA(t)}{\hbar} \begin{pmatrix} Q_1 & Q_2 - 3S_0 \hbar^3 k_-^2 \\ Q_2 - 3S_0 \hbar^3 k_+^2 & Q_1 \end{pmatrix}, \quad (12)$$

with  $Q_1 = 3\gamma_0 \gamma_4 a^2 k \cos \phi / \gamma_1$  and  $Q_2 = Q_1 \gamma_3 / \gamma_4$ . Here we have ignored the contributions from  $F_0^2$  and  $F_0^3$  terms in case of a weak light field. Then the first-order contribution to the steady-state

electronic transition rate induced by carrier-photon interaction via absorption scattering is obtained as

$$W_{\lambda\lambda'}^t(\mathbf{k}, \mathbf{k}') = \frac{2\pi}{\hbar} \left( \frac{eF_0}{4\pi\nu} \right)^2 \frac{|U_{\lambda\lambda'}^t(\mathbf{k})|^2}{4B^2} \delta_{\mathbf{k}', \mathbf{k}} \times \delta[E_{\lambda'}^t(\mathbf{k}') - E_{\lambda}^t(\mathbf{k}) - \hbar\nu], \quad (13)$$

where  $|U_{\lambda\lambda'}^t(\mathbf{k})|^2 = |-3S_0 \hbar^2 k^2 [\lambda' (S_0 \hbar^3 k^3 e^{-i\phi} + S_2 e^{2i\phi}) + \lambda (S_0 \hbar^3 k^3 e^{i\phi} + S_2 e^{-2i\phi})] + [\lambda' (S_0 \hbar^3 k^3 e^{-3i\phi} + S_2) + \lambda (S_0 \hbar^3 k^3 e^{3i\phi} + S_2)] Q_2 / \hbar + (1 + \lambda \lambda') Q_1 B / \hbar|^2$ . Using Poisson Kernel to replace the  $\delta$ -function, we have

$$\sigma_{++}^t(\nu) = \frac{4\sigma_0}{\pi^3 \hbar^2 \nu} \frac{\tau}{(2\pi\nu\tau)^2 + 1} \int_0^\pi d\phi \int_0^\infty \frac{dk}{B^2} f_+ [E_+^t(\mathbf{k})] \times \{1 - f_+[E_+^t(\mathbf{k})]\} G_{++}^t(k, \phi), \quad (14)$$

for transition within the conduction band with  $G_{++}^t(k, \phi) = [Q_1 B - 3S_0 \hbar^3 k^2 (S_0 \hbar^3 k^3 \cos \phi + S_2 \cos 2\phi) + (S_0 \hbar^3 k^3 \cos 3\phi + S_2) Q_2]^2$ . For transition within the valance band, we obtain

$$\sigma_{--}^t(\nu) = \frac{4\sigma_0}{\pi^3 \hbar^2 \nu} \frac{\tau}{(2\pi\nu\tau)^2 + 1} \int_0^\pi d\phi \int_0^\infty \frac{dk}{B^2} f_- [E_-^t(\mathbf{k})] \times \{1 - f_-[E_-^t(\mathbf{k})]\} G_{--}^t(k, \phi), \quad (15)$$

with  $G_{--}^t(k, \phi) = [3S_0 \hbar^3 k^2 (S_0 \hbar^3 k^3 \cos \phi + S_2 \cos 2\phi) - (S_0 \hbar^3 k^3 \cos 3\phi + S_2) Q_2 + Q_1 B]^2$ .

For interband transition channels, we have  $\sigma_{+-}^t(\nu) \approx 0$  and

$$\sigma_{-+}^t(\nu) = \frac{2\sigma_0 \tau}{\pi^2 \hbar^2 \nu} \int_0^\pi d\phi \int_0^\infty \frac{dk}{B^2} e^{-|\tau(2\pi\nu - 2B/\hbar)|} \times f_- [E_-^t(\mathbf{k})] \{1 - f_+[E_+^t(\mathbf{k})]\} G_{-+}^t(k, \phi), \quad (16)$$

where  $G_{-+}^t(k, \phi) = [3S_0 \hbar^3 k^2 (S_0 \hbar^3 k^3 \sin \phi - S_2 \sin 2\phi) - S_0 Q_2 \hbar^3 k^3 \sin 3\phi]^2$  and we have taken an approximation  $\delta(E) \rightarrow e^{-|E|/E_r} / (2E_r)$  to replace the  $\delta$ -function.

### 2.4. AB-stacked multilayer graphene

For AB-stacked  $N$ -layer graphene with  $N \geq 3$ , the electronic Hamiltonian can be approximately decomposed into subsystems equivalent to monolayer or bilayer graphene and the total optical conductivity can be regarded as a summation over each subsystems [18,26,27]. The Hamiltonian of odd-layered graphene is composed of one monolayer-type and  $(N-1)/2$  bilayer-type subbands, while that of even-layered graphene is only composed of  $N/2$  bilayers [28]. When we focus mainly on the optical response to long wavelength radiation field, the reduced effective low-energy Hamiltonian for mono- and bi- layer subsystems can be considered as [28,29]

$$H_{AB}^M = \begin{pmatrix} q\eta_2 & v_0 \hbar k_- \\ v_0 \hbar k_+ & q\eta_5 \end{pmatrix}, \quad (17)$$

and

$$H_{AB}^{Bj} = \begin{pmatrix} \alpha_j \eta_2 & -v_0^2 \hbar^2 k_-^2 / (\mu_j \xi_1) \\ -v_0^2 \hbar^2 k_+^2 / (\mu_j \xi_1) & \beta_j \eta_2 \end{pmatrix}, \quad (18)$$

where  $\eta_2 = -0.02$  eV,  $\eta_5 = 0.04$  eV,  $q = (1-N)/(N+1)$ ,  $u_j = 2 \cos(\kappa_j)$ ,  $\kappa_j = \pi/2 - j\pi/(2N+2)$  and  $j$  denotes the index of bilayer subsystem which ranges as

$$j = \begin{cases} 1, 3, 5, \dots, N-1, & N = \text{even}, \\ 2, 4, 6, \dots, N-1, & N = \text{odd}. \end{cases} \quad (19)$$

In addition, we have  $\alpha_j = \beta_j = [N \cos(2\kappa_j) + 1]/(N+1)$  for even  $N$ ,  $\alpha_j = [(N-1) \cos(2\kappa_j) + 2]/(N+1)$  and  $\beta_j = \cos(2\kappa_j)$  for odd  $N$  [27]. For monolayer subsystem, the corresponding eigenvalue and

eigenfunction can be written as

$$E_{N\lambda}^M(\mathbf{k}) = \frac{g(\eta_2 + \eta_5)}{2} + \lambda \sqrt{\frac{q^2(\eta_2 - \eta_5)^2}{4} + v_0^2 \hbar^2 k^2}, \quad (20)$$

and

$$\psi_{N\lambda\mathbf{k}}^M(\mathbf{r}) = \mathbb{N}_{N\lambda}^M [R_{N\lambda}^M e^{-i\phi}, 1] e^{i\mathbf{k}\cdot\mathbf{r}}, \quad (21)$$

respectively, where  $R_{N\lambda}^M = v_0 \hbar k / (E_{N\lambda}^M(\mathbf{k}) - q\eta_2)$  and  $\mathbb{N}_{N\lambda}^M = [1 + (R_{N\lambda}^M)^2]^{-1/2}$ . For the bilayer subsystem  $B_j$ , the corresponding eigenvalue and eigenfunction are

$$E_{N\lambda}^{B_j}(\mathbf{k}) = \frac{\eta_2(\alpha_j + \beta_j)}{2} + \lambda \sqrt{\frac{\eta_2^2(\alpha_j - \beta_j)^2}{4} + v_0^4 \hbar^4 k^4 / \mu_j^2 \xi_1^2}, \quad (22)$$

and

$$\psi_{N\lambda\mathbf{k}}^{B_j}(\mathbf{r}) = \mathbb{N}_{N\lambda}^{B_j} [R_{N\lambda}^{B_j} e^{-2i\phi}, 1] e^{i\mathbf{k}\cdot\mathbf{r}}, \quad (23)$$

where  $R_{N\lambda}^{B_j} = v_0^2 \hbar^2 k^2 / [\mu_j \xi_1 (\alpha_j \eta_2 - E_{N\lambda}^{B_j}(\mathbf{k}))]$  and  $\mathbb{N}_{N\lambda}^{B_j} = [1 + (R_{N\lambda}^{B_j})^2]^{-1/2}$ . In the presence of a weak and linearly polarized radiation field, the first-order contribution to the steady-state electronic transition rate induced by carrier–photon interaction via absorption scattering for mono- and bi-layer subsystems is obtained as

$$W_{N\lambda\lambda'}^M(\mathbf{k}, \mathbf{k}') = \frac{2\pi}{\hbar} \left( \frac{eF_0 v_0}{4\pi\nu} \right)^2 |U_{N\lambda\lambda'}^M(\mathbf{k})|^2 \delta_{\mathbf{k}', \mathbf{k}} \times \delta[E_{N\lambda'}^M(\mathbf{k}') - E_{N\lambda}^M(\mathbf{k}) - h\nu], \quad (24)$$

where  $|U_{N\lambda\lambda'}^M(\mathbf{k})|^2 = (\mathbb{N}_{N\lambda}^M \mathbb{N}_{N\lambda'}^M)^2 [(R_{N\lambda}^M)^2 + (R_{N\lambda'}^M)^2 + 2 \cos(2\phi) R_{N\lambda}^M R_{N\lambda'}^M]$ , and

$$W_{N\lambda\lambda'}^{B_j}(\mathbf{k}, \mathbf{k}') = \frac{2\pi}{\hbar} \left( \frac{eF_0 v_0^2 \hbar k}{2\pi\nu \mu_j \xi_1} \right)^2 |U_{N\lambda\lambda'}^{B_j}(\mathbf{k})|^2 \delta_{\mathbf{k}', \mathbf{k}} \times \delta[E_{N\lambda'}^{B_j}(\mathbf{k}') - E_{N\lambda}^{B_j}(\mathbf{k}) - h\nu], \quad (25)$$

where  $|U_{N\lambda\lambda'}^{B_j}(\mathbf{k})|^2 = (\mathbb{N}_{N\lambda}^{B_j} \mathbb{N}_{N\lambda'}^{B_j})^2 [(R_{N\lambda}^{B_j})^2 + (R_{N\lambda'}^{B_j})^2 + 2 \cos(2\phi) R_{N\lambda}^{B_j} R_{N\lambda'}^{B_j}]$ , respectively.

For odd AB-stacked multilayer, the intraband optical conductivity of monolayer subsystem is

$$\sigma_{N\lambda\lambda}^M(\nu) = \frac{8\sigma_0 v_0^2}{\pi^2 \nu} \frac{\tau}{(2\pi\nu\tau)^2 + 1} \int_0^\infty dk k \left\{ 1 - f_\lambda [E_{N\lambda}^M(\mathbf{k})] \right\} \\ \times f_\lambda [E_{N\lambda}^M(\mathbf{k})] (\mathbb{N}_{N\lambda}^M)^4 (R_{N\lambda}^M)^2, \quad (26)$$

within the conduction band and valence band. For interband transition channels, we have  $\sigma_{N+ -}^M(\nu) \simeq 0$  and

$$\sigma_{N- +}^M(\nu) = 2\sigma_0 (\mathbb{N}_{N-}^M \mathbb{N}_{N+}^M)^2 [(R_{N-}^M)^2 + (R_{N+}^M)^2] f_- [E_{N-}^M(\mathbf{k})] \\ \times \{1 - f_+ [E_{N+}^M(\mathbf{k})]\}, \quad (27)$$

where  $k = [h^2 \nu^2 - q^2(\eta_2 - \eta_5)^2]^{1/2} / (2v_0 \hbar)$  for an incident radiation frequency  $\nu$  in monolayer subsystem.

As for the  $B_j$  subsystem in AB-stacked multilayer graphene, we have

$$\sigma_{N\lambda\lambda}^{B_j}(\nu) = \frac{32\sigma_0 v_0^4 \hbar^2}{\pi^2 \nu \mu_j^2 \xi_1^2} \frac{\tau}{(2\pi\nu\tau)^2 + 1} \int_0^\infty dk k^3 f_\lambda [E_{N\lambda}^{B_j}(\mathbf{k})] \\ \times \{1 - f_\lambda [E_{N\lambda}^{B_j}(\mathbf{k})]\} (\mathbb{N}_{N\lambda}^{B_j})^4 (R_{N\lambda}^{B_j})^2, \quad (28)$$

for intraband transitions within the conduction band and valence band. For interband transition channels, we have  $\sigma_{N+ -}^{B_j}(\nu) \simeq 0$  and

$$\sigma_{N- +}^{B_j}(\nu) = 4\sigma_0 (\mathbb{N}_{N-}^{B_j} \mathbb{N}_{N+}^{B_j})^2 [(R_{N-}^{B_j})^2 + (R_{N+}^{B_j})^2] f_- [E_{N-}^{B_j}(\mathbf{k})] \\ \times \{1 - f_+ [E_{N+}^{B_j}(\mathbf{k})]\}, \quad (29)$$

where  $k = \{[h^2 \nu^2 - \eta_2^2(\alpha_i - \beta_i)^2] \mu_j^2 \xi_1^2\}^{1/4} / (2^{1/2} v_0 \hbar)$  for an incident radiation frequency  $\nu$  in the  $B_j$  bilayer subsystem.

After combining the contributions from each subsystem, the total optical conductivity for an  $N$ -layer AB-stacked graphene

becomes

$$\sigma_N^{AB}(\nu) = \delta_{N,\text{odd}} \sum_{\lambda, \lambda'} \sigma_{N\lambda\lambda'}^M(\nu) + \sum_j \sum_{\lambda, \lambda'} \sigma_{N\lambda\lambda'}^{B_j}(\nu). \quad (30)$$

## 2.5. ABC-stacked multilayer graphene

The ABC-stacked  $N$ -layer graphene with  $N \geq 3$  constitutes a physical realization of a chiral two-dimensional electron gas (2DEG) with effective low-energy Hamiltonian as [17,29]

$$H_{ABC}^N = \frac{v_0^N}{\gamma_1^{N-1}} \begin{pmatrix} 0 & (\hbar k_-)^N \\ (\hbar k_+)^N & 0 \end{pmatrix}. \quad (31)$$

The corresponding eigenvalue and eigenfunction for an ABC-stacked  $N$ -layer graphene with a chirality  $J=N$  can be written as  $E_\lambda^J(\mathbf{k}) = \lambda(v_0 \hbar k)^N / \gamma_1^{N-1}$  and  $\psi_{\lambda\mathbf{k}}^J(\mathbf{r}) = 2^{1/2} [\lambda, e^{iN\phi}] e^{i\mathbf{k}\cdot\mathbf{r}}$ , respectively. In the presence of a linearly polarized light field, the first-order contribution to the steady-state electronic transition rate induced by carrier–photon interaction via absorption scattering is obtained as

$$W_{\lambda\lambda'}^J(\mathbf{k}, \mathbf{k}') = \frac{2\pi}{\hbar} \left( \frac{eF_0 N v_0^N (\hbar k)^{N-1}}{4\pi\nu \gamma_1^{N-1}} \right)^2 \frac{1 + \lambda \lambda' \cos(2\phi)}{2} \\ \times \delta_{\mathbf{k}', \mathbf{k}} \delta [E_{\lambda'}^J(\mathbf{k}') - E_\lambda^J(\mathbf{k}) - h\nu]. \quad (32)$$

Following the same theoretical approach for calculating the optical conductance, for ABC-stacked  $N$ -layer graphene we have

$$\sigma_{\lambda\lambda}^J(\nu) = \frac{2\sigma_0 N^2 v_0^{2N} \hbar^{2N-2}}{\pi^2 \nu \gamma_1^{2N-2}} \frac{\tau}{(2\pi\nu\tau)^2 + 1} \int_0^\infty dk k^{2N-1} \\ \times f_\lambda [E_\lambda^J(\mathbf{k})] \{1 - f_\lambda [E_\lambda^J(\mathbf{k})]\}, \quad (33)$$

for intraband transitions within the conduction band and valence band. For interband transition channels, we have  $\sigma_{+ -}^J(\nu) \simeq 0$  and  $\sigma_{- +}^J(\nu) = N\sigma_0 f_-(-h\nu/2) [1 - f_+(h\nu/2)]$ .

## 3. Results and discussions

In this study, we consider that the conducting carriers in a graphene system are electrons in the absence of the light radiation. The dark electron density is  $n_0$ . In the presence of the radiation field, the total electron density becomes  $n_e = n_0 + \Delta n_e$ , where  $\Delta n_e$  is the density of photoexcited electrons, and the hole density is  $n_h = \Delta n_e$  due to the law of charge number conservation.

The chemical potential  $\mu_i^\lambda$  for electrons and holes in mono-, bi-, and ABC-stacked multi-layer graphene can be determined, respectively, through  $n_e^i = g \sum_{\mathbf{k}} f_+ [E_+^i(\mathbf{k})]$  and  $n_h^i = g \sum_{\mathbf{k}} \{1 - f_- [E_-^i(\mathbf{k})]\}$ , where  $g=4$  counts for spin and valley degeneracy. For AB-stacked multi-layer graphene, the chemical potential for electrons and holes are determined through  $n_e^N = g \sum_{\mathbf{k}} f_+ [E_{N+}^M(\mathbf{k})] \delta_{N,\text{odd}} + \sum_j f_+ [E_{N+}^{B_j}(\mathbf{k})]$  and  $n_h^N = g \sum_{\mathbf{k}} \{1 - f_- [E_{N-}^M(\mathbf{k})]\} \delta_{N,\text{odd}} + \sum_j \{1 - f_- [E_{N-}^{B_j}(\mathbf{k})]\}$ , respectively. For the calculation of optical transmittance, we take  $\epsilon_1^m = 1.2$ ,  $\epsilon_2^b = 1.3$  and  $\epsilon_2^c = 1.5$  for mono-, bi- and ABC-stacked tri-layer graphene system, respectively, where the effect of the dielectric constant mismatch between graphene film and the substrate layer has been taken into account [30]. Furthermore, the energy relaxation time for a high-density graphene device [31] is found to be about  $\tau \sim 1$  ps. Thus, we take this value for numerical calculations.

In Fig. 1, we show the contributions from different electronic transition channels to the optical conductance for the fixed electron density  $n_e^i$  and hole density  $n_h^i$  at a temperature  $T=300$  K for mono-, bi-, and ABC-stacked tri-layer graphene systems. We can see the following features. (i) In three graphene systems, the optical absorption via inter-band transition from

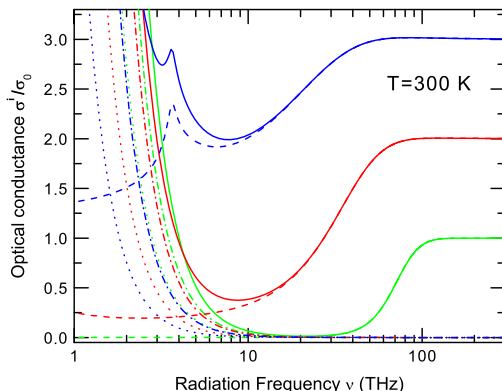


**Fig. 1.** Contributions from different transition channels to optical conductance at a temperature  $T=300\text{ K}$  for carrier densities  $n_e=1.5\times 10^{12}\text{ cm}^{-2}$  and  $n_h=5\times 10^{11}\text{ cm}^{-2}$ . The results obtained from mono-, bi- and ABC-stacked tri-layer graphene are show in green, red and blue curves, respectively. Here,  $\sigma_{++}^i$  (dash dot curve),  $\sigma_{--}^i$  (dot curve) and  $\sigma_{+-}^i$  (dashed curve) are optical conductance induced by intra-band transitions within the conduction band, within the valence band and by inter-band transition from valence band to conduction band, respectively. The solid curve is the total optical conductance and  $\sigma_0=\pi e^2/(2h)$ . (For interpretation of the references to color in this figure caption, the reader is referred to the web version of this article.)

valence band to conduction band gives the main contributions in the frequency regime  $\nu > 20\text{ THz}$ , whereas the intraband transitions give rise to optical absorption in lower frequency regime. (ii) For mono-, bi- and ABC-stacked tri-layer graphene systems, the optical conductance in frequency range  $\nu > 130\text{ THz}$ ,  $\nu > 100\text{ THz}$  and  $\nu > 70\text{ THz}$  depends very weakly on  $\nu$ , whereas it depends strongly on the radiation frequency in the regime  $\nu < 130\text{ THz}$ ,  $\nu < 100\text{ THz}$  and  $\nu < 70\text{ THz}$ , respectively. As we can see, a small absorption peak appears at a frequency about 3.6 THz in ABC-stacked TLG. This small absorption peak is caused by the asymmetry between conduction band and valence band in ABC-stacked TLG. (iii) We find that the optical conductances in high frequency regime for three graphene systems are universal values with  $\sigma_0^m=\pi e^2/(2h)$ ,  $\sigma_0^b=\pi e^2/h$  and  $\sigma_0^t=3\pi e^2/(2h)$ . This confirms that the universal optical conductance per graphene layer is  $\pi e^2/(2h)$ . (iv) Importantly, we can observe absorption windows in the 1–100 THz frequency range for three graphene systems. These absorption windows are induced by the completing absorption channels with different energies due to inter- and intra-band transitions, as shown in Fig. 1. (v) A red-shift and a narrower and taller absorption window can be observed with increasing number of graphene layers.

The optical conductance and corresponding light transmittance of three graphene systems are shown in Fig. 2 as a function of radiation frequency at fixed carrier densities for different temperatures. As can be seen,  $\sigma^i(\nu)$  and  $T^i(\nu)$  depend very little on  $\nu$  in high frequency regime and they do not vary with temperature. These features are in line with experimental findings for monolayer graphene [22]. The optical absorption window can be observed in far infrared to THz frequency regime where both  $\sigma^i(\nu)$  and  $T^i(\nu)$  depend sensitively on temperature. This is in line with the experimental result for mono- [20] and bi-layer [33] graphene systems. We know that the chemical potential for electrons/holes in an electronic system decreases/increases with increasing temperature at a fixed electron/hole density. As a result, due to the Moss-Burstein effect [32], the edge of the optical absorption window shifts to higher energy regime with increasing temperature, as shown in Fig. 2. For monolayer graphene, the width of the optical absorption window decreases with increasing temperature. In bilayer graphene and ABC-stacked TLG systems,

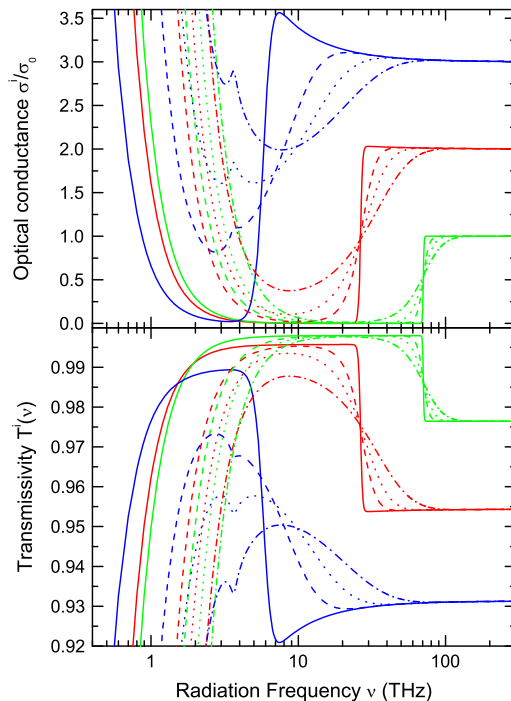


**Fig. 2.** The optical conductance (upper panel) and light transmittance (lower panel) as a function of radiation frequency  $\nu$  at the fixed carrier densities  $n_e=1.5\times 10^{12}\text{ cm}^{-2}$  and  $n_h=5\times 10^{11}\text{ cm}^{-2}$  for different temperatures  $T=10\text{ K}$  (solid line),  $77\text{ K}$  (dashed line),  $150\text{ K}$  (dotted line), and  $300\text{ K}$  (dotted-dashed line). The results obtained from mono-, bi- and ABC-stacked tri-layer graphene systems are show in green, red and blue curve, respectively. (For interpretation of the references to color in this figure caption, the reader is referred to the web version of this article.)

the height and width of the optical absorption window decrease with increasing temperature. A wider and deeper optical absorption window and a sharper cutoff of the optical absorption at the window edges can be observed at lower temperatures, in line with experimental finding for monolayer graphene system [20]. The position of the small absorption peak at the frequency about 3.6 THz in ABC-stacked TLG does not change with varying temperature and the strength of this peak becomes weaker with increasing temperature.

The optical conductance and corresponding transmittance of three graphene systems are plotted in Fig. 3 as a function of the radiation frequency at a temperature  $T=300\text{ K}$  and a fixed hole density  $n_h$  for different electron densities  $n_e$ . For a graphene system placed on a dielectric wafer, applying a positive (negative) gate voltage can pull the electrons (holes) out from the dielectric wafer and inject them into the graphene layer. Then, the electron density in the graphene layer can be varied by the gate voltage [36]. The influence of applying the gate voltage on electronic properties of graphene systems has been investigated theoretically [34,35]. From Fig. 3, we find that in high-frequency regime, the optical conductance does not change with  $\nu$  and depends very little on electron density in three graphene systems. The absorption windows can be observed in the frequency range 2–150 THz. The small absorption peak at about 3.6 THz in ABC-stacked TLG does not depend on electron density and the strength of it becomes weaker with increasing  $n_e$ . Normally, the chemical potential for electrons in the conduction band increases with electron density. Thus, the optical absorption window shifts to higher energy regime with increasing electron density, as shown in Fig. 3. We can see that the height of the absorption window for

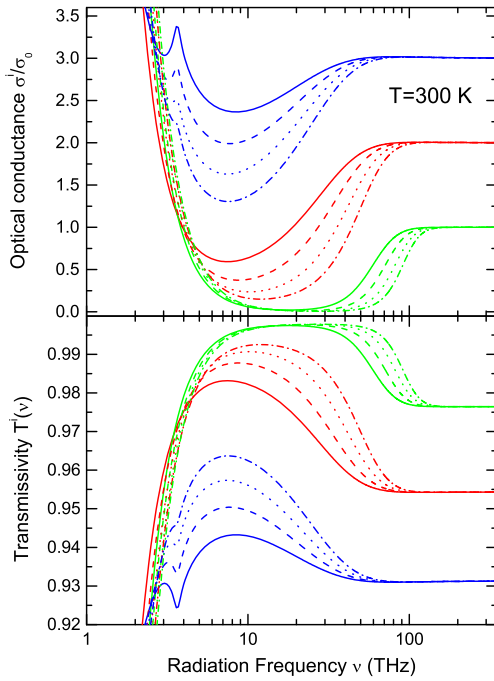


**Fig. 3.** Optical conductance (upper panel) and transmittance (lower panel) as a function of radiation frequency  $\nu$  at a temperature  $T=300$  K and a fixed hole density  $n_h = 5 \times 10^{11} \text{ cm}^{-2}$  for different electron densities  $n_e = 1 \times 10^{12} \text{ cm}^{-2}$  (solid curve),  $n_e = 1.5 \times 10^{12} \text{ cm}^{-2}$  (dashed curve),  $n_e = 2 \times 10^{12} \text{ cm}^{-2}$  (dotted curve), and  $n_e = 2.5 \times 10^{12} \text{ cm}^{-2}$  (dotted-dashed curve). The results obtained from mono-, bi- and ABC-stacked tri-layer systems are shown in green, red and blue curve, respectively. (For interpretation of the references to color in this figure caption, the reader is referred to the web version of this article.)

different graphene systems increases with electron density and a sharper cutoff of the optical absorption at the window edges can be observed for larger electron density. These results suggest that the width and height of the absorption window in mono-, bi- and ABC-stacked tri-layer graphene systems can be tuned by varying electron density in graphene system through applying a gate voltage.

The optical conductance of AB-stacked multi-layer graphene systems is shown in Fig. 4 as a function of radiation frequency at fixed carrier densities for different temperatures. We can see that the universal optical conductance in visual light regime is contributed by the effective low-energy subsystems with the contribution  $\pi e^2/(2h)$  per layer in AB-stacked graphene multilayer. The infrared to THz optical absorption windows can be observed in tri-, tetra- and penta-layer AB-stacked graphene. At lower temperature, a wider and deeper optical absorption window can be achieved and the optical absorption window red-shifts with increasing the layers of graphene sheet. The absorption window also has a red-shift with decreasing temperature. In Fig. 4(a) and (c), we can observe two absorption edges in AB-stacked penta- and tri-layer graphene. These absorption edges are caused by the mini-gaps in AB-stacked multilayer graphene with an odd layer number. In Fig. 4(b), there is no absorption edge because the subsystems in even number AB-stacked multilayer graphene is gapless. These features can be explained with the help of Eqs. (20) and (22). AB-stacked tri-layer graphene has two mini-gaps with  $E_{g1}^3 = 0.03 \text{ eV}$  and  $E_{g2}^3 = 0.01 \text{ eV}$  which correspond to two absorption edges at 7.3 THz and 2.4 THz, respectively. For AB-stacked penta-layer graphene, there are three mini-gaps with  $E_{g1}^5 = 0.04 \text{ eV}$ ,  $E_{g2}^5 = 0.01 \text{ eV}$  and  $E_{g3}^5 = 3.33 \text{ meV}$ . The first two mini-gaps result in two absorption edges at 9.7 THz and 2.4 THz.

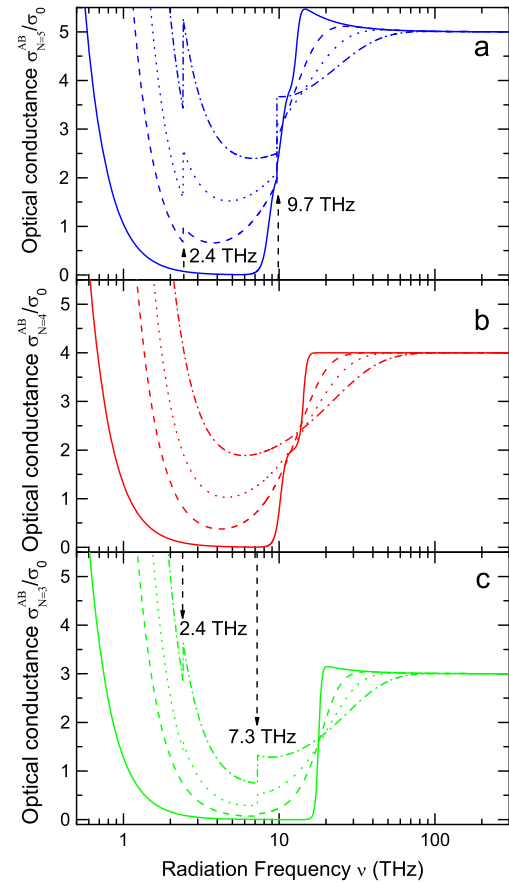


**Fig. 4.** The optical conductance of AB-stacked graphene multilayer as a function of radiation frequency  $\nu$  at the fixed carrier densities  $n_e = 1.5 \times 10^{12} \text{ cm}^{-2}$  and  $n_h = 5 \times 10^{11} \text{ cm}^{-2}$  for different temperatures  $T=10$  K (solid curve),  $77$  K (dashed curve),  $150$  K (dotted curve), and  $300$  K (dotted-dashed curve). The results are shown for the AB-stacked penta-layer (a, blue curve), tetra-layer (b, red curve), and tri-layer graphene (c, green curve). (For interpretation of the references to color in this figure caption, the reader is referred to the web version of this article.)

In the low-frequency regime  $\nu < 1$  THz, the contribution from interband transition is so weak that we cannot observe the third absorption edge in Fig. 4(a). We also find that the height of the absorption edges increases with increasing temperature. In addition, it should be noted that the band gap absorption edges differ a lot from the absorption window edges which are induced by electronic transition around the Fermi-level. From Fig. 4, we can see that the absorption edges in AB-stacked multilayer graphene are within the window area of the absorption window. In a recent work, Hao [18] calculated the optical conductivity in AB-stacked multilayer graphene in full optical spectrum. It should be noted that Ref. [18] studied the optical conductivity through the full band Hamiltonian and reported how the layer number affects the number of near-infrared and ultraviolet absorption peaks. In Ref. [18], the near-infrared absorption peaks are induced by the optical transitions from the lower energy subsystems to the higher energy subsystems near the  $K$  point and the ultraviolet absorption peaks are associated with the Van Hove singularities at  $M$  point. In the present study, we employ the effective low-energy model to study the optical response to the radiation field, with which the infrared to THz optical properties can be examined. Additionally, we have demonstrated that the universal optical conductance in visual regime in AB-stacked multilayer graphene is induced only by the

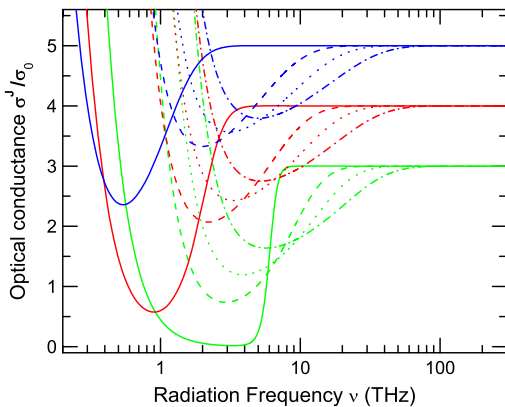


**Fig. 5.** The optical conductance of ABC-stacked graphene multilayer as a function of radiation frequency  $\nu$  at the fixed carrier densities  $n_e = 1.5 \times 10^{12} \text{ cm}^{-2}$  and  $n_h = 5 \times 10^{11} \text{ cm}^{-2}$  for different temperatures  $T = 10 \text{ K}$  (solid curve),  $77 \text{ K}$  (dashed curve),  $150 \text{ K}$  (dotted curve), and  $300 \text{ K}$  (dotted-dashed curve). The results are shown for graphene sheet with 3 (green curves), 4 (red curves), and 5 (blue curves) carbon layers, respectively. (For interpretation of the references to color in this figure caption, the reader is referred to the web version of this article.)

effective low energy subsystems. We find that the layer number of the graphene sheet can affect effectively the absorption windows in AB-stacked graphene multilayer.

The optical absorption spectrum for ABC-stacked multilayer graphene systems are shown in Fig. 5 at the fixed carrier densities for different temperatures. The universal optical conductance is  $N\pi e^2/(2h)$  for a ABC-stacked  $N$ -layer graphene in high frequency regime. There also exists the optical absorption window at low frequency regime in ABC-stacked multilayer graphene. In Fig. 5, we can see that the absorption window red-shifts to low frequency regime with increasing layer number  $N$  or decreasing temperature. Meanwhile, the width and depth of the absorption window decreases with increasing graphene layer number  $N$ . Moreover, we note that the absorption window in Fig. 5 shows some different features from those in Fig. 4. (i) Unlike the abundant low energy subsystems in AB-stacked multilayer graphene, ABC-stacked multilayer graphene only has one effective low energy subsystem. Thus, the relatively richer structure of the absorption window can be observed in AB-stacked multilayer graphene than ABC-stacked systems. (ii) ABC-stacked multilayer graphene has a narrower absorption window than that in AB-stacked multilayer graphene with the same layer number. (iii) The depth of the optical absorption window in AB-stacked multilayer graphene is deeper than that in ABC-stacked graphene multilayer. (iv) At low temperatures, the shift of the absorption window tuned by temperature and layer number of graphene sheet is more obvious in ABC-stacked multilayer. These results suggest that the stacking order in multilayer graphene systems also plays an important role in determining the optoelectrical properties in infrared to THz bandwidth.

The results obtained from this study show that the strength of optical absorption increases with increasing number of graphene layers in whole optical spectrum. In infrared to THz regime, optical absorption windows can be seen in mono- and multi-layer graphene systems with AB- and ABC-stacking. The red-shift of the optical absorption window can be observed with increasing number of graphene layers. The main physical reason behind these interesting features is that the mono- and multi-layer graphene systems have different electronic energy spectra. This can result in different density-of-states for optical transition scattering required by momentum and energy conservation laws in different graphene systems. These theoretical findings suggest that the optoelectronic properties of graphene systems can be tuned and modified not

only by varying temperature and carrier density but also by choosing graphene sheet with different layers and with different stacking orders.

#### 4. Conclusions

In this study, we have developed a simple theoretical approach to study optoelectronic properties of mono- and multi-layer graphene systems with AB- and ABC-stacking. We have examined the dependence of optical absorption/transmission on temperature, electron density, stacking type and number of graphene layers in air/graphene/dielectric-wafer systems. It has been demonstrated theoretically that the optical conductance is universal values  $\sigma_0^N = N\pi e^2/(2h)$  for  $N$ -layer graphene systems in the high frequency regime and they depend very little on temperature, electron density and stacking type. This finding confirms that the optical conductance per graphene layer is given by a universal value  $\sigma_0 = \pi e^2/(2h)$  in the high frequency regime. The corresponding optical transmission coefficients in high frequency regime are about 97.7%, 95.4% and 93.1% for mono-, bi- and ABC-stacked tri-layer graphene, respectively, in agreement with the experimental data [22]. We have shown that there exist optical absorption windows in the radiation frequency range 0.2–150 THz for mono- and multi-layer graphene systems with AB- and ABC stacking. The Drude-like optical conductance and the corresponding high transmittance windows in infrared to THz regime have been verified experimentally [11,19]. The optical absorption windows in few layer graphene systems are induced by different transition energies required for inter- and intra-band transition channels. The depth and width of such absorption windows depend sensitively on the temperature, electron density, stacking type and the number of graphene layers, especially at lower frequency edge. There is a small absorption peak at the frequency about 3.6 THz in ABC-stacked tri-layer graphene system which does not change the position with varying temperature and electron density but the strength of it decreases with decreasing temperature and/or increasing electron density. For AB-stacked multi-layer graphene with an odd layer number, there exists mini-gap induced absorption edges. The number and the position of the absorption edges depend on the graphene layers' number  $N$ . They depend weakly on temperature but the strength of them increase with increasing temperature. At lower temperature and/or larger electron density, we can observe the prominent cutoff of the optical absorption at the window edges in graphene systems. The optical absorption window in AB-stacked  $N$ -layer graphene is wider and deeper than that in ABC-stacked multilayer graphene. The optical absorption window red-shifts and the width of the absorption window decreases with an increase in the number of graphene layers. These theoretical results indicate that mono- and multi-layer graphene with AB- and ABC-stacking have some unique features in infrared to THz bandwidth, which can be utilized for application as infrared or THz optoelectronic devices.

#### Acknowledgments

This work was supported by the Ministry of Science and Technology of China (Grant no. 2011YQ130018), Department of Science and Technology of Yunnan Province, and by the Chinese Academy of Sciences.

#### References

- [1] K.S. Novoselov, A.K. Geim, S.V. Morozov, et al., *Science* 306 (2004) 666.
- [2] H. Hogan, *Photon. Spectra* 42 (2008) 19.

## 附录 D The published papers and preprint related to the thesis

---

- [3] Weiwei Cai, Yanwu Zhu, Xuesong Li, Richard D. Piner, R.S. Ruoff, *Appl. Phys. Lett.* 95 (2009) 123115.
- [4] B. Sensale-Rodriguez, T. Fang, R. Yan, et al., *Appl. Phys. Lett.* 99 (2011) 113104.
- [5] B. Sensale-Rodriguez, R. Yan, M. Zhu, D. Jena, L. Liu, H.G. Xing, *Appl. Phys. Lett.* 101 (2012) 261115.
- [6] C.-C. Lee, S. Suzuki, W. Xie, T.R. Schibli, *Opt. Express* 20 (2012) 5264.
- [7] J. Park, Y.H. Ahn, C. Ruiz-Vargas, *Nano Lett.* 9 (2009) 1742.
- [8] E.J.H. Lee, K. Balasubramanian, R.T. Weitz, M. Burghard, K. Kern, *Nat. Nanotechnol.* 3 (2008) 486.
- [9] T. Mueller, F. Xia, P. Avouris, *Nat. Photon.* 4 (2010) 297.
- [10] G. Konstantatos, M. Badioli, L. Gaudreau, J. Osmond, et al., *Nat. Nanotechnol.* 7 (2012) 363.
- [11] Jason Horng, Chi-Fan Chen, Baisong Geng, Caglar Girit, et al., *Phys. Rev. B* 83 (2011) 165113.
- [12] A.R. Wright, X.G. Xu, J.C. Cao, C. Zhang, *Appl. Phys. Lett.* 95 (2009) 072101.
- [13] Y.S. Ang, S. Sultan, C. Zhang, *Appl. Phys. Lett.* 97 (2010) 243110.
- [14] W. Xu, Y.P. Gong, L.W. Liu, H. Qin, Y.L. Shi, *Nanoscale Res. Lett.* 6 (2011) 250.
- [15] E. McCann, V.I. Fal'ko, *Phys. Rev. Lett.* 96 (2006) 086805.
- [16] F. Guinea, A.H. Castro Neto, N.M.R. Peres, *Phys. Rev. B* 73 (2006) 245426.
- [17] Fan Zhang, Bhagawan Sahu, Hongki Min, A.H. MacDonald, *Phys. Rev. B* 82 (2010) 035409.
- [18] L. Hao, L. Sheng, *Solid State Commun.* 149 (2009) 1962.
- [19] J.M. Dawlaty, S. Shivaraman, J. Strait, et al., *Appl. Phys. Lett.* 93 (2008) 131905.
- [20] A.B. Kuzmenko, E. van Heumen, F. Carbone, D. van der Marel, *Phys. Rev. Lett.* 100 (2008) 117401.
- [21] Z.Q. Li, E.A. Henriksen, Z. Jiang, et al., *Nat. Phys.* 4 (2008) 532.
- [22] R.R. Nair, P. Blake, A.N. Grigorenko, K.S. Novoselov, T.J. Booth, T. Stauber, N.M. R. Peres, A.K. Geim, *Science* 320 (2008) 1308.
- [23] H.M. Dong, W. Xu, J. Zhang, Y.Z. Yuan, *Opt. Commun.* 283 (2010) 3695.
- [24] W. Xu, H.M. Dong, L.L. Li, J.Q. Yao, P. Vasilopoulos, F.M. Peeters, *Phys. Rev. B* 82 (2010) 125304.
- [25] T. Stauber, N.M.R. Peres, A.K. Geim, *Phys. Rev. B* 78 (2008) 085432.
- [26] M. Koshino, T. Ando, *Phys. Rev. B* 77 (2008) 115313.
- [27] M. Koshino, T. Ando, *Solid State Commun.* 149 (2009) 1123.
- [28] M. Koshino, E. McCann, *Phys. Rev. B* 83 (2011) 165443.
- [29] H. Min, A.H. MacDonald, *Prog. Theor. Phys. Suppl.* 176 (2008) 227.
- [30] H.M. Dong, W. Xu, Z. Zeng, T.C. Lu, F.M. Peeters, *Phys. Rev. B* 77 (2008) 235402.
- [31] D. Sun, Z.-K. Wu, C. Divin, X. Li, C. Berger, et al., *Phys. Rev. Lett.* 101 (2008) 157402.
- [32] E. Burstein, *Phys. Rev.* 93 (1954) 632.
- [33] X. Zou, J. Shang, J. Leaw, Z. Luo, Liyan Luo, et al., *Phys. Rev. Lett.* 110 (2013) 067401.
- [34] A.A. Avetisyan, B. Partoens, F.M. Peeters, *Phys. Rev. B* 80 (2009) 195401.
- [35] E. McCann, *Phys. Rev. B* 74 (2006) 161403.
- [36] F. Wang, Y. Zhang, C. Tian, C. Giri, A. Zettl, M. Crommie, Y. Ron Shen, *Science* 320 (2008) 206.

## Infrared to terahertz optical conductivity of *n*-type and *p*-type monolayer MoS<sub>2</sub> in the presence of Rashba spin-orbit coupling

Y. M. Xiao,<sup>1,2,\*</sup> W. Xu,<sup>1,3,†</sup> B. Van Duppen,<sup>2,‡</sup> and F. M. Peeters<sup>2,§</sup>

<sup>1</sup>Department of Physics and Astronomy and Yunnan Key Laboratory for Micro/Nano Materials and Technology, Yunnan University, Kunming 650091, China

<sup>2</sup>Department of Physics, University of Antwerp, Groenenborgerlaan 171, B-2020 Antwerpen, Belgium

<sup>3</sup>Key Laboratory of Materials Physics, Institute of Solid State Physics, Chinese Academy of Sciences, Hefei 230031, China  
(Received 14 July 2016; revised manuscript received 21 September 2016; published 18 October 2016)

We investigate the effect of Rashba spin-orbit coupling (SOC) on the optoelectronic properties of *n*- and *p*-type monolayer MoS<sub>2</sub>. The optical conductivity is calculated within the Kubo formalism. We find that the spin-flip transitions enabled by the Rashba SOC result in a wide absorption window in the optical spectrum. Furthermore, we evaluate the effects of the polarization direction of the radiation, temperature, carrier density, and the strength of the Rashba spin-orbit parameter on the optical conductivity. We find that the position, width, and shape of the absorption peak or absorption window can be tuned by varying these parameters. This study shows that monolayer MoS<sub>2</sub> can be a promising tunable optical and optoelectronic material that is active in the infrared to terahertz spectral range.

DOI: 10.1103/PhysRevB.94.155432

### I. INTRODUCTION

The discovery of atomically thin two-dimensional (2D) materials has created a completely new field of research. These materials are promising for applications in next generation of high-performance nanoelectronics devices [1]. Recently, new types of 2D materials such as monolayer transition metal dichalcogenides MX<sub>2</sub> (M=Mo, W, Nb, Ta, Ti, and X=S, Se, Te) have been synthesized. These 2D materials are formed by layered structures in the form of X-M-X with the chalcogen atoms in two hexagonal planes separated by a plane of metal atoms [2–4]. Transition metal dichalcogenides (TMDCs) have a sizable band gap that can change from indirect in multilayers to direct in a single-layer structure [2]. For example, molybdenum disulfide (MoS<sub>2</sub>) shows a transition from an indirect band gap of 1.29 eV in bulk to a direct band gap near 1.90 eV in its monolayer form at the inequivalent high-symmetry K and K' points [3,5].

Since its first isolation, monolayer MoS<sub>2</sub> [3,6] has been investigated intensively because it exhibits interesting and important electronic and optical properties. Very recently, one has demonstrated that monolayer MoS<sub>2</sub> (ML-MoS<sub>2</sub>) based field-effect transistors (FETs) can have room-temperature on/off ratios of the order of 10<sup>8</sup> and can exhibit a carrier mobility larger than 200 cm<sup>2</sup>/(V s) [7–9]. Other MoS<sub>2</sub> based electronic components such as gas sensors [10], phototransistors, photodetectors with high responsivity [11], and even LEDs [12] have been realized experimentally. Currently, the investigation of ML-MoS<sub>2</sub> has become a fast-growing field of research with great potential for electronics, optics, and optoelectronics.

The electronic band structure for ML-MoS<sub>2</sub> can be calculated in a  $\mathbf{k} \cdot \mathbf{p}$  theory framework [13,14]. Unlike massless Dirac fermions in graphene, the electronic states in monolayer

TMDCs (ML-TMDCs) can be described as massive Dirac fermions. Furthermore, it was found that there exists an intrinsic spin-orbit coupling (SOC) in ML-MoS<sub>2</sub>, which gives rise to a splitting of the conduction and valence bands with opposite spin orientations [13,15]. In a recent work, Li *et al.* [16] calculated the optical conductivity in ML-MoS<sub>2</sub> in the visible range as determined by the interband optical transitions from the valence to the conduction bands. The collective excitations of ML-MoS<sub>2</sub>, e.g., plasmons, and screening have also been examined and discussed [17]. The presence of a strong intrinsic SOC that couples between spin and valley degrees of freedom has led to the proposal that the TMDCs can be interesting materials for valleytronics and spintronics [18–21].

The control of carrier spin dynamics in semiconductor nanostructures is a key issue in spintronics and it can be achieved through the electrical manipulation of the SOC induced by the Rashba effect [22–24]. The investigation of optical properties such as collective excitations [25,26] and optical conductivities [27–30] has been conducted and show how the Rashba effect affects the optical properties of traditional 2D semiconductor based spintronic devices. This indicates that the Rashba effect has a strong influence on the plasmon modes and low-frequency optical spectrum.

When an electric field is applied perpendicular to a ML-MoS<sub>2</sub> flake, inversion symmetry is broken and, according to the Kane-Mele model [31], a Rashba SOC term is added to the Hamiltonian. As a consequence, spin  $\hat{s}_z$  is no longer a good quantum number [31–33] and it becomes possible to have transitions between spin-split electronic states. This enables the observation of spin-related optical phenomena that were found before to be presented in traditional 2D electron gasses (2DEGs) [25–30]. In ML-MoS<sub>2</sub>, there is a combination of both spin-coupling mechanisms with which one can expect to realize interesting spin-optics effects. Moreover, thanks to the tunability of the Rashba SOC with the external electric field, it is possible to turn these effects on and off. Alternatively, one could also deposit various atoms on the MoS<sub>2</sub> surface that can enhance the Rashba SOC as has been demonstrated in gold-doped graphene [34] and Bi<sub>2</sub>Se<sub>3</sub>(001) surfaces [35].

\*yiming.xiao@uantwerpen.be

†wenxu\_issp@aliyun.com

‡ben.vanduppen@uantwerpen.be

§francois.peeters@uantwerpen.be

The effects of the Rashba SOC on the optical properties of graphene have been studied [36–39]. It shows that the Rashba effect strongly affects the optical properties of graphene. In the presence of the Rashba SOC, the optical conductivity of graphene features absorption peaks and kinks which are due to interband transitions between the spin-split states [38,39]. ML-MoS<sub>2</sub> has a low-energy parabolic band which is different from the linear dispersion relation of graphene. In order to understand the ML-MoS<sub>2</sub> material systems more deeply and to explore their further applications in practical devices working in the low-energy bandwidth, it is necessary to examine the roles played by the Rashba SOC in affecting the optoelectronic properties.

Along with numerous theoretical studies, the optical and transport properties of MoS<sub>2</sub> have also been experimentally investigated [3,5,7–9,19–21]. However, most of these works focus on the optoelectronic properties induced by interband transitions between the conduction and valence bands that lie in the visible range of the electromagnetic (EM) spectrum. In this article, we predict that the Rashba effect induces spin-flip transitions that can have a great impact on the optoelectronic response of ML-MoS<sub>2</sub> in the infrared to terahertz range. To the best of our knowledge, very little research has been reported on the optoelectronic properties of ML-MoS<sub>2</sub> in this range of the light spectrum. In this regime, the intrinsic and Rashba SOC can play an important role in determining the optoelectronic response. We intend to study the optical conductivity of ML-MoS<sub>2</sub> in the presence of the Rashba SOC under linear and circular polarized radiation field. By calculating the different contributions of intraband and interband electronic transitions, we examine the effects of *n*- and *p*-type doping (for varying carrier density via chemical doping or applying a gate voltage), temperature, and the Rashba SOC strength on the optical conductivity of ML-MoS<sub>2</sub>. We calculate the electronic band structure of ML-MoS<sub>2</sub> starting from a 4 × 4 matrix Hamiltonian with the addition of the Kane-Mele Rashba SOC.

The present paper is organized as follows. In Sec. II, we describe the band structure and solve for the single-particle states of ML-MoS<sub>2</sub> in the presence of the Rashba effect. The absorptive part of the optical conductivity is evaluated through the standard Kubo formalism in the presence of a linearly and/or circularly polarized radiation field in Sec. III. The optical transition channels for different doping types and doping levels and the results for the absorptive part of the optical conductivity are presented and discussed in Sec. IV. Our main conclusions are summarized in Sec. V.

## II. ELECTRONIC BAND STRUCTURE

In this study we consider a ML-MoS<sub>2</sub> in the *xy* plane on top of a dielectric wafer such as SiO<sub>2</sub> [40,41]. The effective  $\mathbf{k} \cdot \mathbf{p}$  Hamiltonian for a charge carrier (an electron or a hole) in the low-energy regime near the K (K') point in ML-MoS<sub>2</sub> in the presence of the Rashba SOC can be written as [13,15,16,32,33]

$$\hat{H}^{\xi} = \left[ at(\xi k_x \hat{\sigma}_x + k_y \hat{\sigma}_y) + \frac{\Delta}{2} \hat{\sigma}_z \right] \otimes \hat{I} + \xi \gamma_v \frac{\hat{I} - \hat{\sigma}_z}{2} \otimes \hat{s}_z + \gamma_R (\xi \hat{\sigma}_x \otimes \hat{s}_y - \hat{\sigma}_y \otimes \hat{s}_x), \quad (1)$$

where  $\hat{\sigma}_i$  and  $\hat{s}_i$  are the Pauli matrices of the sublattice pseudospin and the real spin, respectively.  $\hat{I}$  is the  $2 \times 2$  unit matrix and the valley index  $\xi = \pm$  refers to the K (K') valley. This Hamiltonian reads in the basis  $\Psi^+ = \{\psi_{A\uparrow}, \psi_{A\downarrow}, \psi_{B\uparrow}, \psi_{B\downarrow}\}^T$  and  $\Psi^- = \{\psi_{A\downarrow}, \psi_{A\uparrow}, \psi_{B\downarrow}, \psi_{B\uparrow}\}^T$  for both valleys explicitly as

$$\hat{H}^{\xi} = \begin{pmatrix} \Delta/2 & 0 & \xi a t k_{-\xi} & 0 \\ 0 & \Delta/2 & 2i\gamma_R & \xi a t k_{-\xi} \\ \xi a t k_{\xi} & -2i\gamma_R & \gamma_v - \Delta/2 & 0 \\ 0 & \xi a t k_{\xi} & 0 & -\gamma_v - \Delta/2 \end{pmatrix}, \quad (2)$$

where  $\mathbf{k} = (k_x, k_y)$  is the wave vector,  $k_{\pm} = k_x \pm ik_y$ ,  $a = 3.193 \text{ \AA}$  is the lattice parameter,  $t = 1.1 \text{ eV}$  is the hopping parameter [13], the intrinsic SOC parameter  $2\gamma_v = 150 \text{ meV}$  is the spin splitting at the top of the valence band in the absence of the Rashba SOC [13,42],  $\Delta = 1.66 \text{ eV}$  is the direct band gap between the valence and conduction band used in our calculation [13,15,16], and  $\gamma_R$  is the Rashba SOC parameter which can be tuned via an electrical field and can be determined by *ab initio* calculation or by fitting with experimental data. Kormányos *et al.* [43] estimated the value of the Rashba parameter for ML-MoS<sub>2</sub> as  $\alpha_R = 0.033 \text{ e\AA}^2 E_z [\text{V}/\text{\AA}]$  for a spin-split two-band model which corresponds to  $\gamma_R = 0.0078 \text{ e\AA}^2 E_z [\text{V}/\text{\AA}]$  in our model with the relation of  $\gamma_R = \alpha_R \Delta / (2at)$  obtained in Ref. [44] where  $E_z$  is the perpendicular electric field. We would like to point out that the Rashba effect can not only be tuned by a gate voltage but can also be enhanced by adatoms as has been realized in graphene [34]. For example, a large Rashba parameter 72 meV is found in monolayer MoTe<sub>2</sub> on a EuO substrate [45].

From the above Hamiltonian, we can describe the spin states in both conduction and valence bands in the presence of the Rashba effect. The corresponding Schrödinger equation for ML-MoS<sub>2</sub> near the valley K (K') can be solved analytically and the eigenvalues are the solutions of the diagonalized equation

$$\varepsilon^4 - A_2 \varepsilon^2 + A_1 \varepsilon + A_0 = 0, \quad (3)$$

where

$$A_0 = (\Delta^2/4 + a^2 t^2 k^2)^2 + \gamma_R^2 \Delta (\Delta + 2\gamma_v) - \Delta^2 \gamma_v^2/4,$$

$$A_1 = \Delta \gamma_v^2 - 4\gamma_v \gamma_R^2,$$

and

$$A_2 = \Delta^2/2 + 2a^2 t^2 k^2 + 4\gamma_R^2 + \gamma_v^2.$$

The energy dispersion  $\varepsilon_{\mathbf{k},\xi} = \varepsilon_{\mathbf{k},\lambda,\nu}$  can be obtained through solving Eq. (3) analytically with the general solution of a quartic equation [46]. Here, we defined the total quantum number  $\xi = (\xi, \lambda, s)$ , where  $\lambda = \pm$  refers to the conduction/valence band and  $s = \pm$  is the spin index and  $\xi$  labels the valley. We often use the quantity  $\nu = \xi s = \pm$  to exploit the valley/spin symmetry of the system.

The corresponding eigenfunction for a state near the K (K') point is

$$|\mathbf{k}, \xi\rangle = \psi_{\xi}(\mathbf{k}, \mathbf{r}) = \mathcal{N}_{\lambda,\nu}(k) [c_1^{\xi}, c_2^{\xi}, c_3^{\xi}, c_4^{\xi}] e^{i\mathbf{k} \cdot \mathbf{r}}. \quad (4)$$

Equation (4) is expressed in the form of a row vector where the values of the eigenfunction elements are

$$\begin{aligned} c_1^\xi &= -2i\gamma_R a^2 t^2 k_{-\xi}^2, & c_2^\xi &= \xi atk_{-\xi} b_1^{\lambda v}, \\ c_3^\xi &= -2i\xi\gamma_R atk_{-\xi} b_0^{\lambda v}, & c_4^\xi &= b_0^{\lambda v} b_2^{\lambda v}, \end{aligned}$$

with

$$\begin{aligned} b_1^{\lambda v} &= \varepsilon_{\mathbf{k},\lambda v}^2 - \gamma_v \varepsilon_{\mathbf{k},\lambda v} + \Delta(2\gamma_v - \Delta)/4 - a^2 t^2 k^2, \\ b_2^{\lambda v} &= b_1^{\lambda v} - 4\gamma_R^2, & b_0^{\lambda v} &= \varepsilon_{\mathbf{k},\lambda v} - \Delta/2. \end{aligned}$$

The normalization coefficient  $\mathcal{N}_{\lambda v}(k)$  can be written as

$$\mathcal{N}_{\lambda v}(k) = 1/\sqrt{h^{\lambda v}}, \quad (5)$$

with  $h^{\lambda v} = 4\gamma_R^2 a^2 t^2 k^2 [a^2 t^2 k^2 + (b_0^{\lambda v})^2] + a^2 t^2 k^2 (b_1^{\lambda v})^2 + (b_0^{\lambda v} b_2^{\lambda v})^2$ .

### III. OPTICAL CONDUCTIVITY

In the present study, we evaluate the optical conductivity in ML-MoS<sub>2</sub> using the standard Kubo formula [47,48]

$$\sigma_{\alpha\beta}(\mathbf{q},\omega) = i \frac{e^2 n_i}{m\omega} \delta_{\alpha\beta} + \frac{1}{\omega} \int_0^\infty dt e^{i\tilde{\omega}t} \langle [j_\alpha^\dagger(\mathbf{q},t), j_\beta(\mathbf{q},0)] \rangle, \quad (6)$$

where  $(\alpha, \beta) = (x, y)$  for a 2D system,  $j_\alpha(\mathbf{q},t)$  is the current density operator,  $\tilde{\omega} = \omega + i\eta$  ( $\eta \rightarrow 0^+$ ), and  $n_i$  is the carrier density for electrons in the conduction band or holes in the valence band. It should be noted that the first term in Eq. (6) is the diamagnetic term [48]. In this paper we concentrate on calculating the real part of the optical conductivity, where this term does not contribute because it is purely imaginary at nonzero frequencies.

In the optical limit of  $\mathbf{q} \rightarrow 0$ , the dynamical optical conductivity for the ML-MoS<sub>2</sub> system at an incident photon frequency  $\omega$  can be written in the Kubo-Greenwood form as [48,49]

$$\begin{aligned} \sigma_{\alpha\beta}(\omega) &= \frac{i e^2}{\omega} \sum_{\xi',\xi} \sum_{\mathbf{k}',\mathbf{k}} \langle \mathbf{k}, \xi | \hat{v}_\alpha^\xi | \mathbf{k}', \xi' \rangle \langle \mathbf{k}', \xi' | \hat{v}_\beta^\xi | \mathbf{k}, \xi \rangle \\ &\times \frac{f(\varepsilon_{\mathbf{k},\xi}) - f(\varepsilon_{\mathbf{k}',\xi'})}{\varepsilon_{\mathbf{k},\xi} - \varepsilon_{\mathbf{k}',\xi'} + \hbar(\omega + i\eta)}, \end{aligned} \quad (7)$$

where the velocity operator  $\hat{v}_\alpha^\xi = \hbar^{-1} \partial \hat{H}^\xi / \partial k_\alpha$ ,  $\eta = \tau^{-1}$ ,  $\tau$  is the transport relaxation time, and  $f(\varepsilon_{\mathbf{k},\xi}) = f(\varepsilon_{\mathbf{k},\lambda v}) = \{\exp[(\varepsilon_{\mathbf{k},\lambda v} - \mu_\lambda)/(k_B T)] + 1\}^{-1}$  is the Fermi-Dirac distribution function with  $\mu_\lambda$  the chemical potential for electrons or holes and the temperature  $T$ . It should be noted that we use a constant relaxation time for the following calculations where the specific scattering events are not considered. Very recently, the intraband optical conductivity for ML-MoS<sub>2</sub> has also been calculated [50], and the evaluation of the relaxation time by impurity scattering had been discussed in Ref. [51]. The longitudinal optical conductivity at valley  $\xi$  can be written as

$$\begin{aligned} \sigma_{xx}^\xi(\omega) &= \frac{i e^2}{\omega} \sum_{\lambda'v',\lambda v} \sum_{\mathbf{k}',\mathbf{k}} w_{\lambda'v',\lambda v}^{xx}(\mathbf{k}',\mathbf{k}) \\ &\times \frac{f(\varepsilon_{\mathbf{k},\lambda v}) - f(\varepsilon_{\mathbf{k}',\lambda'v'})}{\varepsilon_{\mathbf{k},\lambda v} - \varepsilon_{\mathbf{k}',\lambda'v'} + \hbar(\omega + i\eta)}, \end{aligned} \quad (8)$$

where

$$w_{\lambda'v',\lambda v}^{xx}(\mathbf{k}',\mathbf{k}) = \frac{a^4 t^4 k^2 [p^2 + r^2 + 2pr \cos(2\phi)]}{\hbar^2 h^{\lambda v} h^{\lambda'v'}} \delta_{\mathbf{k},\mathbf{k}'},$$

with

$$\begin{aligned} p &= b_0^{\lambda'v'} (4\gamma_R^2 a^2 t^2 k^2 + b_0^{\lambda v} b_2^{\lambda'v'}), \\ r &= b_0^{\lambda v} (4\gamma_R^2 a^2 t^2 k^2 + b_1^{\lambda'v'} b_2^{\lambda v}). \end{aligned}$$

Moreover, the transverse or “Hall” optical conductivity at valley  $\xi$  is

$$\begin{aligned} \sigma_{xy}^\xi(\omega) &= \frac{i \xi e^2}{\omega} \sum_{\lambda'v',\lambda v} \sum_{\mathbf{k}',\mathbf{k}} w_{\lambda'v',\lambda v}^{xy,\xi}(\mathbf{k}',\mathbf{k}) \\ &\times \frac{f(\varepsilon_{\mathbf{k},\lambda v}) - f(\varepsilon_{\mathbf{k}',\lambda'v'})}{\varepsilon_{\mathbf{k},\lambda v} - \varepsilon_{\mathbf{k}',\lambda'v'} + \hbar(\omega + i\eta)}, \end{aligned} \quad (9)$$

where

$$w_{\lambda'v',\lambda v}^{xy,\xi}(\mathbf{k}',\mathbf{k}) = \frac{a^4 t^4 k^2 i(p^2 - r^2) + 2\xi pr \sin(2\phi)}{\hbar^2} \delta_{\mathbf{k},\mathbf{k}'}$$

The  $\eta \rightarrow 0^+$  limit in the above equations can be divided into a principal-value ( $\mathcal{P}$ ) part and a Dirac-delta part through the Dirac identity

$$\lim_{\eta \rightarrow 0^+} \frac{1}{x + i\eta} = \mathcal{P}\left(\frac{1}{x}\right) - i\pi\delta(x). \quad (10)$$

Thus, the optical conductivity can be separated into real and imaginary parts. The real part of the longitudinal optical conductivity and the imaginary part of the Hall optical conductivity at valley  $\xi$  take respectively the forms

$$\text{Re } \sigma_{xx}^\xi(\omega) = \sum_{\lambda'v',\lambda v} \text{Re } \sigma_{xx,\xi}^{\lambda v \lambda' v'}(\omega), \quad (11)$$

with

$$\begin{aligned} \text{Re } \sigma_{xx,\xi}^{\lambda v \lambda' v'}(\omega) &= \int_0^\infty dk \frac{e^2 a^4 t^4 k^3}{2\hbar^3 \omega} \frac{(p^2 + r^2)}{h^{\lambda v} h^{\lambda'v'}} \\ &\times [f(\varepsilon_{\mathbf{k},\lambda v}) - f(\varepsilon_{\mathbf{k},\lambda v} + \hbar\omega)] \\ &\times \delta[\omega - \omega_{\lambda v}^{\lambda'v'}(k)], \end{aligned}$$

and

$$\text{Im } \sigma_{xy}^\xi(\omega) = \sum_{\lambda'v',\lambda v} \text{Im } \sigma_{xy,\xi}^{\lambda v \lambda' v'}(\omega), \quad (12)$$

with

$$\begin{aligned} \text{Im } \sigma_{xy,\xi}^{\lambda v \lambda' v'}(\omega) &= \xi \int_0^\infty dk \frac{e^2 a^4 t^4 k^3}{2\hbar^3 \omega} \frac{(p^2 - r^2)}{h^{\lambda v} h^{\lambda'v'}} \\ &\times [f(\varepsilon_{\mathbf{k},\lambda v}) - f(\varepsilon_{\mathbf{k},\lambda v} + \hbar\omega)] \\ &\times \delta[\omega - \omega_{\lambda v}^{\lambda'v'}(k)], \end{aligned}$$

where the integral of  $\cos(2\phi)$  and  $\sin(2\phi)$  over the angle  $\phi$  is zero in Eqs. (8) and (9), respectively, and  $\omega_{\lambda v}^{\lambda'v'}(k) = (\varepsilon_{\mathbf{k},\lambda'v'} - \varepsilon_{\mathbf{k},\lambda v})/\hbar$  is the energy spacing frequency between the initial and final states.

The total optical conductivity of the system is the summation of the contributions at the two valleys,

$$\sigma_{\alpha\beta}(\omega) = \sum_{\xi=\pm} \sigma_{\alpha\beta}^\xi(\omega). \quad (13)$$

Equation (11) shows that the real part of the longitudinal optical conductivity is the same for both valleys. This means that we can write the real part as  $\text{Re } \sigma_{xx}(\omega) = g_v \text{Re } \sigma_{xx}^{\zeta}(\omega)$  with the valley degeneracy factor  $g_v = 2$ . For the imaginary part, Eq. (12) shows that the system is valley antisymmetric with respect to a change in sign of  $\zeta$ , i.e.,  $\text{Im } \sigma_{xy,+}^{\lambda \nu \lambda' \nu'}(\omega) = -\text{Im } \sigma_{xy,-}^{\lambda \nu \lambda' \nu'}(\omega)$ . This means that the imaginary part of the Hall conductivity vanishes because the contributions from the two valleys cancel each other out.

The absorption of incoming linearly polarized radiation is given by the real part of the longitudinal conductivity. For finite frequency the optical response to circularly polarized radiation with right-handed (+) and left-handed (-) polarizations, the absorptive part of the optical conductivity under circular polarized radiation at valley  $\zeta$  can be found as [16]

$$\text{Re } \sigma_{\pm}^{\zeta}(\omega) = \text{Re } \sigma_{xx}^{\zeta}(\omega) \mp \text{Im } \sigma_{xy}^{\zeta}(\omega). \quad (14)$$

Therefore, in order to calculate the amount of absorbed radiation, we only need to calculate the real part of the longitudinal conductivity as presented in Eq. (11) and the imaginary part of the Hall conductivity as given by Eq. (12).

#### IV. RESULTS AND DISCUSSION

In this study, we consider both *n*-type and *p*-type ML-MoS<sub>2</sub> in the presence of a relatively weak infrared or terahertz radiation field, such that the linear response theory used in this paper is valid [47,52], and that the electron or hole density do not change significantly. This is because the large band gap suppresses the photoexcited electron-hole pairs. This means that only the electronic transitions within the valence or conduction band are included in the present study (i.e.,  $\lambda = \lambda'$ ). The chemical potential  $\mu_{\lambda}$  for electrons in *n*-type and holes in *p*-type ML-MoS<sub>2</sub> can be determined, respectively, through the conservation of carrier numbers

$$n_e = g_v \sum_{\lambda=+, v=\pm} \sum_{\mathbf{k}} f(\varepsilon_{\mathbf{k}, \lambda, v}) \quad (15)$$

and

$$n_h = g_v \sum_{\lambda=-, v=\pm} \sum_{\mathbf{k}} [1 - f(\varepsilon_{\mathbf{k}, \lambda, v})]. \quad (16)$$

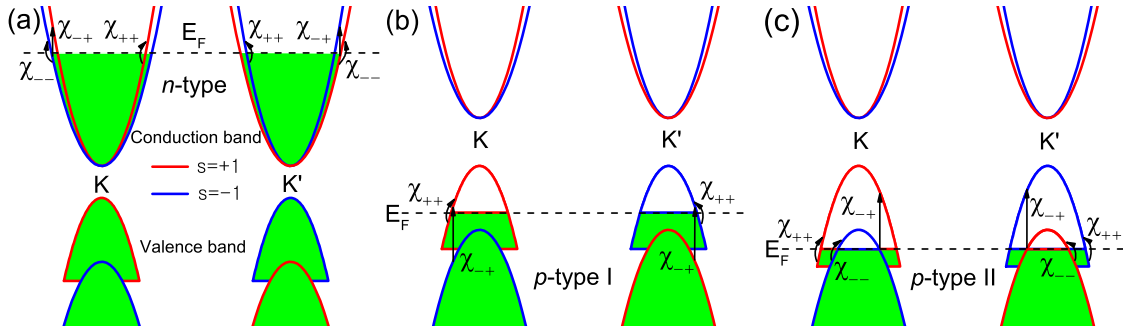


FIG. 1. Schematic presentation of the band structure and the possible optical transition channels in both valleys for *n*-type in (a) and *p*-type I in (b) in ML-MoS<sub>2</sub> with the Fermi level  $E_F$  between the two top points of spin-split valence subbands. In (c), *p*-type II ML-MoS<sub>2</sub> with Fermi energy  $E_F$  for holes below the top point of  $v = -$  valence subband. The possible optical absorption channels are indicated by  $\chi_{vv'}$ .

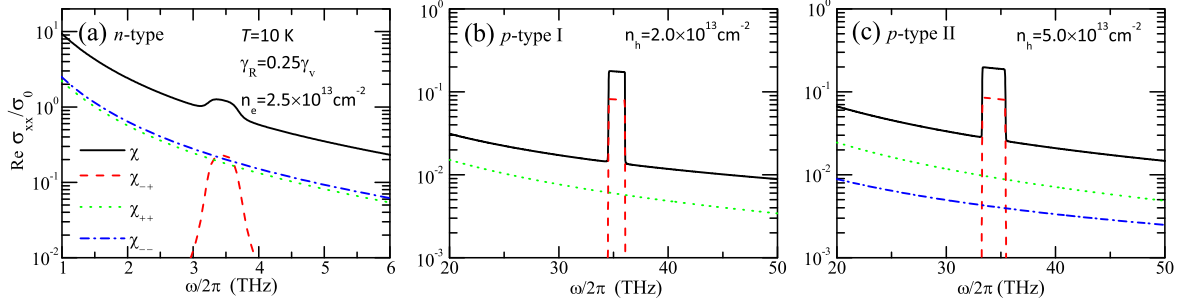


FIG. 2. Finite-temperature contributions from different transition channels to the real part of the longitudinal optical conductivity for different doping types and concentrations as indicated. The contributions to the optical conductivity marked in (a)–(c) correspond to the transition channels shown in Fig. 1 and the black solid curve presented by  $\chi$  is the summation of all the transition channels. Here,  $\sigma_0 = e^2/(4\hbar)$ .

transition channels depend strongly on the doping level in *p*-type samples. For low *p*-type doping, the energy lower valence spin-split subband is fully occupied with electrons. Therefore, free carrier absorption is forbidden for this subband as shown in Fig. 1(b). If the *p*-type doping is larger, the subband can contribute to intraband transitions as indicated in Fig. 1(c). In order to determine the optical absorption, one needs to calculate the real part of the optical conductivity as outlined in the previous section. As a consequence, measuring the optical absorption for different doping levels allows us to determine the conductivity as defined in Eqs. (13) and (14).

In Fig. 2, we show the contributions from different electronic transition channels to optical conductivity at a fixed electron density  $n_e$  for *n*-type ML-MoS<sub>2</sub> and with fixed hole density  $n_h$  for *p*-type I/II ML-MoS<sub>2</sub> at  $T = 10$  K with  $\gamma_R = 0.25\gamma_v$ . We see that the optical conductivity of *n*-type (*p*-type) ML-MoS<sub>2</sub> has contributions from both spin-conserving and spin-flip transitions as indicated by the electronic transition channels in Fig. 1. Due to symmetric dispersion relation at K and K' valleys, the contributions to the optical conductivity in different valleys in Fig. 2 are identical to each other except for the fact that the bands have opposite spin indices for the higher and lower energy bands, respectively. In Fig. 2(b), free carrier absorption only exists in the highest spin-resolved subband because the lowest subband is fully occupied as shown in Fig. 1(b). Therefore, the intraband transitions in *p*-type II ML-MoS<sub>2</sub> contribute more to the optical conductivity than its *p*-type I counterpart. This can be clearly seen in Figs. 2(b) and 2(c). We also notice that the contributions to the optical conductivity via free carrier absorption within the  $v = +$  subband are larger than that within the  $v = -$  subband for *p*-type sample and it is opposite for *n*-type sample. For intraband transitions, which mainly occur in a small low-frequency range, the relaxation time does not vary strongly with frequency. It is shown that the frequency dependence of the free carrier relaxation time in InP depends very little on frequency in the low-frequency range [58]. At the same time, the Rashba effect will also not affect the free carrier relaxation time a lot because the Rashba effect almost does not involve the intraband scattering mechanism. Usually, the Drude model with a single relaxation describes very well the intraband optical conductivity [59].

Spin-conserving intraband transitions give rise to low-frequency THz absorption, whereas spin-flip transitions result

in a wide absorption peak as shown in Fig. 2(a) and a roughly rectangularly shaped spectral absorption as presented in Figs. 2(b) and 2(c). In Fig. 2(a), the total optical conductivity has a wide absorption peak in the low-frequency regime and the total optical conductivity increases at low radiation frequency which shows the usual Drude-like behavior. The wide absorption peak is in the frequency regime 3–3.8 THz which is due to the small spin splitting in the conduction band. The absorption peak shape is due to the smaller energy scale of the transitions in the *n*-type sample. In Figs. 2(b) and 2(c), the total optical conductivity has an absorption window in the high-frequency regime and increases at low radiation frequency as well, while the roughly rectangularly shaped absorption windows in Figs. 2(b) and 2(c) is in the frequency regimes 34.5–36 THz and 33.3–35.5 THz which are induced by the larger spin splitting in the valence band.

In Fig. 3 we show the contributions to the optical absorption of circularly and linearly polarized light field in the two valleys. The optical conductivity consists of a Drude-like part induced by the contribution from intraband transitions that conserve spin, and a narrow absorption window due to spin-flip transitions. Under the linearly and circularly polarized light radiation, the Drude-like part is the same because the contributions to the imaginary part of the Hall conductivity are zero for intraband transitions, which can be seen in Eq. (9). As explained in Sec. III, the absorption of light with linear polarization is proportional to the longitudinal conductivity  $\text{Re } \sigma_{xx}^\xi$ , which is the same for both valleys. However, the absorption of circularly polarized light is also affected by the imaginary part of the Hall conductivity  $\text{Im } \sigma_{xy}^\xi$  which is  $\pm$  opposite for both valleys. As a consequence, the absorption of circularly polarized light is valley-dependent. For the total response to left and right handed circularly polarized light as a function of radiation frequency,  $\sigma_-$  probes mainly the K valley and  $\sigma_+$  the K' one. Additionally, their average is equal to the longitudinal optical conductivity. These interesting findings agree with the results for silicene [55].

The optical conductivity of *n*- and *p*-type II ML-MoS<sub>2</sub> is shown in Fig. 4 as a function of radiation frequency at fixed carrier density and  $\gamma_R$  for different temperatures. For  $\gamma_R = 0.25\gamma_v$  and  $T = 10$  K, the *p*-type doped sample could be regarded as *p*-type I when the hole density  $n_h < 3.36 \times 10^{13} \text{ cm}^{-2}$  and becomes *p*-type II when  $n_h > 3.36 \times 10^{13} \text{ cm}^{-2}$ . In Fig. 4(a), we find that the strength of the wide

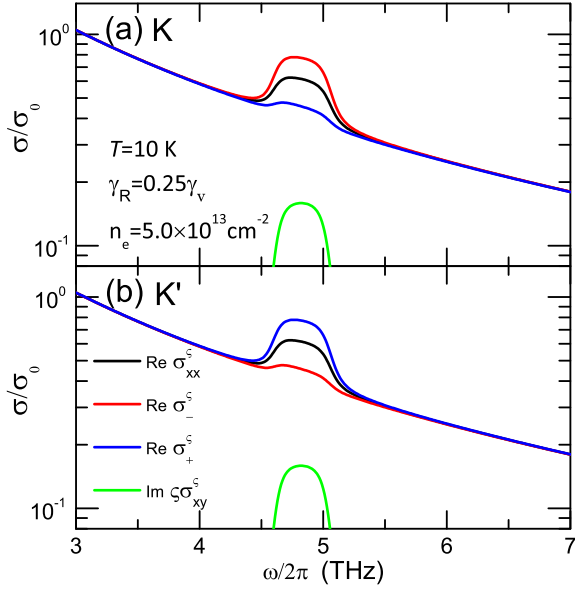


FIG. 3. The absorption part of the optical conductivity to circularly polarized radiation of  $n$ -type ML-MoS<sub>2</sub> at temperature  $T = 10$  K for electron density  $n_e = 5 \times 10^{13} \text{ cm}^{-2}$  and Rashba parameter  $\gamma_R = 0.25\gamma_v$ . The results are shown for (a) the K valley and (b) the K' valley.

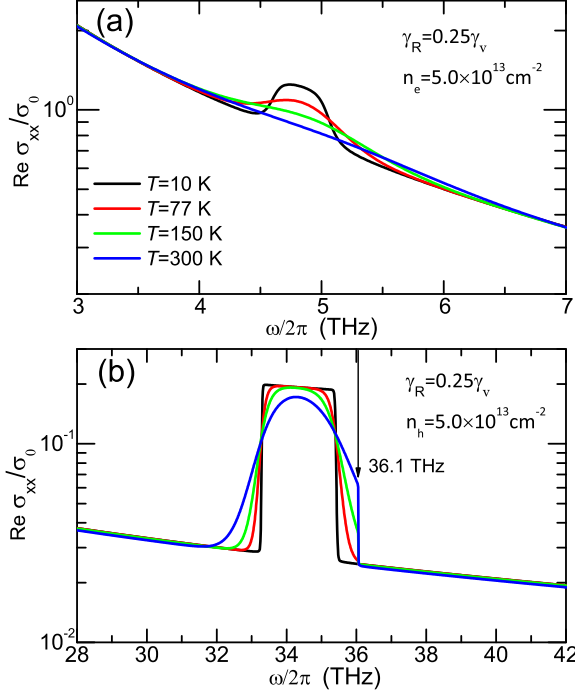


FIG. 4. The real part of the longitudinal optical conductivity as a function of radiation frequency at a fixed carrier density (a) for  $n$ -type and (b) for  $p$ -type ML-MoS<sub>2</sub> for different temperatures.

absorption peak decreases with increasing temperature and vanishes at room temperature. The optical conductivity in Fig. 4(b) has an absorption peak at room temperature and an absorption window at low temperature. At low temperature,  $T = 10$  K, there is a sharper cutoff in absorption window edges. We notice that a hard cutoff at 36.1 THz always exists for the high-temperature cases. With higher temperatures, the electrons in the case of Fig. 1(c) redistribute their states above the Fermi level due to the smoothing of the Fermi-Dirac distribution. Thus, electrons can occupy some states in the top of the  $v = -$  subband and electronic transitions from the  $v = -$  subband to the  $v = +$  subband are possible. However, the top points of the two subbands in the valence band have an energy spacing corresponding to a radiation frequency of 36.1 THz for  $\gamma_R = 0.25\gamma_v$ . Thus, 36.1 THz is the largest optical transition frequency that allows for spin-flip transitions. The Drude-like part of the optical conductivity does not show much difference for different temperatures because the same energy relaxation scattering time is used in the calculation. Generally, we can obtain a stronger absorption peak and a sharper absorption window in the conductivity spectrum at lower temperature. However, the spin-flip transition induced absorption in the  $p$ -type sample can still be observed at room temperature.

In Fig. 5, we show the optical conductivity of  $n$ - and  $p$ -type ML-MoS<sub>2</sub> as a function of radiation frequency for the fixed  $\gamma_R = 0.25\gamma_v$  and  $T = 10$  K for different carrier densities. For ML-MoS<sub>2</sub>,  $n$ - and  $p$ -type doping samples can be realized through the field effect with different source and drain

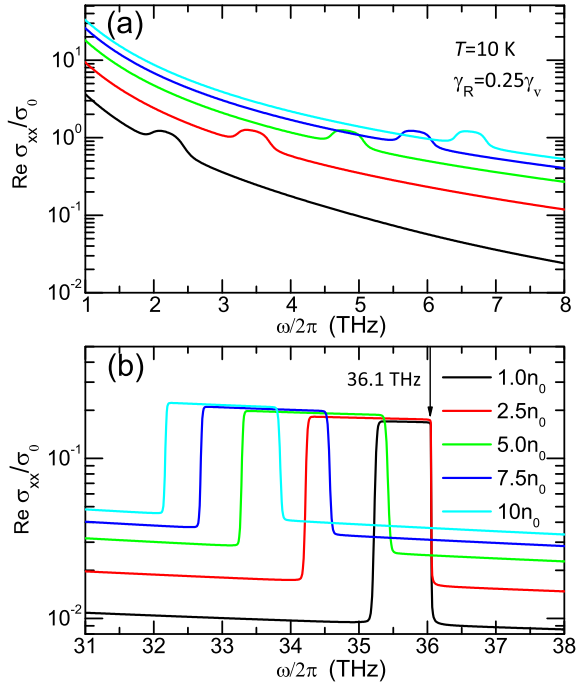


FIG. 5. The real part of the longitudinal optical conductivity as a function of radiation frequency for  $\gamma_R = 0.25\gamma_v$  and  $T = 10$  K and different carrier densities where  $n_0 = 1 \times 10^{13} \text{ cm}^{-2}$ . The results are shown for (a)  $n$ -type and (b)  $p$ -type ML-MoS<sub>2</sub>.

contacts [9,61] and the doping levels can be tuned through the application of a gate voltage. Usually, one could reach high carrier densities [9,62] and we choose the carrier densities with a magnitude of  $10^{13} \text{ cm}^{-2}$  in our calculations. As can be seen in Fig. 5, the contribution to the optical conductivity from intraband transitions increases with increasing carrier density in both *n*- and *p*-type samples. More interestingly, we find that the wide absorption peak in Fig. 5(a) blueshifts to higher frequencies and the absorption window in Fig. 5(b) redshifts to lower frequencies with increasing carrier density. At the fixed Rashba parameter and temperature, the chemical potential for electrons/holes in *n*-/*p*-type samples increases/decreases with increasing carrier density. As a result, the energy required for direct spin-flip transitions increases/decreases with increasing electron/hole density in *n*-/*p*-type ML-MoS<sub>2</sub> due to the Pauli blockade effect [63]. This is how the blueshifts of the absorption peak in the *n*-type sample and the redshifts of the absorption window in the *p*-type sample can occur. In Fig. 5(b), we see that the right boundary of the absorption windows at position 36.1 THz is the largest optical transition frequency for those cases. Apart from the contribution of intra-band transitions, we also find that the strength of the absorption peak in *n*-type samples and the height of the absorption window in *p*-type samples is slightly affected by the carrier density. Besides, the width of the absorption peak in the *n*-type sample varies slightly with electron density and the width of the absorption window in the *p*-type sample varies distinctly with changing hole density. These theoretical results show that the optical absorption of ML-MoS<sub>2</sub> in the THz and infrared regimes can be effectively tuned by varying the carrier density.

In Fig. 6, we plot the low-energy band structure and the energy spacing of spin-split subbands in conduction and

valence bands of ML-MoS<sub>2</sub> as a function of wave vector at the K valley in the presence of the Rashba effect with different Rashba parameters. Usually, the Rashba SOC strength in semiconductors can be tuned by an electric field [22–24]. In Fig. 6(b), near the K point, the energy spacing between two spin-orbit split conduction subbands increases with increasing wave vector or Rashba parameter. With increasing  $\gamma_R$ , the energy spacing turns from a roughly parabolic curve to a roughly linear line and a spin-orbit split gap can be observed at  $ka = 0$  for large  $\gamma_R$ . In Fig. 6(c), one can see that the energy spacing between two-spin split valence subbands decreases with increasing wave vector when  $\gamma_R = 0.1\gamma_v, 0.25\gamma_v$ , and  $0.5\gamma_v$ . When  $\gamma_R = 0.75\gamma_v$ , the energy spacing of spin-split subbands first increases then decreases slightly with increasing wave vector, whereas for  $\gamma_R = \gamma_v$ , the energy spacing of the subbands increases with increasing wave vector. We find that the band structure of ML-MoS<sub>2</sub> can be fine-tuned by the Rashba effect and a more complicated band structure of spin-split subbands with different Rashba parameters can be found in the valence bands.

The optical conductivity of *n*- and *p*-type ML-MoS<sub>2</sub> is shown in Fig. 7 as a function of radiation frequency at the fixed temperature and carrier density for different Rashba parameters. At large carrier density (e.g.,  $5 \times 10^{13} \text{ cm}^{-2}$ ), we find that the top point of the  $v = -$  valence subband and the chemical potential of electrons/holes in *n*-/*p*-type ML-MoS<sub>2</sub> do not vary with changing  $\gamma_R$ . Thus, for a *p*-type ML-MoS<sub>2</sub> with a hole density  $n_h = 5 \times 10^{13} \text{ cm}^{-2}$ , it can be always regarded as *p*-type II for different  $\gamma_R$ . With large carrier density, we find that the dependence of the Fermi level on the Rashba parameter is negligible. With low carrier density, we find that the Fermi level first stays the same with low Rashba

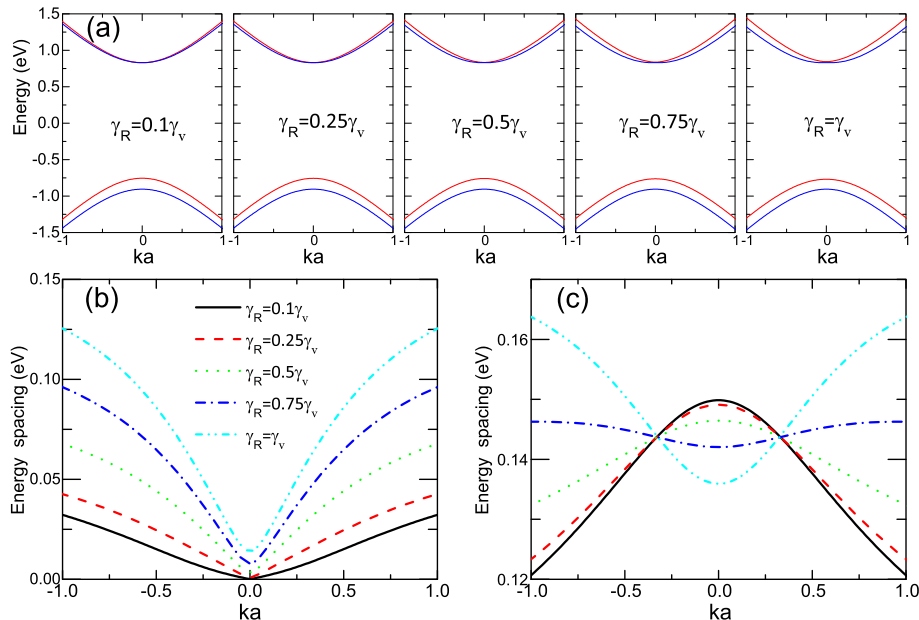


FIG. 6. (a) Low-energy effective band structure of ML-MoS<sub>2</sub> at K valley with different  $\gamma_R$ . The spin-up ( $s = 1$ ) and spin-down ( $s = -1$ ) subbands are denoted by red and blue solid curves, respectively. The energy spacing between two spin-split subbands with different  $\gamma_R$  is shown for (b) conduction band and (c) valence band.

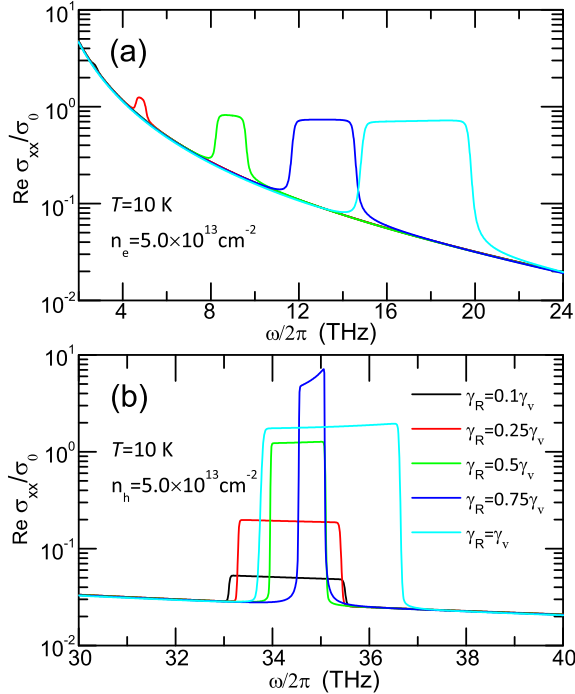


FIG. 7. The real part of the optical conductivity as a function of radiation frequency at fixed temperature  $T = 10$  K and carrier density  $5 \times 10^{13} \text{ cm}^{-2}$  for different Rashba spin-orbit parameters. The results are shown for (a)  $n$ -type ML-MoS<sub>2</sub> and (b)  $p$ -type II ML-MoS<sub>2</sub>.

coupling strength and then decreases slightly with increasing Rashba coupling strength in the  $n$ -type sample, while in the low-density  $p$ -type sample, the Fermi level always decreases slightly with increasing  $\gamma_R$ .

In Figs. 7(a) and 7(b), we see that the Drude-like part of the optical conductivity in  $n/p$ -type ML-MoS<sub>2</sub> is not affected by the value of  $\gamma_R$ . The wide absorption peak in Fig. 7(a) blueshifts and the shape of it turns into an absorption window with increasing  $\gamma_R$ . At the same time, the width of the absorption window increases with increasing  $\gamma_R$  and the height of the absorption window varies slightly. In Fig. 7(b), we can see that there are also absorption windows in the optical conductivity curve with different Rashba parameters but the width and height of them vary a lot with changing  $\gamma_R$ . Through the five sets of data plotted in Fig. 7(b), we find that the widest absorption window can be obtained when  $\gamma_R = \gamma_v$  and the narrowest absorption window is found when  $\gamma_R = 0.75\gamma_v$ . This feature can be derived from Fig. 6(c). We see that the boundaries of these absorption windows in Fig. 7(b) do not match the energy spacings between two spin-split valence subbands at  $ka = 0$  in Fig. 6(c). That means that the boundaries of spin-flip transitions are mainly delimited by the holes' optical transitions near the Fermi level limited by the Fermi-Dirac distribution in the case of a large hole density and low temperature. When  $\gamma_R = 0.75\gamma_v$ , the narrow region of energy spacing in Fig. 6(c) results in the narrowest absorption window in Fig. 7(b) and a blade shape can be seen at the top of the absorption window.

Additionally, the dispersion relation for spin-split conduction subbands in ML-MoS<sub>2</sub> is similar to a traditional 2DEG system in the presence of the Rashba effect. Thus, the results in Fig. 7(a) show some similarities with traditional 2DEGs [27,28]. Due to the complexity of spin-orbit split valence subbands, the height of the absorption windows in Fig. 7(b) varies a lot with changing Rashba parameter which is different from that of traditional 2D systems. As a conclusion, we can say that the optoelectronic properties of ML-MoS<sub>2</sub> with different doping types can be effectively tuned by the Rashba effect.

In order to understand the peculiar phenomenon that the height of the absorption window of a  $p$ -type sample in the presence of the Rashba effect varies a lot with changing Rashba parameter, we would like to examine the role that the intrinsic SOC plays. Although the intrinsic SOC parameter  $\gamma_v$  is a constant that cannot be changed by external field, we would like to show how the intrinsic SOC decides the optical property of ML-MoS<sub>2</sub> by choosing different intrinsic SOC parameters. In Fig. 8, we plot the contributions of the spin-flip transitions to the optical conductivity of  $n$ - and  $p$ -type ML-MoS<sub>2</sub> as a function of radiation frequency at fixed temperature and carrier density. Here, we redefine  $\gamma'_v$  as the intrinsic SOC parameter. Figure 8(a) shows the spin-flip optical conductivity part of Fig. 7(a). With small Rashba coupling strength, we see that the spin-flip contribution of electrons in the  $n$ -type system decreases both in width and in height as the coupling strength decreases. As can be seen from Figs. 8(a)–8(d), the behavior of the optical conductivity with different  $\gamma_R$  is only slightly affected by the intrinsic SOC. The slight difference is caused by the minor modification of the spin split in the conduction band with different  $\gamma'_v$ . From Figs. 8(e)–8(h), we find the following features: (i) With large intrinsic SOC (e.g.,  $\gamma'_v = 75 \text{ meV}, 37.5 \text{ meV}$ ), the height of the absorption window varies strongly with the Rashba parameter. (ii) The heights of the absorption windows change slightly and the shapes of these curves approach those for the  $n$ -type case with a small  $\gamma'_v$ . (iii) In the absence of intrinsic SOC ( $\gamma'_v = 0 \text{ meV}$ ), the optical conductivity curves in Fig. 8(h) are almost identical to those in Fig. 8(d). The ultrafine difference is due to the different scattering times for electrons and holes chosen in our calculation. Indeed, the frequency and Rashba effect would also affect the relaxation time for the interband transitions. As can be seen in Figs. 8(d) and 8(h), the relaxation times used in the energy relaxation approximation only slightly affect the two boundaries of the absorption window and do not affect much the total spin-flip optical conductivity curve. With larger relaxation scattering time which means smaller broadening of scattering states, the spin-flip optical conductivity will approach the result for the long-wavelength optical limit. In this study, we are more interested in the spin-flip transition absorption part which is in the high-frequency regime where the contribution of intraband transitions is weak. Thus, we may safely assume that the energy relaxation time used in the numerical calculation is reliable for describing the optical absorption in the frequency range considered in this study. Therefore, we can see that the intrinsic SOC plays an important role in affecting the optical absorption spectrum of  $p$ -type ML-MoS<sub>2</sub> for changing Rashba SOC strength. In monolayer MX<sub>2</sub>, the intrinsic SOC and the other parameters in Eq. (1)

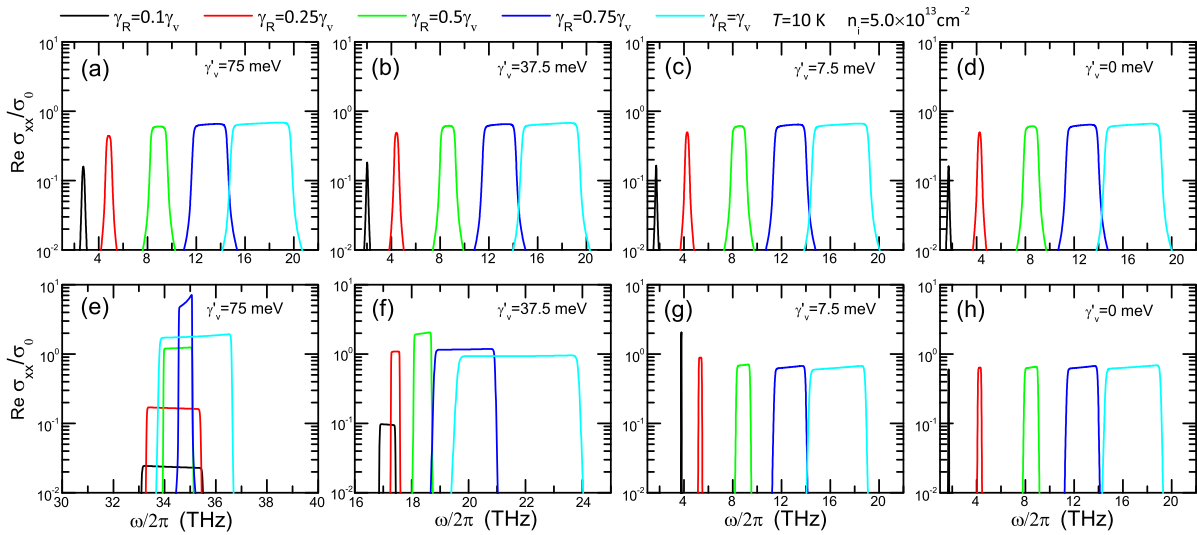


FIG. 8. The real part of the longitudinal optical conductivity contributed from the spin-flip transitions as a function of radiation frequency at fixed temperature and carrier density for different Rashba parameters. Here we use  $\gamma'_v$  to replace  $\gamma_v$  as the intrinsic SOC parameter. The results for different  $\gamma'_v$  are shown for (a)–(d) *n*-type and (e)–(h) *p*-type samples.

vary with different compounds of M and X. Thus, the infrared to THz optical absorption windows with different bandwidths ranges and shapes can also be observed in other ML-TMDC materials in the presence of the Rashba effect.

## V. CONCLUSIONS

In this study, we have investigated the infrared to terahertz optoelectronic properties of *n*- and *p*-type ML-MoS<sub>2</sub> in the presence of the Rashba effect. The optical conductivity is evaluated using the standard Kubo formula. The effects of the polarization of the radiation field, temperature, carrier density, and Rashba parameter on the optical conductivity have been examined. The total optical conductivity contains contributions from different transition channels between different spin states. We have also examined the role that the intrinsic SOC plays in affecting the optoelectronic properties of ML-MoS<sub>2</sub> in the presence of the Rashba effect. The main conclusions we have obtained from this study are summarized as follows.

In ML-MoS<sub>2</sub>, free carrier absorption exists in the entire infrared to terahertz regime. Spin-flip transitions induce wide absorption peaks and absorption windows which range from infrared to THz. Free carrier absorption is weakly affected by the polarization direction of the radiation, temperature, and Rashba parameter but depends strongly on the carrier density. Under circularly polarized radiation, the spin-flip transitions induce a valley-selective absorption. However, the summation over them is the same as the longitudinal optical conductivity.

A stronger absorption peak or sharper absorption window can be observed at lower temperature. The position and width of the absorption peak and absorption window can be effectively tuned by carrier density and Rashba parameter. This suggests that ML-MoS<sub>2</sub> has a wide tunable optical response in the infrared to THz radiation regime.

In the presence of the Rashba effect, the features of optical conductivity in *n*-type ML-MoS<sub>2</sub> are similar to those in 2DEGs and the intrinsic SOC has a strong influence on the optoelectronic property of *p*-type ML-MoS<sub>2</sub>.

We have found that the optoelectronic properties of *n*- and *p*-type ML-MoS<sub>2</sub> can be effectively tuned by the carrier density and Rashba parameter which makes ML-MoS<sub>2</sub> a promising infrared and THz material for optics and optoelectronics. The obtained theoretical findings can be helpful for understanding of the optical properties of ML-MoS<sub>2</sub>. We hope the theoretical predictions in this paper can be verified experimentally.

## ACKNOWLEDGMENTS

Y.M.X. acknowledges financial support from the China Scholarship Council (CSC). This work was also supported by the National Natural Science Foundation of China (Grant No. 11574319), Ministry of Science and Technology of China (Grant No. 2011YQ130018), Department of Science and Technology of Yunnan Province, and by the Chinese Academy of Sciences. B.V.D. is supported by a Ph.D. fellowship from the Flemish Science Foundation.

- 
- [1] K. S. Novoselov, A. K. Geim, S. V. Morozov, D. Jiang, Y. Zhang, S. V. Dubonos, I. V. Grigorieva, and A. A. Firsov, *Science* **306**, 666 (2004).
- [2] Q. H. Wang, K. Kalantar-Zadeh, A. Kis, J. N. Coleman, and M. S. Strano, *Nat. Nanotechnol.* **7**, 699 (2012).

Y. M. XIAO, W. XU, B. VAN DUPPEN, AND F. M. PEETERS

PHYSICAL REVIEW B **94**, 155432 (2016)

- [3] K. F. Mak, C. Lee, J. Hone, J. Shan, and T. F. Heinz, *Phys. Rev. Lett.* **105**, 136805 (2010).
- [4] Zhiming M. Wang, *MoS<sub>2</sub>: Materials, Physics, and Devices* (Springer, Switzerland, 2014).
- [5] A. Splendiani, L. Sun, Y. Zhang, T. Li, J. Kim, C.-Y. Chim, G. Galli, and F. Wang, *Nano Lett.* **10**, 1271 (2010).
- [6] C. Lee, H. Yan, L. E. Brus, T. F. Heinz, J. Hone, and S. Ryu, *ACS Nano* **4**, 2695 (2010).
- [7] B. Radisavljevic, M. B. Whitwick, and A. Kis, *ACS Nano* **5**, 9934 (2011).
- [8] B. Radisavljevic, A. Radenovic, J. Brivio, V. Giacometti, and A. Kis, *Nat. Nanotechnol.* **6**, 147 (2011).
- [9] B. Radisavljevic and A. Kis, *Nat. Mater.* **12**, 815 (2013).
- [10] H. Li, Z. Yin, Q. He, H. Li, X. Huang, G. Lu, D. W. H. Fam, A. I. Y. Tok, Q. Zhang, and H. Zhang, *Small* **8**, 63 (2012).
- [11] Z. Yin, H. Li, H. Li, L. Jiang, Y. Shi, Y. Sun, G. Lu, Q. Zhang, X. Chen, and H. Zhang, *ACS Nano* **6**, 74 (2012).
- [12] R. S. Sundaram, M. Engel, A. Lombardo, R. Krupke, A. C. Ferrari, Ph. Avouris, and M. Steiner, *Nano Lett.* **13**, 1416 (2013).
- [13] D. Xiao, G.-B. Liu, W. Feng, X. Xu, and W. Yao, *Phys. Rev. Lett.* **108**, 196802 (2012).
- [14] A. Kormányos, V. Zólyomi, N. D. Drummond, P. Rakytá, G. Burkard, and V. I. Fal'ko, *Phys. Rev. B* **88**, 045416 (2013).
- [15] H.-Z. Lu, W. Yao, D. Xiao, and S.-Q. Shen, *Phys. Rev. Lett.* **110**, 016806 (2013).
- [16] Z. Li and J. P. Carbotte, *Phys. Rev. B* **86**, 205425 (2012).
- [17] A. Scholz, T. Stauber, and J. Schliemann, *Phys. Rev. B* **88**, 035135 (2013).
- [18] R. Ganatra and Q. Zhang, *ACS Nano* **8**, 4074 (2014).
- [19] K. F. Mak, K. He, J. Shan, and T. F. Heinz, *Nat. Nanotechnol.* **7**, 494 (2012).
- [20] H. Zeng, J. Dai, W. Yao, D. Xiao, and X. Cui, *Nat. Nanotechnol.* **7**, 490 (2012).
- [21] T. Cao, G. Wang, W. Han, H. Ye, C. Zhu, J. Shi, Q. Niu, P. Tan, E. Wang, B. Liu, and J. Feng, *Nat. Commun.* **3**, 887 (2012).
- [22] S. Datta and B. Das, *Appl. Phys. Lett.* **56**, 665 (1990).
- [23] M. M. Glazov, E. Ya. Sherman, and V. K. Dugaev, *Physica E* **42**, 2157 (2010).
- [24] M. W. Wu, J. H. Jiang, and M. Q. Weng, *Phys. Rep.* **493**, 61 (2010).
- [25] W. Xu, *Appl. Phys. Lett.* **82**, 724 (2003).
- [26] X. F. Wang, *Phys. Rev. B* **72**, 085317 (2005).
- [27] D. W. Yuan, W. Xu, Z. Zeng, and F. Lu, *Phys. Rev. B* **72**, 033320 (2005); C. H. Yang, W. Xu, Z. Zeng, F. Lu, and C. Zhang, *ibid.* **74**, 075321 (2006).
- [28] Y. S. Ang, J. C. Cao, and C. Zhang, *Eur. Phys. J. B* **87**, 28 (2014).
- [29] J. Ibañez-Azpíroz, A. Eiguren, E. Ya. Sherman, and A. Bergara, *Phys. Rev. Lett.* **109**, 156401 (2012).
- [30] J. Ibañez-Azpíroz, A. Bergara, E. Ya. Sherman, and A. Eiguren, *Phys. Rev. B* **88**, 125404 (2013).
- [31] C. L. Kane and E. J. Mele, *Phys. Rev. Lett.* **95**, 226801 (2005).
- [32] H. Ochoa and R. Roldán, *Phys. Rev. B* **87**, 245421 (2013).
- [33] J. Klinovaja and D. Loss, *Phys. Rev. B* **88**, 075404 (2013).
- [34] D. Marchenko, A. Varykhalov, M. R. Scholz, G. Bihlmayer, E. I. Rashba, A. Rybkin, A. M. Shikin, and O. Rader, *Nat. Commun.* **3**, 1232 (2012).
- [35] P. D. C. King, R. C. Hatch, M. Bianchi, R. Ovsyannikov, C. Lupulescu, G. Landolt, B. Slomski, J. H. Dil, D. Guan, J. L. Mi, E. D. L. Rienks, J. Fink, A. Lindblad, S. Svensson, S. Bao, G. Balakrishnan, B. B. Iversen, J. Osterwalder, W. Eberhardt, F. Baumberger, and Ph. Hofmann, *Phys. Rev. Lett.* **107**, 096802 (2011).
- [36] T. Stauber and J. Schliemann, *New J. Phys.* **11**, 115003 (2009).
- [37] A. Scholz, T. Stauber, and J. Schliemann, *Phys. Rev. B* **86**, 195424 (2012).
- [38] W. Wang, C. Zhang, and Z. Ma, *J. Phys.: Condens. Matter* **24**, 035303 (2012).
- [39] P. Ingenhoven, J. Z. Bernád, U. Zülicke, and R. Egger, *Phys. Rev. B* **81**, 035421 (2010).
- [40] M. M. Perera, M.-W. Lin, H.-J. Chuang, B. P. Chamlagain, C. Wang, X. Tan, M. M.-C. Cheng, D. Tománek, and Z. Zhou, *ACS Nano* **7**, 4449 (2013).
- [41] K. Dolui, I. Rungger, and S. Sanvito, *Phys. Rev. B* **87**, 165402 (2013).
- [42] Z. Y. Zhu, Y. C. Cheng, and U. Schwingenschlögl, *Phys. Rev. B* **84**, 153402 (2011).
- [43] A. Kormányos, V. Zólyomi, N. D. Drummond, and G. Burkard, *Phys. Rev. X* **4**, 011034 (2014).
- [44] A. O. Slobodenik and D. M. Basko, *2D Mater.* **3**, 035009 (2016).
- [45] J. Qi, X. Li, Q. Niu, and J. Feng, *Phys. Rev. B* **92**, 121403(R) (2015).
- [46] See, e.g., I. N. Bronshtein, K. A. Semendyayev, G. Musiol, and H. Muehlig, *Handbook of Mathematics* (Springer, Berlin, 2007).
- [47] See, e.g., G. D. Mahan, *Many-Particle Physics* (Kluwer Academic, New York, 2000), p. 165.
- [48] Á. Bácsi and A. Virosztek, *Phys. Rev. B* **87**, 125425 (2013).
- [49] See, e.g., M. P. Marder, *Condensed Matter Physics* (Wiley, New York, 2000).
- [50] P. M. Krstajić, P. Vasilopoulos, and M. Tahir, *Phys. Rev. B* **94**, 085413 (2016).
- [51] V. Vargiamidis, P. Vasilopoulos, and G.-Q. Hai, *J. Phys.: Condens. Matter* **26**, 345303 (2014).
- [52] G. Giuliani and G. Vignale, *Quantum Theory of the Electron Liquid* (Cambridge University Press, Cambridge, 2005).
- [53] Y. Song and H. Dery, *Phys. Rev. Lett.* **111**, 026601 (2013).
- [54] H. Shi, R. Yan, S. Bertolazzi, J. Brivio, B. Gao, A. Kis, D. Jena, H. G. Xing, and L. Huang, *ACS Nano* **7**, 1072 (2013).
- [55] L. Stille, C. J. Tabert, and E. J. Nicol, *Phys. Rev. B* **86**, 195405 (2012).
- [56] E. J. Nicol and J. P. Carbotte, *Phys. Rev. B* **77**, 155409 (2008).
- [57] R. Piessens, E. de Doncker-Kapenga, C. W. Überhuber, and D. K. Kahaner, *QUADPACK: A Subroutine Package for Automatic Integration* (Springer-Verlag, Berlin, 1983).
- [58] B. Jensen, *J. Appl. Phys.* **50**, 5800 (1979).
- [59] M. Scheffler, M. Dressel, M. Jourdan, and H. Adrian, *Nature (London)* **438**, 1135 (2005).
- [60] H. Liu and P. D. Ye, *Electron Device Lett. IEEE* **33**, 546 (2012).
- [61] S. Chuang, C. Battaglia, A. Azcatl, S. McDonnell, J. S. Kang, X. Yin, M. Tosun, R. Kapadia, H. Fang, R. M. Wallace, and A. Javey, *Nano Lett.* **14**, 1337 (2014).
- [62] N. T. Cuong, M. Otani, and S. Okada, *J. Phys.: Condens. Matter* **26**, 135001 (2014).
- [63] H. J. Krenner, E. C. Clark, T. Nakaoka, M. Bichler, C. Scheurer, G. Abstreiter, and J. J. Finley, *Phys. Rev. Lett.* **97**, 076403 (2006).

# Multi-component plasmons in monolayer MoS<sub>2</sub> with circularly polarized optical pumping

Y. M. Xiao,<sup>1, 2,\*</sup> W. Xu,<sup>2, 3, †</sup> F. M. Peeters,<sup>1, ‡</sup> and B. Van Duppen<sup>1, §</sup>

<sup>1</sup>Department of Physics, University of Antwerp, Groenenborgerlaan 171, B-2020 Antwerpen, Belgium

<sup>2</sup>Department of Physics and Astronomy and Yunnan Key Laboratory for

Micro/Nano Materials and Technology, Yunnan University, Kunming 650091, China

<sup>3</sup>Key Laboratory of Materials Physics, Institute of Solid State Physics,

Chinese Academy of Sciences, Hefei 230031, China

(Dated: May 22, 2017)

By making use of circularly polarized light and electrostatic gating, monolayer molybdenum disulfide (ML-MoS<sub>2</sub>) can form a platform supporting multiple types of charge carriers. They can be discriminated by their spin, valley index or whether they're electrons or holes. We investigate the collective properties of those charge carriers and are able to identify new plasmon modes. We analyze the corresponding dispersion relation, lifetime and oscillator strength, and calculate the phase relation between the oscillations in the different components of the plasmon modes. All platforms in ML-MoS<sub>2</sub> support a long-wavelength  $\sqrt{q}$  plasmon branch at zero Kelvin. In addition to this, for an  $n$ -component system,  $n - 1$  new plasmon modes appear as acoustic modes with linear dispersion in the long-wavelength limit. These modes correspond to out-of-phase oscillations in the different Fermion liquids and have, although being damped, a relatively long lifetime. Additionally, we also find new modes at large wave vector that are stronger damped by intra-band processes.

## I. INTRODUCTION

Recently, monolayers of transition metal dichalcogenides MX<sub>2</sub> (M=Mo, W, Nb, Ta, Ti, and X=S, Se, Te) have been fabricated [1, 2]. Since then, they are drawing intense interest due to their intriguing physical properties. A monolayer MX<sub>2</sub> (ML-MX<sub>2</sub>) is a trilayer structure in the form of X-M-X with chalcogen atoms (X) in two hexagonal planes separated by a plane of metal atoms (M) [3]. Transition metal dichalcogenides (TMDCs) are indirect band gap semiconductors when stacked in multilayers but have a direct band gap in their monolayer form [1–3]. It has been shown that field-effect transistors (FETs) made from monolayer MoS<sub>2</sub> (ML-MoS<sub>2</sub>) could have a room temperature on/off ratio of up to 10<sup>8</sup> with a mobility higher than 200 cm<sup>2</sup>/Vs [4–6]. With its ultrathin layered structure and an appreciable direct band gap, ML-MoS<sub>2</sub> has great potential applications in nanoelectronics [5], optoelectronics [7, 8], spintronics and valleytronics [9–13].

Investigations of the unique light-matter interaction and many-body effects in ML-MX<sub>2</sub> such as photoluminescence (PL) [10, 11], optical conductivity [14–16], excitons [17], and triions [18] have enriched the understanding of their optical properties. In order to have a better understanding of ML-MX<sub>2</sub> for potential applications, its plasmonic properties are also important.

Plasmons are collective excitations of the electron liquid. They play a fundamental role in the dynamical re-

sponse of electron systems and form the basis of research into optical metamaterials [19, 20]. Since the discovery of atomically thin two-dimensional (2D) graphene [21], it was shown that 2D materials intrinsically feature plasmons and could form a platform for potential applications in plasmonic devices [22]. In recent years, graphene plasmons, in particular, have attracted a lot of interest because of their unique tunability [20], long plasmon lifetime [23], and high degree of electromagnetic confinement [24]. This enables the use of graphene-based plasmonic devices in the spectral range from mid-infrared to terahertz (THz) [25]. The dielectric function of graphene and gapped graphene have also been studied intensively and the corresponding polarization functions were obtained analytically [26–29]. Also plasmons in silicene have been investigated with and without external fields [30, 31]. Collective excitations of the electron liquid in ML-MoS<sub>2</sub> in the absence of external fields have been examined and discussed before [32–34].

Due to its band structure, massless Dirac fermions, massive Dirac fermions and a two-dimensional electron gas all generate a different collective response induced by the inter-particle Coulomb interaction [26–28, 35]. Unlike massless Dirac Fermions in graphene, charge carriers in ML-MoS<sub>2</sub> are described as massive Dirac fermions (MDF) with a strong intrinsic spin-orbit coupling (SOC) giving rise to a splitting of conduction and valence bands with opposite spins [36, 37]. The strong intrinsic SOC preserves the out-of-plane component of the spin as a good quantum number. Moreover, due to the large band gap in the MDF of ML-MoS<sub>2</sub>, its low-energy band structure can also be described by a two-dimensional parabolic band (2DPB) for both the conduction and valence bands with different valley and spin indices [38]. This feature makes the plasmon dispersion of ML-MoS<sub>2</sub> fundamentally different from that of graphene [26, 27, 32]. Indeed,

\*Electronic address: [yiming.xiao@foxmail.com](mailto:yiming.xiao@foxmail.com)

†Electronic address: [wenxu.issp@aliyun.com](mailto:wenxu.issp@aliyun.com)

‡Electronic address: [francois.peeters@uantwerpen.be](mailto:francois.peeters@uantwerpen.be)

§Electronic address: [ben.vanduppen@uantwerpen.be](mailto:ben.vanduppen@uantwerpen.be)

the plasmon dispersion in ML-MoS<sub>2</sub>  $\omega(q) \sim q^{1/2}n^{1/2}$  is similar to a traditional two dimensional electron gas (2DEG) while the plasmon dispersion of graphene is  $\omega(q) \sim q^{1/2}n^{1/4}$ , where  $n$  is the carrier concentration [32].

The optical response of ML-MoS<sub>2</sub> is governed by the dynamics of charge carriers near the Dirac points in reciprocal space, i.e. those residing in one of the two valleys of the energy spectrum. Recently, it was shown that ML-MoS<sub>2</sub> has a remarkable valley selective absorption of circularly polarized light [10–12, 36]. This allows one to address electrons in a single valley. It can be utilized to realize a valley Hall effect [13]. As a consequence, the carrier density in ML-MoS<sub>2</sub> at a specific valley can be tuned through optical pumping [13].

In this way, an optical pumping process can make the electronic system of ML-MoS<sub>2</sub> a tunable multi-component system as shown in Fig. 1. Indeed, by pumping electrons in one valley from the valence band into the conduction band, one generates a system consisting of two liquids of interacting Fermions as shown in Figs. 1(d)-(e). By gating the system, one can change the Fermi level and further fill or empty the conduction or valence bands in both valleys, allowing for an additional component to appear as shown in Figs. 1(a)-(c). As the spin-bands are split in ML-MoS<sub>2</sub>, an additional degree of freedom surfaces because one can use the Fermi level to access only one of the two spin types per valley in the valence band, or both of them, as shown in Figs. 1(b)-(c). In this paper, we investigate the plasmonic response of these different multi-component systems, identify under which conditions new plasmon modes surface and characterize their properties.

The multi-component Fermion system in ML-MoS<sub>2</sub> proves to be a platform for the generation of a variety of collective effects. Apart from the usual plasmon mode intrinsically present in a two-dimensional interacting Fermion liquid [35, 39], we find that in the long-wavelength limit an  $n$ -component system supports  $n - 1$  lightly damped acoustic modes. These modes correspond to oscillations where the different components oscillate with an opposite phase. Furthermore, for large wave vectors, we also find new plasmon modes in spectral regions where Landau damping occurs for some of the components which then exhibit a high decay rate.

The present paper is organized as follows. Sec. II, outlines the theory used to describe plasmons in the multi-component system. In Sec. II A we describe the effective low energy band structure of ML-MoS<sub>2</sub> with both the MDF and 2DPB models and point out their differences and similarities. In Sec. II B, we evaluate the valley-dependent absorption and calculate the carrier density of a photo-excited system under circularly polarized optical pumping. In Sec. II C, we outline the calculations of the finite-temperature polarization function and how plasmons of multi-component systems can be calculated within the random phase approximation. We report and discuss the numerical results for different multi-

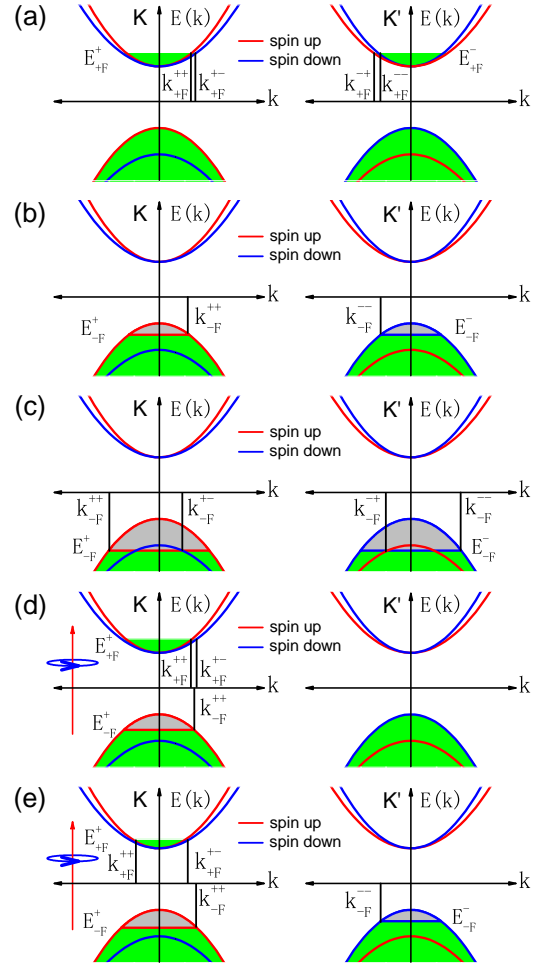


FIG. 1: (Color online) Band structure in the  $K$ -valley (left column) and  $K'$ -valley (right column) of the different ML-MoS<sub>2</sub> systems considered in this study. The bands are colored according to the spin type they represent. The green shading indicates electron occupation while the grey shading indicates hole occupation. In panels (a) - (c) only electrostatic gating is used to change the Fermi level of the systems. In panels (d) - (e) also right-handed circularly polarized light is added to the system in order to pump electrons in the  $K$ -valley from the valence to the conduction band. The Fermi vectors  $k_{\lambda F}^{\text{ss}}$  and Fermi energies  $E_{\lambda F}$  indicated follow Eqs. (6), (8)-(9) and (14)-(15).

component systems in Sec. III. The optical absorption of circularly polarized light in ML-MoS<sub>2</sub> are presented in Sec. III A. We compare the results of massive and hyperbolic models for  $n$ -type ML-MoS<sub>2</sub> in Sec. III B. In Sec. III C, a spin-polarized two-component system at finite temperature is discussed. The valley-polarized three- and four-component systems are discussed in Sec. III D and E, respectively. Finally, our main conclusions are summarized in Sec. IV.

## II. THEORETICAL APPROACH

### A. Electronic band structure and carrier concentration

In this study, we consider a ML-MoS<sub>2</sub> sheet positioned in the x-y plane. The effective Hamiltonian for a carrier (an electron or a hole) around the  $K$  and  $K'$  points in reciprocal space can be written as [36, 37]

$$\hat{H}_0^\zeta = \begin{pmatrix} \Delta/2 & \zeta atk_{-\zeta} \\ \zeta atk_\zeta & -\Delta/2 + \zeta s\gamma \end{pmatrix}, \quad (1)$$

where  $\mathbf{k} = (k_x, k_y)$  being the wavevector,  $k_\pm = k_x \pm ik_y = ke^{\pm i\theta}$ , and  $\theta$  is the angle between  $\mathbf{k}$  and the  $k_x$ -axis,  $\zeta$  is the valley index with  $\zeta = +$  for  $K$  and  $\zeta = -$  for the  $K'$  valley, the spin index  $s = \pm$  for spin-up and spin-down states, the lattice parameter  $a = 3.193$  Å, the hopping parameter  $t = 1.1$  eV [36], the spin-orbit parameter  $\gamma = 75$  meV [40], and  $\Delta$  is the direct band gap equal to 1.66 eV between the conduction and valence bands [36, 37].

The corresponding Schrödinger equation for ML-MoS<sub>2</sub> at valley  $K$  or  $K'$  can be solved analytically and the eigenvalues are given by

$$E_{\lambda\mathbf{k}}^{\zeta s} = \zeta s\gamma/2 + \lambda\Lambda^{\zeta s}(\mathbf{k}), \quad (2)$$

where  $\Lambda^{\zeta s}(\mathbf{k}) = [a^2 t^2 \mathbf{k}^2 + \Delta_{\zeta s}^2]^{1/2}$ ,  $\Delta_{\zeta s} = (\Delta - \zeta s\gamma)/2$ , and  $\lambda = \pm$  refers to conduction/valence band. The corresponding eigenfunction for a carrier in conduction or valence bands near the  $K(K')$  point denoted by  $|\mathbf{k}, \lambda, \zeta, s\rangle$  can be written as

$$\begin{aligned} |\mathbf{k}, +\zeta s\rangle &= [\cos(\vartheta_{\mathbf{k}}^{\zeta s}/2), \zeta \sin(\vartheta_{\mathbf{k}}^{\zeta s}/2)e^{i\zeta\theta}]e^{i\mathbf{k}\cdot\mathbf{r}}, \\ |\mathbf{k}, -\zeta s\rangle &= [-\sin(\vartheta_{\mathbf{k}}^{\zeta s}/2), \zeta \cos(\vartheta_{\mathbf{k}}^{\zeta s}/2)e^{i\zeta\theta}]e^{i\mathbf{k}\cdot\mathbf{r}}, \end{aligned} \quad (3)$$

respectively, in a form of row vector with

$$\cos \vartheta_{\mathbf{k}}^{\zeta s} = \frac{\Delta_{\zeta s}}{\sqrt{a^2 t^2 k^2 + \Delta_{\zeta s}^2}}, \sin \vartheta_{\mathbf{k}}^{\zeta s} = \frac{atk}{\sqrt{a^2 t^2 k^2 + \Delta_{\zeta s}^2}}.$$

The electron (hole) density  $n_\lambda^\zeta$  ( $\lambda = +$  for conduction band and  $\lambda = -$  for valence band) of ML-MoS<sub>2</sub> at valley  $\zeta$  can be written as

$$n_\lambda^\zeta = \frac{1}{(2\pi)^2} \sum_{s=\pm} \int d\mathbf{k}^2 [\delta_{\lambda, -1} + \lambda f_\lambda(E_{\lambda\mathbf{k}}^{\zeta s})], \quad (4)$$

where  $f_\lambda(E_{\lambda\mathbf{k}}^{\zeta s}) = [e^{(E_{\lambda\mathbf{k}}^{\zeta s} - \mu_\lambda^\zeta)/k_B T} + 1]^{-1}$  is the Fermi-Dirac distribution function for electrons and  $\mu_\lambda^\zeta$  is the chemical potential (or Fermi energy  $E_{\lambda\text{F}}^\zeta$  at zero temperature) for electrons in conduction band or holes in valence band at  $\zeta$  valley for a photo-excited quasi-equilibrium system in the present study. At  $T=0$  K, Eq. (4) reduces to the familiar relation between the carrier density and the Fermi vector  $k_{\lambda\text{F}}^{\zeta s}$  for a specific conduction/valence subband with spin index  $s$  and valley index  $\zeta$ ,

$$n_\lambda^\zeta = \sum_{s=\pm} [k_{\lambda\text{F}}^{\zeta s}]^2 / (4\pi). \quad (5)$$

As depicted in Fig. 1, one can use the Fermi level to generate charge carrier liquids with different spins. If the Fermi level lies above the top point of the lowest valence subband for a  $p$ -type ML-MoS<sub>2</sub> as shown in Fig. 1 (b), the lowest subband is fully occupied by electrons and the holes are only distributed in the upper valence subband. The hole density in the upper valence subband is denoted by  $n_-^\zeta$ . This regime holds when the Fermi level satisfies  $E_{-\text{F}}^\zeta \geq -\Delta/2 - \gamma$ , which corresponds to a hole density  $n_-^\zeta \leq (\gamma^2 + \Delta\gamma)/(2\pi a^2 t^2) = 1.679 \times 10^{13}$  cm<sup>-2</sup> at  $\zeta$  valley. The Fermi wave vector and Fermi level for the upper valence subband at valley  $\zeta$  are given by

$$\begin{aligned} [k_{-\text{F}}^{\zeta s}]^2 &= 4\pi n_-^\zeta (\zeta s = 1), \\ E_{-\text{F}}^\zeta &= \gamma/2 - [4\pi a^2 t^2 n_-^\zeta + (\Delta - \gamma)^2/4]^{1/2}. \end{aligned} \quad (6)$$

Then, we consider the other situations as shown in Fig. 1(a) and Fig. 1(c). Using the relation that the Fermi energies for Fermi wavevectors of spin-up and spin-down subbands should be equal, we obtain

$$\Lambda^{\zeta-}(k_{\lambda\text{F}}^{\zeta-}) - \Lambda^{\zeta+}(k_{\lambda\text{F}}^{\zeta+}) = \zeta\lambda\gamma. \quad (7)$$

After combining Eqs. (5) and (7), one can derive the roots of  $[k_{\lambda\text{F}}^{\zeta s}]^2$  as

$$[k_{\lambda\text{F}}^{\zeta s}]^2 = 2\pi n_\lambda^\zeta + \zeta s \left[ \frac{\Delta\gamma}{2a^2 t^2} - \lambda \frac{[\Delta^2\gamma^2 + 8\pi n_\lambda^\zeta a^2 t^2 \gamma^2]^{1/2}}{2a^2 t^2} \right]. \quad (8)$$

Thus, the Fermi energy for a zero temperature system at valley  $\zeta$  with a carrier density  $n_\lambda^\zeta$  is given by

$$E_{\lambda\text{F}}^\zeta = \zeta s\gamma/2 + \lambda\Lambda^{\zeta s}(k_{\lambda\text{F}}^{\zeta s}). \quad (9)$$

The carrier density in a specific electronic branch can also be written as

$$n_\lambda^{\zeta s} = \frac{n_\lambda^\zeta}{2} + \zeta s \left[ \frac{\Delta\gamma}{8\pi a^2 t^2} - \frac{\lambda[\Delta^2\gamma^2 + 8\pi n_\lambda^\zeta \gamma^2 a^2 t^2]^{1/2}}{8\pi a^2 t^2} \right]. \quad (10)$$

The density of state (DOS) can be presented by the imaginary part of the Green function as

$$D_\lambda(E) = \sum_{\zeta s} \frac{|E| - \lambda\zeta s\gamma/2}{2\pi a^2 t^2} \theta[|E| - \lambda\zeta s\gamma/2 - \Delta_{\zeta s}]. \quad (11)$$

When the carrier concentration is low, one can expand Eq. (2) for small deviations from the  $K$  or  $K'$  point. In that case, the low energy electronic band structure of ML-MoS<sub>2</sub> can be written as the 2DPB form for free electron/hole gases as

$$\tilde{E}_{\lambda\mathbf{k}}^{\zeta s} = \lambda \frac{a^2 t^2 \mathbf{k}^2}{2\Delta_{\zeta s}} + \lambda\Delta_{\zeta s} + \frac{\zeta s\gamma}{2}, \quad (12)$$

and the DOS is given by

$$\tilde{D}_\lambda(E) = \sum_{\zeta s} \frac{\Delta_{\zeta s}}{2\pi a^2 t^2} \theta[|E| - \lambda\zeta s\gamma/2 - \Delta_{\zeta s}]. \quad (13)$$

For a *p*-type sample at valley  $\varsigma$  with a hole density  $n_-^\varsigma \leq (\Delta - \gamma)/(\Delta + \gamma)/(2\pi a^2 t^2)$ , the Fermi vector and Fermi level for the upper valence band is

$$\begin{aligned} [\tilde{k}_{\lambda F}^{\varsigma s}]^2 &= 4\pi n_\lambda^\varsigma (\varsigma s = 1), \\ \tilde{E}_{-\text{F}}^\varsigma &= -4\pi a^2 t^2 n_\lambda^\varsigma / (\Delta - \gamma) - \Delta/2 + \gamma. \end{aligned} \quad (14)$$

For the other cases with *n*- or *p*-type doping, the Fermi vector and Fermi level for a specific spin and valley sub-band can be written as

$$\begin{aligned} [\tilde{k}_{\lambda F}^{\varsigma s}]^2 &= 2\pi n_\lambda^\varsigma - \varsigma s \left[ \frac{2\pi n_\lambda^\varsigma \gamma}{\Delta} - \frac{(\Delta^2 - \gamma^2)\gamma}{a^2 t^2 \Delta} \delta_{\lambda, -1} \right], \\ \tilde{E}_{\lambda F}^\varsigma &= \lambda \frac{a^2 t^2 [\tilde{k}_{\lambda F}^{\varsigma s}]^2}{2\Delta_{\varsigma s}} + \lambda \Delta_{\varsigma s} + \frac{\varsigma s \gamma}{2}. \end{aligned} \quad (15)$$

### B. Quasi-equilibrium system by optical pumping

In this section, we solve the Boltzmann equation to obtain the response of charge carriers with different spin- and valley indexes to circularly polarized light. This enables us to find the quasi-equilibrium electron and hole densities in each valley that will be used in the next section to investigate the plasmonic response.

Within the Coulomb gauge, the vector potential of a light field with left ( $\nu = -$ )/right ( $\nu = +$ ) handed polarization is given by [41]

$$A_{\nu=\pm}(t) = \frac{F_0}{\sqrt{2}\omega} \sin(\omega t) (\hat{x} + \nu i \hat{y}). \quad (16)$$

Within first-order perturbation theory, the steady-state electronic transition rate of inter-band transitions between valence and conduction band induced by direct carrier-photon interaction can be obtained by using the Fermi's golden rule, which reads

$$\begin{aligned} W_{\nu, \lambda \lambda'}^{\varsigma s, \mp}(\mathbf{k}, \mathbf{k}') &= \frac{2\pi}{\hbar} \left( \frac{e a t F_0}{\sqrt{2}\hbar\omega} \right)^2 \delta_{\mathbf{k}, \mathbf{k}'} \delta(E_{\lambda' \mathbf{k}'}^{\varsigma s} - E_{\lambda \mathbf{k}}^{\varsigma s} \mp \hbar\omega) \\ &\times [\cos^4(\vartheta_{\mathbf{k}}^{\varsigma s}/2) \delta_{\varsigma \nu, 1} + \sin^4(\vartheta_{\mathbf{k}}^{\varsigma s}/2) \delta_{\varsigma \nu, -1}], \end{aligned} \quad (17)$$

where  $\lambda' = -\lambda$ , the Delta function  $\delta_{\varsigma \nu, \pm 1}$  indicates the valley-dependent selection rule for optical transitions in ML-MoS<sub>2</sub> under a circularly polarized light field, and the  $\mp$  sign in the Delta function refers to absorption (-) or emission (+) of a photon with energy  $\hbar\omega$ .

Due to the fast spin relaxation, compared to the photo-excited carrier life time [13, 42, 43], the photo-excited system in this study can be considered as a quasi-equilibrium system where the carrier distributions in conduction and valence bands can be approximately described by the Fermi-Dirac function with separate chemical potentials for electrons in conduction band and holes in valence band. For nondegenerate statistics, the Boltzmann equation (BE) for each valley and spin subsystem takes the

form

$$\frac{\partial f_{\lambda}^{\varsigma s}(\mathbf{k})}{\partial t} = \sum_{\lambda', \mathbf{k}'} F_{\nu}^{\varsigma s}(\mathbf{k}, \mathbf{k}') - \frac{f_{\lambda}^{\varsigma s}(\mathbf{k}) - f_{\lambda 0}^{\varsigma s}(\mathbf{k})}{\tau}, \quad (18)$$

with  $F_{\nu}^{\varsigma s}(\mathbf{k}, \mathbf{k}') = [W_{\nu, \lambda' \lambda}^{\varsigma s, -}(\mathbf{k}, \mathbf{k}') + W_{\nu, \lambda' \lambda}^{\varsigma s, +}(\mathbf{k}, \mathbf{k}')][f_{\lambda'}^{\varsigma s}(\mathbf{k}') - f_{\lambda}^{\varsigma s}(\mathbf{k})]$ , and  $f_{\lambda}^{\varsigma s}(\mathbf{k}) \simeq f_{\lambda}(E_{\lambda \mathbf{k}}^{\varsigma s})$  is the carrier momentum distribution function and  $f_{\lambda 0}^{\varsigma s}(\mathbf{k})$  represents the initial state in the presence of a dark system.

For the first moment, the mass-balance equation (or rate equation) can be derived after operating with  $\sum_{\mathbf{k}}$  on both sides of the BE. This leads to

$$\frac{\partial n_+^\varsigma}{\partial t} = \frac{\partial n_-^\varsigma}{\partial t} = \sum_s G_{\nu}^{\varsigma s} - \frac{\Delta n^\varsigma}{\tau}, \quad (19)$$

where the carrier generation rate within each subsystem is

$$\begin{aligned} G_{\nu}^{\varsigma s} &= \frac{e^2 F_0^2}{32\hbar^2 \omega} \left[ 1 + \nu \varsigma \frac{2\Delta_{\varsigma s}}{\hbar\omega} \right]^2 \theta(\hbar\omega - 2\Delta_{\varsigma s}) \\ &\times \left[ f_- \left( \frac{\varsigma s \gamma - \hbar\omega}{2} \right) - f_+ \left( \frac{\varsigma s \gamma + \hbar\omega}{2} \right) \right], \end{aligned} \quad (20)$$

$\Delta n^\varsigma$  is the photo-excited carrier density and  $\tau$  is the photo-excited carrier life time which can be measured experimentally [43]. In the steady quasi-equilibrium state of the system, i.e., for  $dn_+^\varsigma/dt = dn_-^\varsigma/dt = 0$ , the mass-balance equation at valley  $\varsigma$  becomes

$$\Delta n^\varsigma = \tau \sum_s G_{\nu}^{\varsigma s}. \quad (21)$$

When one pumps the system with a circularly polarized optical beam, the electrons in the valence band are excited into the conduction band such that a liquid of photo-excited carriers is formed in the conduction band. Therefore, the chemical potential for electrons/holes in conduction/valence band for each valley can be determined through

$$n_{\lambda}^\varsigma = n_{\lambda 0}^\varsigma + \Delta n^\varsigma. \quad (22)$$

where  $n_{\lambda 0}^\varsigma$  is the initial carrier density in conduction or valence band. After combining Eqs. (21) and (22), the photo-excited carrier density can be determined.

From this, also the optical conductivity can be obtained as

$$\begin{aligned} \sigma_{\nu}^{\varsigma s}(\omega) &= \frac{2\hbar\omega G_{\nu}^{\varsigma s}}{F_0^2} = \sigma_0 \left[ 1 + \nu \varsigma \frac{2\Delta_{\varsigma s}}{\hbar\omega} \right]^2 \theta(\hbar\omega - 2\Delta_{\varsigma s}) \\ &\times \left[ f_- \left( \frac{\varsigma s \gamma - \hbar\omega}{2} \right) - f_+ \left( \frac{\varsigma s \gamma + \hbar\omega}{2} \right) \right], \end{aligned} \quad (23)$$

where  $\sigma_0 = e^2/(16\hbar)$ . Finally, we can define the degree of valley-dependent absorption (VA) for light with polarization  $\nu$  as

$$P_{\nu}(\omega) = \frac{\sum_s [\sigma_{\nu}^{+s}(\omega) - \sigma_{\nu}^{-s}(\omega)]}{\sum_s [\sigma_{\nu}^{+s}(\omega) + \sigma_{\nu}^{-s}(\omega)]}. \quad (24)$$

This quantity describes the difference between the absorption (or photo-excited carrier density) at  $K$  and  $K'$  valleys under circularly polarized optical pumping.

### C. Polarization function and plasmons

In this section, we set up the theoretical framework to calculate plasmons in a multi-component system. We work within the Random Phase Approximation (RPA).

When the degeneracy of spin or valley degrees of freedom of an electron/hole gas system is broken, it can be regarded as a multi-component system. For a multi-component system, the component-resolved response functions  $\Pi^{i,i'}(\mathbf{q}, \omega)$  of the interacting electron liquid are given, in the RPA, by the following matrix equation [39, 44]

$$[\Pi^{i,i'}(\mathbf{q}, \omega)]^{-1} = \{\Pi^i(\mathbf{q}, \omega)\}^{-1} \delta_{i,i'} - v_q, \quad (25)$$

where  $\Pi^i(\mathbf{q}, \omega)$  is the non-interacting response function for the  $i$ -th component system and  $v_q = e^2/(2\epsilon_r \epsilon_0 q)$  is the Fourier transform of the Coulomb interaction with  $\epsilon_r = 5$  the relative dielectric constant of the background [32, 33]. The total density-density response function within the RPA can then be written as

$$\Pi^{\text{RPA}}(\mathbf{q}, \omega) = \sum_{ii'} \Pi^{i,i'}(\mathbf{q}, \omega) = \sum_i \Pi^i(\mathbf{q}, \omega) / \epsilon_{\text{RPA}}(\mathbf{q}, \omega), \quad (26)$$

where the RPA dielectric function is defined as

$$\epsilon_{\text{RPA}}(\mathbf{q}, \omega) = 1 - v_q \sum_i \Pi^i(\mathbf{q}, \omega). \quad (27)$$

Plasmons in the RPA can be found from the zeros of the dielectric function  $\epsilon_{\text{RPA}}(\mathbf{q}, \omega(q) - i\eta)$ , where  $\omega(q)$  is the plasmon frequency and  $\eta$  the decay rate of the plasmon [28]. Usually, plasmons can be approximately determined by the roots of the real part dielectric function  $\text{Re}[\epsilon_{\text{RPA}}(\mathbf{q}, \omega)] = 0$  [30, 31], which should also lead to resonance peaks in the energy loss function  $\text{Los}(\mathbf{q}, \omega) = -\text{Im}[\epsilon_{\text{RPA}}]^{-1}$  that can be measured by means of electron energy loss spectroscopy (EELS) [45]. The decay rate (inverse life time) of the weakly damped plasmon is given by

$$\eta = \frac{\text{Im}[\Pi(\mathbf{q}, \omega(q))]}{\{( \partial / \partial \omega) \text{Re}[\Pi(\mathbf{q}, \omega)]\}_{\omega=\omega(q)}}. \quad (28)$$

The imaginary part of the dynamical RPA polarization near the undamped plasmon branch is given by [30, 39]

$$\text{Im}[\Pi^{\text{RPA}}(\mathbf{q}, \omega(q))] = -O(\omega(q))\delta(\omega - \omega(q)), \quad (29)$$

and the oscillator strength of the undamped plasmon mode is defined as

$$O(\omega(q)) = \frac{-\pi}{v_q} \frac{\text{Re}[\Pi(\mathbf{q}, \omega(q))]}{\{( \partial / \partial \omega) \text{Re}[\Pi(\mathbf{q}, \omega)]\}_{\omega=\omega(q)}}. \quad (30)$$

We use the strength of the absorption spectral function  $A(\mathbf{q}, \omega) = -\text{Im}[\Pi^{\text{RPA}}(\mathbf{q}, \omega)]$  [33] to describe the oscillator strength of the damped plasmon modes in the particle-hole excitation spectrum (PHES) ( $\text{Im}[\Pi(\mathbf{q}, \omega)] \neq 0$ ).

For both the undamped and weakly damped plasmon modes, the amplitude of the plasmon oscillation of each component  $N(i)$  can be obtained by calculating the eigenmodes [44] of the real part of the matrix equation (25)

$$[\{\text{Re}[\Pi^i(\mathbf{q}, \omega(q))]\}]^{-1} \delta_{i,i'} - v_q] N(i) = 0, \quad (31)$$

from which we can get the ratio of the plasmon oscillation amplitude

$$N(i)/N(i') = \text{Re}[\Pi^i(\mathbf{q}, \omega(q))] / \text{Re}[\Pi^{i'}(\mathbf{q}, \omega(q))]. \quad (32)$$

We now turn to the calculation of the non-interacting response functions for each component  $\Pi^i$ . We denote each component by the spin and valley index, i.e.  $i = \varsigma, s$  and find

$$\Pi^{\varsigma s}(\mathbf{q}, \omega) = \sum_{\lambda \lambda' \mathbf{k}} \frac{f(E_{\lambda \mathbf{k}}^{\varsigma s}) - f(E_{\lambda' \mathbf{k}+\mathbf{q}}^{\varsigma s})}{\hbar \omega + E_{\lambda \mathbf{k}}^{\varsigma s} - E_{\lambda' \mathbf{k}+\mathbf{q}}^{\varsigma s} + i\delta} C_{\lambda \mathbf{k}, \lambda' \mathbf{k}+\mathbf{q}}^{\varsigma s}, \quad (33)$$

where the structure factor

$$C_{\lambda \mathbf{k}, \lambda' \mathbf{k}+\mathbf{q}}^{\varsigma s} = \frac{1}{2} \left[ 1 + \lambda \lambda' \frac{\Delta_{\varsigma s}^2 + a^2 t^2 \mathbf{k}(\mathbf{k} + \mathbf{q})}{\Lambda^{\varsigma s}(\mathbf{k}) \Lambda^{\varsigma s}(\mathbf{k} + \mathbf{q})} \right], \quad (34)$$

with  $\varphi$  the angle between  $\mathbf{k}$  and  $\mathbf{k} + \mathbf{q}$  with  $\cos \varphi = (k + q \cos \phi) / |\mathbf{k} + \mathbf{q}|$ ,  $\phi$  is the angle between  $\mathbf{k}$  and  $\mathbf{q}$ , and  $f(E_{\lambda \mathbf{k}}^{\varsigma s}) = f_{\lambda}(E_{\lambda \mathbf{k}}^{\varsigma s})$  is the Fermi-Dirac distribution function for electrons.

At long-wavelength ( $\mathbf{q} \rightarrow 0$ ) and low-temperature ( $T \rightarrow 0$  K), we can expand Eq. (34) to second order in  $q$ :

$$C_{\lambda \mathbf{k}, \lambda' \mathbf{k}+\mathbf{q}}^{\varsigma s} \simeq \delta_{\lambda, \lambda'} - \lambda \lambda' \sin^2(\theta_{\mathbf{k}}^{\varsigma s}) q^2 \sin^2 \phi / (4k^2). \quad (35)$$

For intra-band transitions ( $\lambda' = \lambda$ ), the Lindhard ratio can be expanded to second order in  $q$  with the result

$$\frac{f(E_{\lambda \mathbf{k}}^{\varsigma s}) - f(E_{\lambda \mathbf{k}+\mathbf{q}}^{\varsigma s})}{\hbar \omega + E_{\lambda \mathbf{k}}^{\varsigma s} - E_{\lambda \mathbf{k}+\mathbf{q}}^{\varsigma s}} = q \cos \phi \delta(E_{\lambda \mathbf{k}}^{\varsigma s} - E_{\lambda F}^{\varsigma}) \frac{\partial E_{\lambda \mathbf{k}}^{\varsigma s}}{\partial k} \\ \times \left( \frac{1}{\hbar \omega} + \frac{q \cos \phi}{\hbar^2 \omega^2} \frac{\partial E_{\lambda \mathbf{k}}^{\varsigma s}}{\partial k} \right). \quad (36)$$

Because  $C_{\lambda \mathbf{k}, \lambda' \mathbf{k}+\mathbf{q}}^{\varsigma s} \simeq 1$  in the long-wavelength limit, we obtain the real part of the intra-band part of the polarization function as

$$\text{Re}[\Pi_{\text{intra}}(\mathbf{q}, \omega)] = \frac{q^2}{4\pi \hbar^2 \omega^2} \sum_{\lambda \varsigma s} (u_{\varsigma s}^{\lambda} - \Delta_{\varsigma s}^2 / u_{\varsigma s}^{\lambda}) \\ \times \theta(u_{\varsigma s}^{\lambda} - \Delta_{\varsigma s}), \quad (37)$$

with  $u_{\varsigma s}^{\lambda} = |E_{\lambda F}^{\varsigma}| - \lambda \varsigma s \gamma / 2$  where  $E_{\lambda F}^{\varsigma}$  is the Fermi energy for electrons ( $\lambda = 1$ ) in the conduction band or holes ( $\lambda = -1$ ) in the valence band.

For inter-band transitions ( $\lambda' = -\lambda$ ), the real part of the polarization function can be expanded to second order in  $q$  with

$$\text{Re}[\Pi_{\text{inter}}(\mathbf{q}, \omega)] = \frac{-q^2}{32\pi \hbar \omega} \sum_{\lambda \varsigma s} \ln \left| \frac{\hbar \omega + 2u_{\varsigma s}^{\lambda}}{\hbar \omega - 2u_{\varsigma s}^{\lambda}} \right| \\ \times \theta(u_{\varsigma s}^{\lambda} - \Delta_{\varsigma s}). \quad (38)$$

This only contributes by a small amount to the total polarization function in the low frequency regime where plasmons exist.

After using the low- $q$  expansion of the polarization function and neglecting the logarithmic correction, the charge plasmon dispersion in ML-MoS<sub>2</sub> is given by

$$\omega_0(q) = [e^2 q \sum_{\lambda \zeta s} (u_{\zeta s}^\lambda - \Delta_{\zeta s}^2 / u_{\zeta s}^\lambda) \theta(u_{\zeta s}^\lambda - \Delta_{\zeta s}) / (8\pi\epsilon_r\epsilon_0)]^{1/2}. \quad (39)$$

In order to calculate the polarization at arbitrary wave vector  $q$ , we note that the individual valley and spin resolved systems can be regarded as analogous to gapped graphene or silicene [28, 30, 31]. The polarization function depends on  $u_{\zeta s}^\lambda$  which corresponds to a shift of  $\pm\gamma/2$  away from the absolute value of the Fermi level. At zero temperature, the polarization function of an electron liquid with spin  $s$  in the  $\zeta$  valley can be written as

$$\begin{aligned} \Pi_{T=0}^{\zeta s}(\mathbf{q}, \omega) = & \Pi_{0,T=0}^{\zeta s}(\mathbf{q}, \omega) [\tilde{\theta}(\Delta_{\zeta s} - u_{\zeta s}^-) \tilde{\theta}(\Delta_{\zeta s} - u_{\zeta s}^+) \\ & - \theta(u_{\zeta s}^- - \Delta_{\zeta s}) \theta(u_{\zeta s}^+ - \Delta_{\zeta s})] \\ & + \sum_\lambda \Pi_{1,T=0}^{\zeta s \lambda}(\mathbf{q}, \omega) \theta(u_{\zeta s}^\lambda - \Delta_{\zeta s}), \end{aligned} \quad (40)$$

with the step functions

$$\tilde{\theta}(x) = \begin{cases} 1, x \geq 0 \\ 0, x < 0 \end{cases}, \quad \theta(x) = \begin{cases} 1, x > 0 \\ 0, x \leq 0 \end{cases}. \quad (41)$$

The detailed polarization function in the  $(q-\omega)$  plane is presented in the Appendix.

Finally, we note that in order to calculate the response of the system at finite temperature, one can use the following identity to express the Fermi-Dirac function [46]

$$\frac{4k_B T}{e^{(E-\mu)/k_B T} + 1} = \int_{-\infty}^{\infty} \frac{d\mu' \theta(\mu' - E)}{\cosh^2[(\mu' - \mu)/2k_B T]}. \quad (42)$$

Thus, the polarization function could be obtained as an integral transformation of its corresponding zero-temperature polarization function as [47]

$$\begin{aligned} \Pi_T^{\zeta s}(\mathbf{q}, \omega; \mu_+, \mu_-) = & \int_{\Delta/2}^{\infty} \frac{d\mu' \Pi_{1,T=0}^{\zeta s+}(\mathbf{q}, \omega)|_{E_{+F}^\zeta = \mu'}}{4k_B T \cosh^2[(\mu' - \mu_+)/2k_B T]} \\ & + \int_{-\infty}^C \frac{d\mu' \Pi_{1,T=0}^{\zeta s-}(\mathbf{q}, \omega)|_{E_{-F}^\zeta = \mu'}}{4k_B T \cosh^2[(\mu' - \mu_-)/2k_B T]} + \Pi_{0,T=0}^{\zeta s}(\mathbf{q}, \omega) \\ & \times [\mathcal{F}_T(C - \mu_-) - \mathcal{F}_T(\Delta/2 - \mu_+)], \end{aligned} \quad (43)$$

where  $C = \zeta s \gamma - \Delta/2$  and  $\mathcal{F}_T(x) = (e^{x/k_B T} + 1)^{-1}$ , and  $\mu_\lambda^\zeta$  is the chemical potential for conduction and valence bands at valley  $\zeta$  which can be obtained through Eq. (4).

If the ML-MoS<sub>2</sub> system has low carrier density, one can also use a two dimensional parabolic band (2DPB) model to describe the electronic structure as explained in the previous section. The polarization function and plasmons of ML-MoS<sub>2</sub> with the 2DPB model are presented in the Appendix.

### III. RESULTS AND DISCUSSIONS

In this study, we consider both  $n$ - and  $p$ -doped ML-MoS<sub>2</sub>, in the presence and absence of circularly polarized light. We can safely ignore the Rashba spin-orbit coupling because it requires a strong external perpendicular electric field [16]. Therefore, the optical field only couples to the orbital part of the wave function and the spin is conserved during optical transitions. It should be noted that the determination of the photo-excited density in the presence of circularly polarized light in Sec. II B is only suitable for a relatively weak light fields. For high carrier density generated by optical pumping, we extracted the photo-excited carrier density from experimental data [13]. In the following sections, we present numerical calculations for both the plasmon dispersion, energy loss function, plasmon decay rate, plasmon oscillator strength, absorption spectral function and plasmon oscillation ratio to understand the physical characteristics of plasmons in ML-MoS<sub>2</sub>.

#### A. Optical absorption of circularly polarized light

In Fig. 2(a), we show the inter-band optical conductivity of an  $n$ -doped system generated by species of electrons with different valley and spin in response to a right-handed circularly polarized light beam ( $\nu = +$ ). Correspondingly, the valley-dependent absorption (VA) is depicted in Fig. 2(b). The electron density is  $n_e = 1 \times 10^{12} \text{ cm}^{-2}$ , the system is assumed to be at low temperature, i.e.  $T = 4 \text{ K}$  and the lifetime of the photo-excited carriers is  $\tau = 5 \text{ ps}$  [43]. Fig. 2(a) shows that the optical conductivity, and hence the corresponding optical absorption, is the largest in the  $K$  valley when the system is illuminated with right-handed polarized light. When the photon energy is near the edge of the band gap, absorption within the spin-up subband at the  $K$  valley plays a dominant role while the absorption within the spin-down subband is suppressed. This is due to large spin splitting in the valence band. The VA in Fig. 2(b) decreases with increasing photon energy as more transitions become available. Notice the sudden increase in the VA curve which is due to the contribution from the inter-band transitions within the spin-down subband at the  $K$  valley. We notice that one could obtain nearly 100% VA for a circularly polarized light with a photon frequency near the band gap [48].

In Fig. 2(c), we show the photo-excited carrier density under right-handed circularly polarized light at the  $K$  valley as a function of photon energy for a fixed strength of the electrical field. The photo-excited carrier density in Fig. 2(c) is proportional to the sum of the contributions to the spin and valley resolved optical conductivity presented in Fig. 2(a). In Fig. 2(d), we show the photo-excited carrier density in the  $K$  valley as a function of the intensity of the incident radiation. In the presence of circularly polarized light with photon energy  $\hbar\omega = 1.6 \text{ eV}$ ,

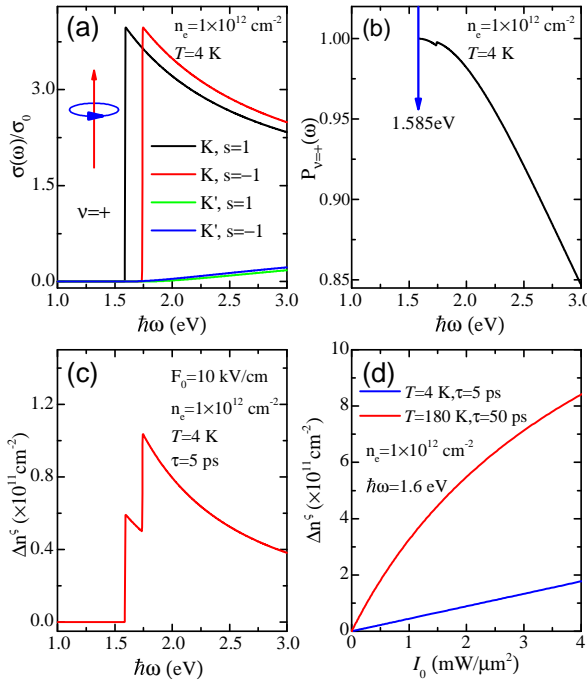


FIG. 2: (Color online) (a) Contributions to the inter-band optical conductivity  $\sigma_v^{ss}(\omega)$  for different valley and spin subsystems and (b) the VA of right-handed ( $\nu = +1$ ) circularly polarized radiation by ML-MoS<sub>2</sub> as a function of photon energy. (c) Photo-excited carrier density due to right-handed circularly polarized light pumping at the  $K$  valley as a function of photon energy. The sudden increase is due to the contribution from the spin-down subsystem. (d) Photo-excited carrier density at  $K$  valley as a function of the radiation intensity  $I_0 \sim F_0^2$  of right-handed circularly polarized light with fixed photon energy, where  $F_0$  is the electric field strength of the incident light.

the VA is nearly 100% which means only electrons in the  $K$  valley are pumped. In the limit of weak light intensities, we observe that the photo-excited carrier density has a linear dependence on the radiation intensity, crossing over to a square root dependency for stronger radiation intensities when  $T=180$  K. Notice that the photo-excited carrier life time varies with temperature [43] and that a larger carrier density can be obtained at higher temperature which can be seen from Eq. (21) and Fig. 2(d).

These results show that in order to efficiently excite charge carriers in a single valley, one has to use a circularly polarized light beam with photon energy close to the bandgap. This will break valley degeneracy in the ML-MoS<sub>2</sub> system and make it a multi-component system. The plasmonic response of these systems is discussed in the next sections.

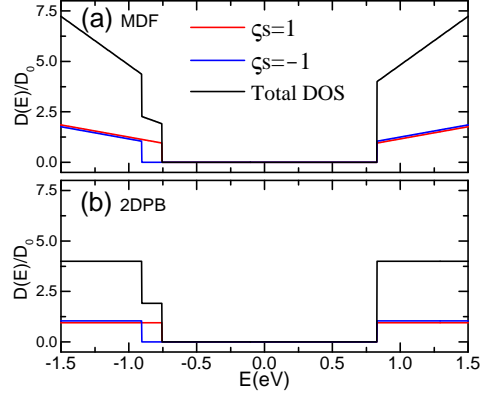


FIG. 3: (Color online) Density of states for charge carriers in ML-MoS<sub>2</sub> with (a) MDF model and (b) 2DPB model, respectively. Here we used the notation  $D_0 = \Delta/(4\pi a^2 t^2)$ .

### B. Comparison between massive and hyperbolic description

Usually, the band structure of ML-MoS<sub>2</sub> is described by a massive Dirac Fermion (MDF) model [36]. However, due to the large band gap in ML-MoS<sub>2</sub>, the effective low-energy band structure of the MDF can also be approximately described by two-dimensional electron/hole gases with two-dimensional parabolic bands (2DPB) if the carrier concentration in the bands is not too large. The relation between these two models was shown before in Eq. (12). In this section we show the equivalence of these two models in describing the optical response of ML-MoS<sub>2</sub>.

In Fig. 3, we plot the density of states (DOS) of ML-MoS<sub>2</sub> for MDF and 2DPB models, respectively. In the energy regime near the bottom/top of the conduction/valence band, the DOS of the two models is very close, while as the energy increases, the two models deviate from each other. This indicates that we can, indeed, use a 2DPB model to describe the band structure of ML-MoS<sub>2</sub> with low carrier density.

In Fig. 4, we compare the plasmonic properties calculated within the two models for an  $n$ -type ML-MoS<sub>2</sub> whose band structure and occupation is shown in Fig. 1(a). We show the electron energy-loss function in the  $(q-\omega)$  plane at zero and room temperature, the plasmon dispersion and the decay rate of these modes. The electron density is fixed at  $n_e = 1 \times 10^{12} \text{ cm}^{-2}$  and equally distributed over the two valleys. In Figs. 4(a) and (e), we compare the zero-temperature energy-loss functions. The plasmon appears as a curve of strong absorption in the long-wavelength limit. For large  $q$ , the plasmon branch merges with the continuum of intra-band single-carrier excitations, which shows up as an increased absorption. Notice that the two models give qualitatively the same results, and also quantitatively they agree very closely.

Panels (b) and (f) of Fig. 4 show the energy-loss func-

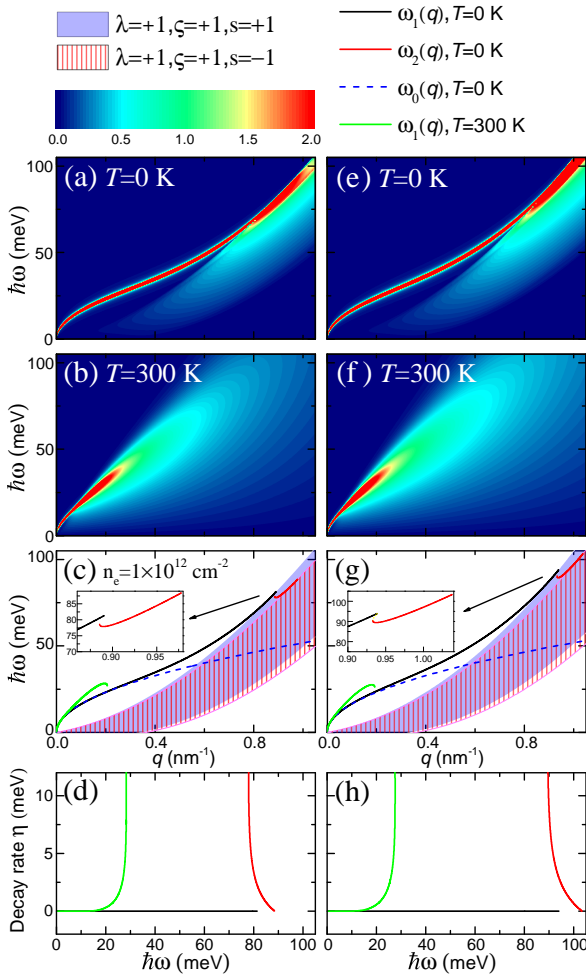


FIG. 4: (Color online) The energy loss function for the MDF model at (a)  $T = 0$  K and (b)  $T = 300$  K. The plasmon dispersion and plasmon decay rate for the MDF model are shown in (c) and (d), respectively. (e)-(h) are the corresponding results of (b)-(e) for the 2DPB model. The insets in (c) and (g) are a zoom of the large  $q$  area as indicated by the arrows. The blue dashed curve corresponds to the zero temperature charge plasmon mode as obtained within the low- $q$  approximation.

tion at room temperature. The result shows that a finite temperature damps the plasmon, inhibiting collective excitations at larger energies and wave vectors. Notice that also here the two models give qualitatively and quantitatively very similar results.

In panels (c) and (g) of Fig. 4 we show the roots of the real part of the dielectric function  $\epsilon_{\text{PRA}}(\mathbf{q}, \omega)$  as solid curves. The black curve is the 2D charge plasmon, responsible for the thin line of enhanced absorption in the previous panels. As shown by the dashed blue curve, in

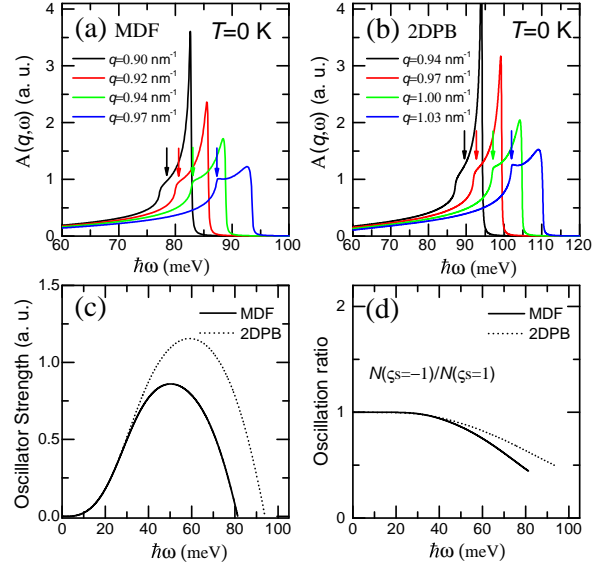


FIG. 5: (Color online) The absorption spectral function of an  $n$ -type ML-MoS<sub>2</sub> for the situation corresponding to Fig. 4 as a function of energy for different fixed wavevectors for (a) the MDF model and (b) the 2DPB model at  $T = 0$  K. (c) The oscillator strength of the zero temperature undamped plasmon for the two models. (d) The oscillation ratio of the two different components in  $n$ -type ML-MoS<sub>2</sub> for the two models. The arrows in (a)-(b) indicate the corresponding plasmon frequency for the second plasmon branch  $\omega_2(q)$ .

the long-wavelength limit this mode coincides with the  $\sqrt{q}$ -plasmon mode from Eq. (39). The green solid curve in these panels shows the plasmon mode for a finite-temperature system. The results show that at room temperature this mode is limited to the long-wavelength regime. Remarkably, in both panels, shown by a solid red curve, there is also a new mode appearing inside the intra-band continuum of the spin-up/spin-down particles at  $K/K'$  valley. This new mode is responsible for the enhanced values of the electron-energy loss function in panels (a) and (e) and is not appearing only due to a breaking of the spin-degeneracy.

In panels (d) and (h) we show the decay rate as a function of the photon energy for each mode. The black solid curve at the bottom of the panel refers to the normal charge plasmon mode. The decay rate for this mode is zero for every energy because it lies outside the particle-hole continuum. The newly found mode, shown by the red curve, however, is partly Landau damped and acquires a finite decay rate. Notice that the decay rate decreases for larger energy and is of the same order of magnitude as that of the normal plasmon mode at room temperature, shown by the green curve in Figs. 4(d) and (h).

In order to characterize the new, partly damped plasmon mode further, in Fig. 5, we show the spectral func-

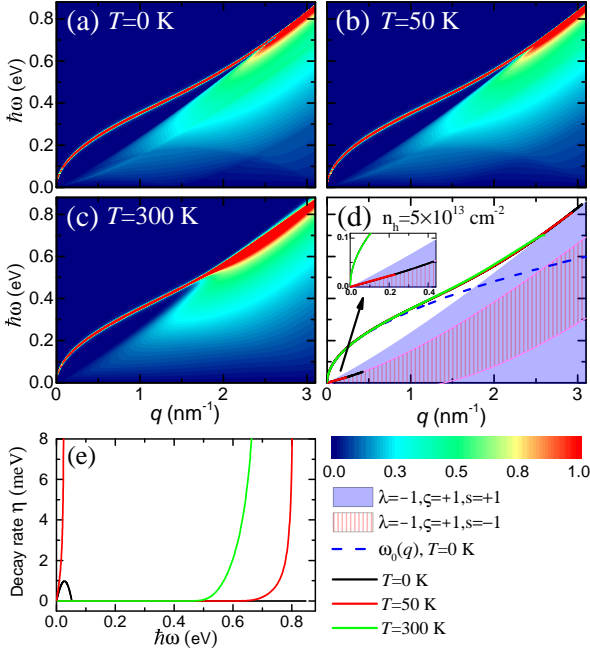


FIG. 6: (Color online) (a)-(c) The energy loss function of strongly doped  $p$ -type ML-MoS<sub>2</sub> in the  $(q, \omega)$  plane for different temperatures. (d) The plasmon dispersion as a function of wavevector for the different temperatures. (e) The plasmon decay rate as a function of plasmon energy for the plasmon modes in (c). The inset in (d) is the zoom of the small  $q$  and  $\omega$  regime as indicated by the arrow.

tion  $A(q, \omega)$  for different values of the wave vector  $q$ . We see that the new mode appears as a shoulder to the spectral function that should be distinguished from the peak in the spectral function at the edge of the particle-hole continuum. Panels (a) and (b) of Fig. 5 show that the MDF and 2DPB models have a qualitative correspondence, but quantitatively they differ slightly. This difference also surfaces when calculating the oscillator strength and the ratio of the amplitudes in both valleys in panels (c) and (d), respectively. It shows that the 2DPB model overestimates the oscillator strength and the plasmon frequency for a given wave vector. However, the qualitative behaviour is similar. We can, therefore, safely use the 2DPB model to investigate the plasmonic properties in ML-MoS<sub>2</sub> bearing in mind that the results might be quantitatively slightly departing.

### C. Spin-polarized two-component system at finite temperature

We now turn to the discussion of a two-component system where the two components are characterized by a different spin. We can obtain this system in MoS<sub>2</sub> by tuning the Fermi level such that the two spin resolved

valence bands are occupied by holes as depicted in Fig. 1(c). Notice that because in the opposite valley the upper and lower valence bands are reversed, there is no macroscopic spin imbalance. Nonetheless, the spin-imbalance in a single valley has an effect on the optical and plasmonic properties of the system as will be shown below.

In Fig. 6 we show the energy loss function, plasmon dispersion and the plasmon decay rate for  $p$ -type ML-MoS<sub>2</sub> using the MDF model at a fixed hole density  $n_h = 5 \times 10^{13} \text{ cm}^{-2}$ . We show results for three different temperatures. The energy loss functions and corresponding plasmon dispersions at each temperature shows that there is a charge plasmon mode in the small  $q$  regime. Notice, however, that in contrast to the  $n$ -type system, the plasmon dispersion is not affected a lot by temperature as is shown in Fig. 6(d). In panel (e), we show the decay rate of the plasmon modes at each temperature and find that also at finite temperature the lifetime is still appreciable, in strong contrast to  $n$ -type ML-MoS<sub>2</sub> discussed in the previous section.

The plasmon branches in Fig. 6(d) also reveal an additional peculiarity in the long-wavelength limit. Indeed, there exists a weakly damped linear acoustic plasmon mode in between the upper boundaries of the intra-band PHES of the two valence subbands. In this region the PHES has a local minimum and it is expected that the mode is, therefore, relatively stable. The new acoustic mode is similar to the one previously discussed in general spin-polarized two-dimensional electron gases [44, 49], but is now present in the absence of a macroscopic spin-imbalance.

In Fig. 7(a), we show the plasmon dispersion of a  $p$ -type ML-MoS<sub>2</sub> for the MDF model with a fixed hole density  $n_h = 5 \times 10^{13} \text{ cm}^{-2}$  as a function of wave vector for the zero temperature case as in Fig. 6(d). From this plot, one can clearly identify the normal  $\omega_1(q)$  plasmon mode, and the new acoustic mode  $\omega_2(q)$ . In Fig. 7(b), we plot the spectral function for fixed plasmon wave vectors. Notice that the linear plasmon mode appears as a peak on top of the background particle-hole weight and, therefore, is expected to be less clear than the distinct  $\omega_1(q)$  plasmon. In panel (c) of Fig. 7, we show the oscillator strength of the  $\omega_1(q)$  plasmon mode, which shows a similar behaviour as observed before.

To identify the character of the newly observed acoustic mode, in Fig. 7(d), we plot the ratio of the amplitude of the oscillation for both spin components. We see that for the new mode, displayed in red, this ratio is negative and approaches  $-1$  in the long-wavelength limit. This means that the density of the two spin components oscillates in anti-phase. Therefore, this mode was labeled before as a spin-plasmon because this means that the carrier density does not oscillate, but it is rather the spin of the carriers that forms an oscillating pattern [44]. As a consequence of the carrier density oscillation being in anti-phase for each spin component, the mode is nearly charge neutral. Inspecting the  $\omega_1(q)$  mode in panel (d) shows that the two spin-components oscillate in-phase

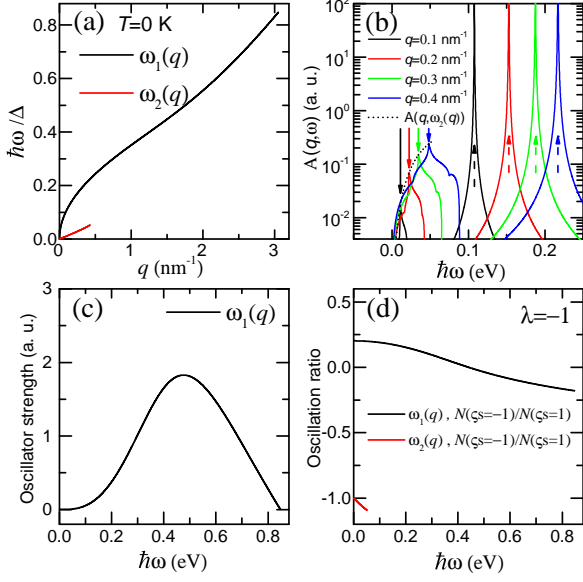


FIG. 7: (Color online) (a) The plasmon dispersion as a function of wave vector for *p*-type ML-MoS<sub>2</sub> at  $T = 0$  K as shown in Fig. 6(d). (b) The absorption spectral function as a function of energy  $\omega$  for fixed wavevectors and the absorption spectral function  $A(q, \omega_2(q))$  (dashed line) for the linear acoustic plasmon  $\omega_2(q)$ . The solid and dashed arrows correspond to the weakly damped linear acoustic plasmon and undamped charge plasmon energies for fixed wavevectors. (c) Plasmon oscillator strength of the undamped plasmon mode  $\omega_1(q)$ . (d) Ratio of the plasmon oscillation amplitudes for the two spin components for the the two plasmon modes as indicated.

for small frequency, but then cross-over to an oscillation in anti-phase. At this crossing point, the amplitude of the oscillation in the spin-down hole liquid is zero, and hence, the plasmon is spin-polarized.

#### D. Valley polarized three-component system

In Fig. 8, we show the plasmonic behaviour of an undoped ML-MoS<sub>2</sub> sheet with a photo-excited carrier density  $\Delta n^+ = 5 \times 10^{11} \text{ cm}^{-2}$  by right-handed circularly polarized light at zero temperature. In Fig. 1(d), the band structure and carrier occupation are shown. In this system, free carriers exist only in the  $K$  valley thanks to the valley-dependent photo-excitation. In the  $K'$  valley, no free carriers exist and, therefore, no plasmon propagation is possible.

This system can be regarded as a three-component system. Indeed, only one spin valence band is depleted by the photo-excitation, generating a single hole liquid, but because of very fast spin relaxation in the conduction band, both spin bands are occupied. This generates two independent free carrier liquids. For this system, the energy loss function in the  $(q-\omega)$  plane is shown in Fig. 8(a)

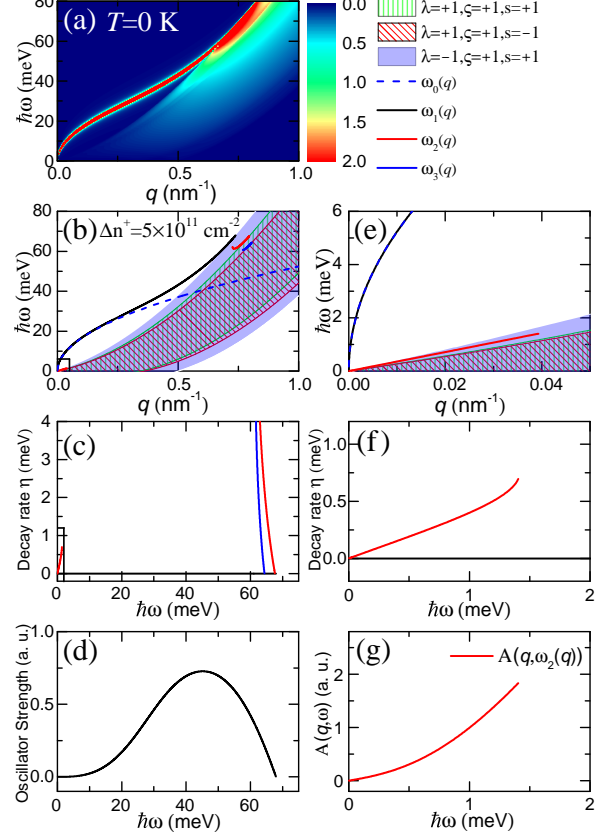


FIG. 8: (Color online) (a) The energy loss function and (b) plasmons dispersion as a function of wave vector for an undoped ML-MoS<sub>2</sub> with a photo-excited carrier density  $\Delta n^+ = 5 \times 10^{11} \text{ cm}^{-2}$  by a right-handed circularly polarized optical pumping. (c) The corresponding plasmon decay rate as a function of plasmon energy. (e)-(f) are the zoom in of the black block areas in (c)-(d). (d) The plasmon oscillator strength of the undamped plasmon  $\omega_1(q)$  as a function of plasmon energy. (g) The absorption spectral function of the weakly damped linear acoustic plasmon model  $\omega_2(q)$ .

and the plasmon dispersion as a function of  $q$  is shown in Fig. 8(b). The plasmon branch shows up clearly in Fig. 8(a) and corresponds to an undamped charge plasmon mode. In Fig. 8(b), we can see that there exist now in total three plasmon modes in three regions divided by the upper boundaries of the intra-band PHES for the three components. These additional modes are responsible for the increased energy loss in that region in the  $q-\omega$  plane. The corresponding plasmon decay rates are shown in Fig. 8(c) and show that the new plasmon modes have indeed a finite lifetime. The undamped charge plasmon mode  $\omega_1(q)$ , however has zero decay rate.

In the small  $q$  limit, there is a weakly damped linear acoustic plasmon mode which we label by  $\omega_2(q)$ . To show this mode more clearly, in Figs. 8(e)-(f) we show a zoom of the black box in Figs. 8(b)-(c). Fig. 8(d) shows that

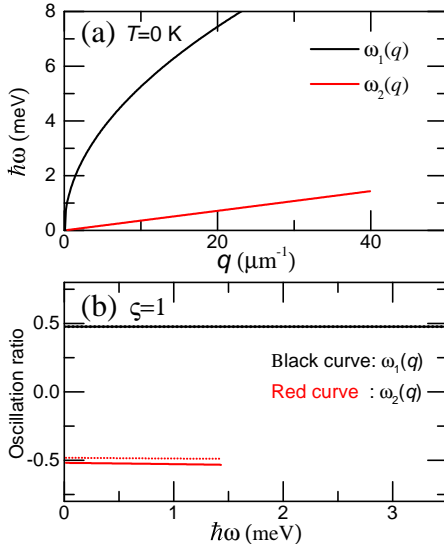


FIG. 9: (Color online) (a) The plasmon dispersion within the 2DPB model of a photo-excited undoped ML-MoS<sub>2</sub>. The carrier density  $\Delta n^+ = 5 \times 10^{11} \text{ cm}^{-2}$  is induced by right handed circularly polarized light pumping. (b) The oscillation ratio between the spin-up conduction subband at the  $K$  valley and the spin-up valence subband at the  $K$  valley (solid lines) and between the spin-down conduction subband at the  $K$  valley and the spin-up valence subband at  $K$  valley (dashed lines). The black and red curves correspond to the results of plasmon modes  $\omega_1(q)$  and  $\omega_2(q)$ , respectively.

the plasmon oscillator strength for  $\omega_1(q)$  increases first and then decreases to zero. For the weakly damped linear acoustic plasmon mode  $\omega_2(q)$  in the small  $q$  regime, the plasmon decay rate and the strength of its absorption spectral function increase with increasing plasmon energy.

In Sec. II C, we obtained the polarization function for each valley and spin subsystem of the MDF model which contains the contribution from both the intra-band transitions within the conduction and valence bands and the inter-band transitions between the conduction and valence bands. Thus, we cannot directly calculate the plasmon oscillation ratio of the different subband components through Eq. (32) with the polarization function of the MDF model for a photo-excited system. Instead, we resort to the description of the system with a 2DPB model.

In Fig. 9, we show the plasmon dispersion and plasmon oscillation ratio for the corresponding situation shown in Fig. 8 but now with the 2DPB model. We find that the plasmon dispersion of 2DPB model in Fig. 9(a) coincides with the results in Fig. 8(e). Within the 2DPB model, we can calculate the ratio's of the amplitude of oscillation in three different components considered in this system. In Fig. 9(b), we show these oscillation ratios as a function of the photon frequency. In these calculations, the amplitude of the oscillation is calculated with respect to

the amplitude of the valence band component. For the undamped plasmon mode  $\omega_1(q)$ , the spin-up and spin-down components in the conduction band and the spin-up component in valence band at  $K$  valley oscillate in phase. Both electron components have an equally large oscillation. For the linear plasmon mode  $\omega_2(q)$ , however, the oscillation ratio between the conduction band and valence band is negative so the oscillation is in anti-phase. In the low- $q$  limit, the summation of the oscillation ratio for the acoustic plasmon mode  $\omega_2(q)$  with the spin-up and down conduction subbands is equal to  $-1$ . This means that the strength of the oscillation in both electron components is also nearly equal, but in anti-phase with the hole liquid. This type of anti-phase behavior was noted before in spin-polarized 2D electron systems[44]. Now, however, the weakly damped linear plasmon is not charge neutral since the anti-phase oscillations occur in oppositely charged liquids of electrons and holes.

#### E. Four-component system

We end the analysis with the discussion of a four-component system. As shown in Fig. 1(e), such a system can be created when a *p*-type ML-MoS<sub>2</sub> is pumped with circularly polarized light. This will excite electrons in one valley into the conduction band. As the spin relaxation time is very small [13, 42], the quasi equilibrium formed in the system consists of an electron pocket in one valley, but with electrons of two spin types with the same Fermi level, and two pockets of holes distributed over the two valleys with different Fermi level.

We assume that the *p*-type doped ML-MoS<sub>2</sub> has an initial hole density  $n_h = 1 \times 10^{12} \text{ cm}^{-2}$ . The photo-excited carrier density is  $\Delta n^+ = 5 \times 10^{11} \text{ cm}^{-2}$ , which is induced by right-handed circularly polarized optical pumping. The energy loss function in Fig. 10(a) shows the typical plasmon pole corresponding to the  $\omega_1(q)$  mode as in the previous systems. In Figs. 10(b) and (e) we, however, find that there exist three new plasmon branches for large photon energy, and two new acoustic modes in the long-wavelength limit. As before, these new modes appear in regions of the intra-band continuum where only some of the components are subject to Landau damping. The quantification of the importance of Landau damping is shown by the decay rate calculated in panels (c) and (f) where it is shown that, remarkably, the acoustic  $\omega_3(q)$  mode is more stable than the acoustic  $\omega_2(q)$  mode even though it can be found deeper in the intra-band electron-hole continuum. Furthermore, as shown in panel (g), the  $\omega_3(q)$  mode is more pronounced in the spectral function than the  $\omega_2(q)$ , so one expects the former to be more easily excited. Finally, the oscillator strength calculated in panel (d) of Fig. 10 shows no qualitative differences due to the presence of the new modes in the intra-band continuum. This means that these modes are the consequence of a redistribution of spectral weight inside the continuum rather than getting it from the regular plas-

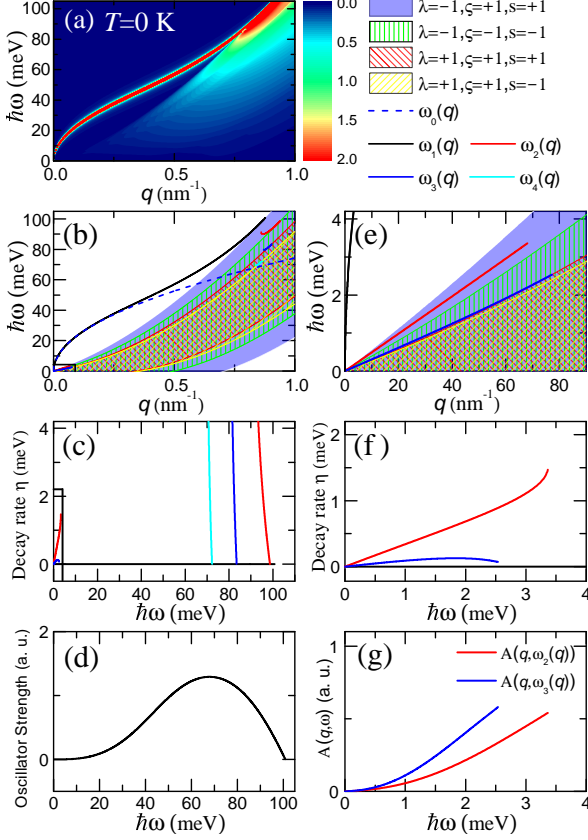


FIG. 10: (Color online) (a) The energy loss function and (b) the plasmon dispersion as a function of wave vector for a photo-excited *p*-type doped ML-MoS<sub>2</sub> with initial hole density  $n_h = 1 \times 10^{12} \text{ cm}^{-2}$  and a photo-excited carrier density  $\Delta n^+ = 5 \times 10^{11} \text{ cm}^{-2}$  induced by pumping with right-handed circularly polarized light. (c) The corresponding plasmon decay rate as a function of plasmon energy. (e) and (f) are the zoom of the black boxes in (b) and (c). (d) The plasmon oscillator strength of the undamped plasmon  $\omega_1(q)$  as a function of plasmon energy. (g) The absorption spectral function of the two weakly damped linear acoustic plasmon modes.

mon.

In Fig. 11, we plot the plasmon dispersion and the oscillation ratio between the different components for the long-wavelength acoustic modes discussed in the previous paragraph. For these results, we investigated the system within the 2DPB model. We find the same long-wavelength modes as before as we show in panel (a).

In panel (b), we calculate the ratio between the amplitudes of the different components in the system for the three different plasmon modes. The solid curves denote the ratio between the amplitude of the oscillations in the spin-up electron pocket and the spin-up hole pocket in the *K* valley. The results show that the  $\omega_1(q)$  mode consists of in-phase oscillations, while for the two other modes the oscillations are in anti-phase. The dashed

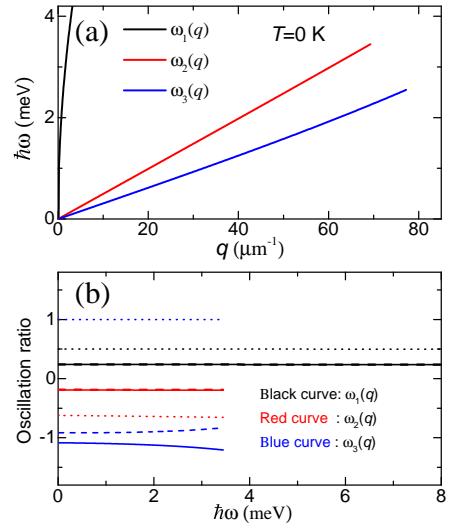


FIG. 11: (Color online) (a) The zero-temperature plasmon dispersion within the 2DPB model of an optically pumped *p*-type doped ML-MoS<sub>2</sub> with a initial hole density  $n_h = 1 \times 10^{12} \text{ cm}^{-2}$  and a photo-excited carrier density  $\Delta n^+ = 5 \times 10^{11} \text{ cm}^{-2}$  realized trough pumping with right-handed polarized light. (b) The ratio of the oscillation amplitudes in the spin-up conduction subband and the spin-up valence subband at *K* valley (solid lines), the ratio between the spin-down conduction subband and the spin-up valence subband at *K* valley (dashed lines) and the ratio between the spin-down valence subband at *K'* valley and the spin-up valence subband at *K* valley (dotted lines). The black, red and blue curves correspond to the results of the plasmon modes  $\omega_1(q)$ ,  $\omega_2(q)$  and  $\omega_3(q)$ , respectively.

curves in the same panel denote the ratio of the oscillation amplitude between the spin-down electron pocket and the hole pocket in the *K*-valley. For this, we find similar results as before, rendering the  $\omega_1(q)$  mode in-phase, while the  $\omega_2(q)$  and  $\omega_3(q)$  modes are in anti-phase. Notice, however, that since we are now considering oscillations in the density of oppositely charged particles, it is the in-phased plasmon that compensate each others charged oscillation. Finally, the dotted curves show the ratio between the hole pockets in both valleys. Notice that, peculiarly, the  $\omega_3(q)$  mode is completely in-phase and that the amplitude for both components is the same in this case. The  $\omega_1(q)$  is also in-phase, as before, and the  $\omega_2(q)$  mode is in anti-phase.

#### IV. CONCLUSIONS

In this study, we examined the plasmonic response of a multi-component system. We took as a platform a ML-MoS<sub>2</sub> system subjected to circularly polarized light. We have shown that this system is capable of supporting multiple plasmon modes and we have quantified the effect of

circular optical pumping within a Boltzmann framework.

We found that all platforms support a long-wavelength  $\sqrt{q}$  plasmon branch at zero Kelvin. As temperature increases, we have shown that for an electron-doped system, the plasmon dispersion is strongly affected, while for a hole-doped system this mode is much more stable.

The main influence of having multiple components in the system is the appearance of new plasmonic modes that are partly damped. We found that for an  $n$ -component system,  $n - 1$  new plasmon modes appear. These new modes manifest themselves in the long-wavelength limit as acoustic modes with a linear dispersion and are in a local minimum of the intra-band continuum. To evaluate their stability, we have calculated the decay rate for each of these modes and found that although they lie in the intra-band continuum, their lifetime is considerable. For larger wave vectors, we found that the multi-component system also supports new modes in regions where only some of the components are subject to Landau damping of the collective oscillation.

We evaluated the character of the new modes by investigating the ratios of the amplitudes of the collective density oscillations of the different components. We found that the oscillation for the regular  $\sqrt{q}$ -mode is in-phase, while for the new acoustic modes anti-phase oscillation is possible. Finally, we evaluated the spectral function, showing how the acoustic modes can be identified.

The characteristic energy scale for plasmon modes in ML-MoS<sub>2</sub> covers not only the infrared but also the THz bandwidth, especially for the low frequency weakly damped linear acoustic plasmon modes. These properties make ML-MoS<sub>2</sub> a promising platform for plasmonic applications in the infrared and THz frequency regime. The theoretical investigations in this paper will help to guide the experimental search for new plasmon modes in ML-MoS<sub>2</sub> systems.

#### ACKNOWLEDGMENTS

Y.M.X. acknowledges financial support from the China Scholarship Council (CSC). B.V.D. is supported by the Flemish Science Foundation (FWO-VI) by a postdoctoral fellowship. This work was also supported by the National Natural Science Foundation of China (Grant No. 11574319, 11304272), Ministry of Science and Technology of China (Grant No. 2011YQ130018), Department of Science and Technology of Yunnan Province, Applied Basic Research Foundation of Yunnan Province (2013FD003), and by the Chinese Academy of Sciences.

#### APPENDIX: ANALYTICAL EXPRESSION OF POLARIZATION FUNCTION

We use  $\omega$  and  $k$  as dimensionless variables to represent  $\hbar\omega$  and  $atk$  for notational simplification. For zero doping,

the polarization function for spin  $s$  band at  $\zeta$  valley is [28]

$$\begin{aligned} \Pi_{0,T=0}^{ss}(\mathbf{q}, \omega) = & -\frac{q^2}{4\pi a^2 t^2} \left\{ \frac{\Delta_{\zeta s}}{q^2 - \omega^2} + \frac{q^2 - \omega^2 - 4\Delta_{\zeta s}^2}{4|q^2 - \omega^2|^{3/2}} \right. \\ & \times \left[ \theta(q - \omega) \arccos \frac{\omega^2 - q^2 + 4\Delta_{\zeta s}^2}{q^2 - \omega^2 + 4\Delta_{\zeta s}^2} \right. \\ & \left. - \theta(\omega - q) \ln \frac{(\sqrt{\omega^2 - q^2} + 2\Delta_{\zeta s})^2}{|\omega^2 - q^2 - 4\Delta_{\zeta s}^2|} \right] \left. \right\} \\ & - i \frac{q^2 \tilde{x}_{\zeta s}^2 \theta(\omega^2 - q^2 - 4\Delta_{\zeta s}^2)}{16a^2 t^2 |\omega^2 - q^2|^{1/2}}, \end{aligned} \quad (44)$$

where  $\tilde{x}_{\zeta s}^2 = 2 - x_{\zeta s}^2$  and  $x_{\zeta s} = \sqrt{|1 + 4\Delta_{\zeta s}^2/(q^2 - \omega^2)|}$ .

For finite doping ( $\lambda = +$  for  $n$ -type doping and  $\lambda = -$  for  $p$ -type doping), the polarization function for the spin  $s$  band at  $\zeta$  valley is

$$\begin{aligned} \Pi_{1,T=0}^{ss\lambda}(\mathbf{q}, \omega) = & -\frac{u_{\zeta s}^\lambda}{2\pi a^2 t^2} + \frac{q^2}{16\pi a^2 t^2 |q^2 - \omega^2|^{1/2}} \\ & \times \begin{cases} iG_>(y_-) - iG_>(y_+), & 1A \\ G_<(y_-) - iG_>(y_+), & 2A \\ G_<(y_+) + G_<(y_-), & 3A \\ G_<(y_-) - G_<(y_+), & 4A \\ G_>(y_+) - G_>(y_-), & 1B \\ G_>(y_+) + iG_<(y_-), & 2B \\ G_>(y_+) - G_>(-y_-) - i\pi\tilde{x}_{\zeta s}^2, & 3B \\ G_>(y_+) + G_>(-y_-) - i\pi\tilde{x}_{\zeta s}^2, & 4B \\ G_0(y_+) - G_0(y_-). & 5B \end{cases} \end{aligned} \quad (45)$$

where  $y_\pm = (2u_{\zeta s}^\lambda \pm \omega)/q$ , and

$$\begin{aligned} G_<(x) &= x(x_{\zeta s}^2 - x^2)^{1/2} + (x_{\zeta s}^2 - 2) \arccos(x/x_{\zeta s}), \\ G_>(x) &= x(x^2 - x_{\zeta s}^2)^{1/2} + (x_{\zeta s}^2 - 2) \operatorname{arccosh}(x/x_{\zeta s}), \\ G_0(x) &= x(x^2 + x_{\zeta s}^2)^{1/2} + (-x_{\zeta s}^2 - 2) \operatorname{arcsinh}(x/x_{\zeta s}). \end{aligned}$$

The regions defining the polarization function in Eq.

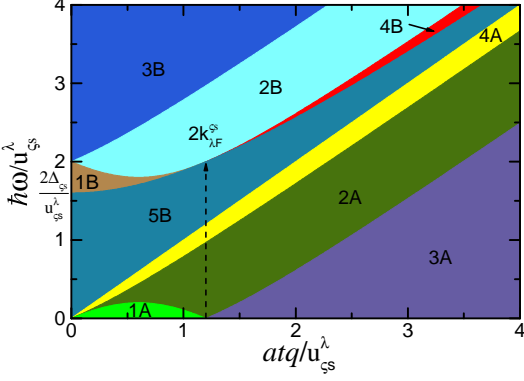


FIG. 12: (Color online) The different regions with different expressions for the polarization function in Eq. (45). Here we have set  $\Delta_{ss} = 0.8u_s^\lambda$ .

(45) are defined as

$$\begin{aligned} 1A : \omega &\leq u_s^\lambda - [(k_{\lambda F}^{ss} - q)^2 + \Delta_{ss}^2]^{1/2}, \\ 2A : \mp u_s^\lambda &\pm [(k_{\lambda F}^{ss} - q)^2 + \Delta_{ss}^2]^{1/2} < \omega \\ &\leq -u_s^\lambda + [(k_{\lambda F}^{ss} + q)^2 + \Delta_{ss}^2]^{1/2}, \\ 3A : \omega &\leq -u_s^\lambda + [(k_{\lambda F}^{ss} - q)^2 + \Delta_{ss}^2]^{1/2}, \\ 4A : -u_s^\lambda &+ [(k_{\lambda F}^{ss} + q)^2 + \Delta_{ss}^2]^{1/2} < \omega < q, \\ 1B : q &\leq 2k_{\lambda F}^{ss}, [q^2 + 4\Delta_{ss}^2]^{1/2} < \omega \\ &\leq u_s^\lambda + [(k_{\lambda F}^{ss} - q)^2 + \Delta_{ss}^2]^{1/2}, \\ 2B : u_s^\lambda &+ [(k_{\lambda F}^{ss} - q)^2 + \Delta_{ss}^2]^{1/2} < \omega \\ &\leq u_s^\lambda + [(k_{\lambda F}^{ss} + q)^2 + \Delta_{ss}^2]^{1/2}, \\ 3B : \omega &> u_s^\lambda + [(k_{\lambda F}^{ss} + q)^2 + \Delta_{ss}^2]^{1/2}, \\ 4B : q &> 2k_{\lambda F}^{ss}, [q^2 + 4\Delta_{ss}^2]^{1/2} < \omega \\ &\leq u_s^\lambda + [(k_{\lambda F}^{ss} - q)^2 + \Delta_{ss}^2]^{1/2}, \\ 5B : q &< \omega \leq [q^2 + 4\Delta_{ss}^2]^{1/2}. \end{aligned}$$

where the Fermi vector  $k_{\lambda F}^{ss} = \sqrt{|u_s^\lambda|^2 - \Delta_{ss}^2}$ .

The polarization function for ML-MoS<sub>2</sub> calculated using the 2DPB model, Eq. (12), can be written as

$$\tilde{\Pi}(\mathbf{q}, \omega) = \sum_{ss\lambda} \tilde{\Pi}_\lambda^{ss}(\mathbf{q}, \omega), \quad (46)$$

where

$$\tilde{\Pi}_\lambda^{ss}(\mathbf{q}, \omega) = \sum_{\mathbf{k}} \frac{f(\tilde{E}_{\lambda\mathbf{k}}^{ss}) - f(\tilde{E}_{\lambda\mathbf{k}+\mathbf{q}}^{ss})}{\omega + \tilde{E}_{\lambda\mathbf{k}}^{ss} - \tilde{E}_{\lambda\mathbf{k}+\mathbf{q}}^{ss} + i\delta}. \quad (47)$$

At zero temperature, the real and imaginary part of the polarization function  $\tilde{\Pi}_{\lambda, T=0}^{ss}(\mathbf{q}, \omega)$  can be written separately as [35, 39]

$$\begin{aligned} \text{Re}\tilde{\Pi}_{\lambda, T=0}^{ss}(\mathbf{q}, \omega) = -\frac{\Delta_{ss}}{2\pi a^2 t^2} \left[ 1 + \sum_{\alpha=\pm} \frac{\alpha \tilde{k}_{\lambda F}^{ss}}{q} \theta(|\nu_\alpha^{ss}|^2 - 1) \right. \\ \left. \times \text{sgn}[\nu_\alpha^{ss}] \sqrt{|\nu_\alpha^{ss}|^2 - 1} \right] \theta(\tilde{u}_s^\lambda - \Delta_{ss}), \end{aligned}$$

and

$$\begin{aligned} \text{Im}\tilde{\Pi}_{\lambda, T=0}^{ss}(\mathbf{q}, \omega) = -\frac{\Delta_{ss}}{2\pi a^2 t^2} \sum_{\alpha=\pm} \frac{\alpha \tilde{k}_{\lambda F}^{ss}}{q} \theta(1 - |\nu_\alpha^{ss}|^2) \\ \times \sqrt{1 - |\nu_\alpha^{ss}|^2} \theta(\tilde{u}_s^\lambda - \Delta_{ss}), \end{aligned} \quad (48)$$

where  $\tilde{u}_s^\lambda = |\tilde{E}_{\lambda F}^s| - \lambda s \gamma / 2$ , the Fermi vector  $\tilde{k}_{\lambda F}^{ss} = \sqrt{2\Delta_{ss}(\tilde{u}_s^\lambda - \Delta_{ss})}$ , and

$$\nu_\alpha^{ss} = \frac{\omega \Delta_{ss}}{q \tilde{k}_{\lambda F}^{ss}} - \alpha \frac{q}{2 \tilde{k}_{\lambda F}^{ss}}. \quad (49)$$

At zero temperature and in the low- $q$  approximation, the charge plasmon dispersion of ML-MoS<sub>2</sub> within the 2DPB model is

$$\tilde{\omega}_0(q) = \left[ e^2 q \sum_{ss\lambda} (\tilde{u}_s^\lambda - \Delta_{ss}) \theta(\tilde{u}_s^\lambda - \Delta_{ss}) / (4\pi\epsilon_r\epsilon_0) \right]^{1/2}. \quad (50)$$

At finite temperature, the full- $q$  polarization function is given by

$$\begin{aligned} \tilde{\Pi}_{\lambda, T}^{ss}(\mathbf{q}, \omega; \tilde{\mu}_\lambda^\lambda) = \int_{-\infty}^{\infty} \frac{d\mu' \tilde{\Pi}_{\lambda, T=0}^{ss}(\mathbf{q}, \omega)|_{\tilde{E}_{\lambda F}^s = \mu'}}{4k_B T \cosh^2[(\tilde{\mu}_\lambda^\lambda - \mu')/2k_B T]} \\ \times \theta(|u'| - \lambda s \gamma / 2 - \Delta_{ss}), \end{aligned} \quad (51)$$

where  $\tilde{\mu}_\lambda^\lambda$  is the chemical potential for conduction or valence subband which can be obtained through Eq. (4).

- [1] K. F. Mak, C. Lee, J. Hone, J. Shan, and T. F. Heinz, *Phys. Rev. Lett.* **105**, 136805 (2010).
- [2] A. Splendiani, L. Sun, Y. Zhang, T. Li, J. Kim, C.-Y. Chim, G. Galli, and F. Wang, *Nano Lett.* **10**, 1271 (2010).
- [3] Q. H. Wang, K. Kalantar-Zadeh, A. Kis, J. N. Coleman, and M. S. Strano, *Nat. Nanotechnol.* **7**, 699 (2012).
- [4] B. Radisavljevic, M. B. Whitwick, and A. Kis, *ACS Nano* **5**, 9934 (2011).
- [5] B. Radisavljevic, A. Radenovic, J. Brivio, V. Giacometti, and A. Kis, *Nat. Nanotechnol.* **6**, 147 (2011).
- [6] S. B. Desai, S. R. Madhvapathy, A. B. Sachid, J. P. Llinas, Q. Wang, G. H. Ahn, G. Pitner, M. J. Kim, J. Bokor, C. Hu, H.-S. P. Wong, and A. Javey, *Science* **354**, 99 (2016).
- [7] O. Lopez-Sanchez, D. Lemke, M. Kayci, A. Radenovic, and A. Kis, *Nat. Nanotechnol.* **8**, 497 (2013).
- [8] H. S. Lee, S.-W. Min, Y.-G. Chang, M. K. Park, T. Nam,

- H. Kim, J. H. Kim, S. Ryu, and S. Im, *Nano Lett.* **12**, 3695 (2012).
- [9] R. Ganatra and Q. Zhang, *ACS Nano* **8** (5), 4074 (2014).
- [10] H. Zeng, J. Dai, W. Yao, D. Xiao, and X. Cui, *Nat. Nanotechnol.* **7**, 490 (2012).
- [11] K. F. Mak, K. He, J. Shan, and T. F. Heinz, *Nat. Nanotechnol.* **7**, 494 (2012).
- [12] T. Cao, G. Wang, W. Han, H. Ye, C. Zhu, J. Shi, Q. Niu, P. Tan, E. Wang, B. Liu, and J. Feng, *Nat. Commun.* **3**, 887 (2012).
- [13] K. F. Mak, K. L. McGill, J. Park, and P. L. McEuen, *Science* **344**, 1489 (2014).
- [14] Z. Li and J. P. Carbotte, *Phys. Rev. B* **86**, 205425 (2012).
- [15] P. M. Krstajić, P. Vasilopoulos, and M. Tahir, *Phys. Rev. B* **94**, 085413 (2016).
- [16] Y. M. Xiao, W. Xu, B. Van Duppen, and F. M. Peeters, *Phys. Rev. B* **94**, 155432 (2016).
- [17] K. He, N. Kumar, L. Zhao, Z. Wang, K. F. Mak, H. Zhao, and J. Shan, *Phys. Rev. Lett.* **113**, 026803 (2014).
- [18] K. F. Mak, K. He, C. Lee, G. H. Lee, J. Hone, T. F. Heinz, and J. Shan, *Nat. Mater.* **12**, 207 (2013).
- [19] H.-T. Chen, W. J. Padilla, J. M. O. Zide, A. C. Gossard, A. J. Taylor, and R. D. Averitt, *Nature (London)* **444**, 597 (2006).
- [20] L. Ju, B. Geng, J. Horng, C. Girit, M. Martin, Z. Hao, H. A. Bechtel, X. Liang, A. Zettl, Y. R. Shen, and F. Wang, *Nat. Nanotechnol.* **6**, 630 (2011).
- [21] K. S. Novoselov, A. K. Geim, S. V. Morozov, D. Jiang, Y. Zhang, S. V. Dubonos, I. V. Grigorieva, A. A. Firsov, *Science* **306**, 666 (2004).
- [22] A. N. Grigorenko, M. Polini, and K. S. Novoselov, *Nat. Photon.* **6**, 749 (2012).
- [23] F. H. L. Koppens, D. E. Chang, and F. J. Garcia de Abajo, *Nano Lett.* **11**, 3370 (2011).
- [24] Z. Fei, A. S. Rodin, G. O. Andreev, W. Bao, A. S. McLeod, M. Wagner, L. M. Zhang, Z. Zhao, M. Thiemens, G. Dominguez, M. M. Fogler, A. H. Castro Neto, C. N. Lau, F. Keilmann, and D. N. Basov, *Nature (London)* **487**, 82 (2012).
- [25] T. Low and P. Avouris, *ACS Nano* **8** (2), 1086 (2014).
- [26] B. Wunsch, T. Stauber, F. Sols, and F. Guinea, *New J. Phys.* **8**, 318 (2006).
- [27] E. H. Hwang and S. Das Sarma, *Phys. Rev. B* **75**, 205418 (2007).
- [28] P. K. Pyatkovskiy, *J. Phys.: Condens. Matter* **21**, 025506 (2009).
- [29] A. Iurov, G. Gumbs, D. Huang, and V. M. Silkin, *Phys. Rev. B* **93**, 035404 (2016).
- [30] B. Van Duppen, P. Vasilopoulos, and F. M. Peeters, *Phys. Rev. B* **90**, 035142 (2014).
- [31] C. J. Tabert and E. J. Nicol, *Phys. Rev. B* **89**, 195410 (2014).
- [32] A. Scholz, T. Stauber, and J. Schliemann, *Phys. Rev. B* **88**, 035135 (2013).
- [33] K. Kechedzhi and D. S. L. Abergel, *Phys. Rev. B* **89**, 235420 (2014).
- [34] H. Hatami, T. Kernreiter, and U. Zülicke, *Phys. Rev. B* **90**, 045412 (2014).
- [35] F. Stern, *Phys. Rev. Lett.* **18**, 546 (1967).
- [36] D. Xiao, G.-B. Liu, W. Feng, X. Xu, and W. Yao, *Phys. Rev. Lett.* **108**, 196802 (2012).
- [37] H.-Z. Lu, W. Yao, D. Xiao, and S.-Q. Shen, *Phys. Rev. Lett.* **110**, 016806 (2013).
- [38] A. Kormányos, V. Zólyomi, N. D. Drummond, and G. Burkard, *Phys. Rev. X* **4**, 011034 (2014).
- [39] G. F. Giuliani and G. Vignale, *Quantum Theory of the Electron Liquid* (Cambridge University Press, Cambridge, UK, 2005).
- [40] Z. Y. Zhu, Y. C. Cheng, and U. Schwingenschlögl, *Phys. Rev. B* **84**, 153402 (2011).
- [41] J. Ibañez-Azpiroz, A. Eiguren, E. Ya. Sherman, and A. Bergara, *Phys. Rev. Lett.* **109**, 156401 (2012).
- [42] Y. Song and H. Dery, *Phys. Rev. Lett.* **111**, 026601 (2013).
- [43] T. Korn, S. Heydrich, M. Hirmer, J. Schmutzler, and C. Schüller, *Appl. Phys. Lett.* **99**, 102109 (2011).
- [44] A. Agarwal, M. Polini, G. Vignale, and M. E. Flatté, *Phys. Rev. B* **90**, 155409 (2014).
- [45] A. Politano and G. Chiarello, *Nanoscale* **6**, 10927 (2014).
- [46] P. F. Maldaque, *Surface Science* **73**, 296 (1978).
- [47] A. Tomadin, D. Brida, G. Cerullo, A. C. Ferrari, and M. Polini, *Phys. Rev. B* **88**, 035430 (2013).
- [48] G. Kioseoglou, A. T. Hanbicki, M. Currie, A. L. Friedman, D. Gunlycke, and B. T. Jonker, *Appl. Phys. Lett.* **101**, 221907 (2012).
- [49] D. Kreil, R. Hobbiger, J. T. Drachta, and H. M. Böhm, *Phys. Rev. B* **92**, 205426 (2015).

## 参 考 文 献

- [1] 冯端, 金国钧, 凝聚态物理学 [M]. 北京: 高等教育出版社, 2003.
- [2] N. W. Ashcroft and N. D. Mermin, Solid state physics [M]. Orlando: Harcourt College publishers, 1976.
- [3] G. E. Moore, Cramming more components onto integrated circuits [J]. Electronics, 1965, 38: 114-116.
- [4] A. B. Fowler, F. F. Fang, W. E. Howard, and P. J. Stiles, Magneto-oscillatory conductance in silicon surfaces [J]. Phys. Rev. Lett., 1966, 16: 901-903.
- [5] T. Ando, A. B. Fowler, and F. Stern, Electronic properties of two-dimensional systems [J]. Rev. Mod. Phys., 1982, 54: 437.
- [6] G. F. Giuliani and G. Vignale. Quantum theory of the electron liquid [M]. Cambridge: Cambridge University Press, 2005.
- [7] K. S. Novoselov, A. K. Geim, S. V. Morozov, D. Jiang, Y. Zhang, S. V. Dubonos, I. V. Grigorieva, A. A. Firsov, Electric field effect in atomically thin carbon films [J]. Science, 2004, 306: 666.
- [8] J. Zhao, H. Liu, Z. Yu, R. Quhe, S. Zhou, Y. Wang, C. C. Liu, H. Zhong, N. Han, Jing Lu, Y. Yao, and K. Wu, Rise of silicene: A competitive 2D material [J]. Prog. Mater. Sci., 2016, 83: 24-151.
- [9] M. E. Dávila, L. Xian, S. Cahangirov, A. Rubio, and G. L. Lay, Germanene: a novel two-dimensional germanium allotrope akin to graphene and silicene [J]. New J. Phys., 2014, 16: 095002.
- [10] F.-F. Zhu, W.-J. Chen, Y. Xu, C.-L. Gao, D.-D. Guan, C.-H. Liu, D. Qian, S.-C. Zhang, and J.-F. Jia, Epitaxial growth of two-dimensional stanene [J]. Nat. Mater., 2015, 14: 1020 - 1025.
- [11] Q. H. Wang, K. K.-Zadeh, A. Kis, J. N. Coleman, and M. S. Strano, Electronics and optoelectronics of two-dimensional transition metal dichalcogenides [J]. Nat. Nanotechnol., 2012, 7: 699-712.
- [12] M. Gmitra, D. Kochan, P. Högl, and J. Fabian, Trivial and inverted Dirac bands and the emergence of quantum spin Hall states in graphene on transition-metal dichalcogenides [J]. Phys. Rev. B, 2016, 93: 155104.
- [13] P. R. Wallace, The band theory of graphite [J]. Phys. Rev., 1947, 71: 622-634.
- [14] J. W. McClure, Diamagnetism of graphite [J]. Phys. Rev., 1956, 104: 666-671.
- [15] J. C. Slonczewski and P. R. Weiss, Band structure of graphite [J]. Phys. Rev., 1958, 109: 272-279.

- [16] R. E. Peierls, Quelques proprietes typiques des corps solides [J]. Ann. I. H. Poincaré, 1935, 59: 177-222.
- [17] L. D. Landau, Zur Theorie der phasenumwandlungen II [J]. Phys. Z. Sowjetunion, 1937, 11: 26-35.
- [18] N. D. Mermin, Crystalline order in two dimensions [J]. Phys. Rev., 1968, 176: 250-254.
- [19] A. H. Castro Neto, F. Guinea, N. M. R. Peres, K. S. Novoselov, and A. K. Geim. The electronic properties of graphene [J]. Rev. Mod. Phys., 2009, 81(1): 109.
- [20] T. Ando, The electronic properties of graphene and carbon nanotubes [J]. NPG Asia Mater., 2009, 1(1): 17-21.
- [21] R. R. Nair, P. Blake, A. N. Grigorenko, K. S. Novoselov, T. J. Booth, T. Stauber, N. M. R. Peres, and A. K. Geim. Fine structure constant defines visual transparency of graphene [J]. Science, 2008, 320(5881): 1308.
- [22] H. K. Min and A. H. MacDonald. Electronic structure of multilayer graphene [J]. Prog. Theor. Phys. Supplement, 2008, 176: 227.
- [23] W. Ren and H.-M. Cheng, The global growth of graphene [J]. Nat. Nanotechnol., 2014, 9: 726-730.
- [24] G. Eda, G. Fanchini, and M. Chhowalla, Large-area ultrathin films of reduced graphene oxide as a transparent and flexible electronic material [J]. Nat. Nanotechnol., 2008, 3: 270-274.
- [25] F. Schwierz, Graphene transistors [J]. Nat. Nanotechnol., 2010, 5: 487-496.
- [26] F. Xia, T. Mueller, R. Golizadeh-Mojarad, M. Freitag, Y. Lin, J. Tsang, V. Perebeinos, and P. Avouris, Photocurrent imaging and efficient photon detection in a graphene transistor [J]. Nano Lett., 2009, 9(3): 1039-1044.
- [27] M. Liu, X. Yin, E. Ulin-Avila, B. Geng, T. Zentgraf, L. Ju, F. Wang, and X. Zhang, A graphene-based broadband optical modulator [J]. Nature, 2011, 474: 64-67.
- [28] G. Ramakrishnan, R. Chakkittakandy, and P. C. M. Planken, Terahertz generation from graphite [J]. Opt. Express, 2009, 17: 16092-16099.
- [29] X. Huang, T. Leng, M. Zhu, X. Zhang, J. Chen, K. Chang, M. Aqeeli, A. K. Geim, K. S. Novoselov, and Z. Hu, Highly flexible and conductive printed graphene for wireless wearable communications applications [J]. Sci. Rep., 2015, 5: 18298.
- [30] K. Sink, B. Wang, and P. Král, Selective ion passage through functionalized graphene nanopores [J]. J. Am. Chem. Soc., 2008, 130: 16448.
- [31] H. Liu, S. Dai and D. Jiang, Insights into CO<sub>2</sub>/N<sub>2</sub> separation through nanoporous graphene from molecular dynamics [J]. Nanoscale, 2013, 5: 9984.
- [32] S. P. Koenig, L. Wang, J. Pellegrino, and J. S. Bunch, Selective molecular sieving through porous graphene [J]. Nat. Nanotechnol., 2012, 7: 728.

- [33] R. R. Nair, P. Blake, J. R. Blake, R. Zan, S. Anissimova, U. Bangert, A. P. Golovanov, S. V. Morozov, A. K. Geim, K. S. Novoselov, and T. Latychevskaia, Graphene as a transparent conductive support for studying biological molecules by transmission electron microscopy [J]. *Appl. Phys. Lett.*, 2010, 97: 153102.
- [34] T. Kuilaa, S. Bosea, P. Khanraa, A. K. Mishrab, N. H. Kimc, and J. H. Leea, Recentadvances in graphene-based biosensors [J]. *Biosens. Bioelectron.*, 2011, 26: 4637-4648.
- [35] S. B. Yang, X. L. Feng, S. Ivanovici, and K. Mullen, Fabrication of grapheneencapsulated oxide nanoparticles: towards high-performance anodematerials for lithium storage [J]. *Angew. Chem. Int. Edn*, 2010, 49: 8408-8411.
- [36] M. D. Stoller, S. J. Park, Y. W. Zhu, J. H. An, and R. S. Ruoff, Graphene-based ultracapacitors [J]. *Nano Lett.*, 2008, 8: 3498 – 3502.
- [37] S. S. Varghesea, B, S. Lonkara, K. K. Singhc, S. Swaminathanb, and A. Abdala, Recent advances in graphene based gas sensors [J]. *Sens. Actuators, B*, 2015, 218: 160-183.
- [38] H. Zeng, J. Dai, W. Yao, D. Xiao, and X. Cui, Valley polarization in MoS<sub>2</sub> monolayers by optical pumping [J]. *Nat. Nanotechnol.*, 2012, 7: 490-493.
- [39] K. F. Mak, K. He, J. Shan, and T. F. Heinz, Control of valley polarization in monolayer MoS<sub>2</sub> by optical helicity [J]. *Nat. Nanotechnol.*, 2012, 7: 494-498.
- [40] T. Cheiwchanchamnangij and W. R. L. Lambrecht, Quasiparticle band structure calculation of monolayer, bilayer, and bulk MoS<sub>2</sub> [J]. *Phys. Rev. B*, 2012, 85: 205302.
- [41] S. B. Desai, S. R. Madhvapathy, A. B. Sachid, J. P. Llinas, Q. Wang, G. H. Ahn, G. Pitner, M. J. Kim, J. Bokor, C. Hu, H.-S. P. Wong, and A. Javey, MoS<sub>2</sub> transistors with 1-nanometer gate lengths [J]. *Science*, 2016, 354: 99.
- [42] B. Radisavljevic, A. Radenovic, J. Brivio, V. Giacometti, and A. Kis, Single-layer MoS<sub>2</sub> transistors [J]. *Nat. Nanotechnol.*, 2011, 6: 147.
- [43] H. Fang, S. Chuang, T. C. Chang, K. Takei, T. Takahashi, and A. Javey, High-performance single layered WSe<sub>2</sub> p-FETs with chemically doped contacts [J]. *Nano Lett.*, 2012, 12(7): 3788-3792.
- [44] 汤鹏, 肖坚, 郑超, 王石, 陈润锋, 类石墨烯二硫化钼及其在光电子器件上的应用[J]. *Acta Phys. -Chim. Sin. (物理化学学报)*, 2013, 29(4): 667-677.
- [45] P. H. Siegel, Terahertz technology [J]. *IEEE T. Microwave Theroy Tech.*, 2002, 50: 910.
- [46] Y.-S. Lee, Principles of Terahertz Science and Technology [M]. New York: Springer, 2009.
- [47] 曹俊诚, 半导体太赫兹源、探测器与应用 [M]. 北京: 科学出版社, 2012.

- [48] M. N. Baibich, J. M. Broto, A. Fert, F. Nguyen Van Dau, F. Petroff, P. Etienne, G. Creuzet, A. Friederich, and J. Chazelas, Giant Magnetoresistance of (001)Fe/(001)Cr Magnetic Superlattices [J]. Phys. Rev. Lett., 1988, 61: 2472.
- [49] G. Binasch, P. Grünberg, F. Saurenbach, and W. Zinn, Enhanced magnetoresistance in layered magnetic structures with antiferromagnetic interlayer exchange [J]. Phys. Rev. B, 1989, 39: 4828(R).
- [50] S. Datta and B. Das, Electronic analog of the electro-optic modulator [J]. Appl. Phys. Lett., 1990, 56: 665.
- [51] 叶良修, 半导体物理学 [M]. 北京: 高等教育出版社, 2009.
- [52] R. Winkler, Spin-orbit coupling effects in two-dimensional electron and hole systems [M]. Berlin: Springer-Verlag, 2003.
- [53] G. Bihlmayer, O. Rader, and R. Winkler, Focus on the Rashba effect [J]. New J. Phys., 2015, 17: 050202.
- [54] G. Dresselhaus, Spin-orbit coupling effects in zinc blende structures [J]. Phys. Rev., 1955, 100: 580.
- [55] R. W. Wood, On a remarkable case of uneven distribution of light in a diffraction grating spectrum [J]. Philos. Mag., 1902, 4: 396-402.
- [56] U. Fano, The theory of anomalous diffraction gratings and of quasi-stationary waves on metallic surfaces (Sommerfeld's waves) [J]. J. Opt. Soc. Am., 1941, 31: 213-222.
- [57] R. H. Ritchie, Plasma losses by fast electrons in thin films [J]. Phys. Rev., 1957, 106: 874-881.
- [58] C. J. Powell and J. B. Swan, Origin of the characteristic electron energy losses in aluminum [J]. Phys. Rev., 1959, 115: 869-875.
- [59] E. A. Stern and R. A. Ferrell, Surface plasma oscillations of a degenerate electron gas [J]. Phys. Rev., 1960, 120: 130-136.
- [60] A. Otto, Excitation of nonradiative surface plasma waves in silver by the method of frustrated total reflection [J]. Z. Physik, 1968, 216: 398.
- [61] E. Kretschmann, Die Bestimmung optischer Konstanten von Metallen durch Anregung von Oberflächenplasmaschwingungen [J]. Z. Physik, 1971, 241: 313.
- [62] S. A. Maier, Plasmonics: Fundamentals and Applications [M]. New York: Springer, 2007.
- [63] 王振林, 表面等离激元研究新进展[J]. 物理学进展, 2009, 29(3): 287-324.
- [64] A. N. Grigorenko, M. Polini, and K. S. Novoselov, Graphene plasmonics [J]. Nature Photon., 2012, 6(11): 749-758.
- [65] X. Luo, T. Qiu, W. Lu b, and Z. Ni, Plasmons in graphene: Recent progress and applications [J]. Mater. Sci. Eng. R, 2013, 74: 351-376.
- [66] G. Gross, G. P. Parravicini, Solid state physics [M]. London: Academic Press, 2003.

- [67] R. Shankar, Principles of quantum mechanics [M]. New York: Plenum, 1994.
- [68] 曾谨言, 量子力学卷 I [M]. 北京: 科学出版社, 2007.
- [69] 黄昆著, 韩汝琦改变, 固体物理学 [M]. 北京: 高等教育出版社, 1988.
- [70] E. N. Economou. Green's functions in quantum physics(Third editon) [M]. Berlin: Springer-Verlag, 2006.
- [71] R. Kubo, Statistical-mechanical theory of irreversible processes. I. general theory and simple applications to magnetic and conduction problems [J]. J. Phys. Soc. Jpn., 1957, 12: 570-586.
- [72] 李正中, 固体理论 [M]. 北京: 高等教育出版社, 2002.
- [73] 丁大同, 固体理论讲义 [M]. 天津: 南开大学出版社, 2001.
- [74] G. D. Mahan, Many-Particle Physics [M]. New York: Kluwer Academic, 2000.
- [75] S. G. Louie and M. L. Cohen, Conceptual foundations of materials: A standard model for ground- and excited-state properties [M]. Amsterdam: Elsevier, 2006.
- [76] M. P. Marder, Condensed Matter Physics [M]. New York: Wiley, 2000.
- [77] P. Nozières and D. Pines, Theory of quantum liquids [M]. New York: Addison-Wesley, 1989.
- [78] H. Ehrenreich and M. H. Cohen, Self-consistent field approach to the many-electron problem [J]. Phys. Rev., 1959, 115: 786.
- [79] J. Hubbard, The description of collective motions in terms of many-body perturbation theory. II. the correlation energy of a free-electron gas [J]. Proc. R. Soc. Lond. A, 1958, 243: 336-352.
- [80] H. Hogan, For a cheaper camera, use curved silicon [J]. Photon. Spectra, 2008, 42: 19.
- [81] W. Cai, Y. Zhu, X. Li, R. D. Piner, and R. S. Ruoff, Large area few-layer graphene/graphite films as transparent thin conducting electrodes [J]. Appl. Phys. Lett., 2009, 95: 123115.
- [82] B. Sensale-Rodriguez, T. Fang, R. Yan, M. M. Kelly, D. Jena, L. Liu, and H. Xing, Unique prospects for graphene-based terahertz modulators [J]. Appl. Phys. Lett., 2011, 99: 113104.
- [83] B. Sensale-Rodriguez, R. Yan, M. Zhu, D. Jena, L. Liu, and H. G. Xing, Efficient terahertz electro-absorption modulation employing graphene plasmonic structures [J]. Appl. Phys. Lett., 2012, 101: 261115.
- [84] C.-C. Lee, S. Suzuki, W. Xie, and T. R. Schibli, Broadband graphene electro-optic modulators with sub-wavelength thickness [J]. Opt. Express, 2012, 20: 5264.
- [85] J. Park, Y. H. Ahn, C. Ruiz-Vargas, Imaging of photocurrent generation and collection in single-layer graphene [J]. Nano Lett., 2009, 9: 1742.

- [86] E. J. H. Lee, K. Balasubramanian, R. T. Weitz, M. Burghard, and K. Kern, Contact and edge effects in graphene devices [J]. *Nat. Nanotechnol.*, 2008, 3: 486.
- [87] T. Mueller, F. Xia, P. Avouris, Graphene photodetectors for high-speed optical communications [J]. *Nature Photon.*, 2010, 4: 297.
- [88] G. Konstantatos, M. Badioli, L. Gaudreau, J. Osmond, M. Bernechea, F. P. G. de Arquer, F. Gatti, and F. H. L. Koppens, Hybrid graphene-quantum dot phototransistors with ultrahigh gain [J]. *Nat. Nanotechnol.*, 2012, 7: 363.
- [89] J. Horng, C.-F. Chen, B. Geng, C. Girit, Y. Zhang, Z. Hao, H. A. Bechtel, M. Martin, A. Zettl, M. F. Crommie, Y. Ron Shen, and F. Wang, Drude conductivity of Dirac fermions in graphene [J]. *Phys. Rev. B*, 2011, 83: 165113.
- [90] A. R. Wright, X. G. Xu, J. C. Cao, and C. Zhang, Strong nonlinear optical response of graphene in the terahertz regime [J]. *Appl. Phys. Lett.*, 2009, 95: 072101.
- [91] Y. S. Ang, S. Sultan, and C. Zhang, Nonlinear optical spectrum of bilayer graphene in the terahertz regime [J]. *Appl. Phys. Lett.*, 2010, 97: 243110.
- [92] W. Xu, Y. P. Gong, L. W. Liu, H. Qin, and Y. L. Shi, Can graphene make better HgCdTe infrared detectors? [J]. *Nanoscale Res. Lett.*, 2011, 6: 250.
- [93] E. McCann and V. I. Fal'ko, Landau-level degeneracy and quantum hall effect in a graphite bilayer [J]. *Phys. Rev. Lett.*, 2006, 96: 086805.
- [94] F. Guinea, A. H. Castro Neto, and N. M .R. Peres, Electronic states and landau levels in graphene stacks [J]. *Phys. Rev. B*, 2006, 73: 245426.
- [95] F. Zhang, B. Sahu, H. Min, and A. H. MacDonald, Band structure of ABC-stacked graphene trilayers [J]. *Phys. Rev. B*, 2010, 82: 035409.
- [96] M. Koshino, T. Ando, Electronic structures and optical absorption of multilayer graphenes [J]. *Solid State Commun.*, 2009, 149: 1123-1127.
- [97] M. Koshino and E. McCann, Landau level spectra and the quantum Hall effect of multilayer graphene [J]. *Phys. Rev. B*, 2011, 83: 165443.
- [98] L. Hao, L. Sheng, Optical conductivity of multilayer graphene [J]. *Solid State Commun.*, 2009, 149: 1962-1966.
- [99] Y. M. Xiao, W. Xu, and F. M. Peeters, Infrared to terahertz absorption window in mono- and multi-layer graphene systems [J]. *Opt. Commun.*, 2014, 328: 135-142.
- [100] J. M. Dawlaty, S. Shivaraman, J. Strait, P. George, M. Chandrashekhar, F. Rara, M. G. Spencer, D. Veksler, and Y. Chen, Measurement of the optical absorption spectra of epitaxial graphene from terahertz to visible [J]. *Appl. Phys. Lett.*, 2008, 93: 131905.
- [101] A. B. Kuzmenko, E. van Heumen, F. Carbone, and D. van der Marel, Universal optical conductance of graphite [J]. *Phys. Rev. Lett.*, 2008, 100: 117401.

- [102] Z. Q. Li, E. A. Henriksen, Z. Jiang, Z. Hao, M. C. Martin, P. Kim, H. L. Stormer, and D. N. Basov, Dirac charge dynamics in graphene by infrared spectroscopy [J]. *Nature Phys.*, 2008, 4: 532.
- [103] H. M. Dong, W. Xu, J. Zhang, Y. Z. Yuan, Terahertz absorption window and high transmission in graphene bilayer [J]. *Opt. Commun.*, 2010, 283: 3695.
- [104] W. Xu, H. M. Dong, L. L. Li, J. Q. Yao, P. Vasilopoulos, and F. M. Peeters, Optoelectronic properties of graphene in the presence of optical phonon scattering [J]. *Phys. Rev. B*, 2010, 82: 125304.
- [105] T. Stauber, N. M. R. Peres, and A. K. Geim, Optical conductivity of graphene in the visible region of the spectrum [J]. *Phys. Rev. B*, 2008, 78: 085432.
- [106] M. Koshino and T. Ando, Magneto-optical properties of multilayer graphene [J]. *Phys. Rev. B*, 2008, 77: 115313.
- [107] H. M. Dong, W. Xu, Z. Zeng, T. C. Lu, and F. M. Peeters, Quantum and transport conductivities in monolayer graphene [J]. *Phys. Rev. B*, 2008, 77: 235402.
- [108] D. Sun, Z.-K. Wu, C. Divin, X. Li, C. Berger, W. A. de Heer, P. N. First, and T. B. Norris, Ultrafast relaxation of excited dirac fermions in epitaxial graphene using optical differential transmission spectroscopy [J]. *Phys. Rev. Lett.*, 2008, 101: 157402.
- [109] J.-H. Chen, C. Jang, S. Xiao, M. Ishigami, and M. S. Fuher, Intrinsic and extrinsic performance limits of graphene devices on SiO<sub>2</sub> [J]. *Nature Nanotechnol.*, 2008, 3: 206-209.
- [110] X. Zou, J. Shang, J. Leaw, Z. Luo, Liyan Luo, C. La-o-vorakiat, L. Cheng, S. A. Cheong, H. Su, J.-X. Zhu, Y. Liu, K. P. Loh, A. H. Castro Neto, Ting Yu, and E. E. M. Chia, Terahertz conductivity of twisted bilayer graphene [J]. *Phys. Rev. Lett.*, 2013, 110: 067401.
- [111] E. Burstein, Anomalous optical absorption limit in InSb [J]. *Phys. Rev.*, 1954, 93: 632.
- [112] F. Wang, Y. Zhang, C. Tian, C. Giri, A. Zettl, M. Crommie, and Y. Ron Shen, Gate-variable optical transitions in graphene [J]. *Science*, 2008, 320: 206.
- [113] E. McCann, Asymmetry gap in the electronic band structure of bilayer graphene [J]. *Phys. Rev. B*, 2006, 74: 161403.
- [114] A. A. Avetisyan, B. Partoens, and F. M. Peeters, Electric-field control of the band gap and Fermi energy in graphene multilayers by top and back gates [J]. *Phys. Rev. B*, 2009, 80: 195401.
- [115] Q. H. Wang, K. Kalantar-Zadeh, A. Kis, J. N. Coleman, and M. S. Strano, Electronics and optoelectronics of two-dimensional transition metal dichalcogenides [J]. *Nat. Nanotechnol.*, 2012, 7: 699.

- [116] K. F. Mak, C. Lee, J. Hone, J. Shan, and T. F. Heinz, Atomically thin MoS<sub>2</sub>: A new direct-gap semiconductor [J]. Phys. Rev. Lett., 2010, 105: 136805 (2010).
- [117] Zhiming M. Wang, MoS<sub>2</sub>: Materials, Physics, and Devices [M]. Switzerland: Springer, 2014.
- [118] A. Splendiani, L. Sun, Y. Zhang, T. Li, J. Kim, C.-Y. Chim, G. Galli, and F. Wang, Emerging photoluminescence in monolayer MoS<sub>2</sub> [J]. Nano Lett., 2010, 10: 1271.
- [119] C. Lee, H. Yan, L. E. Brus, T. F. Heinz, J. Hone, and S. Ryu, Anomalous lattice vibrations of single- and few-layer MoS<sub>2</sub> [J]. ACS Nano, 2010, 4: 2695.
- [120] B. Radisavljevic, M. B. Whitwick, and A. Kis, Integrated circuits and logic operations based on single-layer MoS<sub>2</sub> [J]. ACS Nano, 2011, 5: 9934.
- [121] B. Radisavljevic and A. Kis, Mobility engineering and a metal-insulator transition in monolayer MoS<sub>2</sub> [J]. Nat. Mater., 2013, 12: 815.
- [122] H. Li, Z. Yin, Q. He, H. Li, X. Huang, G. Lu, D. W. H. Fam, A. I. Y. Tok, Q. Zhang, and H. Zhang, Fabrication of single- and multilayer MoS<sub>2</sub> film-based field-effect transistors for sensing NO at room temperature [J]. Small, 2012, 8: 63.
- [123] Z. Yin, H. Li, H. Li, L. Jiang, Y. Shi, Y. Sun, G. Lu, Q. Zhang, X. Chen, and H. Zhang, Single-layer MoS<sub>2</sub> phototransistors [J]. ACS Nano, 2012, 6: 74.
- [124] R. S. Sundaram, M. Engel, A. Lombardo, R. Krupke, A. C. Ferrari, Ph. Avouris, and M. Steiner, Electroluminescence in single layer MoS<sub>2</sub> [J]. Nano Lett., 2013, 13: 1416.
- [125] D. Xiao, G.-B. Liu, W. Feng, X. Xu, and W. Yao, Coupled spin and valley physics in monolayers of MoS<sub>2</sub> and other group-VI dichalcogenides [J]. Phys. Rev. Lett., 2012, 108: 196802.
- [126] A. Kormányos, V. Zólyomi, N. D. Drummond, P. Rakyta, G. Burkard, and V. I. Fal'ko, Monolayer MoS<sub>2</sub>: Trigonal warping, the  $\Gamma$  valley, and spin-orbit coupling effects [J]. Phys. Rev. B, 2013, 88: 045416.
- [127] H.-Z. Lu, W. Yao, D. Xiao, and S.-Q. Shen, Intervalley scattering and localization behaviors of spin-valley coupled dirac fermions [J]. Phys. Rev. Lett., 2013, 110: 016806.
- [128] Z. Li and J. P. Carbotte, Longitudinal and spin-valley Hall optical conductivity in single layer MoS<sub>2</sub> [J]. Phys. Rev. B, 2012, 86: 205425.
- [129] A. Scholz, T. Stauber, and J. Schliemann, Plasmons and screening in a monolayer of MoS<sub>2</sub> [J]. Phys. Rev. B, 2013, 88: 035135.
- [130] R. Ganatra and Q. Zhang, Few-layer MoS<sub>2</sub>: A promising layered semiconductor [J]. ACS Nano, 2014, 8: 4074-4099.
- [131] T. Cao, G. Wang, W. Han, H. Ye, C. Zhu, J. Shi, Q. Niu, P. Tan, E. Wang, B. Liu, and J. Feng, Valley-selective circular dichroism of monolayer molybdenum disulphide [J]. Nat. Commun., 2012, 3: 887.

- [132] M. M. Glazov, E. Ya. Sherman, and V. K. Dugaev, Two-dimensional electron gas with spin-orbit coupling disorder [J]. Physica E, 2010, 42: 2157.
- [133] M. W. Wu, J. H. Jiang, and M. Q. Weng, Spin dynamics in semiconductors [J]. Phys. Rep., 2010, 493: 61.
- [134] W. Xu, Plasmons of a two-dimensional electron gas in the presence of spin orbit interaction [J]. Appl. Phys. Lett., 2003, 82: 724.
- [135] X. F. Wang, Plasmon spectrum of two-dimensional electron systems with Rashba spin-orbit interaction [J]. Phys. Rev. B, 2005, 72: 085317.
- [136] D. W. Yuan, W. Xu, Z. Zeng, and F. Lu, Optical spectrum of a spin-split two-dimensional electron gas [J]. Phys. Rev. B, 2005, 72: 033320.
- [137] C. H. Yang, W. Xu, Z. Zeng, F. Lu, and C. Zhang, Optical spectrum of a two-dimensional hole gas in the presence of spin-orbit interaction [J]. Phys. Rev. B, 2006, 74: 075321.
- [138] Y. S. Ang, J. C. Cao, and C. Zhang, Nonlinear optical conductivity of two-dimensional semiconductors with Rashba spin-orbit coupling in terahertz regime [J]. Eur. Phys. J. B, 2014, 87: 28.
- [139] J. Ibañez-Azpiroz, A. Eiguren, E. Ya. Sherman, and A. Bergara, Spin-flip transitions induced by time-dependent electric fields in surfaces with strong spin-orbit interaction [J]. Phys. Rev. Lett., 2012, 109: 156401.
- [140] J. Ibañez-Azpiroz, A. Bergara, E. Ya. Sherman, and A. Eiguren, Spin-flip transitions and departure from the Rashba model in the Au(111) surface [J]. Phys. Rev. B, 2013, 88: 125404.
- [141] C. L. Kane and E. J. Mele, Quantum spin hall effect in graphene [J]. Phys. Rev. Lett., 2005, 95: 226801.
- [142] H. Ochoa and R. Roldán, Spin-orbit-mediated spin relaxation in monolayer MoS<sub>2</sub> [J]. Phys. Rev. B, 2013, 87: 245421.
- [143] J. Klinovaja and D. Loss, Spintronics in MoS<sub>2</sub> monolayer quantum wires [J]. Phys. Rev. B, 2013, 88: 075404.
- [144] D. Marchenko, A. Varykhalov, M. R. Scholz, G. Bihlmayer, E. I. Rashba, A. Rybkin, A. M. Shikin, and O. Rader, Giant Rashba splitting in graphene due to hybridization with gold [J]. Nat. Commun., 2012, 3: 1232.
- [145] P. D. C. King, R. C. Hatch, M. Bianchi, R. Ovsyannikov, C. Lupulescu, G. Landolt, B. Slomski, J. H. Dil, D. Guan, J. L. Mi, E. D. L. Rienks, J. Fink, A. Lindblad, S. Svensson, S. Bao, G. Balakrishnan, B. B. Iversen, J. Osterwalder, W. Eberhardt, F. Baumberger, and Ph. Hofmann, Large tunable Rashba spin splitting of a two-Dimensional electron gas in Bi<sub>2</sub>Se<sub>3</sub> [J]. Phys. Rev. Lett., 2011, 107: 096802.

- [146] T. Stauber and J. Schliemann, Electronic properties of graphene and graphene nanoribbons with ‘pseudo-Rashba’ spin-orbit coupling [J]. *New J. Phys.*, 2009, 11: 115003.
- [147] A. Scholz, T. Stauber, and J. Schliemann, Dielectric function, screening, and plasmons of graphene in the presence of spin-orbit interactions [J]. *Phys. Rev. B*, 2012, 86: 195424.
- [148] W. Wang, C. Zhang, and Z. Ma, The effect of spin-orbit interaction on optical conductivity in graphene [J]. *J. Phys.: Condens. Matter*, 2012, 24: 035303.
- [149] P. Inganhoen, J. Z. Bernád, U. Zülicke, and R. Egger, Features due to spin-orbit coupling in the optical conductivity of single-layer graphene [J]. *Phys. Rev. B*, 2010, 81: 035421.
- [150] M. M. Perera, M.-W. Lin, H.-J. Chuang, B. P. Chamlagain, C. Wang, X. Tan, M. M.-C. Cheng, D. Tománek, and Z. Zhou, Improved carrier mobility in few-layer MoS<sub>2</sub> field-effect transistors with ionic-liquid gating [J]. *ACS Nano*, 2013, 7: 4449.
- [151] K. Dolui, I. Rungger, and S. Sanvito, Origin of the *n*-type and *p*-type conductivity of MoS<sub>2</sub> monolayers on a SiO<sub>2</sub> substrate [J]. *Phys. Rev. B*, 2013, 87: 165402.
- [152] Z. Y. Zhu, Y. C. Cheng, and U. Schwingenschlögl, Giant spin-orbit-induced spin splitting in two-dimensional transition-metal dichalcogenide semiconductors [J]. *Phys. Rev. B*, 2011, 84: 153402.
- [153] A. Kormányos, V. Zólyomi, N. D. Drummond, and G. Burkard, Spin-orbit coupling, quantum dots, and qubits in monolayer transition metal dichalcogenides [J]. *Phys. Rev. X*, 2014, 4: 011034.
- [154] A. O. Slobodeniuk and D. M. Basko, Spin-flip processes and radiative decay of dark intravalley excitons in transition metal dichalcogenide monolayers [J]. *2D Mater.*, 2016, 3: 035009.
- [155] J. Qi, X. Li, Q. Niu, and J. Feng, Giant and tunable valley degeneracy splitting in MoTe<sub>2</sub> [J]. *Phys. Rev. B*, 2015, 92: 121403(R).
- [156] I. N. Bronshtein, K. A. Semendyayev, G. Musiol, and H. Muehlig, *Handbook of Mathematics* [M]. Berlin: Springer, 2007.
- [157] Á. Bácsi and A. Virosztek, Low-frequency optical conductivity in graphene and in other scale-invariant two-band systems [J]. *Phys. Rev. B*, 2013, 87: 125425.
- [158] P. M. Krstajić, P. Vasilopoulos, and M. Tahir, Spin- and valley-polarized transport in a monolayer of MoS<sub>2</sub> [J]. *Phys. Rev. B*, 2016, 94: 085413.
- [159] V. Vargiamidis, P. Vasilopoulos, and G.-Q. Hai, Dc and ac transport in silicene [J]. *J. Phys.: Condens. Matter*, 2014, 26: 345303.
- [160] Y. Song and H. Dery, Transport theory of monolayer transition-metal dichalcogenides through symmetry [J]. *Phys. Rev. Lett.*, 2013, 111: 026601.

- [161] H. Shi, R. Yan, S. Bertolazzi, J. Brivio, B. Gao, A. Kis, D. Jena, H. G. Xing, and L. Huang, Exciton dynamics in suspended monolayer and few-Layer MoS<sub>2</sub> 2D crystals [J]. ACS Nano, 2013, 7: 1072.
- [162] L. Stille, C. J. Tabert, and E. J. Nicol, Optical signatures of the tunable band gap and valley-spin coupling in silicene [J]. Phys. Rev. B, 2012, 86: 195405.
- [163] E. J. Nicol and J. P. Carbotte, Optical conductivity of bilayer graphene with and without an asymmetry gap [J]. Phys. Rev. B, 2008, 77: 155409.
- [164] R. Piessens, E. deDoncker-Kapenga, C. W. Überhuber, D. K. Kahaner, QUADPACK: a subroutine package for automatic integration [M]. Berlin: Springer-Verlag, 1983.
- [165] B. Jensen, The frequency-dependent relaxation time of free carriers in InP [J]. J. Appl. Phys., 1979, 50: 5800.
- [166] M. Scheffler, M. Dressel, M. Jourdan, and H. Adrian, Extremely slow Drude relaxation of correlated electrons [J]. Nature, 2005, 438: 1135.
- [167] H. Liu and P. D. Ye, MoS<sub>2</sub> dual-gate MOSFET with atomic-layer-deposited Al<sub>2</sub>O<sub>3</sub> as top-gate dielectric [J]. Elect. Dev. Lett. IEEE, 2012, 33: 546.
- [168] S. Chuang, C. Battaglia, A. Azcatl, S. McDonnell, J. S. Kang, X. Yin, M. Tosun, R. Kapadia, H. Fang, R. M. Wallace, and A. Javey, MoS<sub>2</sub> P-type transistors and diodes enabled by high work function MoO<sub>x</sub> Contacts [J]. Nano Lett., 2014, 14: 1337.
- [169] N. T. Cuong, M. Otani, and S. Okada, Gate-induced electron-state tuning of MoS<sub>2</sub>: first-principles calculations [J]. J. Phys.: Condens. Matter, 2014, 26: 135001.
- [170] H. J. Krenner, E. C. Clark, T. Nakaoka, M. Bichler, C. Scheurer, G. Abstreiter, and J. J. Finley, Optically probing spin and charge interactions in a tunable artificial molecule [J]. Phys. Rev. Lett., 2006, 97: 076403.
- [171] O. Lopez-Sanchez, D. Lembke, M. Kayci, A. Radenovic, and A. Kis, Ultrasensitive photodetectors based on monolayer MoS<sub>2</sub> [J]. Nat. Nanotechnol., 2013, 8: 497-501.
- [172] H. S. Lee, S.-W. Min, Y.-G. Chang, M. K. Park, T. Nam, H. Kim, J. H. Kim, S. Ryu, and S. Im, MoS<sub>2</sub> nanosheet phototransistors with thickness-modulated optical energy gap [J]. Nano Lett., 2012, 12: 3695-3700.
- [173] Y. M. Xiao, W. Xu, B. Van Duppen, and F. M. Peeters, Infrared to terahertz optical conductivity of *n*-type and *p*-type monolayer MoS<sub>2</sub> in the presence of Rashba spin-orbit coupling [J]. Phys. Rev. B, 2016, 94: 155432.
- [174] K. F. Mak, K. L. McGill, J. Park, and P. L. McEuen, The valley Hall effect in MoS<sub>2</sub> transistors [J]. Science, 2014, 344: 1489.
- [175] K. He, N. Kumar, L. Zhao, Z. Wang, K. F. Mak, H. Zhao, and J. Shan, Tightly bound excitons in monolayer WSe<sub>2</sub> [J]. Phys. Rev. Lett., 2014, 113: 026803.

- [176] K. F. Mak, K. He, C. Lee, G. H. Lee, J. Hone, T. F. Heinz, and J. Shan, Tightly bound trions in monolayer MoS<sub>2</sub> [J]. *Nat. Mater.*, 2013, 12: 207-211.
- [177] H.-T. Chen, W. J. Padilla, J. M. O. Zide, A. C. Gossard, A. J. Taylor, and R. D. Averitt, Active terahertz metamaterial devices [J]. *Nature*, 2006, 444: 597-600.
- [178] L. Ju, B. Geng, J. Horng, C. Girit, M. Martin, Z. Hao, H. A. Bechtel, X. Liang, A. Zettl, Y. R. Shen, and F. Wang, Graphene plasmonics for tunable terahertz metamaterials [J]. *Nat. Nanotechnol.*, 2011, 6: 630-634.
- [179] F. H. L. Koppens, D. E. Chang, and F. J. Garcia de Abajo, Graphene plasmonics: A platform for strong light-matter interactions [J]. *Nano Lett.*, 2011, 11: 3370-3377.
- [180] Z. Fei, A. S. Rodin, G. O. Andreev, W. Bao, A. S. McLeod, M. Wagner, L. M. Zhang, Z. Zhao, M. Thiemens, G. Dominguez, M. M. Fogler, A. H. Castro Neto, C. N. Lau, F. Keilmann, and D. N. Basov, Gate-tuning of graphene plasmons revealed by infrared nano-imaging [J]. *Nature*, 2012, 487: 82-85.
- [181] T. Low and P. Avouris, Graphene plasmonics for terahertz to mid-infrared applications [J]. *ACS Nano*, 2014, 8(2): 1086-1101.
- [182] B. Wunsch, T. Stauber, F. Sols, and F. Guinea, Dynamical polarization of graphene at finite doping [J]. *New J. Phys.*, 2006, 8: 318.
- [183] E. H. Hwang and S. Das Sarma, Dielectric function, screening, and plasmons in two-dimensional graphene [J]. *Phys. Rev. B*, 2007, 75: 205418.
- [184] P. K. Pyatkovskiy, Dynamical polarization, screening, and plasmons in gapped graphene [J]. *J. Phys.: Condens. Matter*, 2009, 21: 025506.
- [185] B. Van Duppen, P. Vasilopoulos, and F. M. Peeters, Spin and valley polarization of plasmons in silicene due to external fields [J]. *Phys. Rev. B*, 2014, 90: 035142.
- [186] C. J. Tabert and E. J. Nicol, Dynamical polarization function, plasmons, and screening in silicene and other buckled honeycomb lattices [J]. *Phys. Rev. B*, 2014, 89: 195410.
- [187] H. Hatami, T. Kernreiter, and U. Zülicke, Spin susceptibility of two-dimensional transition-metal dichalcogenides [J]. *Phys. Rev. B*, 2014, 90: 045412.
- [188] F. Stern, Polarizability of a two-Dimensional electron gas [J]. *Phys. Rev. Lett.*, 1967, 18: 546.
- [189] A. Agarwal, M. Polini, G. Vignale, and M. E. Flatté, Long-lived spin plasmons in a spin-polarized two-dimensional electron gas [J]. *Phys. Rev. B*, 2014, 90: 155409.
- [190] D. Kreil, R. Hobbiger, J. T. Drachta, and H. M. Böhm, Excitations in a spin-polarized two-dimensional electron gas [J]. *Phys. Rev. B*, 2015, 92: 205426.
- [191] K. Kechedzhi and D. S. L. Abergel, Weakly damped acoustic plasmon mode in transition metal dichalcogenides with Zeeman splitting [J]. *Phys. Rev. B*, 2014, 89: 235420.

- [192] J. Ibañez-Azpiroz, A. Eiguren, E. Ya. Sherman, and A. Bergara, Spin-flip transitions induced by time-dependent electric fields in surfaces with strong spin-orbit interaction [J]. *Phys. Rev. Lett.*, 2012, 109: 156401.
- [193] T. Korn, S. Heydrich, M. Hirmer, J. Schmutzler, and C. Schüller, Low-temperature photocarrier dynamics in monolayer MoS<sub>2</sub> [J]. *Appl. Phys. Lett.*, 2011, 99: 102109.
- [194] A. Politano and G. Chiarello, Plasmon modes in graphene: status and prospect [J]. *Nanoscale*, 2014, 6: 10927.
- [195] P. F. Maldague. Many-body corrections to the polarizability of the two-dimensional electron gas [J]. *Surface Science*, 1978, 73: 296-302.
- [196] A. Tomadin, D. Brida, G. Cerullo, A. C. Ferrari, and M. Polini, Nonequilibrium dynamics of photoexcited electrons in graphene: Collinear scattering, Auger processes, and the impact of screening [J]. *Phys. Rev. B*, 2013, 88: 035430.
- [197] G. Kioseoglou, A. T. Hanbicki, M. Currie, A. L. Friedman, D. Gunlycke, and B. T. Jonker, Valley polarization and intervalley scattering in monolayer MoS<sub>2</sub> [J]. *Appl. Phys. Lett.*, 2012, 101: 221907.
- [198] X. Li, J. T. Mullen, Z. Jin, K. M. Borysenko, M. B. Nardelli, and K. W. Kim, Intrinsic electrical transport properties of monolayer silicene and MoS<sub>2</sub> from first principles [J]. *Phys. Rev. B*, 2013, 87: 115418.
- [199] R. J. Nicholas, M. Watts, D. F. Howell, F. M. Peeters, X.-G. Wu, J. T. Devreese, L. van Bockstal, F. Herlach, C. J. G. M. Langerak, J. Singleton, and A. Chevy, Cyclotron resonance of both magnetopolaron branches for polar and neutral optical phonon coupling in the layer compound InSe [J]. *Phys. Rev. B*, 1992, 45: 12144(R).
- [200] D. F. Howell, R. J. Nicholas, C. J. G. M. Langerak, J. Singleton, T. J. B. M. Janssen, and A. Chevy, Two-dimensional magnetopolaron coupling to both homopolar and longitudinal optic phonons in the layer compound InSe [J]. *J. Phys.: Condens. Matter*, 1989, 1: 7493.
- [201] Y. Zhan, Z. Liu, S. Najmaei, P. M. Ajayan, and J. Lou, Large-area vapor-phase growth and characterization of MoS(2) atomic layers on a SiO(2) substrate [J]. *Small*, 2012, 8(7): 966-971.
- [202] H. Yan, T. Low, W. Zhu, Y. Wu, M. Freitag, X. Li, F. Guinea, P. Avouris and F. Xia, Damping pathways of mid-infrared plasmons in graphene nanostructures [J]. *Nature Photon.*, 2013, 7: 394-399.
- [203] E. H. Hwang, R. Sensarma, and S. Das Sarma, Plasmon-phonon coupling in graphene [J]. *Phys. Rev. B*, 2010, 82: 195406.
- [204] K. Kaasbjerg, K. S. Thygesen, and K. W. Jacobsen, Phonon-limited mobility in *n*-type single-layer MoS<sub>2</sub> from first principles [J]. *Phys. Rev. B*, 2012, 85: 115317.

- [205] K. Kaasbjerg, K. S. Bhargavi, and S. S. Kubakaddi, Hot-electron cooling by acoustic and optical phonons in monolayers of MoS<sub>2</sub> and other transition-metal dichalcogenides [J]. Phys. Rev. B, 2014, 90: 165436.
- [206] B. Scharf, V. Perebeinos, J. Fabian, and P. Avouris, Effects of optical and surface polar phonons on the optical conductivity of doped graphene [J]. Phys. Rev. B, 2013, 87: 035414.
- [207] B. Scharf, V. Perebeinos, J. Fabian, and I. Žutić, Magneto-optical conductivity of graphene on polar substrates [J]. Phys. Rev. B, 2013, 88: 125429.
- [208] Ha-Jun Sung, Duk-Hyun Choe, and K. J. Chang, The effects of surface polarity and dangling bonds on the electronic properties of monolayer and bilayer MoS<sub>2</sub> on α-quartz [J]. New J. Phys., 2014, 16: 113055.
- [209] J. Schiefele, J. Pedrós, F. Sols, F. Calle, and F. Guinea, Coupling light into graphene plasmons through surface acoustic waves [J]. Phys. Rev. Lett., 2013, 111: 237405.
- [210] Y. Lin, X. Ling, L. Yu, S. Huang, A. L. Hsu, Y.-H. Lee, J. Kong, M. S. Dresselhaus, and T. Palacios, Dielectric screening of excitons and trions in single-layer MoS<sub>2</sub> [J]. Nano Lett., 2014, 14: 5569-5576.
- [211] E. J. G. Santos, and E. Kaxiras, Electrically driven tuning of the dielectric constant in MoS<sub>2</sub> layers [J]. ACS Nano, 2013, 7(12): 10741 – 10746.
- [212] Y. Liu and R. F. Willis, Plasmon-phonon strongly coupled mode in epitaxial graphene [J]. Phys. Rev. B, 2010, 81: 081406(R).
- [213] Z. Fei, G. O. Andreev, W. Bao, L. M. Zhang, A. S. McLeod, C. Wang, M. K. Stewart, Z. Zhao, G. Dominguez, M. Thiemens, M. M. Fogler, M. J. Tauber, A. H. Castro-Neto, C. N. Lau, F. Keilmann, and D. N. Basov, Infrared nanoscopy of dirac plasmons at the graphene-SiO<sub>2</sub> interface [J]. Nano Lett., 2011, 11: 4701-4705.
- [214] V. W. Brar, M. S. Jang, M. Sherrott, S. Kim, J. J. Lopez, L. B. Kim, M. Choi, and H. Atwater, Hybrid surface-phonon-plasmon polariton modes in graphene/monolayer h-BN heterostructures [J]. Nano Lett., 2014, 14: 3876-3880.
- [215] X. Yang, X.-T. Kong, B. Bai, Z. Li, H. Hu, X. Qiu, and Q. Dai, Substrate phonon-mediated plasmon hybridization in coplanar graphene nanostructures for broadband plasmonic circuits [J]. Small, 2015, 11(5): 591-596.

## 攻读博士期间发表论文、获得奖励与科研项目参与情况

### 科技论文发表情况：

- [ 1 ] Y. M. Xiao, W. Xu, B. Van Duppen, and F. M. Peeters. Infrared to terahertz optical conductivity of *n*-type and *p*-type monolayer MoS<sub>2</sub> in the presence of Rashba spin-orbit coupling [J]. Physical Review B, 2016, 94: 155432.
- [ 2 ] Y. M. Xiao, W. Xu, and F. M. Peeters. Infrared to terahertz absorption window in mono- and multi-layer graphene systems [J]. Optics Communications, 2014, 328: 135-142.
- [ 3 ] Y. M. Xiao and W. Xu, Terahertz optical conductance of *n*-type monolayer MoS<sub>2</sub> [J]. Integrated Ferroelectrics, 2014, 153(1): 171-176.
- [ 4 ] Y. X. Hou, W. Xu, J. G. Hu and Y. M. Xiao. Quantized acoustic-phonon modes in metallic nanowire structures [J]. Rare Metal Materials and Engineering, 2015, 44(12): 3019-3022.
- [ 5 ] W. L. Dou, W. Xu, S. H. Xu, G. T. Fei and Y. M. Xiao. Near-infrared reflection spectra of copper nanowire array structures [J]. Advanced Materials Research, 2015, 1118: 125-128.
- [ 6 ] Y. M. Xiao, W. Xu, F. M. Peeters, and B. Van Duppen. Multi-component plasmons in monolayer MoS<sub>2</sub> with circularly polarized optical pumping. (Submitted to PRB)

### 博士研究生阶段所获得奖励

- [ 1 ] 2015年国家建设高水平大学公派研究生联合培养项目奖学金，国家留学基金委
- [ 2 ] 2015年宝钢优秀学生奖，宝钢教育基金会
- [ 3 ] 2014年博士研究生国家奖学金，教育部
- [ 4 ] 2014年第十一届岳虹研究生奖学金一等奖，云南大学

**项目主持和参与情况：**

- [1] 主持云南大学校级项目研究生科研课题“新型二维电子气材料的光电特性”(ynuy201453)
- [2] 参与国家自然基金青年基金项目“亚波长金属-石墨烯复合结构中的强束缚混合模式及其在红外吸收器中的应用研究”(No. 11304272) (项目负责人：丁岚副教授)
- [3] 参与自然科学基金面上项目“强太赫兹激光和强磁场作用下二维电子气系统的基本磁光电特性研究”(No. 11574319) (项目负责人：徐文教授)
- [4] 参与科技部国家重大科学仪器设备开发专项“相干强太赫兹源科学仪器设备开发项目”(2011YQ130018)(项目子负责人：徐文教授)
- [5] 参与云南省高端科技人才引进计划项目(项目负责人：徐文教授)
- [6] 参与云南省海外高层次人才引进计划项目(项目负责人：徐文教授)

## 致    谢

自从二零零六年我开始到云南大学进行学习，到现在已经是第十一个年头了。通过这么多年来的学习，我从由对知识和科学的研究的憧憬到现在一步一步迈入科学的研究的领域并初窥门径。在这个期间，如果没有众亲友的鼓励和支持，没有各位老师的指导和帮助，我是无法一步一步顺利的走到今天的。正是有了众多人对我的关心和帮助，本博士论文才得以圆满完成。

我要特别感谢我的导师徐文教授。徐文教授学识渊博，具有前瞻性的国际化科研视野，在跟随徐文教授近 7 年时间的学习期间，他不厌其烦的给我解惑授业，使我获益匪浅。正是由于他的鼓励与支持，我才能一步一步的走到今天并完成博士阶段的学业。感谢徐老师在我研究生学习阶段所付出的大量心血。在毕业后的学习和科研工作中，一定不忘导师的教诲，争取取得更好的成绩。

我博士学位论文的完成也同样离不开联合培养项目中外方导师给予的支持和帮助。感谢比利时安特卫普大学的 F. M. Peeters 教授给我提供了宝贵的在比利时安特卫普大学凝聚态理论组进行为期一年博士生联合培养的学习机会并感谢国家留学基金委的资助。Peeters 教授是本领域在国际上十分具有影响力的物理学家，在他的组里的学习经历进一步的提高了我对先进研究方法的掌握和加深了我对本领域的认识。感谢 F. M. Peeters 教授和 Ben Van Duppen 博士在我博士学习期间对我悉心的指导，在不断的学习和讨论中，我不仅完成了博士论文中的部分研究课题，也使我自身在这个过程中得到了显著的提高。

感谢物理与天文学院的张晋老师、何垚老师、刘铸老师、王毓德老师、李云德老师、丁岚老师、王登科老师等在课堂上的授课解惑以及学业上给我提供的帮助。感谢学校和学院所有给我授课及帮助的老师，没有他们的关心和支持，我是难以完成博士阶段的学业的。

感谢实验室的同门以及和我一起生活和学习的同学们。尤其是在博士研究生学习阶段，他们的陪伴使得博士阶段的生活丰富多彩。

感谢我的父母及所有亲人对我一如既往的支持。他们对我的成长和学业付出了太多太多。唯有在以后的工作和生活中加倍努力和奋斗，才能不负他们对我的期望。

最后，向所有关心和支持我的人再次表示由衷的谢意！

# Curriculum Vitae

Address: 2 Cuihu Beilu, Wuhua District, 650091 Kunming  
Room 207, Physical Building, Yunnan University

Phone number: +86-15087197010

Email: yiming.xiao@foxmail.com

Photo:



## Basic information

Name: Yiming Xiao  
Birthday: July 31, 1989  
Nationality: Chinese

Gender: Male  
Place of birth: Hanchuan, Hubei  
Major: Condensed Matter Physics

## Education

- 2013.09-2017.07 **PhD student**, Yunnan University, School of Physics and Astronomy, Condensed Matter Physics, Supervisor: Prof. Dr. Wen Xu.
- 2015.12-2016.12 **Joint PhD visiting**, Universiteit Antwerpen, Condensed Matter Theory, Supervisors: Prof. Dr. F. M. Peeters, Dr. Ben Van Duppen.
- 2010.09-2013.06 **Master in Science**, Yunnan University, School of physical science and technology, Condensed Matter Physics, Supervisor: Prof. Dr. Wen Xu.
- 2006.09-2010.06 **Bachelor in Science**, Yunnan University, School of physical science and technology, Basis of Mathematics and Physics (Physical orientation).

## Language skill

Chinese (native), English (fluent)

## Research skills

Necessary analytical, numerical and graphing skills such as Fortran programming, Origin graphing, Latex Lettering, ect.

## Research interests

Theoretical investigations of the electronic, optical, optoelectronic properties of atomic layer two dimensional electron gas (2DEG) systems, eg., optical conductivity/absorption, plasmon.

## Awards

- 2015 Joint PhD Programme CSC scholarship awarded by China Scholarship Council  
2015 Baosteel excellent student award, Baosteel Education Foundation

- 2014 National scholarship for PhD students awarded by Ministry of Education of China  
 2014 First grade Yuehong graduate students scholarship awarded by Yunnan University  
 2013 Scientific research awards Donglu Yingcai scholarship awarded by Yunnan University  
 2012 Second grade Yuehong graduate students scholarship awarded by Yunnan University  
 2012 Second grade Outstanding graduate students scholarship awarded by Yunnan University

### Publication list

1. **Y. M. Xiao**, W. Xu, F. M. Peeters, and B. Van Duppen, *Multi-component plasmons in monolayer MoS<sub>2</sub> with circularly polarized optical pumping.* (Submitted to PRB)
2. **Y. M. Xiao**, W. Xu, B. Van Duppen, and F. M. Peeters, *Infrared to terahertz optical conductivity of n-type and p-type monolayer MoS<sub>2</sub> in the presence of Rashba spin-orbit coupling.* **Physical Review B** **94**, 155432 (2016).
3. **Y. M. Xiao**, W. Xu, and F. M. Peeters, *Infrared to terahertz absorption window in mono- and multi-layer graphene systems.* **Optics Communications** **328**, 135-142 (2014).
4. **Y. M. Xiao** and W. Xu, *Terahertz Optical Conductance of n-type Monolayer MoS<sub>2</sub>.* **Integrated Ferroelectrics** **153:1**, 171-176 (2014).
5. **Y. M. Xiao**, W. Xu, Y. Y. Zhang and F. M. Peeters, *Optoelectronic properties of ABC-stacked trilayer graphene.* **Phys. Status Solidi B** **250:1**, 86-94 (2013).
6. **Yiming Xiao**, Wen Xu, Yaya Zhang and Jiaguang Hu, *Terahertz plasmon and surface-plasmon modes in hollow nanospheres.* **Nanoscale Research Letters** **7**, 578 (2012).
7. Y. X. Hou, W. Xu, J. G. Hu and **Y. M. Xiao**, *Quantized Acoustic-Phonon Modes in Metallic Nanowire Structures.* **Rare Metal Materials and Engineering** **44** (12), 3019-3022 (2015).
8. W. L. Dou, W. Xu, S. H. Xu, G. T. Fei and **Y. M. Xiao**, *Near-infrared reflection spectra of copper nanowire array structures.* **Advanced Materials Research** **1118**, 125-128 (2015).
9. Yaya Zhang, Wen Xu, Shaohui Xu, Guangtao Fei, **Yiming Xiao** and Jiaguang Hu, *Optical properties of Ni and Cu nanowire arrays and Ni/Cu superlattice nanowire arrays.* **Nanoscale Research Letters** **7**, 569 (2012).
10. J. G. Hu, W. Xu, **Y. M. Xiao** and Y. Y. Zhang, *The two-dimensional phononic crystal band gaps tuned by the symmetry and orientation of the additional rods in the center of unit cell.* **ACTA PHYSICA SINICA** **61**, 234302 (2012).
11. Y. Y. Zhang, **Y. M. Xiao**, G. T. Duan, F. H. Su, W. P. Cai and W. Xu, *Optical Properties of Gold Nanosphere Arrays Formed on Polystyrene Templates.* **Integrated Ferroelectrics** **136:1**, 66-70 (2012).